EXPLORING THE MECHANISMS BEHIND NONDIFFUSIVE TRANSPORT IN A SIMPLE TURBULENCE MODEL

By

Douglas Ogata

A Dissertation Submitted in Partial Fulfillment of the Requirements

for the Degree of

Doctor of Philosophy

in

Physics

University of Alaska Fairbanks

May 2017

APPROVED:

David Newman, Committee Chair
Raul Sánchez, Committee Member
Renate Wackerbauer, Committee Member
Chung-Sang Ng, Committee Member
Renate Wackerbauer, Chair
Department of Physics
Paul Layer, Dean
College of Natural Science and Mathematics
Michael Castellini, *Dean of the Graduate School*

Abstract

Elements for nondiffusive transport have been identified in a plasma turbulence model based on the slab drift-wave model. Motivated by the self-organized criticality paradigm, a standard set of drift-wave equations in doubly-periodic spatial domain has been elevated to include a flux-driven background profile with critical gradients. The profile is maintained by the turbulence induced flux from the source to the sink. Tracers that follow the Lagrangian trajectories are the primary transport characterization technique. The competition between down-gradient relaxations and self-generated flows highlights the dual reactions to local steepening of profile gradients, which leads to different transport regimes. An additional external sheared flow further inhibits down-gradient transfer and acts as another critical threshold condition that can lead to flow-driven instabilities.

Superdiffusive transport is observed primarily when radial relaxation events dominate while subdiffusive character become more prominent with self-generated and external poloidal flows. Diffusive transport exists when the superdiffusive and subdiffusive components are in balance. The interplay between turbulent relaxation and self-generated sheared poloidal flows, that form the basis for the transport explored in this model, is absent unless a flux-driven setup is used. Most of the rich dynamics were not present when running the simplified model without an equation for background profile evolution.

Nondiffusive transport characteristics can also be recovered from a passive scalar field that is advected by the turbulent flow with an inherent diffusivity. The spread of a highly localized cloud of tracers and a passive scalar field reasserts the equivalence between the Lagrangian and quasi-Lagrangian frames. The coincidence between the passive scalar field with the tracers provide a regime of validity where existing experimental technique can be used to characterize transport from two-dimensional experimental data.

The results from this work highlight the key features of flux-driven turbulent transport leading to nondiffusive transport. Specifically, the dual reactions to the local steepening of profile gradients exposes the multiscale feature of turbulent transport that becomes more apparent under a flux-driven profile. The quantification of nondiffusive transport characteristics from the evolution of a passive scalar can have important implication towards the fundamental understanding of fluid turbulence and turbulent transport.

Table of Contents

List of Figures

List of Tables

List of Appendices

Acknowledgements

The recognition is separated primarily into the professional and personal dimensions; though, there are individuals who belong in both dimensions. Here, I recognize the specific individuals who had significantly impacted me through this journey and, directly and indirectly, contributed to the completion of this thesis. Firstly, I recognize the funding sources for the invaluable opportunity. Secondly, I express my gratitude for the individuals in my professional dimension. Thirdly, I credit the individuals who have, in several ways, enriched this journey personally. This work would not be possible without the support from these particular individuals.

This work was supported in by US DOE contract number DE-FG02-04ER54741 with UAF and in part by a grant of HPC resources from the Arctic Region Supercomputing Center at the University of Alaska Fairbanks. This material is also based upon work supported by the U.S. Department of Energy, Office of Science, Office of Workforce Development for Teachers and Scientists, Office of Science Graduate Student Research (SCGSR) program. The SCGSR program is administered by the Oak Ridge Institute for Science and Education (ORISE) for the DOE. ORISE is managed by ORAU under contract number DE-AC05-06OR23100.

Secondly, I credit my committee members starting with my advisor D. Newman for the opportunity, guidance, counsel, patience, and support over several years; R. Sánchez for the counsel, patience, and for initially introducing me to this topic; R. Wackerbauer for counsel and motivational remarks that kept me afloat; and C.-S. Ng for keeping me honest. I credit U. Bhatt for invaluable comments on my writing. I thank the past and present UAF Physics Department and its affiliates who have guided me; A. Otto, C. Price, J. Olson, C. Szuberla, A. Chowdhury, J. Talbot, H. Zhang, A. Rybkin, S. Avdonin, and D. Maxwell. I also recognize the individuals in the administrative positions who patiently walk me through the logistics; S. Stevens, J. Armstrong, and E. Craig. Next, I recognize the individuals in my professional dimension who have contributed to the entire experience; J. Reynolds-Barredo, S. Panta, H. Hartle, and J. Nicolau. I also thank the individuals who were at Princeton Plasma Physics Laboratory (PPPL) during my visit for invaluable discussions; S. Zweben, A. Diallo, D. Stotler, T. Wilks, J. Krommes, T. Stoltzfus-Dueck, and J. Maddox.

In the personal dimension, I am eternally grateful for my immediate family for their unconditional support; J. Ogata, S. Ogata, and C. Ogata. I recognize the following individuals who have invariably added colors and textures into this journey; C. Christensen, D. Damba, D. Chu, C. Chu, C. Frare, J. Power, A. Gädeke, M. Copper, J. LaFranceschina, M. Graybill, J. DiTommaso, A. Winkleman, R. Edon, C. Bodily, C. Alvizuri, and I. Rutzen. Lastly, I credit the individuals of HHS 2-20 FA 4ID OIF 03/04.

Chapter 1 Introduction

Tokamak design for terrestrial nuclear fusion becomes unstable under relevant fusion conditions due to the required and unavoidable density and temperature gradients. To put this in perspective, the challenge of the next generation tokamak ITER is one of the greatest engineering tasks of all time[1]. The central magnet of ITER must withstand a force of about $6 \times 10^7\, N$, which is twice the peak thrust of a Saturn V rocket at $3.3 \times 10^7\, N$[2]. The core temperature must reach above $2.3 \times 10^8\, K$, which is an order of magnitude hotter than the center of the Sun at $1.5 \times 10^7\, K$. Large disruption events can rapidly quench plasma confinement by expelling energy to the containment vessel, which becomes detrimental to the material and structural integrity of a fusion device. Sustained confinement is also another key issue that limits the feasibility of nuclear fusion in a tokamak configuration[3–5]. Due to turbulence, the transport rates for prolonged operation can be greater than particle collision, which tends to effectively relax density and temperature gradients required for sustained nuclear fusion conditions. Hence, there is a need to understand plasma turbulence and, more importantly, transport due to plasma turbulence in order to improve plasma confinement under fusion conditions. The existing complexity of interactions in confined plasma makes the task of simulating every single particle and its interaction for practical applications computationally expensive and often intractable. Accurate and precise predictions based on fundamental plasma equations seldom yield timely results such as transport fluxes in order to guide device operation. Hence, there is a strong interest in developing reduced transport models or low-dimensional models that can explore dynamics to understand turbulent transport in the context of plasma prediction and control. The limited success of existing transport models is due primarily to their reliance on the diffusive paradigm, which does not include the lack of extended correlations between disparate scales. In addition, experimental results suggest that transport in regimes suitable for plasma confinement exhibit characteristics that are not in the standard classical diffusive paradigm. This has motivated a complimentary approach allows the construction of effective transport models based on the self-organized criticality (SOC) paradigm. The SOC approach applied to nonequilibrium systems represents a more feasible and practical approach towards constructing effective transport models.

In fusion plasmas, turbulence is a natural consequence of the steep gradients supported by the magnetic topology required to maintain hot plasmas far from equilibrium. Due to the efficient mixing induced by turbulence that tends to restore the plasma to equilibrium, plasma turbulence generally degrades plasma confinement where the transport associated with turbulence limits the performance of tokamak devices in most operating regimes[6]. In order to achieve sustainable fusion conditions, a significant understanding of turbulence and turbulent transport is required to predict, mitigate, and control transport due to turbulence. There is a trend towards understanding plasma turbulence globally in

contrast to previous analyses that focused on linear instabilities. A paradigm that allows probing into nonequilibrium systems is the SOC perspective, which embodies a group of properties for driven nonequilibrium systems near marginal stability. The nonlinear interaction between the input power and the turbulence naturally causes the plasma profiles to be close to marginal. Under the SOC paradigm for turbulent transport, the nondiffusive transport framework has been developed to account for the transport properties evident in SOC systems. The trend towards a more general approach is supported by observation throughout nuclear fusion history that transport measurements deviate from the fundamental paradigm for conventional diffusive transport[7]. Although this thesis is focused on tokamak fusion plasmas, the interpretation has broader applications due to the inference of SOC dynamics.

This thesis is based on several paradigms with the ultimate goal of achieving sustainable terrestrial nuclear fusion. The following sections motivate the work performed in this thesis by introducing the relevant paradigms beginning with a brief summary of the tokamak design for nuclear fusion in Sec. 1.1, which then leads into the required computational challenge and the need for low-dimensional transport models in Sec. 1.1.1. The turbulent transport paradigm is then introduced in Sec. 1.2 with a subsection on the commonly used drift-wave paradigm in Sec. 1.2.1. The SOC paradigm is then introduced as a complimentary approach towards understanding turbulent transport in Sec. 1.3 with an emphasis on the nondiffusive transport framework in Sec. 1.3.1. The nondiffusive framework then leads into a discussion about transport diagnostics pertaining to this thesis using the tracers in Sec. 1.3.2 and a passive scalar in Sec. 1.3.3. The introduction then ends with an outline of the following chapters in Sec. 1.4.

1.1 Nuclear fusion basics

Nuclear fusion promises to provide an almost limitless supply of power that can theoretically fuel societal growth. The energy production process resembles the nuclear reaction that naturally occurs in the core of stars. Nuclear fusion energy comes from the fusing of light nuclei. Several competing approaches and devices have been built to harness atomic energy for power generation. Due to the relatively high reaction cross-section at somewhat attainable average temperatures, the most common nuclear reaction of interest for sustainable nuclear fusion is the deuterium and tritium (D-T) reaction;

$$ {}^{2}_{1}\mathrm{H}(20\,\mathrm{keV}) + {}^{3}_{1}\mathrm{H}(20\,\mathrm{keV}) \rightarrow {}^{4}_{2}\mathrm{He}(3.5\,\mathrm{MeV}) + {}^{1}_{0}\mathrm{n}(14.1\,\mathrm{MeV}). $$

The attractive aspect of this reaction is the energy amplification on the order of ~ 700 from the initial energy investment. The D-T reaction is favored due to the relatively high fusion reactivity $\langle \sigma v \rangle$ and a broad maximum at about 60 keV (Fig. 1.1). The averaged reactivity is generally defined as $\langle \sigma v \rangle = \int_0^\infty \sigma(v) v f(v)\, dv$, which is the integral over the cross-section

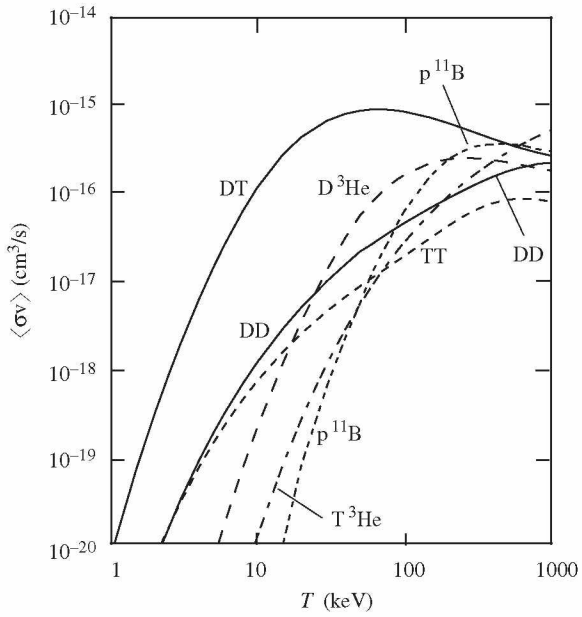

Figure 1.1: The average fusion reactivity $\langle \sigma v \rangle$ for D-T reaction peaks at smaller thermal energy compared to other fusion reactions such as D-D or D-^{3}He[8].

of the reaction $\sigma(v)$ for all relative velocities v and over the distribution of particles $f(v)$ [8]. The particle distribution $f(v)$ is usually modeled as the Maxwell-Boltzmann distribution function. The average reactivity provides a measure of the probability of reaction per unit time and per unit density. The next most probable fusion reaction is the deuterium and deuterium (D-D) reaction at temperatures less than 25 keV (Fig. 1.1). The deuterium and Helium-3 reaction (D-^{3}He) is the second most probable reaction at moderately large temperatures $25\,\text{keV} < T < 250\,\text{keV}$ (Fig. 1.1). The D-T reaction may become less favorable at higher fuel temperatures due to the decrease in $\langle \sigma v \rangle$ compared to other reactions that increase with higher temperatures.

With the average fuel temperatures reach around 20 keV, the state of matter becomes plasma where the bulk medium is ionized. Exploiting the property that charged particles, momentum and heat move more rapidly along a magnetic field, fusion is achieved using the magnetic confinement concept. A common measure for the success of sustained nuclear fusion is the "ignition" concept, which is interpreted from Lawson's criterion[9]. Ignition occurs when the plasma is self-heated by the byproduct α particles. Using a zeroth order estimate, the alpha heating rate exceeds the plasma energy loss rate for ignition to occur. This provides a rough estimate for the necessary ion density n_i, ion temperature T_i, and confinement time τ_E. The combination of these quantities $n_i T_i \tau_E$ must be larger than a critical value of around $3 \times 10^{21}\, keV \cdot s/m^3$ [10]. The trend in the triple product naturally coincides with the increasing computational capabilities as shown in Fig. 1.2. The confinement time τ_E is intrinsically associated with the thermal relaxations time, which is

primarily determined by losses through turbulent transport.

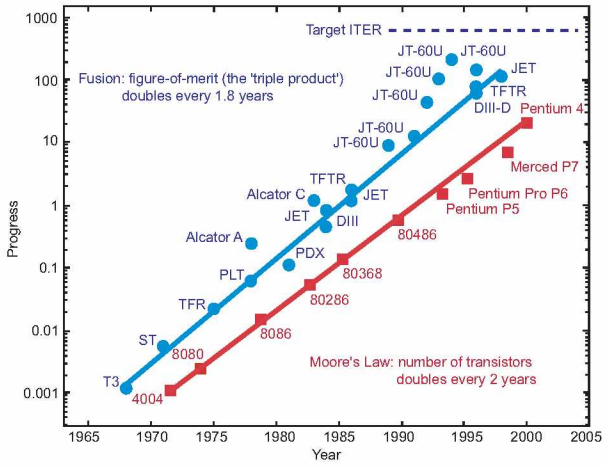

Figure 1.2: The fusion power performance measure or the triple product ($n_i T_i \tau_E$) highlights the performance from various tokamak device naturally linked to the increase in computational capabilities. The next generation tokamak, ITER, aims to have a performance that gives $n_i T_i \tau_E \sim 3 \times 10^{21}\, keV \cdot s/m^3$ [11].

The necessary high temperature for nuclear fusion presents an immediate challenge for confinement. Plasma interacts with the confining electromagnetic fields that can then lead to unstable behaviors where the plasma tend to rearrange and relax to a lower energy state. Naturally, nuclear fusion reaction is extinguished as the plasma achieves a lower energy thermodynamically favored state. In effect, more external energy is required to maintain the plasma at a high temperature, which consequently fuels more instabilities. The instabilities act as potential energy channels for the plasma to lower its energy state.

The tokamak configuration is one of the several competing device designs used to achieve sustainable nuclear fusion [12,13]. Historically, the preference for the tokamak design for magnetic confinement over stellerators and magnetic mirrors has historical roots in the 1970's [14]. Electromagnets are used to generate magnetic fields to confine ionized gas or plasma in a vacuum vessel that resembles a large donut. Initially, a gas such as D-T mix is injected in a vacuum on the order of 10^{-12} Torr. The plasma is heated to high temperatures ($\sim 10\,$keV), initially by a current and then by auxiliary heating schemes such as microwave heating and neutral particle injection. External heating methods such as wave heating or neutral beams are required because of the inverse dependence of plasma resistivity on its temperature $\eta \propto T^{-3/2}$. The shape of the machine creates a large magnetic trap where magnetic field lines form a set of nested surfaces called magnetic flux surfaces (Fig. 1.3). The magnetic field lines are usually described according to the spatial coordinates: the toroidal direction ϕ around the torus, the angular coordinate poloidal direction θ in a plane perpendicular to ϕ, and the coordinate for radial direction r as shown schematically in Fig. 1.3. The radial outward direction is usually referred to as the radial direction increasing

from the major radius R towards the larger torus radius $R+a$. The minor radius is usually denoted by a, and the major radius is R. The toroidal magnetic field B_ϕ is generated by external poloidal electromagnets while the poloidal field B_θ comes from the plasma current. The combined magnetic fields create a helical twist of nested magnetic surfaces with different winding number of the field lines that depend on the safety factor $q(r) = \boldsymbol{B} \cdot \nabla\phi / \boldsymbol{B} \cdot \nabla\theta$. The helical twist in the magnetic fields also compensate for particle drifts outwards towards the vacuum vessel wall. Without the twisted field lines, the particle drifts would generate a vertical electric field, which would then cause a net outward radial velocity due to the strong axial symmetric magnetic field[12]. Due to this magnetic configuration, the inboard side of the torus $R - a < r < R$ is stable while the outboard side $R > r > R + a$ is susceptible to instabilities that tend to yield radially outward transport. The radial profile of $q(r)$ creates a magnetic field topology that aids plasma confinement. At the edge of the device, the magnetic field lines terminate by plasma facing components. The region where the magnetic field lines transition from closed to open is referred to as the separatrix.

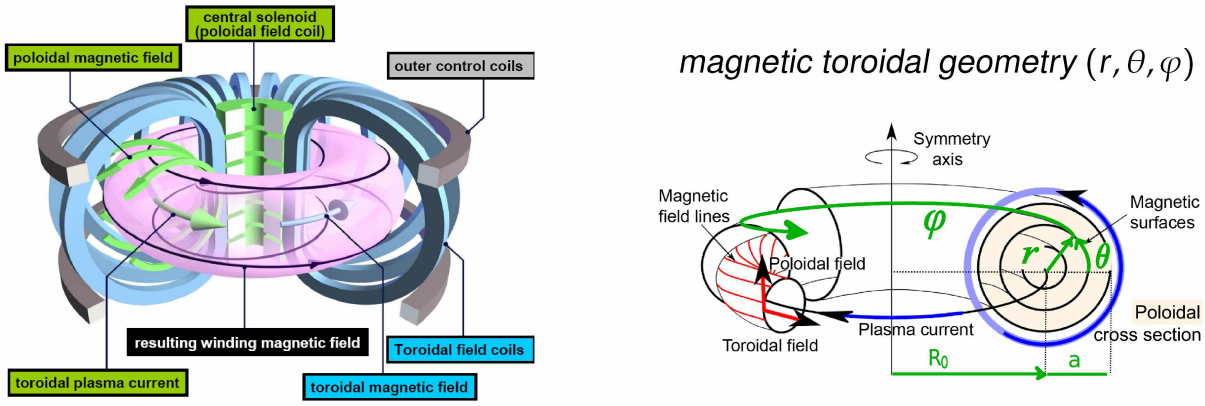

Figure 1.3: Tokamak magnetic field topology generated by electro-magnets creates a helical twist of magnetic surfaces (left). Typical toroidal coordinates define ϕ as the toroidal angle, θ as the poloidal angle, and r as the minor radius (right)[15].

Sufficiently heated plasmas reach a regime called the low-confinement regime or "L-mode", which is characterized by stiff temperature profiles[13]. However, the confinement empirically degrades with increasing heating power $\tau_E \propto P^{-0.5}$ where P is measured in MW[14]. A better confinement operational regime known as the high confinement or "H-mode" is achieved when a large enough heating power is deposited in the tokamak plasma[16,17]. This regime of improved confinement almost doubles the confinement time and has been attributed to power thresholds and strongly associated with divertor tokamaks that has a magnetic separatrix[18]. The H-mode advanced operational regime can be accessed in different confinement devices with different types of heating sources[14]. The confinement in this regime is usually characterized by steep density and temperature gradients at the plasma edge (Fig. 1.4), which is associated with the creation of an edge transport

barrier with a typical width on the order of cm[18]. Fluctuations in the edge region also decreased significantly as compared to the fluctuations in the L-mode confinement regime (Fig. 1.4). The transition from L-mode to H-mode is attributed to the generation of poloidal sheared flow[18,19], which acts as a mechanism to decorrelate the transport from the core to the edge. The steepening of the profiles near the edge consequently corresponds to an increase in the density and temperature in the core, which provides more suitable conditions for nuclear fusion. However, due to the steeper pressure and current gradients associated with the H-mode, the free energy becomes sufficiently large enough to drive instabilities that then transport the energy from the core to the edge of the device in the form of quasi-periodic oscillations called edge-localized-modes (ELMs)[13]. The ELMs can result in catastrophic heat loads on the divertor and complete loss of plasma confinement.

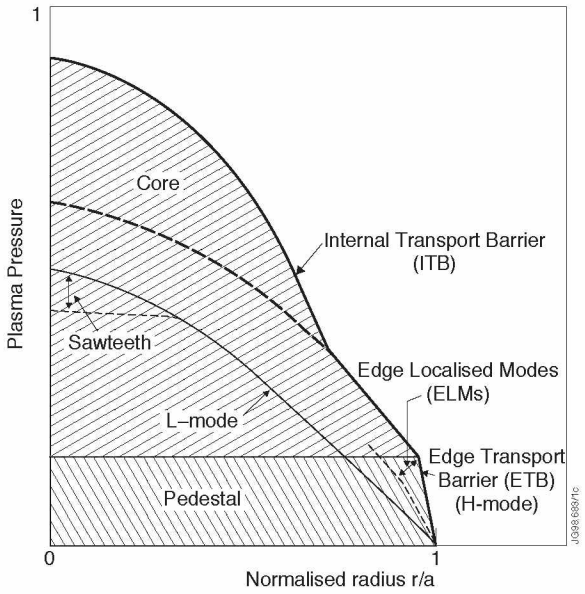

Figure 1.4: The plasma pressure profile corresponding to most advanced operational regimes is associated with transport barriers. H-mode confinement regime shows a peaked core temperature due to a transport barrier as compared to the L-mode operational regime[20].

The anisotropic background magnetic geometry in the tokamak design creates a distinguishing feature in tokamak turbulence from neutral fluids, which affects the character and the evolution of turbulence. Low frequency perturbations that have long wavelength character occur in the toroidal direction while turbulence in the perpendicular direction extends to the Larmor radius scale, which is on the order of the gyroradius of a charged particle in the presence of a uniform magnetic field. In addition, core plasmas tend to be weakly collisional with typical mean free paths larger than the system size. Waves are prominent in tokamak plasmas due to the large free-energy sources such as through current density and pressure gradients. Turbulence is responsible for most of the particle and energy transport across magnetic field lines. Typically, waves that contribute to turbulence occur

at frequencies below the ion cyclotron frequency and often exhibit electrostatic character. The broad category of drift-waves is the most prominent area of study due to the excitation from density and temperature gradients.

In next-generation tokamak facilities such as ITER, plasma disruptions are capable of producing large heat fluxes that can damage in-vessel components, coils, and the vacuum vessel. In order to minimize risk in tokamak devices, the ability to predict and mitigate plasma disruptions will ensure the success of magnetically confined plasma for nuclear fusion. Since the discovery of the H-mode, other advanced operational regimes have also been discovered that give better confinement than the L-mode regime. Advanced operational regimes are usually achieved with the formation of transport barriers[14], which is also shown in the cartoon of the plasma profile in Fig. 1.4. Therefore, accurate predictions of plasma characteristics during device operation is of great interest in order to achieve the desired ignition condition for sustainable terrestrial nuclear fusion. Although recent computational advances have enabled numerical simulations to play an increasing role in understanding fusion plasmas, limitations on computational capabilities still necessitate complimentary modeling strategies and paradigms of understanding.

1.1.1 Computational challenge in tokamak plasmas

Since the 1950's, the pursuit for sustainable nuclear fusion has been one of the scientific and technological challenges in the twentieth and twenty-first century. The complex coupling between the particles and the long-range fields give rise to collective dynamics such as a variety of waves and instabilities. Relevant physics such as transport of particles and energy often span over ten decades of space and time scales. Although the fundamental physics governing these processes such as Maxwell's equations are well known, the coupling between various scales limit tractable solutions under realistic conditions. The success of the magnetic confinement depends on the integrated validation between experiment and theory with the aid of high-performance computing.

Magnetically confined plasma for nuclear fusion is characterized by a variety of space and time scales (Fig. 1.5). The spatial scales come from electron orbit ($\sim 10^{-5}\,\mathrm{m}$) to the distance along magnetic field lines ($\sim 100\,\mathrm{m}$). The time scale varies from the electron orbit ($\sim 10^{-11}\,\mathrm{s}$) to the diffusion time of electrical current through the plasma ($\sim 10^{2}\,\mathrm{s}$)[21]. The most comprehensive approach is to solve the equations of motion for all particles exposed to external and self electromagnetic fields. This method can be categorized as the Klimontovich-Maxwell or Newton-Maxwell system[22]. The particle dynamics easily become impossible to evolve when considering a realistic tokamak plasma which usually contains $10^{22} - 10^{23}$ particles. This limitation on existing computational ability then leads to approximations and need for a hierarchal modeling approach. A conventional approach to the plasma model hierarchy begins with the kinetic model, which derives from the Klimontovich or Newton description of particles. The kinetic model is a statistical treatment of the single

specie particle phase space $f_\alpha(\boldsymbol{r}, \boldsymbol{v}, t)$ at position $\boldsymbol{r}$ with velocity $\boldsymbol{v}$ at time t leading to the Maxwell-Boltzman system of equations[22],

$$\frac{\partial f_\alpha}{\partial t} + \boldsymbol{v} \cdot \frac{\partial f_\alpha}{\partial \boldsymbol{r}} + \frac{q_\alpha}{m_\alpha} (\boldsymbol{E} + \boldsymbol{v} \times \boldsymbol{B}) \cdot \frac{\partial f_\alpha}{\partial \boldsymbol{v}} = \sum_\beta C(f_\alpha, f_\beta) + \sum_\alpha S(f_\alpha) \tag{1.1}$$

where the particle density is defined as the zeroth moment in velocity space

$$\rho(\boldsymbol{r}, t) = \sum_\alpha q_\alpha \int f_\alpha(\boldsymbol{r}, \boldsymbol{v}, t)\, d\boldsymbol{v} \tag{1.2}$$

and the current density is the first velocity moment

$$\boldsymbol{J}(\boldsymbol{r}, t) = \sum_\alpha q_\alpha \int \boldsymbol{v} f_\alpha(\boldsymbol{r}, \boldsymbol{v}, t)\, d\boldsymbol{v}. \tag{1.3}$$

Particle and field interactions are separated into microscopic scales involving particle collisions represented by the collision operator $C(f_\alpha, f_\beta)$ and long-range interaction through the electromagnetic fields as described by the standard Maxwell equations

$$\begin{aligned} \boldsymbol{\nabla} \times \boldsymbol{B} &= \mu_0 \boldsymbol{J} + \mu_0 \epsilon_0 \frac{\partial \boldsymbol{E}}{\partial t} \\ \boldsymbol{\nabla} \times \boldsymbol{E} &= -\frac{\partial \boldsymbol{B}}{\partial t} \\ \boldsymbol{\nabla} \cdot \boldsymbol{E} &= \frac{\rho}{\epsilon_0} \\ \boldsymbol{\nabla} \cdot \boldsymbol{B} &= 0 \end{aligned} \tag{1.4}$$

At high temperatures, such as in the core of tokamak plasmas ($\sim 10\,\mathrm{keV}$), particle Coulomb collisions are responsible for momentum and energy exchanges that scale as $T^{-3/2}$ [12]. Consequently, collisions provide a smaller contribution to the transport and occur on longer time scales compared to the plasma at lower temperatures. Charged particles experience resonant interactions with the electromagnetic field in weakly collisional plasmas, which requires the evolution of the Vlasov equation (Eq. 1.1) coupled to Maxwell equations (Eq. 1.4). The Vlasov-Maxwell system describes a six-dimensional problem (three spatial directions and three velocity dimensions) and provides the most fundamental description of a high-temperature collisionless plasma. Particle collisions involving exchange of momentum and energy become more prominent when plasma becomes denser and/or colder such as in the edge regions. Collisional effects tend to attenuate local phase-space singularities. As collisions become important, the Fokker-Plank equation becomes the preferred model. In this model, a collision operator $C(f_\alpha, f_\beta)$ simulates the small angle Coulomb scattering and can account for inelastic scattering of impurities such as ionization, recombination, and charge exchange.

Even though the Vlasov-Maxwell system is a reduced kinetic description compared

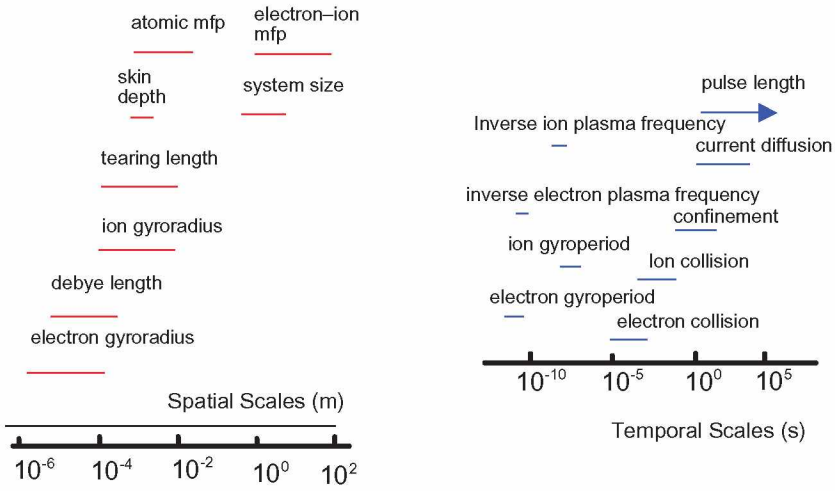

Figure 1.5: Typical space and time scales in magnetically confined plasmas for nuclear fusion[23].

to the Klimontovich-Maxwell system, it still involves a large range of spatial and temporal scales that need to be resolved (Fig. 1.6). In order to make the problem more tractable, the six dimensional Vlasov or Fokker-Planck equations for each species are often reduced to five-dimensional gyrokinetic equations that tracks three spatial gyro-center coordinates, one parallel velocity, and the adiabatic invariant[24,25]. The gyrokinetic model reduces the computational cost by gyro-averaging the Vlasov equation; averaging over the high-frequency contribution due to gyro-motion of particles[24]. The model then describes the evolution of a distribution of particle guiding centers in five dimensional phase space. The applicability regime of the gyrokinetic model compared to other approaches is shown in Fig. 1.6. The intrinsic nonlinear character still imposes a larger number of grid points, which requires the most robust high performance computing environment.

Fluid equations are more suitable to describe interactions on large spatial scales and at low frequencies. The fluid model is derived by averaging the kinetic equations over the velocity space and separate the dynamics for different species, particularly ions and electrons. A hierarchy of fluid equations emerge as velocity moments of the kinetic equations, which leads to an ongoing discussion in modeling with connections to the study of neutral fluids. The magnetohydrodynamic (MHD) equations describe a single fluid macroscopic model and is obtained by further approximations on the fluid equations. The MHD model is useful in studying plasma equilibrium and stability. An example of the range of validity for corresponding simulation models is shown in Fig. 1.7.

According to the report on Integrated Simulations submitted at the request of U.S. Department of Energy (DOE) Office of Fusion Energy Sciences (FES) in 2015[26], the U.S. nuclear fusion community has assessed the recent progress in magnetic fusion design and identified outstanding challenges in integrated modeling: (1) disruption physics, (2) plasma

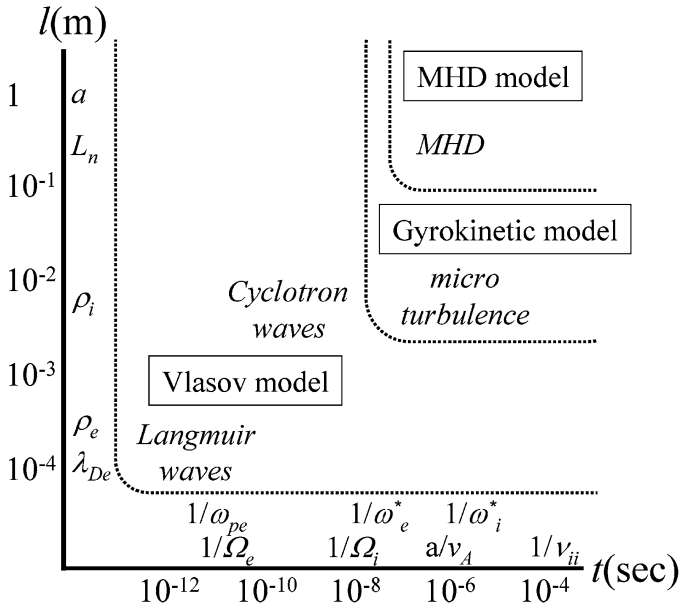

Figure 1.6: Spatial and temporal applicability of the gyrokinetic model as compared to the Vlasov model and the MHD model[24].

boundary physics, and (3) whole device modeling. Disruption physics addresses the potential catastrophic damage to a fusion reactor due to large disruption events. Mitigation and control of large disruptions would provide stability and retain the structural integrity of the vessel walls due to large heat loads. Plasma boundary physics deals with wall degradation due to prolonged nuclear fusion operation and maintaining heat fluxes within material limits. Whole device modeling investigates reactor performance, which provide future predictions for future machine operations. Simulations have been used extensively in order to manage current challenges to the magnetic fusion scheme. Proposed thrusts in high-performance computing are: (1) multiphysics and multiscale coupling, (2) numerical optimization and uncertainty quantification, (3) data analysis, management, and assimilation, and (4) software integration and performance. The scope of this thesis pertains to the multiscale coupling category where novel algorithms and computing solutions are needed to investigate the dynamics that span disparate orders of magnitude in spatio-temporal scales.

In order to solve the unprecedented challenge towards sustainable nuclear fusion, current classes of codes already exist. Typically, tokamak plasma simulations have taken advantage of the separation of scales in order to remain applicable in isolated plasma regimes (Fig. 1.8). Simulation models are often developed from simplified sets of equations or reduced equations, which have limits on space and time scales. There is a persistent demand to increase simulation domains to capture plasma phenomena occurring on different time and space scales. An integrated simulation is desired as a result of strongly coupled processes such as during plasma disruptions. A major plasma disruption is one of the most dramatic events that can occur in tokamak plasmas. It is usually described as a catastrophic global

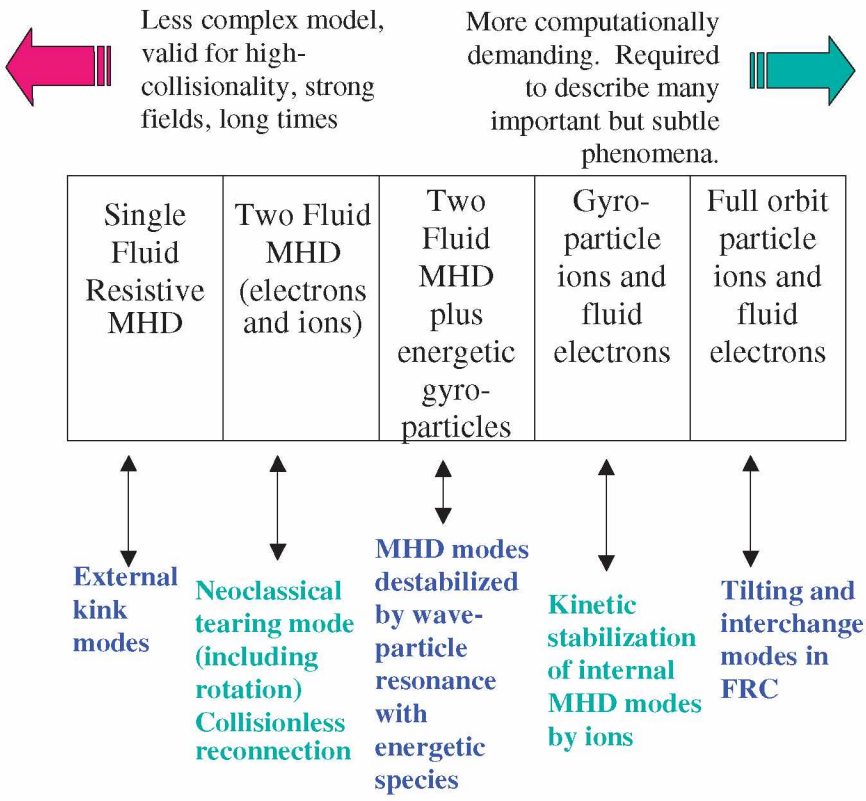

Figure 1.7: An example of macroscopic simulations showing the range of complexity and computational demand with corresponding physics applications[23]

.

collapse of a plasma discharge that is associated with an almost instantaneous break down of the magnetic geometry resulting in an immediate loss of plasma confinement[23]. The input plasma energy such as the plasma current and external heating of the plasma is primarily released as large thermal loads that can cause major structural damage to the device. A major challenge is to understand the responsible physical mechanism in order to predict and mitigate such events.

Modern large scale codes are used primarily for first-principles simulations investigating individual phenomena in realistic three-dimensional geometry. Integrated models consisting of lower dimensions with significant empirical elements are used for modeling and designing experiments. According to recent reports on computational requirements for high fidelity global simulations of tokamak plasma, petascale and larger computational resources are required[23,27]. Projected computational time is in excess of 13×10^9 hours and storage of more than 140 PB (PB $= 2^{50}$ bytes) to meet FES research objectives in 2017[27]. Codes that evolve both the small scale fluctuations and the large scale profile evolutions such as GYSELA consume, on average, about 10^6 hours on 10^4 cores and generating more than 20 TB (TB $= 2^{40}$ bytes) of storage[15]. Typically, the state-of-the-art codes for plasma in

tokamak geometry such as GTS and XCG-family can easily require more than 10^4 cores to advance about 10^9 particles[27]. The current computational capability progression allows a qualitative comparison between experimental facilities of varying sizes and computational requirements (Tab. 1.1). Owing in part to computational advances, fusion power performance has followed a somewhat predictable trend (Fig. 1.2). Hence, in order to simulate the next generation tokamak ITER, the number of computational elements must be in the exascale (10^{11}). Together with increased computational requirements, the time required for a typical simulation increases with increasing complexity. Despite the explosive progress in expanding computational capabilities measured terms of calculations per second (FLOPS), there is a compromise between accuracy and time to solution. Higher fidelity models require more time to complete (Fig. 1.7). Core transport simulations using gyrokinetic codes with two species in whole device modeling studies consume about tens of thousands of computational cores while the simulation for an actual device with multi-species - electrons, ions, deuterium, tritium, alpha particles, helium ash, carbon, tungsten, beryllium - will consume more that hundreds of thousands cores.

Table 1.1: An example comparing computational elements and experimental devices shows increasing computational requirement for simulation[26].

	giga	tera	peta	exa
Elements	10^5	10^7	10^9	10^{11}
Device	CDX-U	DIII-D/NSTX	DIII-D/NSTX	ITER
Time range	single event	single event	multiple	multiple
Model	resistive MHD	2-fluid	2-fluid	kinetic-MHD

Historically, modeling strategies have persisted due to the gap between the physical model and experimental measurements. Conventional theory requires simplifications in order to discover tractable solutions in special limits, which are often posed in terms of equilibrium states. However, the feasibility of sustainable nuclear fusion requires analysis of dynamical processes that usually cannot be approached by conventional theory. Often, fusion plasmas are maintained far from equilibrium where non-equilibrium techniques are often supported by numerical simulations. Simulations naturally attempt to connect between experiment and analytical theory by taking advantage of applied mathematics, computer science, and high-performance computers. Several types of framework have been developed in order to support the current FES goals[23].

Apart from the need to model the plasma itself, plasma facing materials also face challenges such as high heat loads and radiation damage. The high energy flux of 14.1 MeV neutrons lead to structural damage and modification of thermal properties of plasma facing components[28]. In turn, this process usually degrades the overall performance of tokamak type machines. Due to limited experience with such a high neutron flux, simulations are nec-

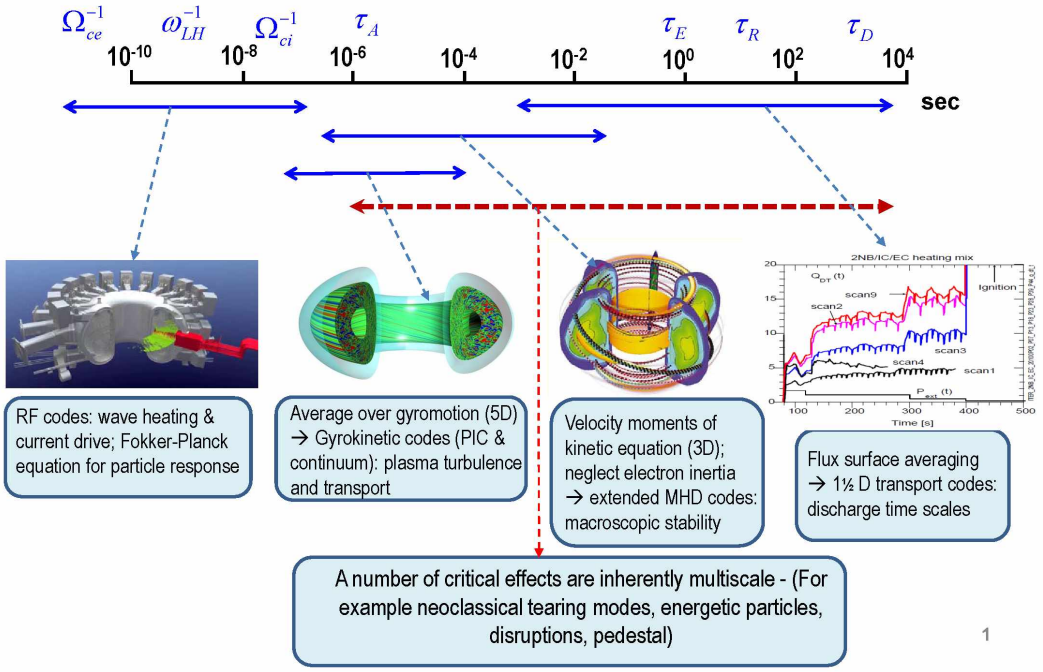

Figure 1.8: An example of the applicability of simulation codes to specific time scale regime[26].

essary to predict material changes in the context of fusion plasmas. A typical workflow uses information from quantum-mechanical models for the material configurations, molecular-mechanics for neutron induced defects, and dynamical models for evolution of defects and dislocations. The challenges for sustainable nuclear fusion involve integration of a variety of specialized knowledge that spans multiple spatial and temporal scales. The coupling and interaction between all the scales becomes an underlying motive for investigation, which leads into parallelism with non-equilibrium systems, in particular SOC systems.

The interest in different approaches to turbulence characterization also stems from the keen awareness of the progress towards sustainable magnetically confined plasma for nuclear fusion. Due to delayed research achievements and an increasing investment in next generation tokamak design, funding sources (i.e., U.S. Department of Energy (DOE)) have been pushing for insurance in this venture. The estimated cost for ITER in 2016 is €13 billion with U.S. contribution of $4.6 to $4.8 billion through 2035. The costs are expected to grow as the deadline to completion is delayed[29]. The success of this scientific endeavor towards sustainable nuclear fusion power increasingly requires milestones and a guarantee of safe machine operations. This has led to the need to understand the basic physical mechanisms underlying processes such as large plasma disruptions that can damage the machine.

Although large plasma disruptions can be avoided, the free energy in the gradients

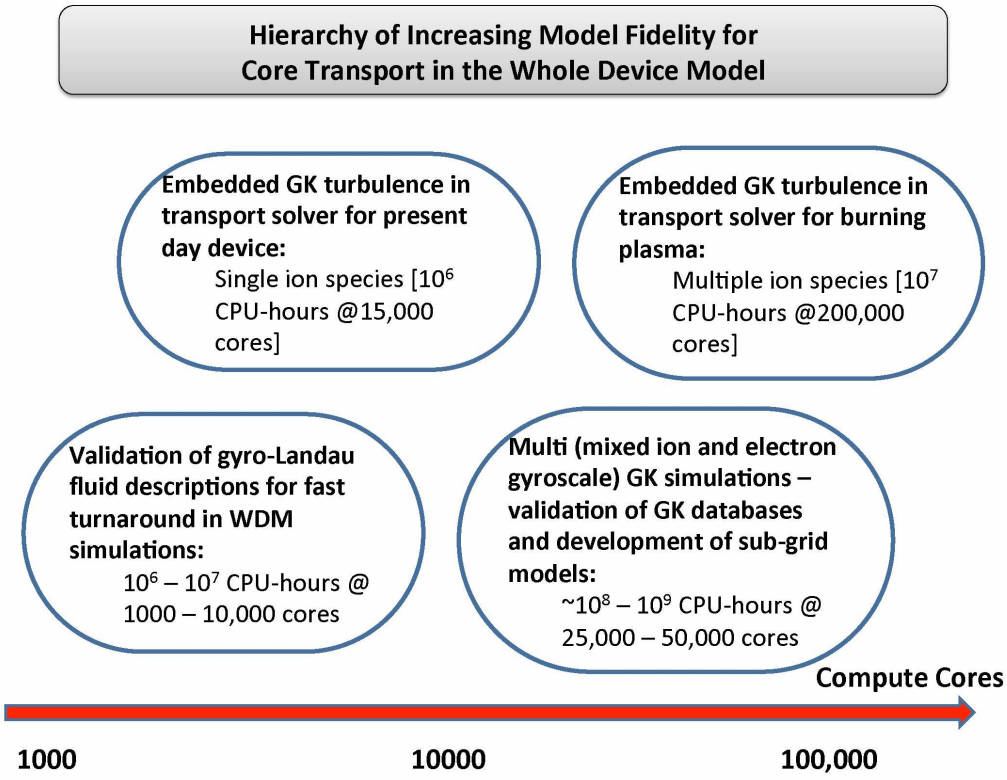

Figure 1.9: An example of model hierarchy comparing required computational cores and time to solution for whole device modelling[26].

of density and temperature can still drive turbulence, which represents particle, momentum, and heat loses across the nested magnetic fields. Transport losses due to plasma turbulence is experimentally observed to be significantly larger than expected values due to collisional relaxation. These transport losses will be important for continuous device operation since the feasibility of nuclear fusion will be determined largely by the balance between fusion self-heating and turbulent transport losses. The dynamics of drift-type turbulence have been extensively studied and are thought to be responsible for cross-field transport[30].

1.2 Turbulent transport paradigm

In tokamak plasmas, the neoclassical transport theory[31] is primarily based on the combination of particle orbits in a slowly varying magnetic field configuration and Coulomb collisions. Although this theory has been well established, experiments show a larger transport. For instance, the neoclassical transport theory predicts τ_E for electrons and ions almost up to two orders of magnitude longer than experimentally measured. Plasma turbulence is thought to be a primary contributor to the rapid loss of confinement. The transport process resulting from plasma turbulence is often referred to as anomalous transport[14].

Hence, to understand transport losses that reduce the confinement time requires necessary to investigate turbulence. Techniques to account for anomalous transport (i.e., neoclassical transport or decomposing the flux into a diffusive and a pinch part) reference the paradigm of characteristics scales. The collisional character imposes the local perspective and implies a characteristic scale posed by the dynamics[32].

Turbulence has been an enigma for the past millennium. The most common example of a fluid turbulence is contained in the Navier-Stokes equation where it remains an open challenge to find globally regular solutions[33]. Properties of turbulence closely resemble spatio-temporal chaos. Although there is no official definition for turbulence, turbulence include the following aspects: sensitivity to initial conditions, has a mixing property that is much more rapid than diffusion, and encompasses a wide range of spatial lengths[34]. One of the topics of great interest when studying fluid turbulence is the enhanced mixing property. Within a turbulent flow, a scalar quantity can be transported and mixed much more rapidly than molecular diffusion. This enhanced mixing property can either be beneficial or a detrimental depending on the focus. For instance, the rapid mixing process allow homogenization of distinct scalar quantities where dilution is required as in salt water and fresh water. On the other hand, the enhanced transport can be detrimental in the dispersion of highly concentrated pollutants in the atmosphere or the ocean.

The study of turbulence can be categorized into several approaches: statistical, structural, and deterministic[35]. The statistical approach associates turbulence to be random. The most common concept arising from this approach is the Reynolds averaging method. For an arbitrary flow field $\boldsymbol{u}$, Reynolds averaging usually involves separating the mean from the fluctuations $\boldsymbol{u} = \bar{\boldsymbol{u}} + \tilde{\boldsymbol{u}}$ where $\bar{\boldsymbol{u}}$ is the mean component and $\tilde{\boldsymbol{u}}$ is the fluctuating component. Although this flow decomposition permits solutions in specific regimes, a common concern with this process involves the closure due to the nonlinear terms, which is often referred to as the Reynolds stress term. Numerous works have been dedicated to understanding this term. The structural approach identifies coherent structures in the flow field. Due to the existence of vorticity $\boldsymbol{\omega} = \boldsymbol{\nabla} \times \boldsymbol{u}$, the flow field can be categorized in terms of a hierarchy of vortices. Flow does not necessarily always have distinguishable structures. The deterministic approach is the most direct approach in studying fluid turbulence. This method becomes more common due to increased computing power. Some of the common approaches are direct numerical simulation (DNS) and large eddy simulation (LES). However, there are still some drawbacks arising from the broadband nature of fluid turbulence that requires resolution on all scales, which is computationally expensive. For instance, a common assumption in the deterministic approach is to truncate and introduce an approximation at the dissipation scales. Due to the property of fluid turbulence that spans over multiple spatial and temporal scales, direct simulation of fluid turbulence still exceeds current computational capabilities. The computational time for a simulation can take much longer than running a physical experiment. Hence, there is still a need to study

the interactions over various spatial and temporal scales with reduced models.

Given the well-known scientific difficulties of turbulence in neutral fluids[34], turbulence in plasmas add another layer of complexity due to the coupling of the multiple charged species with the electro-magnetic fields. A primitive deterministic approach such as through the DNS scheme to plasma turbulence immediately requires six dimensions as compared to the neutral fluid turbulence that requires three dimensions. The conventional paradigm of characteristic scales establishes that slow time-scale fluctuations defined with spatial scales smaller than the plasma dimension dominate the losses of heat and particles. Fluctuation-driven loss rates exceed collision-driven loss rates[36], which motivates interest in understanding fluctuations. Fluxes quantify fluctuation-driven losses, which is dependent on the correlations between fluctuating fields. For instance, the continuity equation for the electron number density can be written as

$$0 = \frac{\partial n_e}{\partial t} + \boldsymbol{\nabla} \cdot (n_e \boldsymbol{u}_e) \,. \tag{1.5}$$

Since there are no losses in the toroidal and poloidal direction along connected flux surfaces, the net loss occurs in the radial direction. In parallel with the statistical treatment of turbulence, by separating n_e into the ensemble-averaged and fluctuating part $n_e = \langle n_e \rangle + \tilde{n}_e$ and considering an equilibrium of the mean radial flow $\langle u_{r,e} \rangle = 0$, the average electron density is governed by

$$0 = \frac{\partial \langle n_e \rangle}{\partial t} + \frac{\partial \Gamma_e}{\partial r} \tag{1.6}$$

where the fluctuation-induced radial particle flux is $\Gamma_{e,r} = \langle \tilde{u}_{e,r} \tilde{n}_e \rangle$. The change in the average density comes from both the amplitude of the fluctuations as well as the correlations between the fluctuating quantities. Due to the impact on the average density quantity from the fluctuations, there is a need to understand and quantify the fluctuations that ultimately provide a net transport in $\langle n_e \rangle$[19]. The most commonly used fluctuation diagnostics are Langmuir probes, coherent laser scattering, reflectometers, heavy-ion beam probe (HIBP), and beam emission spectroscopy (BES)[14,37]. Experimental measures have shown that electrostatic turbulence dominate the plasma edge transport[14].

Plasma in a strong guided magnetic field $\boldsymbol{B}$ undergoes a motion that gyrates in a circular pattern perpendicular to the magnetic field lines. This is often called the $E \times B$ drift $\boldsymbol{u}_E = \boldsymbol{E} \times \boldsymbol{B}/B^2$, which is independent of the charge. Ions and electrons drift in the same direction with the same velocity. With electrostatic field, $\vec{E} = -\boldsymbol{\nabla}\tilde{\phi}$, the velocity can be defined, to the first order, as $\tilde{\boldsymbol{u}}_E = \boldsymbol{B} \times \boldsymbol{\nabla}\tilde{\phi}/B^2$ where $\tilde{\phi}$ is the fluctuation in the electrostatic potential and $\boldsymbol{B}$ is the magnetic field. The fluctuation-induced particle flux can be represented in Fourier space as $\Gamma_e = \sum_{\boldsymbol{k},\omega} \tilde{n}_e(\boldsymbol{k},\omega) \left[ik_\theta \tilde{\phi}^*(\boldsymbol{k},\omega)/B \right]$ [10]. When the density fluctuation is proportional to the gradient of $\tilde{n}_e$, Fick's law gives $\Gamma_e = -D_{ql} d\tilde{n}_e/dr$ where D_{ql} is the quasi-linear diffusion coefficient expressed as $D_{ql} = \sum_{\boldsymbol{k},\omega} \left| k_\theta \tilde{\phi}(\boldsymbol{k},\omega)/B \right|^2 \tau_c(k)$ where $\tau_c(k)$ is a correlation time in the scale k^{-1}. In order to determine the level of fluctuations, a

mixing-length rule is used to approximate $e\tilde{\phi}(k)/k_B T_e = (k_\perp L_P)^{-1}$ where L_P is a pressure gradient length and $\phi(k)$ is now the root-mean-squared value averaged over time. With this estimation, $e\tilde{\phi}(k,\omega)/k_B T_e = (\gamma_k/\omega_P^*)\,(k_\perp L_P)^{-1}$ where an improvement to the estimate includes the growth rate γ_k compared to the diamagnetic frequency $\omega_P^* = k_B T_e/eL_P$. The mixing-length diffusion coefficient then becomes $D_{ml} = \sum_k \gamma_k/k_\perp^2$ using $\tau_c(k) \propto \gamma_k^{-1}$. This quasi-linear approach calculates transport fluxes using the linearly unstable eigenmodes, an approximation which is limited when applied to turbulence where the non-linear interactions of several modes dominate. The two-step recipe of determining the transport coefficients through the fluxes has been implemented in transport models with some success[38]. However, the underlying paradigm relies heavily on characteristic scales, which can contradict the observed behavior of plasma profiles in fusion relevant regimes. A common paradigm that involves characteristics scales is drift-wave turbulence.

1.2.1 Drift-wave turbulence

Transport across magnetic fields is due to low-frequency drift-wave fluctuations[30,39]. This transport is believed to be driven by the collective electric field with wavenumber greater than the Debye shielding $k\lambda_D \ll 1$ where $\lambda_D^2 = \epsilon_0 k_B T/ne^2$. Under slowly varying conditions, the fluid equations are an appropriate treatment of the plasma. The drift motion of charged particles arise from the density and temperature gradients in magnetized plasma, which result in electron and ion diamagnetic currents $\boldsymbol{J}_s$ where the subscript s denotes the particle specie across the magnetic field $\boldsymbol{B}$. The first order drift comes from the guiding center motion that produces the $\boldsymbol{E}\times\boldsymbol{B}$ drift across the magnetic field. Including the density and temperature gradients, the drift velocities $V_{D,s} = (q_s n_s B)^{-1}\,\partial_r P_s$ where $P_s = n_s k_B T_s$ produce collective oscillations that are called drift-waves.

In the 1970's, the study of drift-wave turbulence became a standard approach to studying anomalous transport in tokamak plasmas[14]. This focus cemented the drift-wave paradigm for anomalous transport. Without resistivity, the MHD equations describe plasma that is confined in a tube of magnetic flux, which is often referred to as the frozen-flux condition. Although the MHD equations aptly describe several plasma characteristics such as plasma equilibrium and gross plasma stability, they cannot describe separate ion and electron motion that lead to additional important plasma phenomena. The added degree of freedom due to separate ion and electron dynamics introduces a source of destabilization often referred to as the universal instability drive. The universal instability drive refers to the always present potential for instability when there is a spatial gradient in the particles' distribution function. This instability mechanism can convert particle thermal energy into wave energy. In turn, the electromagnetic fields from the waves can then induce stochastic particle motion, which leads to anomalous transport resulting in the loss of particles and energy from magnetically confined systems. Consequently, the separate ion and electron dynamics allows for resistivity, which then modifies the frozen-flux condition. As a result,

particles can move across the magnetic field lines.

For a small localized excess ion charge, the plasma rotates around the potential maximum $\phi > 0$ with a velocity $\boldsymbol{v}_E = \boldsymbol{E} \times \boldsymbol{B}/B^2$. The potential maximum also corresponds to the density and electron pressure maximum in the adiabatic response $\tilde{n}_e/N \simeq e\phi/k_B T_e$. Without a density or temperature gradient, the cell rotates without plasma transport. With a gradient in the x-direction, there is a net transport of the structure perpendicular to the gradient that follows from the integrated convective flux $\Gamma_s = A^{-1} \int_S n_s \boldsymbol{v}_E \cdot d\boldsymbol{A}$. The adiabatic electron response underlies the standard Hasegawa-Mima model[40], which excludes the density dynamics and only contains the polarization drift nonlinearity. The model predicts an inverse cascade from small radial scales (large $k_\perp$) to large radial scales (small $k_\perp$). The nonadiabatic behavior deviates from the adiabatic approximation such that $\tilde{n}_e = Ne\phi/k_B T_e\,(1 - i\delta_k)$. The $i\delta_k$ term describes the electron dissipation from transport coefficients in the collisional regime and from the resonant electron-wave interactions in the collisionless regime[30]. A positive phase shift of $i\delta_k$ causes the density maxima to lead the potential maxima, which then leads to an exponential growth. On the other hand, a negative phase shift becomes an exponential decay. This phase shift between density and potential leads to an imbalance in the convective fluxes, which then leads to a net transport of density down gradient. The structures then move perpendicular to the gradient with the diamagnetic drift speed $V_{D,e} = k_B T_e/eBL_n$ where $L_n^{-1} = -\partial_r \ln N$. The nonadiabatic electron response introduces the $E \times B$ nonlinearity that describes the advection on nonadiabatic electrons. The $E \times B$ nonlinearity transfers energy, nonlocally, from large to small radial scales[41]. As a result, each nonlinearity dominate at different scales[42,43], which then suggests self-consistent evolution of the nonlinearities acting on different scales.

Drift-wave turbulence diffusivities remain larger than neoclassical collisional ion diffusivities. The scaling of the drift-wave thermal diffusivity $\chi_i^{DW} \propto T^{3/2}/B^2 L_n$ compared to the neoclassical thermal diffusivity $\chi_i^{neo} \propto n/T^{1/2} B_\theta^2$ causes the thermal flux to increase rapidly with increasing temperature[30]. The turbulent diffusion acts on the temperature and density profiles to cause them to relax back toward marginal stability, which yields a certain stiffness to the profiles. Drift-wave turbulence in tokamak plasmas have been modeled using critical thresholds and switching functions obtained from the synthesis between theory and simulations[44].

Despite the well-established neoclassical transport theory and the drift-wave paradigm for anomalous transport, there are still open issues regarding the correspondence between measurements and the understanding of plasma turbulence that enables significant confinement losses. In order to understand transport in turbulent tokamak plasma, the following elements must be incorporated into the paradigm: long correlation lengths, fast propagation, dynamics near marginality, affect of transport by sheared flows, and a multimode transport model[14]. Core fluctuation measurements give radial correlation lengths for the

fluctuations to be much shorter than the minor radius of the device, which conflicts with the long correlation lengths required for the larger transport. Experimental evidence also shows that propagation time scales occur faster than diffusive propagation such as the ballistic propagation of heat pulses[45]. Profile resilience and the existence of marginal stability allow nonlinear multiscale interactions, which cannot be accounted for under the different flavors of quasi-linear transport flux approximations.

Recent interest in nonequilibrium systems has led to slightly different but complimentary approach to studying fluid turbulence through SOC systems. A common feature of SOC systems is the absence of a clear separation of scales that allows the identification of equilibrium states. The complexity in confined plasmas exhibits many multiscale features such as turbulence and intermittency, which have been studied using simulations and experiments. As a consequence, the observed features such as scaling laws or profile consistency and the lack of characteristics scales provide increasing appeal of the SOC paradigm for tokamak plasmas. Multiscale interactions tend to violate the assumptions of locality and the lack of correlations behind the classical diffusive model paradigm. These observations coupled with the discrepancy between local transport theory such as the neoclassical theory build a foundation to shift attention to a nondiffusive transport model.

1.3 The SOC paradigm

Nonequilibrium phenomena are ubiquitous in nature. They are often characterized as open and spatially extended dissipative dynamical systems that exhibit stochastic features without clear characteristic scales in the dynamics[32]. The multiscale features prevent the identification of and display of properties such as turbulence and intermittency. Among the many approaches to nonequilibrium systems such as phase transition and catastrophe approach, the SOC approach arises from the need to understand the nature of critical phenomena and multiscale interactions that can account for both the large scale features and the coupling across different scales. Initially, the SOC paradigm was demonstrated using sandpile models, which is then widely applied to avalanche phenomena. It then became a framework that describes a class of systems where the relevant processes occur on all scales, which compliments the features of low-dimensionality systems where the dominant features are global. The SOC approach in fusion plasmas has proven to be a different but a complimentary approach to the traditional view of turbulent transport in tokamaks. Radial transport in tokamak plasmas tend to drive the plasma profiles close to marginal stability while turbulence plays a critical role in regulating the confinement and transport in these near-marginal regimes. In part, due to the mismatch between measurements and existing transport theory, the SOC paradigm motivates the consideration of self-consistent profile evolutions and the coupling between various spatial and temporal scales[46]. This phenomenology observed in fusion relevant conditions has motivated the SOC paradigm as an alternative view that compliments the first principles approach. The SOC paradigm has

also permeate to other disciplines that study nonequilibrium systems such as earthquakes, forest fires, and landslides[32]. Extreme events are also features of these complex driven systems.

The SOC approach is a paradigm applied towards understanding the evolution of nonequilibrium systems[47]. The SOC paradigm was first stated by Bak, Tang, and Wisendfeld[48], and has inspired many inter-disciplinary works in various scientific disciplines. Due to its success and prominence, the characteristics and identifications of SOC have been under ongoing controversial discussions[47]. Several physical systems under continuous input and dissipation of energy exhibit similar phenomenological traits such as intermittency and occurring over many scales. The conventional approach towards understanding these types of systems is to focus on the detailed plasma physics of an energy transfer event in isolation such as investigating the onset of instability and instability mechanisms. This approach becomes very laborious when addressing multiple spatio-temporal scales. Alternatively, all scales can be considered, which cause the system to be strongly coupled. The strong spatio-temporal coupling led to power-law correlations. Homogeneous turbulence is a classical example of this phenomenon, but it does not necessarily qualify as having SOC characteristics. A distinguishing character from SOC systems with phase transitions is the lack of a turnable or control parameter such as temperature.

The SOC paradigm became a prominent approach to fusion plasmas[49–54]. The sandpile models used in SOC are one of the simplest mathematical realizations of externally driven systems that tend to be far from equilibrium with an instability threshold. The SOC archetype provides tangible models to investigate more complex non-equilibrium systems. These types of models reproduce some of the basic phenomenology observed in fusion plasmas such as profile stiffness and the rapid propagation of perturbations[55]. The basic concept of SOC as applied to fusion plasmas can be captured with a one-dimensional running sandpile model[56]. This model is built on simple rules that controls how the grains are distributed on discretized spatial cells $\{n : 0 \dots N\}$ due to deposition of sand. The addition of a single sand grain in each cell of existing height h_n is simply $h_n \to h_n + 1$. The local gradient is then calculated according to the forward difference $Z_n = h_n - h_{n+1}$. If the gradient exceeds the specified critical gradient Z_c, the sand in cell n will be redistributed to the next cell $n + 1$ by an amount D. Thus, for $Z_n > Z_c$, cell n becomes unstable and redistributes the sand down-gradient to cell $n + 1$ that yields $h_n \to h_n - D$ and $h_{n+1} \to h_{n+1} + D$. The transfer of sand down-gradient modifies the local height of sand (Fig. 1.10). The boundary conditions demand that that the first cell is bounded ($Z_0 = 0$) and an open boundary at the other end ($Z_N = h_N$). As a result, there is a net flow from first cell to the last cell.

Under steady-state conditions, the sandpile model exhibits interesting dynamics depending on the parameters of the model such as the critical gradient Z_c, the number of sand grains being transferred D, and the rate and method of sand deposition. The height of each cell varies depending on the transfer of sand grains from the neighboring up-gradient

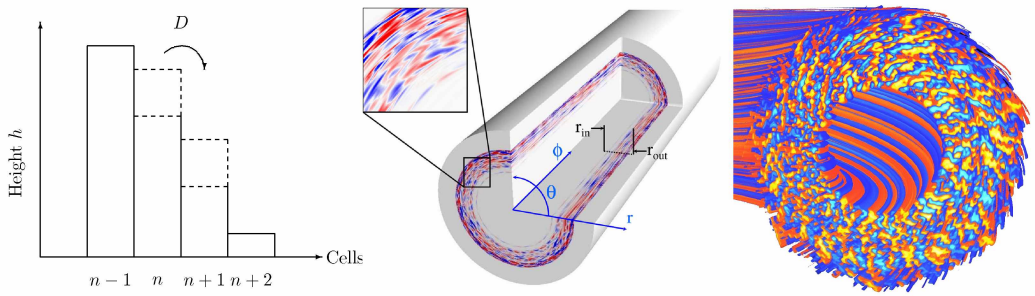

Figure 1.10: SOC characters are displayed in models with increasing complexity: sandpile model with simple rules in one-dimension (left), a 2D resistive drift-wave simulation in cylindrical geometry[57] (middle), and GYSELA code with 3D geometry showing ion temperature fluctuations in the turbulent saturated phase[15] (right).

cell, which allows time histories to be encoded into the profile. Once sand grains begin to topple down-gradient, the transfer of sand grains stops when the local gradient is below the critical value $Z_n < Z_c$. The sand grains redistribute down-gradient from the starting cell to the ending cell, which increases the probability of any cell within this range to become unstable and start another avalanche event. The spatial extent of the down-gradient transfer or an avalanche event can extend from one cell to the system size depending on the profile. When the profile sits near Z_c on average, any sand deposition would be transported down-gradient. This state is referred to as the marginal state. On the other hand, continuous down-gradient transfer occurs when the sandpile is overdriven when the local gradients remain $Z_n > Z_c$ on average. This scenario occurs predominantly when rate of the addition of sand becomes greater than the transfer down-gradient. The submarginal state occurs when $Z_n < Z_c$ on average, which is associated with a slow addition of sand grains compared to the transfer of grain from neighboring cells D. With only these simple rules, the sandpile model can display diverse characteristics[58]. They are applicable to many physical systems that are slowly driven far from equilibrium, open, and consist of critical conditions such as in turbulent transport in fusion plasmas. The turbulence model in this work is based on the following inherited SOC ingredients from the sand pile model:

- an evolving profile,
- the fueling process,
- the existence of a critical gradient,
- and the gradient relaxation process.

Analogies between the SOC ingredients captured in the sandpile model and the turbulent transport paradigm in tokamak plasmas are shown in Tab. 1.2. As with the sandpile model, the interplay between the fueling rate and the relaxation process enhanced by a critical gradient is coupled with the response from an evolving profile that acts as a source of free

Table 1.2: Analogies between the turbulent transport in fusion plasmas, the sandpile model, and the turbulence model for this work, the modified DTEM[46,51].

Turbulent transport in toroidal plasmas	Sandpile model	Modified DTEM
Localized fluctuation (eddy)	Grid site (cell)	Turbulence fluctuations
Critical threshold for local instability	Critical sandpile slope (Z_c)	Local critical gradient parameters
Local eddy-induced transport	Number of grains moved if unstable (D)	Local eddy transport
Total energy/particle content	Total number of grains (total mass)	Integrated background profile
Heating noise/background fluctuations	Random rain of grains	Background profile fluctuations
Energy/particle flux	Sand flux	Background profile flux
Mean temperature/density profiles	Average slope of sandpile	Background profile
Transport event	Avalanche	Transport event
Sheared electric field	Sheared flow (sheared wind)	Self-generated and external sheared $E \times B$ flow

energy through the profile gradient. The transport is then dictated by the nonlinear dissipation or loss processes at the plasma edge that ultimately absorbs the excess free energy from the system. The relaxation process relating to the down-gradient transfer inherently sets up a timescale for which the system can exhibit SOC characteristics. This timescale is often referred to as the the transport timescale, which can be several order of magnitudes larger than the electron timescale ($\Omega_{ce}^{-1} \sim 10^{-10}\, s$) (Fig. 1.5 or Fig. 1.8). The main distinction here between the sandpile model and the turbulence model in this work is that the amount of down-gradient transfer depends on the growth rate coming from the instability induced by the driving profile. The turbulence dictates the amount of relaxation arising from steepening of the local gradient, which then allows the profile to exhibit "stiffness" as it hovers around the critical gradient value[59]. As a consequence of the presence of critical gradients in tokamak plasmas, the transport rate increases substantially when the gradients exceed certain thresholds. The enhanced transport typically occurs in the form of avalanches where excess particles and free energy are dissipated to the boundaries. Subsequently, the process relaxes the profiles until they return within their marginal states. This feature then permits a dynamic steady state where the profiles exhibit stiffness or resilience. In parallel with the SOC paradigm, the ingredients for SOC-like character are independent from the specific details of the instability that drives the turbulence such as the ion-temperature-gradient (ITG) or the trapped-electron-modes (TEM)[46,50]. The emphasis is the competition between the driving mechanism and the relaxation process, which then

encodes memory into the profile that allows for transport events that vary spatially and temporally. The current model is limited to only one instability pertaining to turbulence, namely the dissipative-trapped-electron-mode (DTEM), which is quite different for the actual tokamak plasmas. Other transport channels exist and will compete to dissipate excess energy input in order to relax the large gradient involved to achieve sustainable confined fusion plasmas. The applicability of the SOC paradigm requires that the state satisfies the aforementioned ingredients[46].

Turbulence and intermittency were observed in the edge regions of tokamak plasmas[50,55,60] and prompted the use of SOC paradigm in the plasma edge region. A complete simulation of this system requires multiple fields and many parameters, which is numerically expensive due to the complexity of both the coupling between the fields and the large parameter space. As a result, a reduced dimension model is desired in order to study the phenomenon of interest without expensive simulations. Historically, simulations of turbulent transport have approximated the plasma dynamics by separating the spatial and temporal scales. For instance as shown in Fig. 1.8, the ion dynamics occurring on the order of $\Omega_{ie}^{-1} \sim 10^{-8}\, s$ has a small influence on the dynamics on the order of the confinement time $\tau_E \sim 1\, s$. However, a number of observed phenomena have parallels in the SOC paradigm, which couples a vast range of time scales. The interest in confinement and turbulent transport become a profoundly multiscale problem. As a consequence of the available computational resources and the separation of scales hypothesis, several past simulations resolve the dynamics within a certain range of scales that tend to be much smaller than the transport timescale.

The separation between equilibrium and fluctuation scales underlies the justification for developing a mean field theory of transport[10]. The results from these shorter timescale simulations are then used as inputs into simulations on the transport timescale, which then determines the profile relaxations. This has been a common recipe for constructing transport models based on a quasi-linear theory that combines with a mixing-length coefficient as discussed previously in Sec. 1.2. The fluctuations from equilibrium evolve on profiles that are somewhat stationary, which is referred to as a fixed-gradient evolution as oppose to a flux-driven gradient. The flux-driven gradient corresponds to the scenario where the evolution of plasma profiles is maintained by the flux originating from the sources. The flux from the sources then determines the average plasma profiles. From evolving the dynamics in the fixed-gradient scenarios, the results are then used to estimate the transport coefficients from turbulent fluxes, which are then employed in a simulation that evolves the plasma profiles. The effective transport coefficients which are determined from the turbulent fluxes with fixed gradient profiles are often fit with the form of Fick's law[61] $\Gamma \propto D\nabla n$ and have been used to set the transport coefficients when the profiles can evolve. The strategy of evolving the turbulence and the profiles separately due to disparate timescales has been successful in obtaining insights on the detailed physical mechanisms but remains

incomplete when considering the observed phenomena occurring on transport scales. This strategy inherently limits both the spatial and temporal correlations that are inherent in the SOC paradigm, which is a cornerstone of physical non-equilibrium systems.

Although reasonably applicable and attractive to fusion plasmas, the SOC characteristics need to be determined from experimental measurements. Even though the ingredients for SOC are immediately satisfied for tokamak plasmas, observations are still needed to support and establish the validity of the paradigm. A review article of experimental evidence supporting the existence of SOC in tokamak plasmas has been compiled recently[46]. One of the requirements for a non-equilibrium system displaying SOC-like characteristics involve the existence of a critical gradient. This has been shown through perturbative studies by measuring the stiffness of the profiles for the electron temperature T_e profile but less clearly with T_i profile. Density and pressure profiles have been shown to be less stiff in the core region than the temperature profiles, but coincide closely with the drift-wave turbulence in the edge region.

Signatures and SOC properties remain points of contention due to various interpretations[47]. However, they strongly suggest that tokamak plasmas operate near a marginal state[46]. Due to the limited accessibility to the plasma state in the core region of tokamak plasmas, a majority of data used to determine SOC characteristics have been measured in the edge region from probe measurements[60,62,63]. The self-similarity signature of SOC dynamics is usually determined by R/S analysis pioneered by Hurst[64] where the self-similarity exponent H measures the persistence in a time series. The self-similarity scaling is measured from the scaling of the R/S in the mesorange such that $[R/S](\tau) \sim \tau^H$ where τ is the time lag. Different power-law regions in the R/S correspond to different dynamics (Fig. 1.11) for number of unstable cells in a sandpile model[58]. An uncorrelated time series yields $H \sim 0.5$, a persistent time series yields $H > 0.5$, and an anti-persistence time series gives a scaling of $H < 0.5$. In the edge region of tokamak plasmas, the self-similarity ranges from $0.4 < H < 0.8$ depending on the measured location, which then reflects the dominant dynamics in that region. The presence of persistent signals in the edge region suggests correlated radial transport[46].

An experiment dedicated to the analysis of avalanche behavior examined the electron temperature fluctuations $\delta T_e/T_e$ in L-mode DIII-D deuterium tokamak plasma discharge[65,66]. The plasma condition needs to be free from coherent and oscillatory behavior, which can interfere with the correlation analysis used to characterize avalanches. The most prominent signature of the avalanches comes from the electron-cyclotron-emission (ECE) diagnostic that has a spatial resolution of about $1\,cm$ to $2\,cm$ covering most of the minor plasma radius. Density diagnostics from the beam-emission-spectroscopy (BES) system, microwave reflectometry, and far infrared (FIR) gave mixed results. Radial avalanches were identified using the radial cross-correlations between each of the 32 ECE channels (Fig. 1.12). The outward propagation of the maximum in the cross-correlation is identified

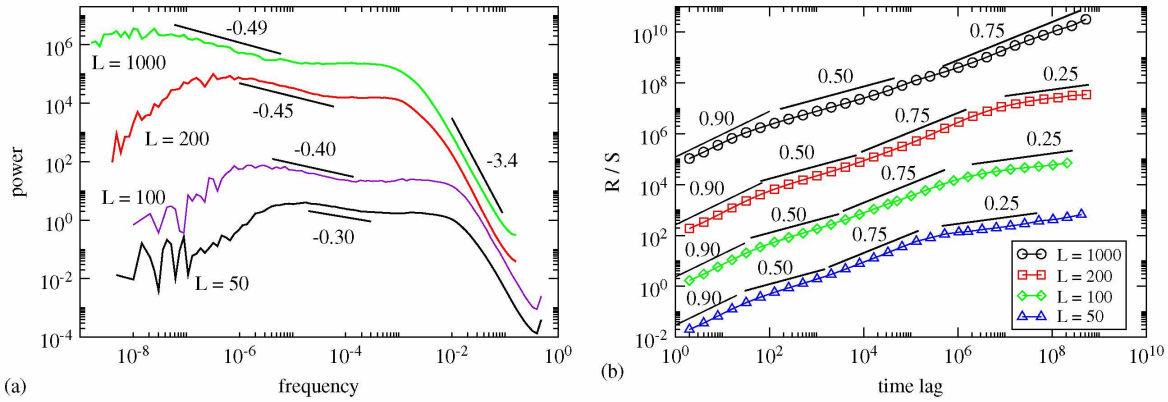

Figure 1.11: R/S analysis (b) with corresponding power spectra (a) for the number of unstable cells in a sand pile model [58].

as an avalanche event.

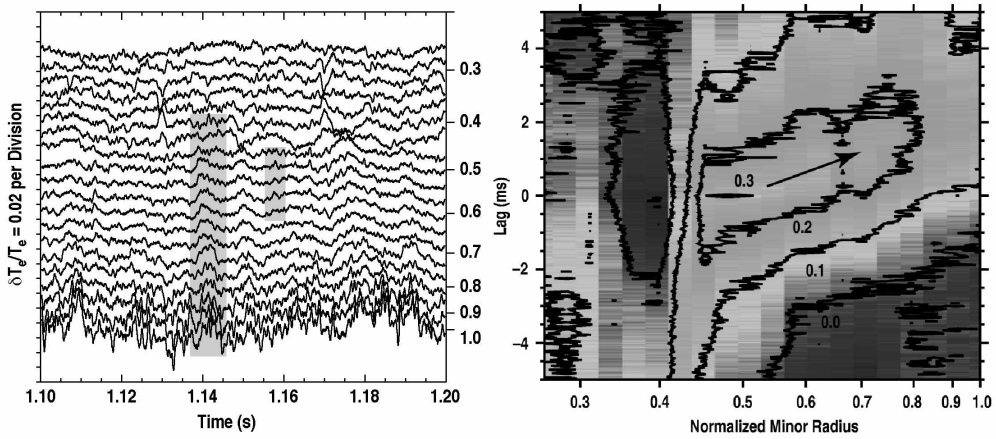

Figure 1.12: Time series of ECE signals from different channels corresponding to different radial positions (left) shows avalanche events (gray bands). The contour plot of cross-correlation of each ECE channel with a channel at $r/a = 0.45$ (right) shows the motion of the maximum correlation (arrow) that moves radially outward [65].

The attractiveness of the SOC paradigm in fusion plasmas motivates the need for simultaneous evolution of both the turbulence and the plasma profiles has been recognized. A comprehensive survey of the simulations with flux-driven plasma profiles have been documented in the review article by Sánchez and Newman [46]. Initially, fluid simulations present the most feasible demonstrations of transport characters arising from flux-driven plasma profiles due to their relative reduction in variables compared to gyro-kinetic simulations [50]. Several aspects of the SOC characteristics were investigated using both 2D and 3D fluid codes, for instance, the effect of a subdominant diffusion channel and the impact of zonal flows on the cross-flow transport [57]. Characteristics of SOC similar to that of

the sandpile model have been observed, for example, profile relaxations, radial avalanches, and submarginal profiles on average. Recent improvements in computational capabilities, flux-driven gradient scenarios have become more feasible. The SOC dynamics have been investigated in a flux-driven, global, full-f gyrokinetic simulations with the GT5D code[67]. Historically, gyrokinetic codes[25] have been evolved in the δf scenario where only the perturbation of the entire particle distribution f (Eq. 1.1) is evolved. A full-f evolution then corresponds to the evolution of both the fluctuations and the mean profiles. The more recent global full-f gyrokinetic simulations such as GT5D[67] and GYSELA[68,69] (Fig. 1.10) in simplified 3D tokamak geometry corroborate the results from fluid simulations where avalanches become prominent with flux-driven plasma profiles. Transport becomes dominated with persistent correlations for scales extending beyond the turbulent decorrelation scales.

Observations and numerical evidence display a natural tendency towards SOC-like characteristics in fusion plasmas, which then affects the transport characteristics and, ultimately, the plasma confinement time. Confined fusion plasmas require conditions such as a large pressure, which in turn imposes steep gradients in both temperature and density that acts as sources of free energy. Due to the natural tendency for gradients to relax or equilibrate with their surroundings, turbulence becomes an efficient method of mixing. This process results in transport events that are often much larger than collisional transport often referred to as anomalous transport[14]. A physical model of the avalanche process is based on the SOC paradigm where local perturbations propagate over all length scales and survive over long-time scales. Typical attributes to SOC dynamics are scale invariance and self-similarity. Avalanches in the plasma turbulent transport have been investigated in reduced or low-dimensional models[25]. The SOC paradigm presents a different prism to view the turbulent transport phenomena in tokamak plasmas, which is independent of the detailed instability mechanism and the geometry of the system. Plasma fluid models and gyrokinetic models produce similar transport characteristics when the SOC ingredients are included. Regardless of the complexity of the model, the elements of SOC can naturally accommodate the scaling of energy confinement time with system size contrasting to a diffusive framework. As a consequence, there is a need to develop a transport description that takes into considerations the transport characteristics in SOC-like systems, which are compiled in the nondiffusive transport framework.

1.3.1 Nondiffusive transport

Tokamak plasmas exhibit characteristics that coincide with nonequilibrium systems such as high dimensionality in its dynamics that lead to predominantly stochastic features[32]. An important characteristic and tendency of tokamak plasmas is the existence of density and temperature gradients above which the transport rate increases drastically. The enhanced transport relaxes the profiles until they are within their marginally stable

states, at which the transport rate decreases. The overall transport process is nonlinearly regulated by dissipation or loss processes at the plasma edge. There is then a need to quantify transport through turbulence.

In the spirit of the SOC paradigm, the nondiffusive transport framework was likewise built on the concept of the transport equation that is independent of the underlying details. Due to high computational costs associated with evolving plasmas using the basic equations, the feasibility of using this approach for transport prediction during device operation becomes limited. The strategy towards a transport equation description comes from the need to reduce the number of variables in a complex systems such that transport predictions during machine operation can be performed within a reasonable amount of time in order to guide and provide predictions during experiments. In order to reduce the number of variables in complex systems, some assumptions of the statistical or probabilistic type must be made. The kinetic equation[70] for real dynamical systems appears as a compromise between two alternative types of descriptions: dynamical and statistical. Dynamical descriptions employ force relations whereas statistical descriptions aim to use statistical assumptions to simplify the complex force interactions. The kinetic equation approach is in parallel to statistical mechanics theory of gases where stochastic elements such as the probability distribution of gas molecules are used to account for the state of the system instead of keeping track of the phase space variables of each molecule. In the process of reducing the complexity, kinetic equations do not fully describe the dynamics, and some features of the dynamics can never be obtained (or recovered) as compared with the dynamical description. In this sense, kinetics can contain constraints that contradict with the dynamics and also are not applicable for some parameter ranges. The requirement from a probabilistic element allows for the kinetic equations to be derived by introducing some stochastic process relevant to the phenomena.

The two descriptions provide two complimentary approaches to describe physical systems where the dynamical or comprehensive description derives from force equations while the kinetic description appeals to the phenomenological approach. Since the dynamical approach often involves large number of variables, it becomes too complex to solve. Assumptions are usually made in order to reduce the number of variables. Sometimes, these reductions neglect necessary ingredients for appropriate overall statistics. The kinetic approach bypasses the large number of variables by starting with the overall statistics of the phenomenon itself. However, due to the initial assumption on the reduced statistics, particular details of the phenomenon cannot be recovered. Often, the two approaches remain irreconcilable due to the constructions and motivations for a particular phenomenon. The diffusion equation is a simple example of a kinetic equation. The SOC paradigm then provides the necessary elements to build a transport equation that can more accurately describe the transport in a turbulent medium.

An existing and ubiquitous paradigm that describes transport in a medium is the

classical diffusion equation. Being classed as a kinetic type approach, the classical diffusion describes the transport process without addressing the underlying details of the physical interactions. Underlying the classical diffusion equation is the lack of memory and the central limit theorem that allows the interactions of several random variables to converge into a Gaussian distribution. The Markov process or the Brownian motion are all possible ways to arrive at the classical diffusion equation. The nondiffusive framework takes a very similar approach to the classical diffusion equation, but the stochastic element changes due to the SOC paradigm. In the SOC paradigm, the multiscale property cannot be described within the classical diffusion paradigm.

In order to describe memory and extended spatial correlations, the underlying paradigm needs to change. There are two principal approaches to construct a transport equation motivated in part by the SOC paradigm: continuous time random walk (CTRW) and the family of fraction Levy motions (fLm). A more detailed introduction to this approach has been published in a recent review article[46]. Although the two approaches to a more general transport equation are intrinsically different, they asymptotically describe the same resulting transport equation. A similar approach to constructing a more general transport equation is also possible[71]. The converged transport equation is referred to as the fractional transport equation (FTE), which is often described by the propagator. A propagator or the Green's function is the probability that gives the temporal evolution of the initial condition of a δ-function. The CTRW formalism is a generalization of the standard random walk framework, which can be more intuitive to understand. A walker moving in one spatial dimension in time can be described by a probability associating with a step-size as well as a waiting-time probability. The step-size distribution describes the probability of a walker making a step of size Δx while the waiting-time distribution gives the probability of making the step in a time duration Δt. These probabilities then become the propagator of a density of walkers $n(x,t)$. The general solution of a density of walkers under the CTRW approach can be described through the propagator P_{CTRW} as

$$n(x,t) = \int_0^t dt' \int_{-\infty}^{\infty} dx' P_{\mathrm{CTRW}}(x-x', t-t') S(x',t') \tag{1.7}$$

where $S(x,t)$ is any source that can include an initial condition $S(x,t) = S_{\mathrm{ext}}(x,t) + n_0(x)\delta(t-t_0)$. The propagator for the CTRW is the probability that gives the temporal evolution of the initial condition $n_0(x) = \delta(x-x_0)$. The distribution choices for the standard random walk solution are a Gaussian distribution for the step-sizes and an exponential distribution for the waiting-times. The Gaussian step-size distribution comes from the central limit theorem, which gives a finite variance that describes the finite transport characteristic spatial scale of a population of walkers. The exponential waiting-time distribution describes the vanishing memory of a population of walkers that then defines a finite characteristic temporal scale.

In order to include memory and large spatial correlations, the family of stable Levy distributions $L_{\gamma,\theta,\sigma}(x)$ are used instead to describe the CTRW process. The analytical closed form for $L_{\gamma,\theta,\sigma}(x)$ only exists in the Fourier domain $x \rightarrow k$, $L_{\gamma,\theta,\sigma}(k) = \exp\left\{-\sigma^{\gamma}|k|^{\gamma}\left[1 - i\beta \mathrm{sgn}(k)\tan(\pi\gamma/2)\right]\right\}$ [72]. These distributions are described by the three parameters: $\gamma \in (0,2]$ the tails of the distribution, $\theta \in [-1,1]$ the symmetry, and σ the width of the distribution. The width σ is related to the moments of the distribution $\langle|\Delta x|^{s}\rangle^{1/s} \propto \sigma$ where the moments are finite only for $s < \gamma$. The Gaussian distribution is recovered when $\gamma = 2$ and $\theta = 0$. In a similar manner to the underlying assumption of the classical diffusion equation, this family of stable Levy distributions also satisfy the weak central limit theorem, which enables the combined probability of several Levy-distributed variables to converge to a stable Levy distribution [70]. Using a more general family of distributions, the appropriate choices for the step-size distributions are constrained to the symmetric Levy $L_{\alpha,0,\sigma}$ where $\alpha \in (0,2]$, and the waiting-time distributions are limited to the positive asymmetric Levy distributions $L_{\beta,1,\tau}$ where $\beta \in (0,1]$. The order α denotes the spatial exponent associated with the stable symmetric Levy distribution for the spatial domain $x \in (-\infty,\infty)$, and the order β reflects the asymmetric stable Levy distributions in the time domain such that $t \in [0,\infty)$. The selection of the distribution functions then define P_{CTRW} that disregards characteristic scales. For large-scale behavior and long times, P_{CTRW} converges asymptotically to the propagator for the FTE in the Laplace-Fourier domain, $P_{\mathrm{CTRW}}(s,k) \sim s^{\beta-1}/\left[\left(\sigma^{\alpha}/\tau^{\beta}\right)|k|^{\alpha} + s^{\beta}\right]$ [73]. With the CTRW approach, the FTE of a density of walkers can then be described in a form similar to the classical diffusion equation using fractional derivative operators [74];

$$\frac{\partial n}{\partial t} = {}_0D_t^{1-\beta}\left[\frac{\sigma^{\alpha}}{\tau^{\beta}}\frac{\partial^{\alpha} n}{\partial|x|^{\alpha}}\right] + S_e(x,t) \tag{1.8}$$

where the left-side and right-side Riemann-Liouville fractional derivatives are defined as

$$\begin{aligned} {}_aD_x^{\gamma} f(x) &= \frac{1}{\Gamma(p-\gamma)}\frac{d^p}{dx^p}\left[\int_a^x \frac{f(x')dx'}{(x-x')^{\gamma-p+1}}\right] \\ {}^bD_x^{\gamma} f(x) &= \frac{-1}{\Gamma(p-\gamma)}\frac{d^p}{d(-x)^p}\left[\int_x^b \frac{f(x')dx'}{(x-x')^{\gamma-p+1}}\right] \end{aligned} \tag{1.9}$$

such that p is an integer satisfying the condition $p-1 \leq \gamma < p$. The fractional derivative over the domain $x \in (-\infty,\infty)$ is reduced using the identity

$$\frac{\partial^{\gamma} f}{\partial|x|^{\gamma}} = -\frac{1}{2\cos(\pi\gamma/2)}\left[{}_{-\infty}D_x^{\gamma} + {}^{\infty}D_x^{\gamma}\right] f(x). \tag{1.10}$$

The integro-differential operators over the whole domain and time history mathematically express the absence of characteristic scales. The classical diffusion then becomes a subset of the FTE by assigning $\alpha = 2$ and $\beta = 1$ in Eq. 1.8. The CTRW definition defines the FTE

through the exponents α and β. With the use of fractional derivative operators, the FTE is elevated to a type of fractional kinetic equation[75] that incorporates, in a natural way, the non-Gaussian and long-range dependence that often violates the restrictive assumptions of locality and lack of correlations that underlies the conventional statistical mechanical paradigm of the classical diffusion equation[32,70].

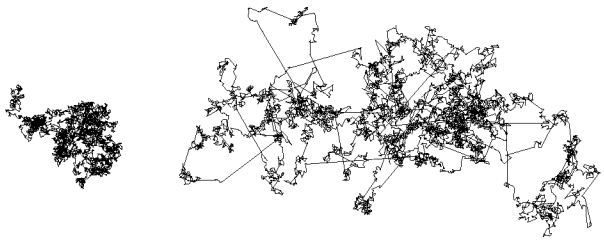

Figure 1.13: A cartoon compares a particle ($\sim$ 7000 steps) experiencing Brownian motion (left) and fLm (right)[75].

An alternate approach to obtaining the FTE is through the fractional Levy motions, which is defined through the Langevin formalism that follow a particle trajectory, which is the basis of the Lagrangian view of turbulent transport[76]. A particle trajectory in one-dimension is defined with a Gaussian distributed noise $\eta(t)$, $X(t) = X_0 + \int_0^t dt' \eta(t')$ where $\langle \eta(t)\eta(t') \rangle = \sigma^2 \delta(t - t')$ and σ^2 is the variance. A natural generalization of this motion is the fractional Levy motions (fLm), which is defined as

$$X(t) = X_0 + \frac{1}{\Gamma(H - 1/\alpha + 1)} \int_0^t dt' \left(t - t'\right)^{H-1/\alpha} \eta_\alpha(t') \tag{1.11}$$

where $\eta_\alpha(t)$ is now the stable symmetric Levy distributions $L_{\alpha,0,\sigma}(t)$ and H is the self-similar exponent. According to this formalism, $H < 1/\alpha$ describes anti-persistent motion, $H > 1/\alpha$ reflects persistent motion, and $H = 1/\alpha$ denotes uncorrelated motion. This then limits the parameter space for H to $H \in (0, 1/\alpha]$ when $\alpha < 1$ and $H \in (0, 1]$ for $1 < \alpha < 2$[72]. The fractional Brownian motion (fBm) is described when $\alpha = 2$. When the particle paths are averaged over multiple realizations, the evolution of the density of particles in terms of the propagator $P_{\text{fLm}}(x - x', t - t')$,

$$n(x,t) = \int_0^t dt' \int_{-\infty}^{\infty} dx' P_{\text{fLm}}(x - x', t - t') S(x', t'), \tag{1.12}$$

which has a similar form to Eq. 1.7. While the CTRW formulation requires specifying two probability distributions, one for the step-size and another for the waiting-time, the fLm approach only specifies the combined correlated noise statistics through the symmetric Levy $L_{\alpha,0,\sigma}\left[(x - x_0)/t^H\right]$. A walker undergoing the standard random walk motion compared with Levy flights is shown in Fig. 1.13. In the same vein as the CTRW, the propagator for the fLm can be asymptotically shown to converge in Laplace-Fourier space $P_{\text{fLm}}(s, k) \sim$

$s^{\alpha H-1}/\left[\sigma^{\alpha}|k|^{\alpha}+s^{\alpha H}\right]$. To reiterate, the classical diffusion limit is obtained by setting $\alpha = 2$ and $H = 1/2$. The fLm approach characterizes the particle motion through the exponents α and H, and the relation $\alpha H = \beta$ allows translation between different exponents. The collection of the exponents H, α, and β is often referred to as the transport exponents due to their relevance to the FTE that describes a more general transport process than the conventional classical diffusion equation.

Though the propagators for the CTRW and the fLm are different, they both converge asymptotically to the FTE in the large-scale and long-time limit. The FTE describes transport without characteristic scales, which makes this formulation attractive to SOC dynamics to describe turbulent transport in tokamak plasmas. To date, the transport exponents for the FTE have been quite challenging to extract analytically from dynamical equations such as from the plasma equation Eq.1.1. Based on the construction of the FTE from CTRW and fLm formulations, the transport exponents for the FTE can be extracted using different methods[46]. In the context of turbulent transport, most of the techniques to determine the transport exponents require information on the velocity flow.

The information of the flow is recovered from the flow trajectories or through the velocity signals on a fixed grid. Turbulent flow information can be described according to two principal viewpoints: Lagrangian and Eulerian[34]. The Lagrangian perspective follows the fluid trajectory,

$$\frac{d\boldsymbol{R}}{dt} = \boldsymbol{u}\left(\boldsymbol{R}(t), t\right) \tag{1.13}$$

where $\boldsymbol{R}(t) = \boldsymbol{R}(t'|\boldsymbol{r}, t)$ denotes the fluid trajectory at position $\boldsymbol{r}$ at time t starting at an earlier time t' and $\boldsymbol{u}(\boldsymbol{R}, t)$ is the velocity of the fluid $\boldsymbol{R}(t)$. This is identical to the fLm formulation without the noise term. With a Gaussian distributed noise, the path trajectory evolves in terms of a stochastic differential equation $\dot{\boldsymbol{R}} = \boldsymbol{u}\left(\boldsymbol{R}(t), t\right) + \sqrt{2\kappa}\dot{\boldsymbol{\eta}}(t)$ where $\boldsymbol{\eta}(t)$ now has components in each spatial dimension[77,78]. Under the condition of statistical homogeneity of the Eulerian velocity, the velocity in the Lagrangian frame is related to the Eulerian frame by $\boldsymbol{U}(t) = \boldsymbol{u}\left[\boldsymbol{R}\left(t'|\boldsymbol{r}, t\right), t\right]$ where the Eulerian velocity $\boldsymbol{u}$ is evaluated along the fluid trajectory path $\boldsymbol{R}$[77]. Statistical homogeneity of the Eulerian velocity implies that the Lagrangian velocity is independent of the initial position. The Lagrangian frame is often used as the basis for analytical description of transport such as the frame used in the fLm approach of the FTE. Tracers or massless tracked particles following the fluid flow provide information in the Lagrangian frame. This frame gives a more intuitive sense of transport and is more appropriate in circumstances such as the dispersion of localized sources. The Eulerian viewpoint measures a quantity on a fixed grid, which is more accessible in practice. For instance, a grid of temperature sensors simultaneously monitor temperatures at various fixed locations. One of the techniques in the Eulerian frame is to track a passive scalar field Θ that evolves according to the advection equation with minimal diffusion κ;

$$\frac{\partial\Theta}{\partial t} + \boldsymbol{u}\cdot\nabla\Theta = \kappa\nabla^2\Theta + f_{\Theta}\left(\boldsymbol{r}, t\right). \tag{1.14}$$

The source and initial condition is encoded in $f_\Theta(\boldsymbol{r}, t)$. The passive scalar field also evolves independently from the quantities generating the flow as opposed to an active scalar field that influences the flow through local forces. Active fields are functionally related to the velocity. Eq. 1.14 coincides with the ensemble average over several realizations of $\eta(t)$ in the Langevin equation, which then relates to the fLm formulation of the FTE.

Though a general translation between the two frames only exist in special circumstances, both viewpoints provide equivalent and valuable information on turbulent transport. The transport exponents for the FTE can be determined through the Lagrangian and Eulerian frames. In this work, the principal methods of determining the transport exponents for the FTE are outlined. Sec. 1.3.2 outlines the primary Lagrangian technique based on the Lagrangian velocities to determine H through R/S analysis and α from the probability distributions. Sec. 1.3.3 outlines the Eulerian technique using the propagator fitting method that is applied to both the spreading of a tracer could and the distribution of the passive scalar field.

1.3.2 Extracting transport exponents in the Lagrangian frame

In the Lagrangian frame, tracers are used to determine the by following a velocity trajectory. Tracers provide the time history of a given flow, which then determines the temporal correlations of the velocities. The spread of tracers provide the spatial correlations between the velocities. In this work, the combined transport characteristics will be quantified under the fLm approach towards the construction of FTE (Eq. 1.8). This means that the transport exponents that need to be quantified are H and α. The self-similar exponent H can be recovered from a plethora of methods such as detrended-fluctuations-analysis (DFA), R/S, or structure function analysis. In this work, the R/S method is preferred due to its resilience to random noise[62]. The method measures the maximum excursion of a given signal compared to the standard deviation in order to estimate the self-similar exponent H over a time duration $[R/S] \propto \tau^H$ where the time duration $\tau \in (\tau_1, \tau_2)$ denotes the mesorange. The mesorange specifies the intermediate range of time lags where we estimate H between τ_1 and τ_2. Among the various definitions for the R/S, this work uses a slightly modified form from Hurst's original definition[64]. Given a time series of length N represented as $\{X_k : 1 \leq k \leq N\}$, the definition for this work is

$$[R/S]_n = \frac{1}{M_n} \sum_{m=0}^{M_n - 1} \frac{\max(0, W_{1,n,m}, \ldots, W_{n,n,m}) - \min(0, W_{1,n,m}, \ldots, W_{n,n,m})}{\sigma_{n,m}^{1/\alpha}} \tag{1.15}$$

where $W_{k,n,m} = X_{1+\tau_m} + \cdots + X_{k+\tau_m} - k\bar{X}_{n,m}$ for $k \leq n$. The mean is defined as $\bar{X}_{n,m} = \sum_{i=1}^{n} X_{i+\tau_m}/n$ respective to a signal of length n. The α-variance for a time segment of length n is defined as $\sigma_{n+m} = \sum_{i=1}^{n} \left(X_{i+\tau_m} - \bar{X}_{n,m}\right)^\alpha / (n-1)$. The number of equal time segments M_n is usually defined as an integral division of the entire time series length

N by the time lag segment n, $M_n = N/n$. The shift in the time series data is then $\tau_m = m/M_n = m\,(n/N)$. This form for calculating the R/S is similar to the one used by Hurst with an additional averaging operation over equal time segments. A consequence of this is that the curves become smoother and samples over equal time segments. The R/S method tends to overestimate random noise by yielding a scaling of $H \sim 0.55$ [64].

Both the dynamics and the statistics of the velocity information are required to quantify the transport according to the FTE. The R/S analysis provides a measure of the dynamics pertaining to the temporal persistence or memory of the velocity flow. The statistics of the flow are characterized by the probability distribution of the velocities, which is a measure of spatial correlations. The relationship between the velocity statistics and transport arises from the mean-squared displacement, which is a measure of the spread of the tracers due to the underlying velocity flow. The mean squared displacement of the tracers $\Delta\boldsymbol{R}\,(\boldsymbol{r},t) = \boldsymbol{R}\,(\boldsymbol{r},t) - \boldsymbol{R}\,(\boldsymbol{r},0)$ can be expressed in terms of the velocity correlations as [77],

$$\frac{d}{dt}\left\langle [\Delta\boldsymbol{R}(\boldsymbol{r},t)]^2 \right\rangle = 2\int_0^t \left\langle \boldsymbol{U}(t)\cdot\boldsymbol{U}(t')\right\rangle dt' \tag{1.16}$$

where $\boldsymbol{U}(t)$ represents the Lagrangian velocity. The Lagrangian decorrelation time $\tau_d = \int_0^\infty dt'\left\langle \boldsymbol{U}(0)\cdot\boldsymbol{U}(t')\right\rangle / \left\langle \boldsymbol{U}^2(0)\right\rangle$ provides a measure of persistence and relates to the characteristics of the velocity flow underlying the transport.

Under an isotropic and incompressible flow field $\boldsymbol{u}(\boldsymbol{r},t)$, the equation associated with the transport of tracer density is $0 = \partial_t n + (\boldsymbol{u}\cdot\nabla)\,n$, which is the passive scalar advection equation Eq. 1.14 in the absence of forcing and diffusion. The flow velocity $\boldsymbol{u}$ is the Eulerian frame velocity. By separating the contribution between the mean quantity and the fluctuation $n = n_0 + \tilde{n}$ with a zero mean flow $\boldsymbol{u} = \tilde{\boldsymbol{u}}$, there is an equation for the evolution of mean quantity and the fluctuating part;

$$\begin{aligned} \frac{\partial n_0}{\partial t} &= -\left\langle \tilde{\boldsymbol{u}}\cdot\nabla\tilde{n}\right\rangle, \\ \frac{\partial\tilde{n}}{\partial t} + \tilde{\boldsymbol{u}}\cdot\nabla\tilde{n} &= -\tilde{\boldsymbol{u}}\cdot\nabla n_0 + \left\langle \tilde{\boldsymbol{u}}\cdot\nabla\tilde{n}\right\rangle \end{aligned} \tag{1.17}$$

where $\langle\ldots\rangle$ denotes the ensemble average. The fluctuation part $\tilde{n}$ is then written in terms of a propagator $\partial_t P + \tilde{\boldsymbol{u}}\cdot\nabla P = \delta\,(\boldsymbol{r}-\boldsymbol{r}',t-t')$ with a formal solution $P\,(\boldsymbol{r}-\boldsymbol{r}',t-t') = \delta\,(\boldsymbol{r}'-\boldsymbol{R}\,(t'|\boldsymbol{r},t))$ [79] where the fluid trajectory is solved backwards in time $\boldsymbol{R}\,(t'|\boldsymbol{r},t)$. Using the propagator solution for $\tilde{n}(\boldsymbol{r}',t')$, the time evolution of the mean part n_0 becomes

$$\frac{\partial n_0}{\partial t} = \boldsymbol{\nabla}\cdot\int_0^t dt'\left\{\left\langle \tilde{\boldsymbol{u}}(\boldsymbol{r},t)\tilde{\boldsymbol{u}}\left[\boldsymbol{R}\left(t'|\boldsymbol{r},t\right),t'\right]\cdot\boldsymbol{\nabla}n_0\left[\boldsymbol{R}\left(t'|\boldsymbol{r},t\right),t'\right]\right\rangle\right\} \tag{1.18}$$

where flow correlations at previous times t' and the current time t are contained inside the time integral. Eq. 1.18 describes the velocity correlation between the current velocity flow $\tilde{\boldsymbol{u}}(\boldsymbol{r},t)$ and previous velocities following the fluid path $\boldsymbol{R}\,(t'|\boldsymbol{r},t)$. This form is slightly

reminiscent of the Lagrangian decorrelation time τ_d. With a locality approximation[79] such that

$$\nabla n_0 \left[\boldsymbol{R}\left(t'|\boldsymbol{r},t\right),t' \right] \simeq \nabla n_0 \left(\boldsymbol{r},t'\right) \tag{1.19}$$

Eq. 1.18 is then reduced to

$$\frac{\partial n_0}{\partial t} \simeq \nabla \cdot \left[\int_0^t dt' \boldsymbol{C}^L(t',t) \cdot \nabla n_0(\boldsymbol{r},t') \right] \tag{1.20}$$

where the Lagrangian correlation matrix is defined as

$$\boldsymbol{C}^L(t',t) = \left\langle \tilde{\boldsymbol{u}}(\boldsymbol{r},t) \tilde{\boldsymbol{u}} \left[\boldsymbol{R}\left(t'|\boldsymbol{r},t\right),t' \right] \right\rangle . \tag{1.21}$$

The characteristics of the flow in Eq. 1.18 in relation to H are also contained in the time history integral[79]. Eq. 1.18 can be generalized without the locality hypothesis (Eq. 1.19), which requires determining the joint probability function of the velocities. This then provides a connection between H and the transport equation Eq. 1.18 such that the characteristics of the flow is represented by the exponents H plus others that determine the joint probability distribution of the flow. With the choice of the family of stable Lévy distributions due to the central limit theorem, the other exponent required to characterize the flow characteristics in Eq. 1.18 is $\alpha \in (0,2]$.

1.3.3 Extracting transport exponents in the quasi-Lagrangian frame

An alternate method to characterize the transport exponents is by fitting the propagator of FTE directly to the evolution of a highly localized initial perturbation. This method can be applied to both tracers (Eq. 1.13) and passive scalars (Eq. 1.14). The passive scalar evolves Eq. 1.14 with an initial perturbation $f_\Theta(\boldsymbol{r},t) = \Psi(\boldsymbol{r}-\boldsymbol{r}_0)\delta(t)$. Hence, the propagator solution for the passive scalar field is exactly identical to the fLm formulation (Eq. 1.12),

$$\Theta(\boldsymbol{r},t) = \int_0^t dt' \int dr' P_\Theta \left(\boldsymbol{r}-\boldsymbol{r}',t-t'\right) f_\Theta(\boldsymbol{r}',t') \tag{1.22}$$

where $P_\Theta\left(\boldsymbol{r}-\boldsymbol{r}',t-t'\right) = \left\langle \delta\left(\boldsymbol{r}'-\boldsymbol{R}\left(t'|\boldsymbol{r},t\right)\right)\right\rangle_{\boldsymbol{\eta}}$ is the propagator for the passive scalar field averaged over many realizations of the noise $\boldsymbol{\eta}(t)$. When following a fluid path, a scalar quantity $\theta(t)$ evolves as $d\theta/dt = f_\Theta\left(\boldsymbol{R}(t),t\right)$[80]. The solution of the scalar quantity is $\theta(t) = \int_0^t dt' f_\Theta\left(\boldsymbol{R}\left(t'|\boldsymbol{r},t\right),t'\right)$. The passive scalar field is then averaged over realizations of $\boldsymbol{\eta}$ or all Lagrangian paths terminating at position $\boldsymbol{r}$ and at time t

$$\Theta(\boldsymbol{r},t) = \left\langle \theta(t) \right\rangle_{\boldsymbol{\eta}} = \left\langle \int_0^t dt' f_\Theta \left(\boldsymbol{R}\left(t'|\boldsymbol{r},t\right),t'\right) \right\rangle_{\boldsymbol{\eta}} . \tag{1.23}$$

Due to this correspondence between the tracers and the passive scalar field, the propagator fitting for both the tracer cloud and the distribution of the passive scalar field provides

methods for determining the transport exponent of the FTE. The main differences between the tracers and the passive scalar field are the diffusion term and the statistics. Tracers are limited by the number of tracked markers while the passive scalar inherently samples the spatial domain with a small diffusion.

Although the techniques to determine the exponents can be categorized under these two viewpoints, the mean flow is usually not considered when describing turbulent transport. In the Eulerian frame where the fluid velocities are measured in a fixed reference frame respective to the flow, the estimation of the transport exponents are usually quantified through the spreading of a highly localized initial perturbation. In order to quantify the spreading without the effects of a mean flow, the analysis is done in a co-moving frame with the mean flow such that $\tilde{\zeta}(\boldsymbol{r},t) = \zeta\left(\boldsymbol{r} + \boldsymbol{R}(0|\boldsymbol{r}_0,t)\right)$ where ζ represents either the distribution of the tracer cloud or the passive scalar field, and $\boldsymbol{R}(0|\boldsymbol{r}_0,t)$ is the Lagrangian trajectory of the origin of the cloud at $\boldsymbol{r}_0$ starting at time $t = 0$. The shift in the frame is referred to as the quasi-Lagrangian frame[77]. The quasi-Lagrangian frame becomes more appropriate since the mean flow of the perturbation is removed, and the spreading of the perturbation is tracked in the frame that moves with the centroid of the perturbation[77]. This quasi-Lagrangian frame follows the same evolution as the Eulerian frame with an advective term replaced by $\tilde{\boldsymbol{u}}(\boldsymbol{r},t) - \tilde{\boldsymbol{u}}(\boldsymbol{r}_0,t)\cdot\nabla$ where $\tilde{\boldsymbol{u}}(\boldsymbol{r}_0,t)$ which represents the velocity of the origin of the cloud.

The FTE (Eq. 1.8) describes a more general transport equation than the classical diffusion equation. The FTE relaxes the constraints on having characteristic spatial and temporal scales, which allows the description of transport generating from SOC systems. The transport exponents of the FTE can be determined by several methods based on both the Lagrangian and Eulerian viewpoints of fluid flow. Despite the inherent equivalence between the Lagrangian and the Eulerian viewpoints, the Eulerian frame is more feasible for measurements, especially in tokamak plasmas.

1.4 Outline

The context of this thesis falls under a broader model hierarchy of modeling approaches that aim to describe and express general physical processes in qualitative terms. One of the achievements of this thesis is the development of a model with essential elements that bridges the gap between first principles and holistic models for turbulent transport in tokamak plasmas. Although the constructed model is based primarily in tokamak fusion research, the approach is more general in the context of the modeling approach hierarchy that spans the gap between two paradigms. With this approach, the calculated quantities cannot be directly translated into improvements for the current operation of current or next generation tokamaks. Nonetheless, the physical processes discussed in this thesis can aid in verification, validation, and optimization of current knowledge that embodies the area of multiphysics and multiscale coupling in accordance to the current FES goals (Sec. 1.1.1).

The new contribution of this model is the integration of flux-driven elements in order to construct a flux-driven simulation, which then leads to the inevitable dual reactions to the steepening of local gradients that then yield nondiffusive transport characteristics. The unsurprising competition due to the steepening of local gradients naturally occurs when the turbulence and the driving profile are evolved simultaneously, which has been uncommon in conventional transport modeling. A similar reasoning used to develop the transport equation (Sec. 1.3.1) is being applied to the modeling approach in this thesis. The complex coupling based on the comprehensive approach between the profile and the turbulence is replaced with more simple interactions in order to capture the flux-driven mechanism. This model allows numerically inexpensive investigations of nondiffusive transport characteristics, which are often not possible under conventional fixed-gradient models or numerically expensive under flux-driven conditions. The model remains sufficiently simple but still contain complex turbulent dynamics, which is in the essence of the SOC paradigm. Chapter 2 discusses in detail in the construction of the flux-driven elements that provide the feedback between the turbulence and the driving profile. The primary model employed in this thesis is constructed at the junction of the the drift-wave paradigm (Sec. 1.2) and the turbulence relaxation mechanism motivated by the SOC paradigm (Sec. 1.3). Chapter 2 identifies the relative importance of each nondiffusive element to the overall transport by identifying nondiffusive transport characteristics through tracers (Sec. 1.3.2). Chapter 3 further discusses how the transport character changes in the presence of external poloidal flows and in regimes with active flow-driven instabilities. The reoccurring theme in Chapter 2 and 3 is that the classical diffusion paradigm only exists in specific parametric regimes when the nondiffusive elements are in balance. In consequence, classical diffusion exists only in certain regimes and is not necessarily a limiting case when self-consistent flux-driven profile is involved.

Due to the nature of fluid turbulence (Sec. 1.2), the process of obtaining turbulent transport characteristics from one realization of the turbulent state usually requires several realizations. The results in Chapter 4 demonstrate a possible approach towards characterizing turbulent transport in a more general manner under the nondiffusive transport framework and with a single realization of the turbulent state. Based on the SOC paradigm to within the turbulent transport phenomenology, principal transport diagnostics were constructed under the nondiffusive transport framework (Sec. 1.3.1). The Lagrangian frame information (Sec. 1.3.2) identifies the transport characteristics in Chapters 2 and 3. Chapter 4 presents the equivalence of the tracers (Sec. 1.3.2) and a passive scalar (Sec. 1.3.3), which validates the bridge between the Lagrangian and the Eulerian frame. The equivalence of the two viewpoints in turbulence presents a possible method of extracting nondiffusive transport exponents using conventional experimental techniques through one realization of the turbulent state. Fundamentally, there is sufficiently enough information in one turbulence realization in order to deduce the turbulent transport without the need for statistical average over several realizations. The passive scalar contains an infinite number of tracers.

This result bridges the nondiffusive transport framework from analytical interpretations to experimental measurements. The results in Chapter 4 have important implications toward the fundamental understanding of fluid turbulence by identifying nondiffusive transport signatures in plasma experiments and, more generally, in any turbulent medium.

Confinement time in tokamak plasmas remains a crux in the quest for sustainable terrestrial nuclear fusion. Due to our limited ability to simulate the entire device, modeling remains an essential and integrative part towards sustainable fusion. Despite the explosive improvements in tokamak plasmas over the past 60 years, confinement time required for sustainable fusion remains limited by turbulent transport. Hence, improvements to the confinement time requires understanding of turbulence and, more importantly, the transport due to turbulence. The results from this thesis propel a new paradigm towards understanding the long-standing enigma of turbulent transport. The developed model in this thesis defies the conventional modeling approach by integrating an existing model with holistic elements. In consequence, the results demonstrates the need for flux-driven elements and an appropriate paradigm in order to understand the fundamental puzzle of turbulent transport. The diagnostic tools based on the new paradigm of understanding have been shown in this work to relate two fundamental perspectives on turbulent transport, which can have significant implications towards understanding turbulent transport. This then allows a possible pathway to bridge the gap between analytical and experimental measures of turbulence. The importance of these results is summarized in Chapter 5.

[1] G. Neilson, in *Magnetic Fusion Energy*, edited by G. H. Neilson (Woodhead Publishing, 2016) pp. 3 – 5.

[2] D. C. Pace, W. W. Heidbrink, and M. A. Van Zeeland, Physics Today **68**, 34 (2015).

[3] M. Kikuchi, Energies **3**, 1741 (2010).

[4] H. R. Koslowski, Fus. Sci. Tech. **61**, 96 (2012).

[5] H. Zohm, in *Magnetic Fusion Energy*, edited by G. H. Neilson (Woodhead Publishing, 2016) pp. 7 – 30.

[6] S. Benkadda, C. R. Physique **7**, 692 (2006).

[7] R. J. Bickerton, Plasma Phys. Control. Fusion **39**, 339 (1997).

[8] S. Atzeni and J. Meyer-ter-Vehn, *The Physics of Inertial Fusion: Beam Plasma Interaction, Hydrodynamics, Hot Dense Matter* (Claredon Press, Oxford, 2004).

[9] J. D. Lawson, Proceedings of the Physical Society. Section B **70**, 6 (1957).

[10] X. Garbet, C. R. Physique **7**, 573 (2006).

[11] K. Ikeda, Nucl. Fusion **50**, 014002 (2010).

[12] J. P. Friedberg, *Plasma Physics and Fusion Energy* (Cambridge University Press, New York, NY, 2007).

[13] J. Wesson, *Tokamaks*, 3rd ed. (Oxford University Press, Oxford, 2004).

[14] B. A. Carreras, IEEE Trans. Plasma Sci. **25**, 1281 (1997).

[15] V. Grandgirard and G. Latu, in *Curie, un an après* (Bruyères-le-Châtel, 2013).

[16] F. Wagner, G. Becker, K. Behringer, D. Campbell, A. Eberhagen, W. Engelhardt, G. Fussmann, O. Gehre, J. Gernhardt, G. v. Gierke, G. Haas, M. Huang, F. Karger, M. Keilhacker, O. Klüber, M. Kornherr, K. Lackner, G. Lisitano, G. G. Lister, H. M. Mayer, D. Meisel, E. R. Müller, H. Murmann, H. Niedermeyer, W. Poschenrieder, H. Rapp, H. Röhr, F. Schneider, G. Siller, E. Speth, A. Stäbler, K. H. Steuer, G. Venus, O. Vollmer, and Z. Yü, Phys. Rev. Lett. **49**, 1408 (1982).

[17] F. Wagner, Plasma Phys. Control. Fusion **49**, B1 (2007).

[18] J. W. Connor and H. R. Wilson, Plasma Phys. Control. Fusion **42**, R1 (2000).

[19] P. W. Terry, Rev. Mod. Phys. **72**, 109 (2000).

[20] JET Team (prepared by M.L. Watkins), Nucl. Fusion **39**, 1227 (1999).

[21] A. Fasoli, S. Brunner, W. A. Cooper, J. P. Graves, P. Ricci, O. Sauter, and L. Villard, Nat. Phys. **12**, 411 (2016).

[22] D. R. Nicholson, *Introduction to Plasma Theory* (John Wiley & Sons, New York, 1983).

[23] W. M. Tang and V. S. Chan, Plasma Phys. Control. Fusion **47**, R1 (2005).

[24] Y. Idomura, T.-H. Watanabe, and H. Sugama, C. R. Physique **7**, 650 (2006).

[25] X. Garbet, Y. Idomura, L. Villard, and T. Watanabe, Nucl. Fusion **50**, 043002 (2010).

[26] P. Bonoli and L. C. McInnes, *Report of the Workshop on Integrated Simulations for Magnetic Fusion Energy Sciences*, Technical Report (U.S. Department of Energy: Office of Science, 2015).

[27] R. A. Gerber and H. J. Wasserman, *Large Scale Computing and Storage Requirements for Fusion Energy Sciences: Target 2017*, Technical Report (Ernest Orlando Lawrence Berkeley National Laboratory, 2013).

[28] R. Maingi, in *Magnetic Fusion Energy*, edited by G. H. Neilson (Woodhead Publishing, 2016) pp. 31 – 59.

[29] D. Kramer, Physics Today **69**, 36 (2016).

[30] W. Horton, Rev. Mod. Phys. **71**, 735 (1999).

[31] S. Hirshman and D. Sigmar, Nucl. Fusion **21**, 1079 (1981).

[32] A. S. Sharma, M. J. Aschwanden, N. B. Crosby, A. J. Klimas, A. V. Milovanov, L. Morales, R. Sánchez, and V. Uritsky, Space Sci. Rev. **198**, 167 (2016).

[33] C. L. Fefferman, "Existence and smoothness of the navier-stokes equation," in *The Millennium Prize Problems*, edited by J. Carlson, J. Arthur, and A. Wiles (American Mathematical Society, Providence, RI, 2006) pp. 57–67.

[34] M. Lesieur, *Turbulence in Fluids*, 4th ed. (Springer, New York, NY, 2008).

[35] G. T. Chapman and M. Tobak, "Observations, theoretical ideas, and modeling of turbulent flows—past, present, and future," in *Theoretical Approaches to Turbulence*, edited by D. L. Dwoyer, M. Y. Hussaini, and R. G. Voigt (Springer New York, New York, NY, 1985) pp. 19–49.

[36] C. P. Ritz, R. V. Bravenec, P. M. Schoch, R. D. Bengtson, J. A. Boedo, J. C. Forster, K. W. Gentle, Y. He, R. L. Hickok, Y. J. Kim, H. Lin, P. E. Phillips, T. L. Rhodes, W. L. Rowan, P. M. Valanju, and A. J. Wootton, Phys. Rev. Lett. **62**, 1844 (1989).

[37] P. Hennequin, C. R. Physique **7**, 670 (2006).

[38] A. G. Peeters, C. Angioni, and G. Tardini, C. R. Physique **7**, 592 (2006).

[39] G. R. Tynan, A. Fujisawa, and G. McKee, Plasma Phys. Control. Fusion **51**, 113001 (2009).

[40] A. Hasegawa and K. Mima, Phys. Rev. Lett. **39**, 205 (1977).

[41] M. Wakatani and A. Hasegawa, Physics of Fluids **27**, 611 (1984).

[42] D. E. Newman, P. W. Terry, P. H. Diamond, Y.-M. Liang, G. G. Craddock, A. E. Koniges, and J. A. Crottinger, Phys. Plasmas **1**, 1592 (1994).

[43] V. Naulin, K. H. Spatschek, S. Musher, and L. I. Piterbarg, Phys. Plasmas **2**, 2640 (1995).

[44] M. Kotschenreuther, G. Rewoldt, and W. Tang, Comp. Phys. Comm. **88**, 128 (1995).

[45] F. Ryter, R. Neu, R. Dux, H.-U. Fahrbach, F. Leuterer, G. Pereverzev, J. Schweinzer, J. Stober, W. Suttrop, ASDEX Upgrade Team, F. De Luca, A. Jacchia, and J. Kinsey, Nuclear Fusion **40**, 1917 (2000).

[46] R. Sánchez and D. E. Newman, Plasma Physics and Controlled Fusion **57**, 123002 (2015).

[47] N. W. Watkins, G. Pruessner, S. C. Chapman, N. B. Crosby, and H. J. Jensen, Space Sci. Rev. **198**, 3 (2016).

[48] P. Bak, C. Tang, and K. Wiesenfeld, Phys. Rev. A **38**, 364 (1988).

[49] P. H. Diamond and T. S. Hahm, Phys. Plasmas **2**, 3640 (1995).

[50] B. A. Carreras, D. Newman, V. E. Lynch, and P. H. Diamond, Phys. Plasmas **3**, 2903 (1996).

[51] D. E. Newman, B. A. Carreras, and P. H. Diamond, Phys. Lett. A **218**, 58 (1996).

[52] R. O. Dendy and P. Helander, Phys. Rev. E **57**, 3641 (1998).

[53] S. C. Chapman, N. W. Watkins, R. O. Dendy, P. Helander, and G. Rowlands, Geophys. Res. Lett. **25**, 2397 (1998).

[54] R. Sánchez, D. Newman, and B. Carreras, Nucl. Fusion **41**, 247 (2001).

[55] C. Hidalgo, B. P. van Milligen, and M. A. Pedrosa, C. R. Physique **7**, 679 (2006).

[56] T. Hwa and M. Kardar, Phys. Rev. A **45**, 7002 (1992).

[57] J. A. Mier, R. Sánchez, L. García, B. A. Carreras, and D. E. Newman, Phys. Rev. Lett. **101**, 165001 (2008).

[58] R. Woodard, D. E. Newman, R. Sánchez, and B. A. Carreras, Physica A: Stat. Mech. App. **373**, 215 (2007).

[59] X. Garbet, P. Mantica, F. Ryter, G. Cordey, F. Imbeaux, C. Sozzi, A. Manini, E. Asp, V. Parail, R. Wolf, and the JET EFDA Contributors, Plasma Phys. Control. Fusion **46**, 1351 (2004).

[60] R. Sánchez, B. P. van Milligen, D. E. Newman, and B. A. Carreras, Phys. Rev. Lett. **90**, 185005 (2003).

[61] A. Fick, Phil. Mag. Series 4 **10**, 30 (1855).

[62] B. A. Carreras, B. P. van Milligen, M. A. Pedrosa, R. Balbín, C. Hidalgo, D. E. Newman, E. Sánchez, M. Frances, I. García-Cortés, J. Bleuel, M. Endler, C. Riccardi, S. Davies, G. F. Matthews, E. Martines, V. Antoni, A. Latten, and T. Klinger, Phys. Plasmas **5**, 3632 (1998).

[63] B. A. Carreras, V. E. Lynch, D. E. Newman, R. Balbín, J. Bleuel, M. A. Pedrosa, M. Endler, B. van Milligen, E. Sánchez, and C. Hidalgo, Phys. Plasmas **7**, 3278 (2000).

[64] H. E. Hurst, Trans. Amer. Soc. Civil Eng. **116**, 770 (1951).

[65] P. A. Politzer, Phys. Rev. Lett. **84**, 1192 (2000).

[66] P. A. Politzer, M. E. Austin, M. Gilmore, G. R. McKee, T. L. Rhodes, C. X. Yu, E. J. Doyle, T. E. Evans, and R. A. Moyere, Phys. Plasmas **9**, 1962 (2002).

[67] M. Nakata and Y. Idomura, Nucl. Fusion **53**, 113039 (2013).

[68] G. Dif-Pradalier, P. H. Diamond, V. Grandgirard, Y. Sarazin, J. Abiteboul, X. Garbet, P. Ghendrih, A. Strugarek, S. Ku, and C. S. Chang, Phys. Rev. E **82**, 025401 (2010).

[69] Y. Sarazin, V. Grandgirard, J. Abiteboul, S. Allfrey, X. Garbet, P. Ghendrih, G. Latu, A. Strugarek, and G. Dif-Pradalier, Nuclear Fusion **50**, 054004 (2010).

[70] G. Zaslavsky, Phys. Rep. **371**, 461 (2002).

[71] A. V. Milovanov and J. J. Rasmussen, Phys. Lett. A **378**, 1492 (2014).

[72] G. Samorodnitsky and M. S. Taqqu, *Stable Non-Gaussian Processes* (Chapman & Hall, New York, NY, 1994).

[73] R. Sánchez, B. A. Carreras, and B. P. van Milligen, Phys. Rev. E **71**, 011111 (2005).

[74] I. Podlubny, *Fractional Differential Equations* (Academic Press, San Diego, CA, 1999).

[75] R. Metzler and J. Klafter, J. Phys. A: Math. Gen. **37**, R161 (2004).

[76] I. Calvo, R. Sánchez, and B. A. Carreras, J. Phys. A: Math. Theor. **42**, 055003 (2009).

[77] G. Falkovich, K. Gawędzki, and M. Vergassola, Rev. Mod. Phys. **73**, 913 (2001).

[78] K. R. Sreenivasan and J. Schumacher, Phil. Trans. R. Soc. A **368**, 1561 (2010).

[79] R. Sánchez, B. A. Carreras, D. E. Newman, V. E. Lynch, and B. P. van Milligen, Phys. Rev. E **74**, 016305 (2006).

[80] A. Celani, M. Cencini, A. Mazzino, and M. Vergassola, New J. Phys. **6**, 72 (2004).

Chapter 2 Investigation of the interaction between competing types of nondiffusive transport in drift wave turbulence[1]

2.1 Abstract

Radial transport in turbulence dominated tokamak plasmas has been observed to deviate from classical diffusion in certain regimes relevant for magnetic confinement fusion. These situations at least include near-marginal turbulence, where radial transport becomes superdiffusive and mediated by elongated radial structures (or avalanches), and transport across radially-sheared poloidal flows, where radial subdiffusion often ensues. In this paper, the interaction between the very different physical ingredients responsible for these two types of nondiffusive dynamics (namely, turbulent profile relaxation close to a local threshold and the interaction with radially-sheared zonal flows) is studied in detail in the context of a simple two-dimensional electrostatic plasma fluid turbulence model based on the dissipative trapped electron mode (DTEM). It is shown that, depending on the relative relevance of each of these ingredients, that can be tuned in various ways, a variety of non-diffusive radial transport behaviors can be found in the system. The results also illustrate the fact that the classical diffusion paradigm is often insufficient to describe turbulent transport in systems with self-generated flows and turbulent profile relaxations.

2.2 Introduction

The sustainable confinement of fusion plasmas in a tokamak concept has been a topic of active research for many years now. Inside the separatrix, radial transport in fusion plasmas typically dictates plasma confinement, stability, and plasma-wall interactions. Radial transport in most fusion plasmas has shown to be dominated by turbulence, resulting in transported quantities that mix faster than molecular diffusion, and a broadband spectrum of fluctuations[1]. Hence, there is a need to understand turbulent transport in tokamak plasmas in order to achieve and maintain fusion plasmas for longer durations in future machines.

In the last few decades, the dynamics of turbulent transport in tokamak plasmas have been shown to be much richer than a mere increase in transport coefficients. In particular, the nature of radial transport itself may often become non-diffusive[2]. Numerical simulations have shown that, in near-marginal regimes in which the separation of timescales between fluctuations and profile modification is importantly reduced, radial transport can be endowed with superdiffusive features in which radial transport takes place via avalanch-

[1]D. Ogata, D. E. Newman, and R. Sánchez. Investigation of the interaction between competing types of nondiffusive transport in drift wave turbulence. Submitted to Physics of Plasmas (POP51153).

ing[3–6]. On the other hand, numerical simulations have also shown that radial transport through regions with strong, radially-sheared zonal flows can become subdiffusive[7]. The physical ingredients that seem to be responsible for these behaviors are quite different. In the superdiffusive cases, a proper profile evolution in the presence of a local instability threshold is essential to get the correct transport dynamics. In the subdiffusive one, the self-consistent generation and evolution of the zonal flows is needed. However, making numerical simulations in which both profile evolution and zonal flow dynamics are done self-consistently and simultaneously is very difficult, because of the huge computational requirements. As a result, most numerical simulations of tokamak turbulence traditionally use fixed background profiles, thus including only zonal flow dynamics. In fact, it was in this type of simulations that the subdiffusive nature of radial transport across zonal flows was identified[7]. Much less frequently, simulations are done that evolve background profiles self-consistently with the turbulence, using what is known as a flux-driven setup. Although flux-driven simulations are becoming more common due to the availability of more powerful supercomputers, even in gyrokinetics[8,9], still just a handful of these runs have focused on studying the non-diffusive nature of radial transport. Regretfully, zonal flow dynamics have often been played down or even removed to simplify the calculations, as was the case of the simulations in which the superdiffusive nature of radial transport was first identified in plasma turbulence[4].

The importance of understanding the complete interaction between profile modification and zonal flow dynamics and assess the resulting transport dynamics depending on their relative strength is however self-evident when considering that the ITER tokamak, due to its larger temperatures, will probably operate frequently in near-marginal conditions, where profiles should be expected to vary in timescales not that separate from those of turbulence. In addition, it is also expected that self-consistent zonal flows will lend a hand in keeping turbulent transport under controlled in ITER. Flux-driven, gyro-kinetic simulations in realistic geometries will be needed to undertake this type of studies. However, past experience has often shown that gyrokinetic simulations are not only very expensive, but also very complicated to interpret due to the large number of elements included, both physical (geometry, physics included, etc.) and numerical (algorithms used, simplifications to speed up calculations, etc.). Thus, there is much to be gained by having a first glimpse, in the context of nondiffusive transport, at how the interaction between profile evolution and self-generated flows may look like in a simplified setup, where the relevant ingredients can be easily isolated from other complications and where the knobs that allow tuning its relative importance could be more easily identified.

This paper intends to do precisely this. It carries out a study of this interaction in a simple slab drift-wave turbulence model, extensively studied in the past in a fixed-gradient setup[10,11], to which simultaneous and self-consistent profile evolution and zonal flow dynamics have been added. As will be shown in what follows, quite meaningful results

are readily available from this model. Simply by modifying the parameters that define it, different transport regimes are accessible in which the mutual interaction between flows and profile relaxation changes, and that have allowed us to understand better what determines the final nature of radial transport and also how to modify it. We expect these results to be extremely helpful to shed light on the underlying physics and facilitate the interpretation of future results from much more complex, flux-driven, fluid and gyrokinetic simulations.

The paper is organized as follows: Sec. 2.3 describes both the DTEM turbulence model that will be used and how profile relaxation and zonal flow dynamics have been added to it; also, the free knobs available to us in order control the interaction between them will be discussed; Sec. 2.4 describes the diagnostics that will be used to characterize the nature of the turbulent transport in each of the different simulations analyzed. In particular, the meaning of the transport exponent H, also known as the Hurst exponent[12], will be explained. The next two sections contain the main results of this study. First, we describe in Sec. 2.5 the main features of the steady-states reached by several simulations for a representative collection of free parameter values; then, in Sec. 2.6, the nature of transport is characterized by determining the transport exponent H of each simulation. A coherent explanation of all these results will be given in Sec. 2.7, with special focus on pointing out the relevant physics in each case. Finally, the paper concludes by speculating on how our results may translate to more realistic tokamak plasmas in Sec. 2.8.

2.3 Numerical model

In this work, a drift-wave model is used for the turbulence due to its ubiquitous nature, sometimes categorized as "universal instabilities", as they occur in most confined plasma configurations. As is known, any non-uniform density plasma maintained by a strong magnetic field is susceptible to drift-wave instabilities[13]. The drift-wave instabilities access the thermal energy as the plasma expands across the magnetic field and many of their characteristics, including its turbulence spectrum and nonlinear cascades[11,14], have been quantified numerically in the past using fixed-background setups. The dissipative electron mode (DTEM) forms the basic structure of our model. It is derived from the two-fluid plasma equations by assuming cold ions, trapped electrons, and quasineutrality[10,15–17]. The geometry used here is that of a doubly-periodic two-dimensional slab, perpendicular to a constant magnetic field, with $x \in [0, 1]$ as the radial direction and $y \in [0, 1]$ as the poloidal direction.

The evolution equations of our model are:

$$\begin{aligned}
\frac{d}{dt}\left[\left(1-\sqrt{\epsilon}-\rho_s^2\nabla_\perp^2\right)\phi\right] &= -\left[1-\sqrt{\epsilon}\,\xi\right]C_s\rho_s R_{nl}\left(n,\phi,P\right)+\nu\sqrt{\epsilon}\left(n-\phi\right)-\mu\rho_s^2\nabla_\perp^4\phi \\
\frac{dn}{dt} &= \xi C_s\rho_s R_{nl}\left(n,\phi,P\right)+\nu_{eff}\left(\phi-n\right) \\
\frac{dP}{dt} &= S+D_P\nabla_\perp^2 P
\end{aligned} \tag{2.1}$$

where ϕ is the fluctuating potential, n is the fluctuating density and P is the background density. The first two equations are very similar to the standard DTEM model[11,14], but include an additional dependence on the background profile P via the nonlinear function $R_{nl}\left(n,\phi,P\right)$, that we discuss later. The third equation represents the profile evolution, and includes a nonuniform (in radius) source term S, also discussed later, in order to implement a flux-driven setup. The coupling with the fluctuations happens through the Lagrangian derivative, $d/dt=\partial_t+\boldsymbol{u}\cdot\boldsymbol{\nabla}_\perp$ where $\boldsymbol{u}=C_s\rho_s\hat{\boldsymbol{z}}\times\boldsymbol{\nabla}_\perp\phi$, the usual turbulent $E\times B$ drift. The meaning of the coefficients in the model is, otherwise, pretty standard. $\rho_s=\left(k_BT_e/eB\right)/C_s$ is the ion gyroradius, $C_s=\sqrt{k_BT_e/m_i}$ is the ion sound speed, ϵ is the inverse machine aspect ratio that defines the trapped electron fraction in velocity space $v_\parallel<\sqrt{\epsilon}v$[17], μ is the viscosity coefficient, ν is the electron collisional relaxation due to trapping and detrapping, and $\nu_{eff}=\nu/\sqrt{\epsilon}$. The term $\xi=(1+\alpha\eta_e)$ contains the instability criterion where $\eta_e[=2]$ is the ratio between the electron temperature gradient and the electron density gradient, and $\alpha=3/2$ for the instability criterion for destabilization of DTEM modes by electron collision[10,13]. Coordinates are normalized such that $t\to t\Omega_i$, $x\to x/10.0\rho_s$, and $y\to y/10.0\rho_s$.Finally, the parameter ν specifies the toroidal force balance that translates as a phase lag between n and ϕ.

We proceed to discuss first the source term in the background profile evolution equation. The periodic (x and y) source S used (see Fig. 2.1) has been chosen to introduce the radial inhomogeneity needed to generate zonal flows, as well as to provide the means to establish a flux-driven, evolving background profile. It is defined as:

$$S(x)=S_0\left[G(x-x_{\text{source}})-G(x-x_{\text{sink}})\right], \tag{2.2}$$

where $G(x)$ is a narrow, normalized Gaussian distribution, and S_0 represents an injection rate. Thus, injection is centered around $x_{\text{source}}[=0.25]$ and extraction at $x_{\text{sink}}[=0.75]$. At steady state, the net amount lost at the sink will balance, on average, what is gained at the source. The background profile will evolve consistently with this balance. Since the source only depends on x, the gradient of the profile is mostly directed along the radial direction, with weaker poloidal dependencies induced by the turbulence. It must also be noted that, since the background profile equation is a convective equation involving energy injection at primarily low-k wavenumbers, a diffusion term proportional to D_P has been added to prevent the formation of extremely steep gradients at high k.

Next, we discuss the two nonlinearities in the DTEM model: the so-called $E \times B$ nonlinearity, that results from the advection of the fluctuating density $\boldsymbol{u} \cdot \boldsymbol{\nabla}_\perp n = C_s \rho_s \hat{\boldsymbol{z}} \times \boldsymbol{\nabla}_\perp \phi \cdot \boldsymbol{\nabla}_\perp n$, and the polarization drift nonlinearity, that arises from the advection on the normalized vorticity $\boldsymbol{u} \cdot \boldsymbol{\nabla}_\perp \left(\nabla_\perp^2 \phi\right) = C_s \rho_s^3 \hat{\boldsymbol{z}} \times \boldsymbol{\nabla}_\perp \phi \cdot \boldsymbol{\nabla}_\perp \left(\nabla_\perp^2 \phi\right)$. The main characteristics of these two nonlinearities have been extensively studied numerically in a fixed-background context[10,14,18]. The $E \times B$ nonlinearity is dominant at small k wave numbers and provides a non-local cascade of energy towards large k. In contrast, the polarization drift nonlinearity is dominant at large k and causes a cascade of energy towards small wave numbers[10]. The nonlinearities do however act to transport momentum in a conservative way, therefore without changing the total momentum.

Lastly, we describe the nonlinear function $R_{nl}\left(n, \phi, P\right)$ that sets up the coupling between the background profile equation and the local turbulence. It is defined as:

$$\begin{aligned} R_{nl}\left(n, \phi, P\right) = f_d \left[g\left(L^{-1}_{\langle P \rangle_y, x} \right) L^{-1}_{\langle P \rangle_y, x} \left(-\frac{\partial \phi}{\partial y} \right) \right] + \\ + \left(1 - f_d\right) \left[g\left(L^{-1}_{P,y} \right) L^{-1}_{P,y} \frac{\partial \phi}{\partial x} - g\left(L^{-1}_{P,x} \right) L^{-1}_{P,x} \frac{\partial \phi}{\partial y} \right] \end{aligned} \tag{2.3}$$

To understand the meaning of this equation, it is better to focus first on just its first line. The main ingredient there is the function $g\left(L^{-1}_{s,z}\right)$, that provides the threshold condition on the background profile in order to locally drive the instability, and that is a key element for the establishment of superdiffusive transport dynamics[3,19]. It is a function of the gradient of some arbitrary quantity, $s = s(z)$, that we express as $L^{-1}_{s,z} = \partial_z s / s_0$ [s_0 is just a normalization constant], and that becomes non-zero (which then makes R_{nl} equal to its fixed-background value for the DTEM model) only above a prescribed threshold value for this gradient. More specifically, g, is constructed as a symmetric combination of hyperbolic tangent functions (see Fig. 2.1, right frame):

$$\begin{aligned} g\left(L^{-1}_{s,z}\right) = \frac{1}{2} \left[2 + \tanh\left(\kappa \left(L^{-1}_{s,z} - L^{-1}_{c,s,z} \right) \right) - \right. \\ \left. - \tanh\left(\kappa \left(L^{-1}_{s,z} + L^{-1}_{c,s,z} \right) \right) \right] \end{aligned} \tag{2.4}$$

where $L^{-1}_{c,s,z}$ is a prescribed critical value for the gradient of field s in the z direction, and κ denotes the steepness of the hyperbolic tangent function [The value of the steepness κ has been fixed at $\kappa = 20$ in order to model a step function more closely.]. The symmetric combination of tangent functions ensures that instability is independent of the sign of the local gradient, only on its magnitude.

Therefore, the threshold function g appearing in the first line of Eq. 2.3 introduces a critical radial gradient in the poloidally-averaged background profile, $\langle P \rangle_y$. On the other hand, the factor that multiplies g, $L^{-1}_{\langle P \rangle_y, x} \partial_y \phi$, represents the coupling between the local turbulence and the background profile. It comes from evaluating the fluctuating turbulent

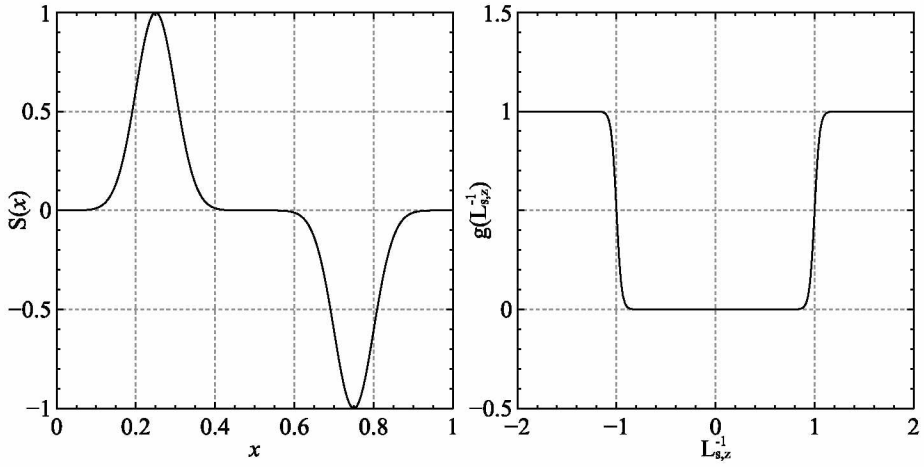

Figure 2.1: The poloidally symmetric source profile $S(x)$ (left) is composed of two normal distributions positioned at different locations with the positive amplitude denoting a source and the negative amplitude is a sink. The switch function $g\left(L_{s,z}^{-1}\right)$ (right) is composed of two hyperbolic tangent functions for symmetry.

advection of the mean profile,

$$\boldsymbol{u}\cdot\boldsymbol{\nabla}P=\left(\frac{\hat{z}\times\boldsymbol{\nabla}\phi}{B}\right)\cdot\boldsymbol{\nabla}P=\frac{1}{B}\left(\frac{\partial^x}{\partial\phi^x}\frac{\partial^y}{\partial P^y}-\frac{\partial^y}{\partial\phi^y}\frac{\partial^x}{\partial P^x}\right), \tag{2.5}$$

that, when assuming a very fast equilibration along the field lines (here, along the y direciton), reduces to:

$$\boldsymbol{u}\cdot\boldsymbol{\nabla}\langle P\rangle_y=-C_s\rho_s\frac{\partial^x}{\partial\langle P\rangle_y^x}\frac{\partial^y}{\partial\phi^y}=-C_s\rho_s L_{\langle P\rangle_y,x}^{-1}\frac{\partial^y}{\partial\phi^y}. \tag{2.6}$$

The second line in Eq. 2.3 has been added to allow us to explore variations of the threshold term just described. In particular, we are interested in reproducing possible tokamak-relevant situations in which the equilibration along the field lines may not be so fast compared with turbulent timescales; in those cases, magnetic surface equilibration (that is, poloidal and toroidal equilibration) of background profiles should not be expected. We must however introduce this possibility in the model in a rather ad-hoc way, since the magnetic field is here perpendicular to the xy plane and there is no parallel transport. For that reason, it is done by considering a linear combination of two threshold conditions whose relative importance is weighted by the factor $f_d\in[0,1]$. The first condition, given by the first line in Eq. 2.3 just described, includes a threshold condition on the radial (i.e., along x) gradient of the poloidally (along y) averaged background profile, $\langle P\rangle_y=\ell_y^{-1}\int_0^1 P(x,y)\,dy$. Thus, it is somewhat analogous to a tokamak situation in which fast parallel transport allows for equilibration of any poloidal inhomogeneities. The second line of Eq. 2.3, introduces the second threshold condition as a function of the local poloidal (in y) and radial (in x) gradients instead. Thus, this term would represent situations in which the lack of sufficiently

fast parallel transport makes relevant the response of local turbulence to local gradients. These local gradients modify the local drift velocities that perform the advection on P, thus resulting in a more inhomogeneous, anisotropic drive for the turbulence leading to larger Reynolds stresses to drive sheared flows. The local threshold condition also adds an additional mechanism to equilibrate gradients via parallel motion, which is absent in the parallel equilibration term proportional to $n - \phi$ in the potential equation.

In summary, the set of equations of the DTEM model described in Eq. 2.1 contains all the elements needed to produce both near-marginal transport (through the profile evolution equation and the threshold condition included in the evolution equations for the fluctuations) and transport across zonal flows (that will be generated via the Reynolds stress represented by the two nonlinearities of the DTEM model) simultaneously and self-consistently. The free parameters of the model are the drive strength, S_0, the parallel equilibration factor f_d and the critical gradient threshold $L_{c,P,x}^{-1}$. By changing their values, one can increase [or decrease] the intensity of the zonal flows as well as the distance of the background profile from marginality. In what follows, we will describe several simulations (see, for example, Fig. 2.2) that explore these parameter variations and investigate the resulting changes in the nature of radial transport. This analysis will allow us to understand better the interplay between self-generated flows and near-marginal turbulent transport.

To conclude this section, we provide some details about the numerical scheme used to solve Eq. 2.1. The spatial domain considered is a doubly-periodic grid of 256×256 nodes in the Fourier space spanned by k_x and k_y. The scheme used is a standard spectral one, properly modified to avoid any aliasing problems, that uses the pseudo-spectral method to deal with nonlinearities. The temporal integration is done implicitly, using a scaled preconditioned Generalized Minimal Residual (GMRES) solver that combines well-established integration schemes[20]. Parallelization is achieved by using MPI and by taking advantage of parallel Fast Fourier Transform (FFT) routines[21] as well as other parallel numerical integration routines. All simulations have been initialized with random phases for all Fourier harmonics, and they have been advanced in time until a suitable quasi-steady state, with approximate balance between drive and losses, is established. As an illustration, some snapshots of the vorticity field obtained at the steady state of representative simulations used in this paper are shown in Fig. 2.2. In the figure, the position in radius of sink and source is shown by means of two vertical, dashed red lines.

2.4 Transport diagnostics

There are many ways to characterize the nature of transport in a system[22,23]. Traditionally, transport of any conserved quantity P is termed diffusive if it can be described by an equation of the type,

$$\frac{\partial P}{\partial t} = \chi \frac{\partial^2 P}{\partial x^2}, \tag{2.7}$$

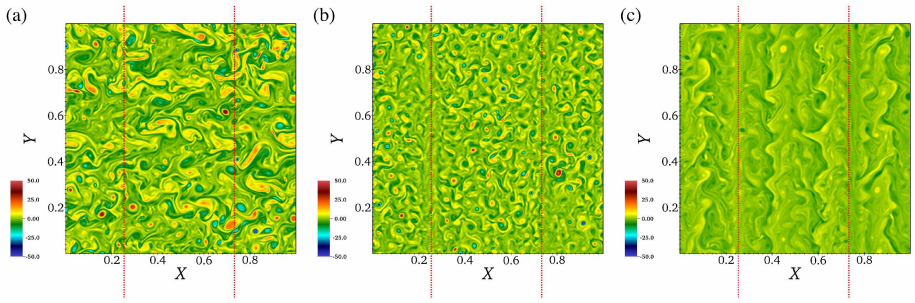

Figure 2.2: Snapshots of the vorticity field (i.e., $\nabla^2\phi$) in XY space at the steady-state for simulations carried out with $S_0 = 5$, $L^{-1}_{c,P,x} = 1, L^{-1}_{c,\langle P\rangle_y,x} = 1$ and $L^{-1}_{c,P,y} = 0$, for various values of f_d: (a) $f_d = 0.0$, (b) $f_d = 0.6$, and (c) $f_d = 1.0$.

where χ is a transport coefficient. This equation implies that the local flux of the transported quantity is $\Gamma_P = -\chi\partial_x P$, thus pointing down the gradient, what is known as Fick's law. By extension, some authors define nondiffusive transport as any situation in which the evolution of P follows instead a transport equation of the form:

$$\frac{\partial^\beta P}{\partial t^\beta} = \chi_{\alpha,\beta}\frac{\partial^\alpha P}{\partial|x|^\alpha}. \tag{2.8}$$

where $\beta \in (0, 1]$ and $\alpha \in (0, 2]$ are known as fractional transport exponents, and $\chi_{\alpha,\beta}$ is the fractional transport coefficient. The operators that appear in this equation are fractional derivatives, and they provide smooth interpolants in between integer derivatives[24]. In contrast to the integer derivatives, that are local operators, fractional derivatives are integro-differential operators that are non-local in their variable of definition (either space or time). Thus, the type of transport that can be captured by Eq. 2.8 may be intrinsically non-local (if $0 < \alpha < 2$ and non-Markovian if $0 < \beta < 1$). However, the exponent of most interest to us is the exponent $H = \beta/\alpha$. Transport is termed superdiffusive when $H > 1/2$, diffusive if $H = 1/2$ (even if $\beta \neq 1$ and $\alpha \neq 2$, as in the usual diffusive equation), and subdiffusive when $H < 1/2$. The reason for these names is that any population of particles, whose transport is governed by Eq. 2.8 and that are initially localized in x, will spread faster (if $H > 1/2$) or slower (if $H < 1/2$) than its diffusive counterpart.

As with the classical diffusion equation (Eq. 2.7), that can be derived from "microscopic considerations" that assume Gaussian fluctuations and lack of memory, the fractional transport equation (Eq. 2.8) can be obtained by assuming "microscopic" Lévy distributed fluctuations and self-similar memory. It is well known that the classical diffusion equation can be obtained as the long-term, long-distance limit of either a continuous time random walk (CTRW) in which particles are advanced with Gaussian-distributed step-sizes, separated by exponentially-distributed waiting times. Also, the diffusion equation can be obtained from the "microscopic" Langevin equation, that expresses the position of each

particle being transported as:

$$x(t) = x_0 + \int_0^t \xi(t')dt'. \tag{2.9}$$

In the same long-term, long-distance limit, by assuming a random forcing ξ with Gaussian statistics and zero time correlation except at zero lag, the classical diffusion equation is recovered.

Similarly, the fractional transport equation can be derived from a [still badly called random] CTRW[25] in which steps are distributed according to a symmetric α-Lévy distribution with tail index $\alpha \in (0, 2)$ and waiting-times distributed according to an extremal β-Lévy distribution with tail index $\beta \in (0, 1)$[22,23,26]. It can also be derived as the long-term, long-distance limit of the generalized Langevin equation[27,28]

$$x(t) = x_0 + \frac{1}{\Gamma(H - 1/\alpha + 1)} \int_0^t (t - t')^{H-1/\alpha} \xi_\alpha(t')dt', \tag{2.10}$$

that assumes a non-random forcing with symmetric α-Lévy statistics and a correlation in time characterized with a Hurst exponent $H \in (0, 1)$[12]. In that case, $\beta = \alpha H$ in the transport equation.

The connections of Eq. 2.8 with "microscopic formulations" can be exploited to come up with methods to determine the fractional exponents α, β and H in practical situations, and thus to provide ways to characterize the nature of transport. Among the different methods available, in this paper we will focus on one that exploits the connection with Eq. 2.10, permitting us to easily determine the exponent we are interested in, H, by following the trajectories of massless tracer particles as they are advected by the turbulence. That is, by integrating in time their velocity, that is given by,

$$\dot{\boldsymbol{R}}(t) = \boldsymbol{E} \times \boldsymbol{B}/B^2 = C_s \rho_s \hat{\boldsymbol{z}} \times \boldsymbol{\nabla}_\perp \phi, \quad \boldsymbol{R}(t_0) = \boldsymbol{r_0}, \tag{2.11}$$

since the advection in our model is done by the turbulent fluctuating $E \times B$ velocity.

In order to estimate the H exponent, we benefit from the fact that it represents the self-similarity exponent of the process described by Eq. 2.10. Therefore, it can also be obtained also as the correlation (or Hurst) exponent of its derivative, or time series of the increments of the process. Or, in discrete form, of its velocity series along the Lagrangian trajectory. The method we have chosen to determine this correlation exponent is the well-known R/S technique, that has been reliably used for more than sixty years[12]. Given a velocity series of length N represented as $\{V_k : 1 \leq k \leq N\}$, one just needs to construct the so-called rescaled range:

$$(R/S)_n = \frac{\max(0, X_1, \ldots, X_n) - \min(0, X_1, \ldots, X_n)}{\sigma_n^{1/s}} \tag{2.12}$$

where $X_k = V_1 + \cdots + V_k - k\bar{V}_n$ for $k \leq n$. The mean is defined as $\bar{V}_n = \sum_{i=1}^{n} V_i/n$. The s-variance is defined as $\sigma_n = \sum_{i=1}^{n} \left(V_i - \bar{V}_n\right)^s / (n-1)$, with $s < \alpha$, being $\alpha < 2$ the tail-exponent characterizing the velocity statistics (or, if Gaussian-distributed, $\alpha = 2$). It then happens that, if the signal is correlated with Hurst exponent H (and therefore, its integrated path is self-similar with the same exponent), one finds that,

$$(R/S)_n \propto n^H, \tag{2.13}$$

from which the exponent is readily obtained. It is fair to say that the R/S method has been criticized in the literature because it tends to somewhat overestimate exponents (for instance, R/S tends to yield $H \sim 0.55$ for random signals instead of 0.5), but it is extremely resilient to both noise and periodic perturbations[29], which is why it is our method of choice. It is also worth to note that the statistics of the determination of H are greatly improved by averaging the rescaled range for time n over all non-overlapping segments of size n in which the full time series can be broken, procedure that we have extensively used in this work.

2.5 Main features of the steady-state background profiles

In this section we will describe the main features of the steady-state background profiles obtained for the different sets of simulations examined. Each simulation, once suitable values for the local critical gradient $L_{c,P,x}^{-1}$ ($L_{c,P,y}^{-1} = 0$ is always used, so a poloidal drive for turbulent transport always exist), the source injection rate, S_0, and the parallel equilibration fraction, f_d, have been prescribed, was advanced in time until an steady-state was reached in which sources and sinks balanced and the background profile P fluctuated around a well defined average shape. As diagnostics, several (spatially integrated) quantities of interest were monitored, including $W_P \propto \int_0^1 \int_0^1 |P|^2 \, dxdy$ and $W_{\text{turb}} \propto \int_0^1 \int_0^1 \left(|n|^2 + |\phi|^2\right) dxdy$, which respectively provide proxies for the total background and fluctuating energies. The arrival to the steady-state was revealed by having $\langle W_P \rangle_t \sim$ constant and $\langle W_{\text{turb}} \rangle_t \sim$ constant, as well as $\langle \partial_x P \rangle_{y,t} \sim$ constant (i.e., a well-defined mean background profile), over many eddy turnover times. The level of turbulent activity was monitored using the quantities $\delta W_{\text{turb}} / \langle W_{\text{turb}} \rangle_t$ and $\delta W_P / \langle W_P \rangle_t$ where $(\delta W_{\text{turb}})^2 = \left\langle (W_{\text{turb}} - \langle W_{\text{turb}} \rangle_t)^2 \right\rangle_t$ and $(\delta W_P)^2 = \left\langle (W_P - \langle W_P \rangle_t)^2 \right\rangle_t$, and with $\langle \cdot \rangle_t$ standing for time averaging. These quantities are related, respectively, to the overall amplitude of the turbulence and its effect on distributing the free energy stored in the background profile. It must be kept in mind that, in systems with both linear and nonlinear terms, relative large values of $\delta W_{\text{turb}} / \langle W_{\text{turb}} \rangle_t$ reveal bursty turbulent activity, while large $\delta W_P / \langle W_P \rangle_t$ values are associated to very active background profile modifications, both effects being associated to the action of nonlinear terms. The time-average shape of the gradient of the (poloidally-averaged) background profile, $\langle \partial_x P \rangle_{y,t}$, is coupled to the values of these quantities as well. Thus, in cases in which $\delta W_{\text{turb}} / \langle W_{\text{turb}} \rangle_t$

Table 2.1: Values used for the three free parameters in the simulations discussed in text.

	$L_{c,P,x}^{-1}$	S_0	f_d
Critical-gradient threshold runs	$0-1.6$	5	0
Fueling rate runs	1	$4-20$	0
Parallel equilibration runs	1	5	$0-1$

is large, which implies large levels of turbulence-induced transport, smaller $\langle \partial_x P \rangle_{y,t}$ values are obtained for the same source. On the other hand, large $\delta W_P / \langle W_P \rangle_t$ values are often indicative of near-marginality. That is, of profiles locally wandering around the local instability threshold values. Finally, small values of both $\delta W_{\text{turb}} / \langle W_{\text{turb}} \rangle_t$ and $\delta W_P / \langle W_P \rangle_t$ are usually a reflection of a dominant contribution from the linear terms, and larger values of the gradient of the background profile are then expected.

In order to examine the change in transport dynamics in a context of competing zonal flow development and turbulent profile modifications, we have run three different sets of simulations, in which just one of the three available free parameters is varied while keeping the other two fixed. The explored range of parameters is shown in Table 2.1. To guide the reader about what we are looking at in each set it suffices to say that, by increasing from zero the critical gradient threshold, $L_{c,P,x}^{-1}$, we were able to explore states in which the dominance of self-generated flows is gradually replaced by more prominent radial turbulent relaxations (or avalanches). In addition, scenarios in which the source injection rate S_0 was varied test the resiliency of the avalanche relaxation dynamics. Finally, the cases in which the parallel equilibration f_D was increased from zero assess the importance of the parallel equilibration dynamics on the transport relaxation process.

2.5.1 Effect of varying the critical gradient threshold $L_{c,P,x}^{-1}$.

The effect on the steady-state radial gradient of the background profile, $\langle \partial_x P \rangle_{y,t}$, of using different values of $L_{c,P,x}^{-1}$ for a fixed source $S_0 = 5$ is shown in Fig. 2.3. In all cases, $f_d = 0$, which means that parallel equilibration is not being considered. In yellow, the steady-state profile in the (almost) absence of turbulence is shown, as obtained by considering the regime where the turbulent advection is small compared to the diffusion term $D_P \gg u\rho_s$. Since the diffusive flux is proportional to the local gradient, and the whole source at $x_{\text{source}} = 0.25$ had to be transported diffusively to the sink location at $x_{\text{sink}} = 0.75$, this case exhibits the largest gradients of all in the central region.

The case run with $L_{c,P,x}^{-1} = 0$ (no critical gradient, shown in magenta circles) corresponds to the case in which the profile is always unstable and turbulence is always active. This regime is known as one of supermarginal turbulence. On average, $\langle \partial_x P \rangle_{y,t}$ sits at a much lower value than the diffusion dominated profile in between the sink and the source. This situation corresponds, as we mentioned earlier, to significant values for $\delta W_{\text{turb}} / \langle W_{\text{turb}} \rangle_t$ in the central region (or the order of $\sim 5\%$), a signal for significant levels of turbulent trans-

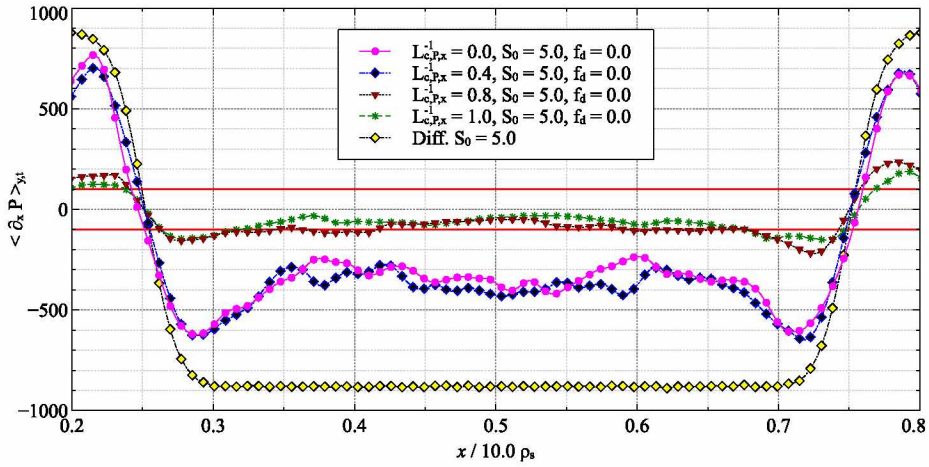

Figure 2.3: The time and poloidal averaged background gradient profiles at steady state, $\langle \partial_x P \rangle_{y,t}$, show that the profiles approach near-marginality as $L^{-1}_{c,P,x}$ is increased (see explanation in text). The red lines corresponding to the (properly normalized) critical gradient parameter $L^{-1}_{c,P,x} = 1$ have been included for reference. The source is located at $x_{\text{source}} = 0.25$, and the sink is at $x_{\text{sink}} = 0.75$.

port. On the other hand, $\delta W_P / \langle W_P \rangle_t$ is much smaller which, as we will see soon, implies a modest level of profile modification ($\delta W_P / \langle W_P \rangle_t \simeq 0.9\%$). This level of fluctuations is sufficient to establish significant radial turbulent fluxes that can transport P from the source to the sink while maintaining smaller gradient values than in the diffusive case, as clearly seen in Fig. 2.3. The situation is quite different, however, near the source and sink locations. The local inhomogeneity and anisotropy induced by the shape of Eq. 2.2 at those regions drives strong radially-sheared, poloidal flows (see Fig. 2.4) that reduce turbulent fluctuations in those regions to a minimum. Therefore, the radial turbulent transport in these regions is very small, which causes the gradients to increase to diffusive levels in order to maintain the flux of excess free energy through the diffusive channel.

We discuss next the cases with a finite critical gradient threshold for the same source S_0. Three different values have been studied, respectively shown in Fig. 2.3 using black crosses ($L^{-1}_{c,P,x} = 0.4$), black stars ($L^{-1}_{c,P,x} = 0.8$) and red squares ($L^{-1}_{c,P,x} = 1$). Focusing first on the central region between source and sink, it seems clear that increasing the value of the threshold initially leaves the average background gradient $\langle \partial_x P \rangle_{y,t}$ quite unchanged ($\delta W_{\text{turb}} / \langle W_{\text{turb}} \rangle_t \simeq 7\%$ and $\delta W_P / \langle W_P \rangle_t \simeq 0.9\%$ for $L^{-1}_{c,P,x} = 0.4$). However, for the largest two threshold values, the background gradient has decreased quite a bit from the $L^{-1}_{c,P,x} = 0$ case (indeed, $\left\langle W_P(L^{-1}_{c,P,x} = 0) \right\rangle_t / \left\langle W_P(L^{-1}_{c,P,x} = 1) \right\rangle_t \sim 25$ and $\delta W_P / \langle W_P \rangle_t \simeq 20\%$). This reduction in the total free gradient energy is due to more vigorous turbulent relaxations (indeed, $\delta W_{\text{turb}} / \langle W_{\text{turb}} \rangle_t \simeq 10\%$ for $L^{-1}_{c,P,x} = 1.$) associated to significant turbulent profile modification, which is the first telltale evidence of transport having reached near-marginality. This is also apparent from Fig. 2.3, where the (properly normalized) critical threshold value or $L^{-1}_{c,P,x} = 1$ has been included in red. Clearly, the

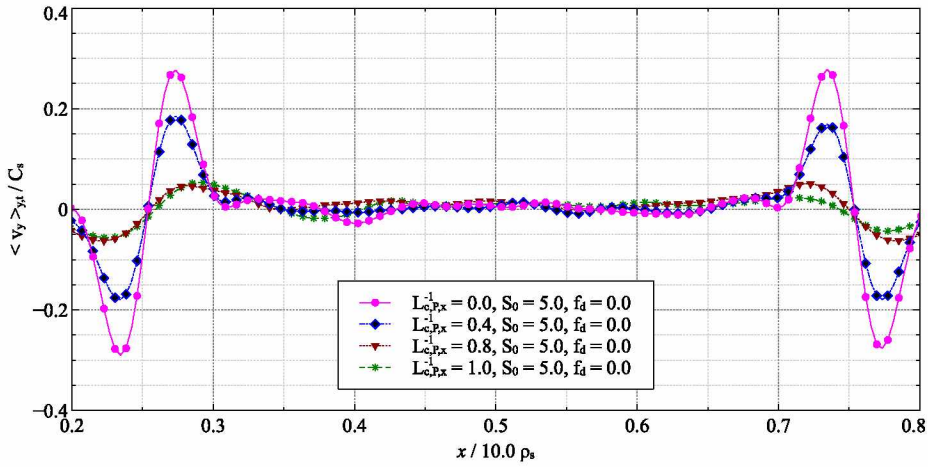

Figure 2.4: Time and poloidal averaged poloidal velocity $\langle v_y \rangle_{y,t}$ at steady state shows a trend that self-generated flows near the sources become less prominent with increasing values of $L^{-1}_{c,P,x}$. The source is located at $x_{\text{source}} = 0.25$, and the sink is at $x_{\text{sink}} = 0.75$.

average gradient shows regions above and below that threshold line, as expected in near-marginal conditions. In contrast, for the smallest thresholds, profiles are above marginal. Therefore, its gradient is set by the source and the level of fluctuations achieved, instead of by the local gradient threshold.

2.5.2 Effect of varying the fueling rate S_0

A characteristic property of near-marginal turbulent steady-states is profile resilience. Or, in other words, the lack of sensitivity of the profile share to the strength of the drive, being instead determined mostly by the local threshold value. To investigate whether our model also exhibits this property, we have run several simulations with the critical threshold parameter fixed to $L^{-1}_{c,P,x} = 1$ which, as discussed in the previous subsection, corresponds to a near-marginal state for $S_0 = 5$ [and $f_d = 0$]. In each run the fueling rate has been set to a value in between 5 and 20. The resulting steady-state gradient profiles are shown in Fig. 2.5, where they can be seen to remain stiff over the central region between sink and source, as expected, for $5 < S_0 < 10$. At sufficiently larger fuelling rates, though, the situation changes dramatically. For $S_0 = 20$, the system is capable of driving a noticeable self-generated sheared poloidal flow (see Fig. 2.6) that inhibits turbulent transport near the source and sink, leading to a steepening of the averaged profile to compensate for the reduction of turbulence transport as clearly shown in Fig. 2.5. The average gradient actually steepens until it reaches values similar to those obtained in the absence of a critical gradient (i.e., for $L^{-1}_{c,P,x} = 0$), as shown in Fig. 2.5, which implies that a sufficiently strong drive can develop self-generated flows capable of bringing the average profile back to a supermarginal state, where the gradient profile will be set by the source and the fluctuation levels, not the local threshold ($\delta W_P / \langle W_P \rangle_t \simeq 20\%$ for $S_0 = 5.0$ and $\delta W_P / \langle W_P \rangle_t \simeq 2.6\%$ for $S_0 = 20$).

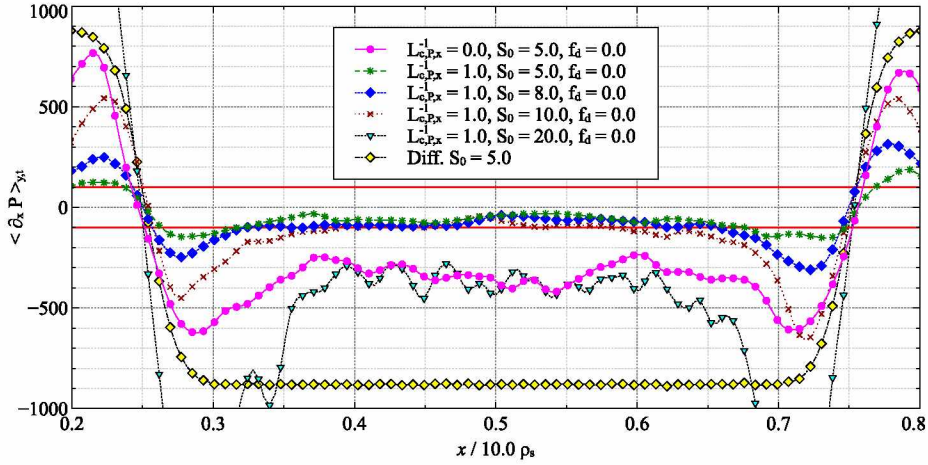

Figure 2.5: Time and poloidal averaged background gradient profiles $\langle \partial_x P \rangle_{y,t}$ at the quasi-steady state show that turbulent transport, although initially dominant and near-marginal, is reduced by the strong sheared poloidal flow driven at sufficiently large fueling rate, which brings profile back above marginality. The red lines correspond to the critical gradient parameter $L^{-1}_{c,P,x} = 1.0$. The source is located at $x_{\rm source} = 0.25$, and the sink is at $x_{\rm sink} = 0.75$

2.5.3 Effect of the parallel equilibration factor, f_d.

The last effect we have studied is whether the assumption (or not) of fast parallel equilibration changes the overall near-marginal transport dynamics of the model. We have carried out several simulations using $L^{-1}_{c,P,x} = 1$, $L^{-1}_{c,<P>_y,x} = 0$, $L^{-1}_{c,P,y} = 0$ and $S_0 = 5$. These values correspond to a near-marginal steady-state for $f_d = 0$, as we showed in the previous sections. The fact that $L^{-1}_{c,P,y} = 0$ means that there is always free energy available to excite turbulence in the poloidal direction. The factor f_d has been varied between 0 and 1. The resulting steady-state gradient profiles are shown in Fig. 2.7. Curiously, the average gradients seem pretty similar at the two limiting values, $f_d = 0$ and $f_d = 1$, while the profile becomes closer to the supermarginal state (i.e., $L^{-1}_{c,P,x} = 0$) when local and poloidally-averaged threshold conditions have a similar importance ($f_d = 0.4$). The dynamics are however very different, as seen clearly when looking at the time (and poloidally) averaged poloidal flow (i.e., $\langle v_y \rangle_{y,t}$), as shown in Fig. 2.8. Strong zonal flows play an important role in this change, since they exist only at the sink and source regions for $f_d \ll 1$, while the dominant threshold condition is the local one, but are seen to extend more and more until they cover the whole domain for $f_d \sim 1$, after the poloidally-averaged threshold condition begins to dominate.

2.6 Determination of fractional transport exponents

In this section we will determine the fractional transport exponents that better captures the transport dynamics of each of the simulations discussed in Sec. 2.5.1. In this

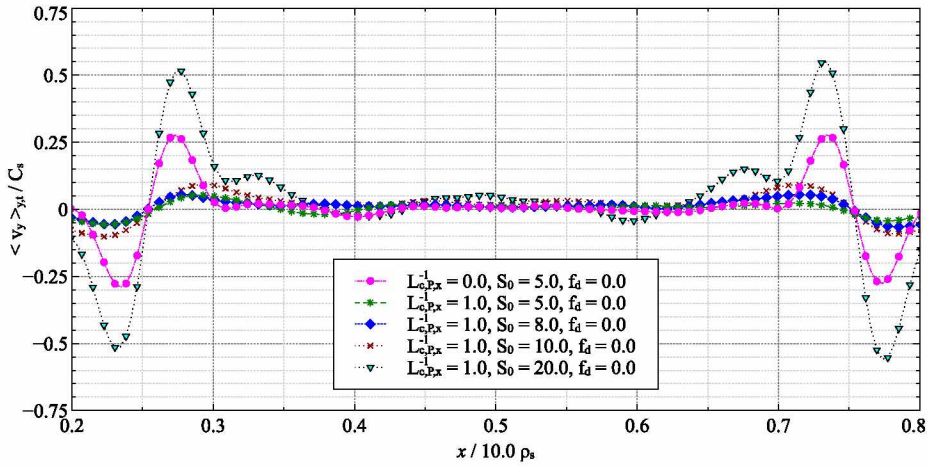

Figure 2.6: Time and poloidal averaged poloidal velocities $\langle v_y \rangle_{y,t}$ over the steady state show that, when the fueling rate becomes sufficiently large (here, $S_0 = 20.0$), the self-generated flows can effectively switch off turbulent transport and lead the profile out of near-marginality. The source is located at $x_{\rm source} = 0.25$, and the sink is at $x_{\rm sink} = 0.75$.

way, we will be able to characterize quantitatively the nondiffusive nature of turbulent transport in the DTEM model as the dominance on transport dynamics is displaced from turbulent profile relaxation processes to zonal flows or viceversa. The methods described in Sec. 2.4 have been used for this task. Thus, the exponent H has been determined using the R/S analysis on the (x or y component of the) Lagrangian velocity time series of tracers advected by the turbulence.

2.6.1 Variation of the critical gradient threshold $L^{-1}_{c,P,x}$.

The rescaled ranges (i.e., R/S) obtained for the tracer Lagrangian velocities some simulations from the set in which the critical gradient threshold, $L^{-1}_{c,P,x}$, is varied are shown in Fig. 2.9 as a function of time lag [As we mentioned earlier, for these simulations $S_0 = 5$ and $f_D = 0$] . Two different scaling regions are apparent, separated at lag $\tau\Omega_i \sim 1$. The region for $\tau\Omega_i < 1$ exhibits a Hurst exponent close to 1, both for the x and y velocity components. This region is related to the autocorrelation of the time series with itself and tells us that single-eddy dynamics extend all the way up to timescales of the order of $\tau\Omega_i \sim 1$. It is however irrelevant to determine the nature of long-term, long-distance transport dynamics. The second region, for $\tau\Omega_i < 1$ is the interesting one since, in a diffusive system, one should find $H \sim 0.5$ [or, since we are using R/S, $H \sim 0.55$] for timescales larger than single-eddy timescales. Instead, here we find that $H \sim 0.8$ along the x direction for $L^{-1}_{c,P,x} = 0.8$ and $L^{-1}_{c,P,x} = 1$, the cases with near-marginal gradient profiles, as we discussed in the previous section. This means that the nature of radial transport is superdiffusive, as one would expect from a near-marginal turbulent system in which transport is dominated by radial avalanches. On the other hand, transport is diffusive, or mildly subdiffusive, for $L^{-1}_{c,P,x} = 0$

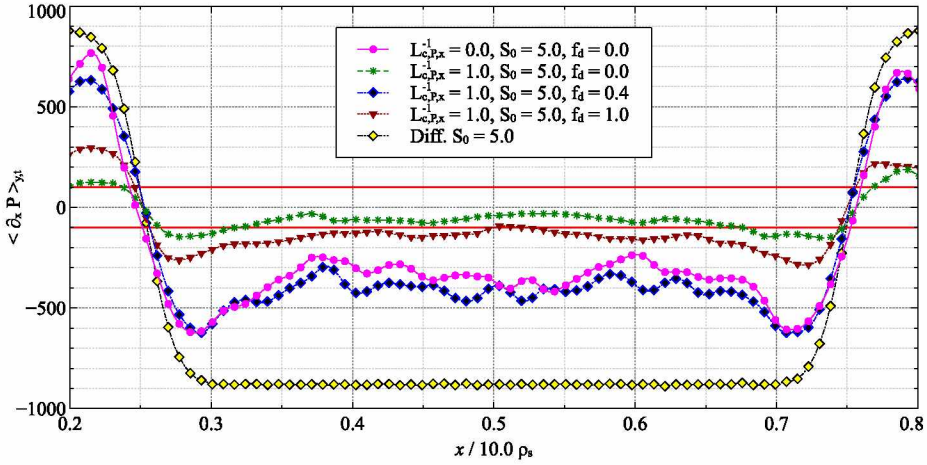

Figure 2.7: Time and poloidal averaged background gradient profiles $\langle \partial_x P \rangle_{y,t}$ over a period of quasi-steady state show that turbulence transport is reduced in the presence of sheared poloidal flow near sources with larger parallel equilibration, which causes the profiles to steepen in order to increase diffusive transport. The red lines correspond to the critical gradient parameter $L^{-1}_{c,P,x} = 1$. The source is located at $x_{\rm source} = 0.25$, and the sink is at $x_{\rm sink} = 0.75$

and $L^{-1}_{c,P,x} = 0.4$, since $H \sim 0.49$. This behavior is also consistent with the presence of supermarginal turbulence and the weakly radially-sheared poloidal flows that we discussed in the previous section. Regarding the nature of poloidal transport for timescales $\tau\Omega_i > 1$, it is interesting to note that the Hurst exponent values are now reversed. $H \sim 0.6$ (weakly superdiffusive) is obtained for $L^{-1}_{c,P,x} = 0$ and $L^{-1}_{c,P,x} = 0.4$, whilst $H \sim 0.5$ (diffusive, or weakly subdiffusive) for $L^{-1}_{c,P,x} = 0.8$ and $L^{-1}_{c,P,x} = 1$.

We have collected the Hurst exponents along x and y obtained for all the simulations examined that varied $L^{-1}_{c,P,x}$ in Fig. 2.10. The trends suggested by Fig. 2.9 become now much more apparent. Superdiffusive behavior along one direction is clearly correlated with subdiffusive behavior along the other. In addition, it is clear that there is a minimum value of the critical threshold $L^{-1}_{c,P,x}$ (close to 0.75) for near-marginal conditions to be established, in which avalanches dominate radial transport. Below this threshold value, zonal flow dynamics become dominant and reshape the nature of transport towards the type of subdiffusion characteristic of transport across zonal flows. The more subdiffusive, the stronger the radial shear of the poloidal flows is.

2.6.2 Variation of the fuelling rate S_0

We proceed next to determine the fractional exponent H for the set of simulations in which the source S_0 is varied [As we mentioned earlier, for these simulations $L^{-1}_{c,P,x} = 1$ and $f_D = 0$]. The rescaled ranges obtained for the tracer velocities of some selected simulations are shown in Fig. 2.11. Focusing again on the timescales of interest for transport (i.e.,

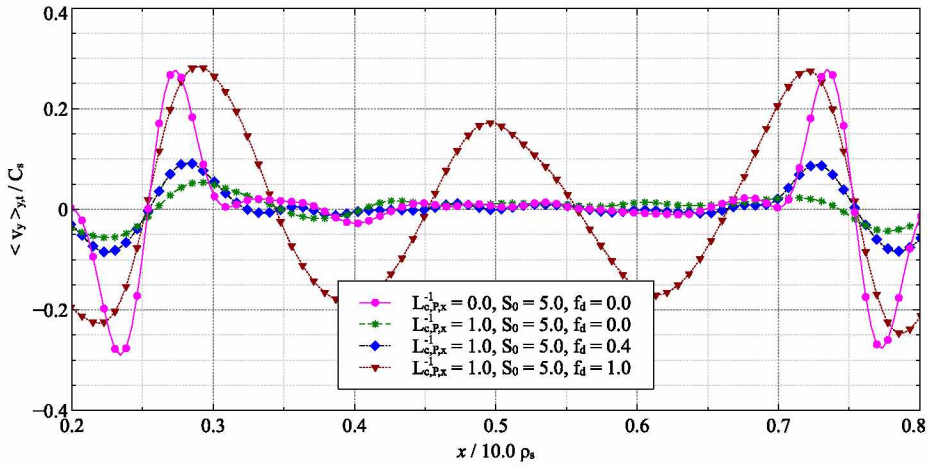

Figure 2.8: Time and poloidal averaged poloidal velocities $\langle v_y \rangle_{y,t}$ over a period of quasi-steady state show the self-generated poloidal flows increase with larger contribution from the poloidally averaged gradient term. When $f_d = 1.0$, the large eddies are capable of provide adequate down-gradient transport in the presence of noticeable sheared poloidal flows. The source is located at $x_{\text{source}} = 0.25$, and the sink is at $x_{\text{sink}} = 0.75$

$\tau\Omega_i > 1$), we find that $H \sim 0.8$ in the radial direction for $S_0 = 5 - 10$, clear superdiffusive behavior. For $S_0 = 20$, the radial Hurst exponent drops to $H \sim 0.53$, transport thus becoming diffusive, or mildly subdiffusive. This abrupt change is consistent with what was described in the previous section for the background gradient, that moved from submarginal to supermarginal conditions at $S_0 = 20$, due to the increasing excitation of larger zonal flows that could extend over the whole domain, away from source and sinks. The behavior along the poloidal (i.e., y) direction also follows the trend previously described, with $H \sim 0.51$ (diffusive, or mildly subdiffusive) for $S_0 = 5 - 10$, and $H \sim 0.58$ (mildly superdiffusive) for $S_0 = 20$.

A more complete picture of these trends is shown in Fig. 2.12, where the values of H obtained for all simulations in this set are shown. Clearly, radial transport remains superdiffusive for $S_0 < 10 - 12$. The fact that H varies very little in this range is a consequence (or a symptom) of the type of profile resiliency that is characteristic of near-marginal turbulent transport. As expected, transport in the perpendicular direction (y) is then diffusive or mildly subdiffusive. For $S_0 > 12$, however, the situation begins to change and, for $S_0 > 15$, it is completely reversed. Strong poloidal flows have become dominant, turbulence has become supermarginal and radial transport becomes diffusive or mildly subdiffusive.

2.6.3 Local vs. averaged gradient drives

We describe next the values for the fractional exponent H obtained for the set of simulations in which f_D is varied from 0 to 1 [In them, $L^{-1}_{c,\langle P\rangle_y,x} = 0, L^{-1}_{c,P,x} = 1$; $L^{-1}_{c,P,y} = 0$

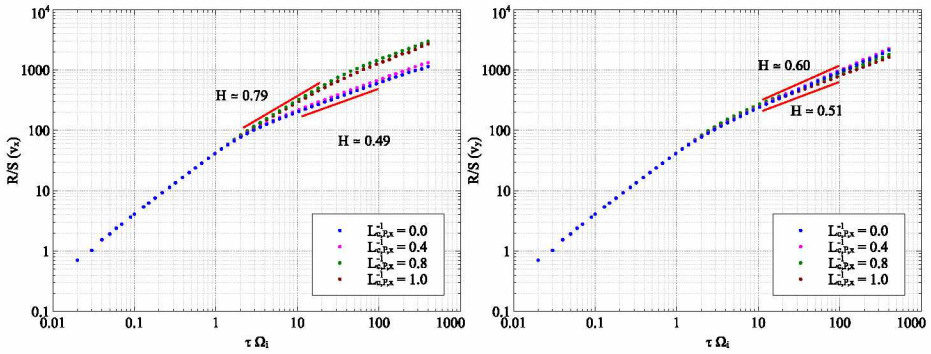

Figure 2.9: R/S for tracer velocity v_x (left) shows a distinct mesorange region when $L^{-1}_{c,P,x} > 0.8$ coinciding to prominent radial relaxation events while R/S for v_y (right) changes only slightly.

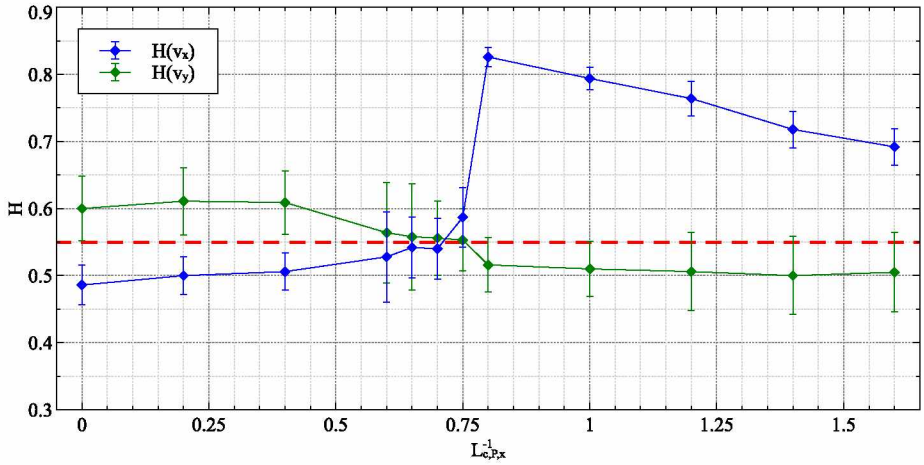

Figure 2.10: Transport exponent H shows a trend towards slightly radial subdiffusion for $L^{-1}_{c,P,x} < 0.75$ and radial superdiffusion for $L^{-1}_{c,P,x} > 0.75$. The classical diffusion signature limit is at $H_{R/S} \sim 0.55$. The source constant is $S_0 = 5.0$, and the parallel equilibration fraction is $f_d = 0.0$.

and $S_0 = 5$] in order to explore the importance of parallel equilibration in the dynamics. Fig. 2.13 shows the rescaled ranges obtained for the tracer Lagrangian velocities in a few selected simulations. Regarding radial motion (i.e., along x), it is interesting to note that superdiffusive behavior is only found for $f_d = 0$ ($H \sim 0.8$), whilst strong subdiffusive behavior ($H < 0.4$) is found in all other cases shown. Consistently with our previous findings, transport in the poloidal direction shows the opposite trend, with diffusive or mild subdiffusion for the case with $f_d = 0$, and superdiffusive motion for all others.

A more precise analysis can be done using Fig. 2.14, that collects the H values obtained for all runs made with varying f_D. The figure clearly shows that, as poloidal equilibration becomes sufficiently strong (i.e., for $f_D > 0.2$ in this particular set), superdiffusive radial [poloidal] transport is abruptly replaced by subdiffusive [superdiffusive] transport. The more subdiffusive, the more dominant poloidal equilibration becomes, and the stronger

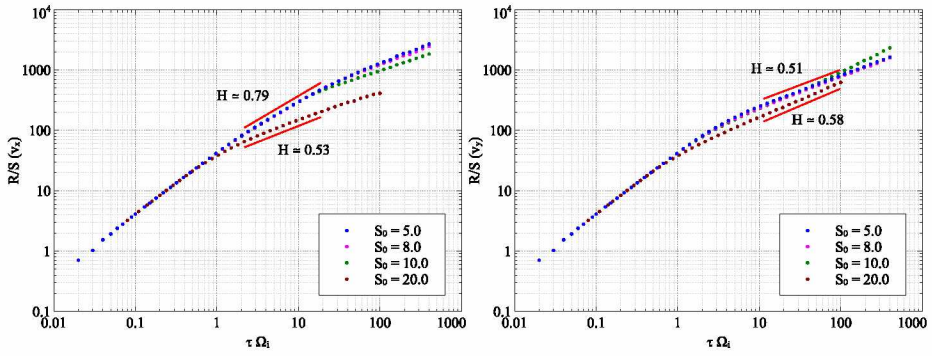

Figure 2.11: R/S for tracer velocity v_x (left) shows a distinct meso-scale region for values of S_0 exhibiting dominating radial relaxation events while R/S for v_y (right) remain close to $H(v_y) \sim 0.5$ even with the increase in the self-generated poloidal flow.

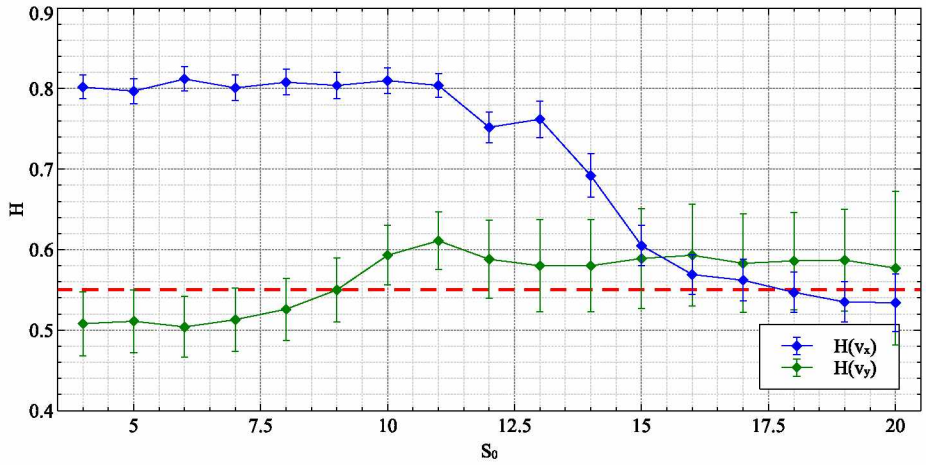

Figure 2.12: Transport exponent H for varying source constant S_0 $[L_{c,P,x}^{-1} = 1.0,\ f_D = 0]$ shows a gradual transition in radial transport from superdiffusive to diffusive.

and more radially-extended the poloidal flows become, as we saw in the previous subsection.

2.7 Discussion

It seems clear, from the results just described, that the interaction between self-consistently evolved background profiles and turbulence can yield a large variety of (radial) turbulent transport dynamics. On the one hand, in cases in which the background profiles manage to stay close to near-marginality at steady-state and when flows remain small, transport behaves superdiffusively, as expected from the typical coherent, down- or up-the-gradient profile relaxation that is usually called "avalanche". On the other hand, when the radial shear of the turbulence-driven poloidal flows manages to become large, they can not only decorrelate the coherent avalanches and turn the nature of radial transport more diffusive, but even make it behave subdiffusively. The physical mechanisms responsible for subdiffusion in this case have already been described somewhere, and were due to the en-

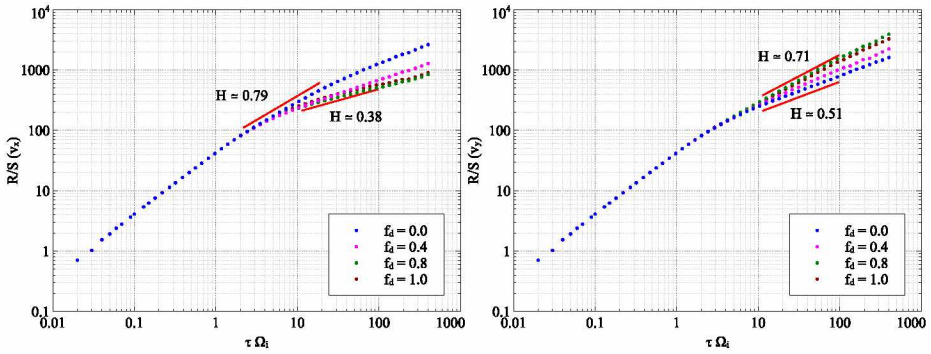

Figure 2.13: Rescaled ranges (R/S) for tracer velocities v_x (left) and v_y (right) for various f_D values.

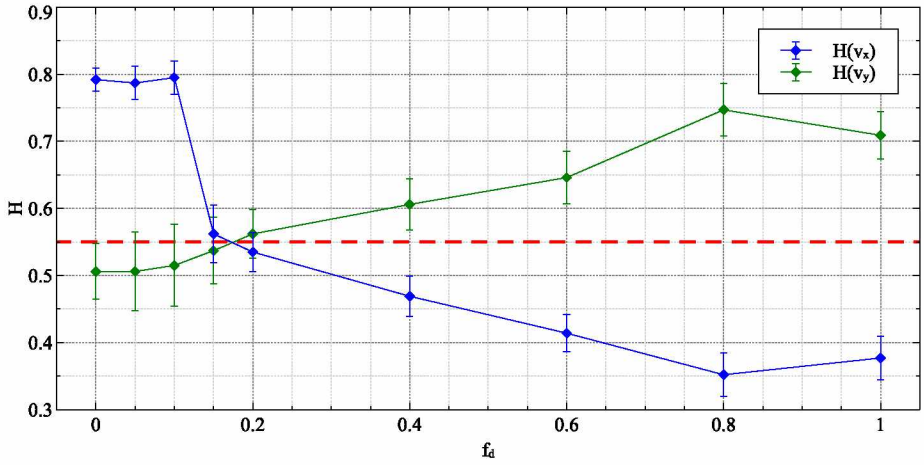

Figure 2.14: The Hurst parameter shows radial superdiffusion at the largest local gradient contributions ($f_d \to 0$) and subdiffusion at the largest poloidal averaged contribution ($f_d \to 1$) [$S_0 = 5.0$, $L^{-1}_{x,n,c} = 1.0$ are used]. Poloidal transport shows the reverse trend as expected.

hancement (or repression) of a certain sign of the parallel (to the magnetic field) fluctuating vorticity.

In the simulations presented in this paper, we have shown that these turbulent poloidal flows, being driven by the Reynolds stresses if sufficiently non-homogeneity and anisotropy exists in the turbulence[30], always appear first close to the source and sink region where gradients are large, particularly in the radial direction. In the presence of a constant source, however, these flows can be suppressed by increasing the critical threshold, $L^{-1}_{c,P,x}$, that reduces the level of fluctuations needed to balance the source, in spite of the larger inhomogeneity. This reduces the Reynolds stresses, and the subsequent flows. At the same time, larger radial structures may develop (see Fig. 2.15), due to the shift to a larger growth rate. In this situation, it becomes easier that the steady-state of the system remains close to near-marginality, as we showed in Sec. 2.5.1, that makes coherent relaxations down-gradient (i.e., avalanches) more frequent. As a result, radial transport becomes superdiffusive, as

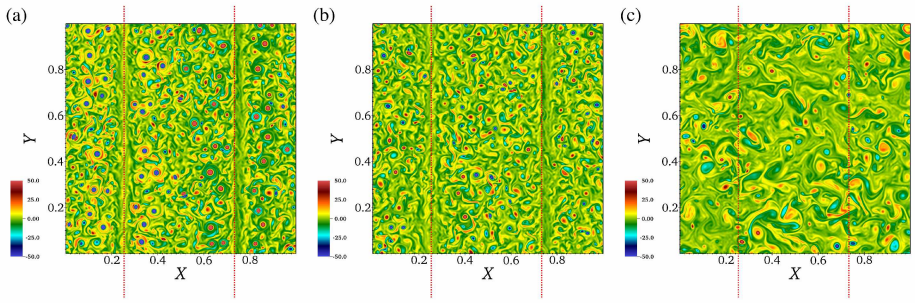

Figure 2.15: Snapshot of the vorticity field in real space, $\nabla^2\phi$, for the cases run using the critical threshold values of $L_{c,P,x}^{-1}$: (a) $L_{c,P,x}^{-1} = 0.0$, (b) $L_{c,P,x}^{-1} = 0.6$, and (c) $L_{c,P,x}^{-1} = 1.0$. Larger radial (x-direction) structures in (c) are more prominent resulting from the shift to a larger growth rate due to the critical gradient, which then induces stronger turbulence relaxations. Down-gradient transfer is dominated by smaller structures for (a) and (b) where turbulence relaxation is balanced by the transfer across self-generated flows.

confirmed by the variation of the H exponent found in our runs and shown in Fig. 2.10. The change in dynamics seem, however, to happen rather abruptly, which may point to a dynamical transition.

On the other hand, the opposite happens when the source S_0 is increased for a constant critical threshold, $L_{c,P,x}^{-1}$. The larger source increases the inhomogeneity in the near regions while, at the same time, results in larger levels of fluctuations in order to reach a balance between the larger source and the turbulent induced fluxes (see Fig. 2.16). Consequently, it becomes easier for poloidal flows to be driven by the Reynolds stresses. If the initial steady-state was one of near-marginality, in which radial transport takes place mainly via radial avalanches, an increase of the external drive thus results in profiles becoming supermarginal, and in (radial) transport becoming more diffusive. Or, if the poloidal flows become sufficiently sheared in radius, even subdiffusive. This is what the simulations showed in Sec. 2.5.2, and what the Hurst analysis confirmed as can be seen in Fig. 2.12. Again, the change in dynamics takes place rather suddenly, pointing to the possibility of a dynamical transition.

Finally, we have also shown that the dynamics of zonal flow generation and saturation may be greatly impacted by the presence (or absence) of efficient parallel equilibration (along y, in our case). As a result, the overall radial transport dynamics is affected as well. A system whose steady-state profile is near-marginal in the absence of parallel equilibration (that is, when $f_D = 0$ in our model) can transit to supermarginal profiles due to the development of very large poloidal flows that are no longer mostly present at the source and sink locations, where the inhomogeneity is larger, but that may extend over the whole system. The reason here is that, by introducing parallel equilibration, the anisotropy has been increased enormously everywhere in the system. Indeed, the x and y direction, are now also distinguished by which is the dominant way in which they react to local gradients: by turbulent-induced fluxes in the x direction, by parallel equilibration along y. As

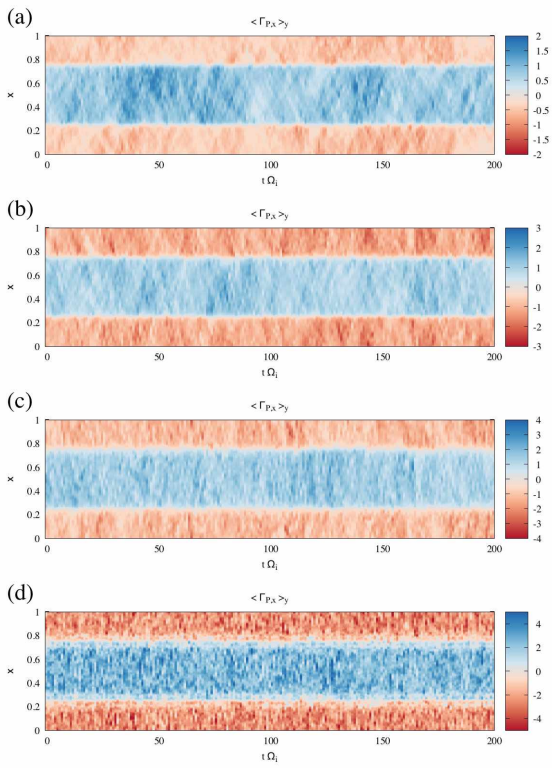

Figure 2.16: The poloidally averaged flux, $\langle \Gamma_{P,x} \rangle_y = \langle v_x P \rangle_y$, reflects the competition between turbulent relaxation and self-generated poloidal flows for selected values of S_0: (a) $S_0 = 5.0$ close to marginal state with sparse large relaxation events, (b) $S_0 = 8.0$ maintains superdiffusive transport, (c) $S_0 = 10.0$ self-generated flows begin to decorrelate down-gradient transfers, and (d) $S_0 = 20.0$ supermarginal state with strong flows near the sources..

a result, larger radial structures develop (see Fig. 2.2). The resulting larger anisotropy, in combination with the inhomogeneity introduced by the source, fuels the Reynolds stresses system-wide and generates the large poloidal flows whose action on the turbulence makes the profiles supermarginal, and radial transport becomes strongly subdiffusive, as was shown in Sec. 2.5.3. The Hurst analysis also suggests that this change in nature is rather abrupt (happening at $f_D \sim 0.2$ in our case, as shown in Fig. 2.14), maybe reminiscent of a dynamical transition. Parallel equilibration also permits the formation of larger radial structures (see the third frame in Fig. 2.2), which set up a state in which down-gradient transfer from the source to the sink may be accomplished within a couple of eddies despite the self-generated poloidal flows across the entire profile, which also enhances subdiffusion.

2.8 Conclusions

In this paper, the interaction between self-consistently evolved profiles, turbulence and turbulence-driven zonal flows has been explored in the context of a simplified drift-wave

turbulence model. Although instances of non-diffusive behavior in plasma turbulence have been previously studied, the results obtained with our model are perhaps more compelling in the sense that they illustrate clearly how the resulting radial transport can be superdiffusive, diffusive, or subdiffusive depending on several factors. Namely, how strongly the system is driven (i.e, by changing S_0), the degree of effectiveness of turbulence to relax profiles (by changing $L_{c,P,x}^{-1}$, that sets the growth rate and how near profiles can be to marginal values) and the degree of competition offered by other transport mechanisms (parallel equilibration, by changing $f_d = 0$). The existence of this rich dynamical zoology is one of the main results of the paper, as well as the understanding gained on how one can transition from one regime to another in dynamical space by modifying the free parameters of the model.

The results presented here should also serve as a warning, once more, of the dangers of doing turbulent transport studies numerically by using fixed-gradient setups. The numerical evolution of turbulence in the presence of frozen background profiles often can produce diffusive transport. The interplay between turbulent relaxation and self-generated sheared poloidal flows, that form the basis for the transport explored in this model, is however absent unless a flux-driven setup is used. Indeed, most of the rich dynamics shown here were not present when running our simplified DTEM model without an equation for background profile evolution.

All of the above points to flux-driven, global gyrokinetic simulations as the more adequate tool to carry out similar studies in tokamak-relevant situations. The work presented here can serve as a guide of what should be expected, both from a physics and a methodological point of view. We feel that the study of the role of parallel equilibration in this context might be particularly relevant in tokamaks, particularly close to the plasma edge where collisional drag is a factor, or in the neighborhood of low-order rational surfaces, where equilibration along the field line may still yield significant on-surface variations.

2.9 Acknowledgements

This work was supported in by US DOE contract number DE-FG02-04ER54741 with UAF and in part by a grant of HPC resources from the Arctic Region Supercomputing Center at the University of Alaska Fairbanks.

2.10 References

[1] E. Doyle, W. Houlberg, Y. Kamada, V. Mukhovatov, T. Osborne, A. Polevoi, G. Bateman, J. Connor, J. Cordey, T. Fujita, and et al., Nucl. Fusion **47**, S18 (2007).

[2] R. Sánchez and D. E. Newman, Plasma Phys. Control. Fusion **57**, 123002 (2015).

[3] P. Diamond and T. Hahm, Phys. Plasmas **2**, 3640 (1995).

[4] B. A. Carreras, D. Newman, V. E. Lynch, and P. H. Diamond, Phys. Plasmas **3**, 2903 (1996).

[5] X. Garbet and R. Waltz, Phys. Plasmas **5**, 2836 (1995).

[6] Y. Sarazin and P. Ghendrih, Phys. Plasmas **5**, 4214 (1998).

[7] R. Sánchez, D. Newman, J. Leboeuf, V. Decyk, and B. Carreras, Phys. Rev. Lett. **101**, 205002 (2008).

[8] Y. Idomura, H. Urano, N. Aiba, and S. Tokuda, Nucl. Fusion **49**, 065029 (2009).

[9] Y. Sarazin, V. Grandgirard, J. Abiteboul, S. Allfrey, X. Garbet, P. Ghendrih, G. Latu, A. Strugarek, and G. Dif-Pradalier, Nucl. Fusion **50**, 054004 (2010).

[10] D. E. Newman, P. W. Terry, P. H. Diamond, Y.-M. Liang, G. G. Craddock, A. E. Koniges, and J. A. Crottinger, Phys. Plasmas **1**, 1592 (1994).

[11] V. Naulin, A. H. Nielsen, and J. J. Rasmussen, Phys. of Plasmas **6**, 4575 (1999).

[12] H. E. Hurst, Trans. Amer. Soc. Civil Eng. **116**, 770 (1951).

[13] W. Horton, Rev. Mod. Phys. **71**, 735 (1999).

[14] D. E. Newman, P. W. Terry, P. H. Diamond, and Y. Liang, Phys. Fluids B **5**, 1140 (1993).

[15] P. W. Terry, A. S. Ware, and D. E. Newman, Phys. Plasmas **1**, 3974 (1994).

[16] G. G. Craddock, A. E. Koniges, J. A. Crotinger, P. H. Diamond, D. E. Newman, and P. W. Terry, Phys. Plasmas **1**, 1877 (1994).

[17] R. E. Waltz, Phys. Fluids **28**, 577 (1985).

[18] D. E. Newman, P. W. Terry, and P. H. Diamond, Phys. Fluids B **4**, 599 (1992).

[19] D. E. Newman, B. A. Carreras, and P. H. Diamond, Phys. Lett. A **218**, 58 (1996).

[20] A. C. Hindmarsh, P. N. Brown, K. E. Grant, S. L. Lee, R. Serban, D. E. Shumaker, and C. S. Woodward, ACM Trans. Math. Softw. **31**, 363 (2005).

[21] M. Frigo, SIGPLAN Not. **34**, 169 (1999).

[22] R. Metzler and J. Klafter, Phys. Reports **339**, 1 (2000).

[23] G. Zaslavsky, Phys. Rep. **371**, 461 (2002).

[24] I. Podlubny, *Fractional Differential Equations* (Academic Press, San Diego, California, 1999).

[25] E. Montroll and H. Scher, J. Stat. Phys. **9**, 101 (1973).

[26] R. Sánchez, B. A. Carreras, and B. P. van Milligen, Phys. Rev. E **71**, 011111 (2005).

[27] R. Sánchez, B. A. Carreras, D. E. Newman, V. E. Lynch, and B. P. van Milligen, Phys. Rev. E **74**, 016305 (2006).

[28] I. Calvo, R. Sánchez, and B. A. Carreras, J. Phys. A: Math. Theor. **42**, 055003 (2009).

[29] B. A. Carreras, B. P. van Milligen, M. A. Pedrosa, R. Balbín, C. Hidalgo, D. E. Newman, E. Sánchez, M. Frances, I. García-Cortés, J. Bleuel, M. Endler, C. Riccardi, S. Davies, G. F. Matthews, E. Martines, V. Antoni, A. Latten, and T. Klinger, Phys. Plasmas **5**, 3632 (1998).

[30] P. W. Terry, Rev. Mod. Phys. **72**, 109 (2000).

Chapter 3 Tuning non-diffusive transport dynamics in self-consistent drift wave turbulence by means of externally-applied flows[1]

3.1 Abstract

The reduction of turbulent transport across sheared flow regions has been known for a long time in magnetically confined toroidal plasmas. However details of the dynamics are still unclear, in particular in what refers to the changes caused by the flow on the nature of radial transport itself. In a companion paper, we have shown in a simplified model of drift wave turbulence that, when the background profile is allowed to evolve self-consistently with fluctuations, a variety of transport regimes ranging from superdiffusive to subdiffusive open up depending on the properties of the underlying turbulence [D. Ogata et al, *Physics of Plasmas* (submitted, 2016)]. In this paper, we explore the usefulness and limitations of externally applied sheared flows in order to tune at will the desired transport dynamics in these type of scenarios.

3.2 Introduction

Radial transport in magnetically confined fusion plasmas has been an area of active investigation for many years. Methods for regulating radial turbulent transport could provide a balance between improved confinement and ash removal. There is a large body of work with experiments on various devices and plasmas simulations of different kinds have shown that sheared flows tend to suppress transport across the flow[1–3]. In fact, it is this type of transport reduction that is believed to be responsible for the access to improved confinement in current tokamak configurations, where a large radially-sheared poloidal flow appears at the so-called pedestal region near the plasma edge.

However, there are still many aspects of the process by which sheared flows reduce transport across them that remain unclear. Traditionally, it has been thought that the main action of a sheared flow on turbulent fluctuations is to reduce its size perpendicular to the direction of the flow, which leads to a reduced effective transport coefficient in that direction. However, recent studies with ion-temperature-gradient (ITG) gyrokinetic turbulence in a tokamak geometry have shown that, if the radial shear in the poloidal flow is sufficiently large, the intimate nature of the transport process changes, becoming subdiffusive instead of just diffusive[4,5]. An important limitation of these simulations, though, was that they were carried out using the commonly used fixed-gradient setup, in which the background profiles are kept fixed while turbulence is evolved. Background

[1]D. Ogata, D. E. Newman, and R. Sánchez. Tuning non-diffusive transport dynamics in self-consistent drift wave turbulence by means of externally-applied flows. Submitted to Physics of Plasmas (POP51264).

evolution is however important in this context, particularly if the background profiles remain close to near-marginal conditions, when the separation of timescales between turbulence and profile evolution narrows. In near-marginal conditions, coherent relaxations of the profile can propagate both down and up the background gradients (the so-called "avalanches") leading to superdiffusive transport[6,7]. There are theoretical reasons to expect that sheared flows should have an important impact on these coherent relaxations[8]. Regretfully, the kind of flux-driven numerical plasma simulations needed to explore these questions, in which background profiles, turbulence and flows should be advanced simultaneously and self-consistently, remain very expensive numerically, specially in a gyrokinetic context. Thus, studies on the nature of radial transport in these conditions, although relevant for next-step tokamaks such as ITER, have remained scarce[9].

In order to shed some light onto this matter, we have constructed a simpler two-dimensional flux-driven model, based on drift-wave turbulence in a bi-periodic slab geometry, that includes the simultaneous, self-consistent evolution of profiles, turbulence and flows, whose relative simplicity allows for sufficiently long simulations. In a companion paper[10], we characterized the transport dynamics of the model that may exhibit a whole range of transport dynamics, going from superdiffusive to subdiffusive simply by varying the parameters that define it. The mechanisms responsible for this behavior were easily identified, being related to the ability of the turbulence-induced transport can relax supra-marginal profiles back below the local thresholds, the degree of competition offered by other transport mechanisms and the importance of the flows self-generated by the turbulence. In this paper, we explore instead the possibilities of control offered by externally applied flows in order to tune at will the desired transport dynamics of the system.

With that idea in mind, we have included an external poloidal flow within the simple drift-wave model as is described in Sec. 3.3. The changes induced in the transport dynamics by the external flows are monitored by means of a characteristic transport exponent, H, that is introduced in Sec. 3.4, as well as the technique to measure it using tracer particles[11]. The next sections discuss the results obtained with the model. First, in order to connect the results with previous work, Sec. 3.5 presents the modifications of the characteristics of transport induced by the externally imposed flows in the case in which turbulence is evolved with a fixed-profile. Then, in Sec. 3.6, the same cases are re-analyzed but using instead a flux-driven setup in which proper background evolution is enabled. Finally, Sec. 3.7 summarizes the main results of the work.

3.3 Drift-wave turbulence model

The model that will be used in this paper is based on a collisional drift-wave model for plasma turbulence[12]. The model is formulated in a bi-periodic slab geometry that assumes a constant perpendicular magnetic field. The spatial domain is a periodic square in the xy plane. The coordinate $x \in [0, 1]$ mimics the radial direction (in a magnetic

toroidal configuration), while the coordinate $y \in [0,1]$ emulates the poloidal direction. The governing evolution equations for this electrostatic model are three:

$$\begin{aligned}
\frac{d}{dt}\left[\left(1-\sqrt{\epsilon}-\rho_s^2\nabla_\perp^2\right)\phi\right] &= -\left[1-\sqrt{\epsilon}\,\xi\right]C_s\rho_s R_{nl}\left(n,\phi,P\right)+\nu\sqrt{\epsilon}\left(n-\phi\right)-\mu\rho_s^2\nabla_\perp^4\phi \\
\frac{dn}{dt} &= \xi C_s\rho_s R_{nl}\left(n,\phi,P\right)+\nu_{eff}\left(\phi-n\right) \\
\frac{dP}{dt} &= S+D_P\nabla_\perp^2 P
\end{aligned} \tag{3.1}$$

where n is the fluctuating density, ϕ is the fluctuating potential, and P is the background profile. The first two equations are essentially the same as those of the standard DTEM model[12,13], except in that they include an additional dependence on the background profile P via the nonlinear function $R_{nl}\left(n,\phi,P\right)$, that we discuss later. The third equation, on the other hand, gives the evolution of the background profile P in the presence of an external drive S. The definitions and meanings of the coefficients appearing in the model are also quite standard: $\rho_s = \left(k_B T_e/eB\right)/C_s$ is the ion gyroradius, $C_s = \sqrt{k_B T_e/m_i}$ is the ion sound speed, $\xi = (1+\alpha\eta_e)$ where $\eta_e = \partial\left(\ln T\right)/\partial\left(\ln n\right) = 2$ and $\alpha = 3/2$ for the instability criterion for destabilization of DTEM modes by electron collision[12], ϵ is the inverse aspect-ratio that gives the trapped electron fraction, μ is the viscosity coefficient, ν is the electron collisional relaxation due to trapping and detrapping, and $\nu_{eff} = \nu/\sqrt{\epsilon}$. The trapped electron fraction ϵ affects the instability of the drift-waves in relations to the regime of collisionality ν[12].

The adiabatic limit of the model is achieved when $\nu \to \infty$, in which the relationship between n and ϕ reduces to the "$i\delta_k$" approximation[14] that specifies the nonadiabatic trapped electron response. The turbulence evolution is then described through a single equation where n responds to ϕ nonlocally[12,15,16]. Mid-sized tokamaks operate in this high collisional regime where the ion detrapping occurs before banana orbits are formed[12], which then allows for a phase shift between n and ϕ. The coupling term $n-\phi$ is defined to evolve with the $k_y = 0$ modes unlike models with zonal flows[2] such as the modified Hasegawa-Wakatani model[17]. Equilibrium across flux surfaces between n and ϕ is still maintained in order to restrict the development of zonal flows. The hydrodynamic limit occurs when $\nu \to 0$, which decouples the n from the ϕ evolution equation. The equation for ϕ resembles a 2D neutral fluid equation while the n equation becomes that of a passive scalar. Large tokamaks are in this low collisional regime[12].

In the evolution of the background profile, P, S is the source term and D_P is a classical diffusion coefficient. It must be noted that the inclusion of an evolution equation for P makes the simulation flux-driven, which means that the local flux $\boldsymbol{\Gamma}_P = \boldsymbol{u}P$, where $\boldsymbol{u} = C_s\rho_s\hat{\boldsymbol{z}}\times\boldsymbol{\nabla}\phi$, adapts itself to balance the incoming net drive. This drive is constructed as the sum of a Gaussian of a fixed-width, $G_w(x)$, and prescribed positive height, S_0, located at $x_{\text{source}} = 0.25$ and another Gaussian equal in magnitude but of reversed sign at

$x_{\text{sink}} = 0.75$:

$$S(x) = S_0 \left[G_w(x - x_{\text{source}}) - G_w(x - x_{\text{sink}}) \right]. \tag{3.2}$$

S_0 represents the injection rate. It is set to $S_0 = 5$ in all simulations in this paper.

The model permits the self-generation of flows via the Reynold stress term, that expresses itself in the form of two non-linearities, but requires turbulence to be sufficiently inohomogeneous and anisotropic for significant flow generation[1,18]. The first nonlinearity is the $E \times B$ nonlinearity, that appears in the n evolution equation and represents the advection on the fluctuating density n, given by the term $\boldsymbol{u} \cdot \boldsymbol{\nabla}_\perp n = C_s \rho_s \hat{\boldsymbol{z}} \times \boldsymbol{\nabla}_\perp \phi \cdot \boldsymbol{\nabla}_\perp n$. The second is the polarization drift nonlinearity, that arises from the advection on the vorticity, $\nabla^2_\perp \phi$, and is given by the term $\boldsymbol{u} \cdot \boldsymbol{\nabla}_\perp \left(\nabla^2_\perp \phi \right) = C_s \rho_s^3 \hat{\boldsymbol{z}} \times \boldsymbol{\nabla}_\perp \phi \cdot \boldsymbol{\nabla}_\perp \left(\nabla^2_\perp \phi \right)$. The interplay of these two nonlinearities has been studied extensively in simulations that, in contrast to the ones performed here, assumed a fixed background gradient[13,15,16,19]. The polarization drift nonlinearity is found to be dominant at large wave numbers due to difference in the k^2 coming from the vorticity term.

In addition to self-generated sheared flows, the possibility of having externally-imposed flows has also been introduced in the model through the advective derivative operator, $d/dt = \partial_t + (\boldsymbol{u}_0 + \boldsymbol{u}) \cdot \boldsymbol{\nabla}$. The external flow is defined as $\boldsymbol{u}_0 = C_s \rho_s \hat{\boldsymbol{z}} \times \boldsymbol{\nabla} \phi_0$, being ϕ_0 an externally defined electrostatic potential with a radial profile given by $\phi_0 = \Phi_0 \cos(2\pi x)$. In this way, the velocity profile is $\boldsymbol{u}_{\text{ext}} \sim \Phi_0 \sin(2\pi x)\, \hat{\boldsymbol{y}}$, reaching its maximum shear at $x = 0.5$. The external flow remains incompressible since $\boldsymbol{\nabla} \cdot \boldsymbol{u}_0 = 0$. It must be noted that the external electrostatic profile ϕ_0 is not included in the parallel dynamics; therefore, ϕ_0 is not added to the term proportional to the difference $n - \phi$ in the evolution equation for ϕ.

We discuss next the nonlinear function $R_{nl}(n, \phi, P)$, that includes the threshold condition that introduces the possibility of profiles being near-marginal. The term is defined as:

$$\begin{aligned} R_{nl}(n, \phi, P) = {} & f_d \left[g\left(L^{-1}_{\langle P \rangle_y, x} \right) L^{-1}_{\langle P \rangle_y, x} \left(-\frac{\partial \phi}{\partial y} \right) \right] \\ & + (1 - f_d) \left[g\left(L^{-1}_{P,y} \right) L^{-1}_{P,y} \frac{\partial \phi}{\partial x} + g\left(L^{-1}_{P,x} \right) L^{-1}_{P,x} \frac{\partial \phi}{\partial y} \right] \end{aligned} \tag{3.3}$$

Its meaning is explained in depth in the companion paper[10], but we repeat the fundamentals here for clarity. The main ingredient is the function $g(L^{-1}_{s,z})$, defined as:

$$\begin{aligned} g(L^{-1}_{s,z}) = \frac{1}{2} \big[& 2 + \tanh\left(\kappa \left(L^{-1}_{s,z} - L^{-1}_{c,s,z} \right) \right) - \\ & - \tanh\left(\kappa \left(L^{-1}_{s,z} + L^{-1}_{c,s,z} \right) \right) \big] \end{aligned} \tag{3.4}$$

where $L^{-1}_{c,s,z}$ is a prescribed critical value for the gradient of field s in the z direction, $\kappa [= 20]$ prescribes the steepness of the hyperbolic tangent function, and $L^{-1}_{s,z} := \partial_z s / s_0$ is the local gradient (s_0 is an arbitrary normalization constant). The main point is that $g(L_{s,z})$ essentially vanishes if $L^{-1}_{s,z} < L^{-1}_{c,s,z}$, and is equal to one if $L^{-1}_{s,z} > L^{-1}_{c,s,z}$, thus introducing

a threshold for the excitation of turbulence in the problem. It is the combination of the presence of this term and the flux-driven setup that permits the system to stay near-marginality if the proper conditions are met. Eq. 3.3 includes however several possible thresholds, weighted by the $f_d \in (0,1)$ factor. The first line introduces a threshold on the radial gradient of the poloidally averaged background profile; the second line, two thresholds, one on the local radial gradient of the background profile, another on the local poloidal gradient. This combination has been introduced to make possible the study of the importance of a partial parallel equilibration across magnetic surfaces[10], which might be an issue in tokamaks, particularly closer to the edge where dynamics are more collisional, or in the neighborhood of rational surfaces. Indeed, if $f_d = 1$, it is assumed that any inhomogeneities along y are quickly equilibrated, and that only the poloidally-averaged background profile (denoted by $\langle\cdot\rangle_y$) matters in terms of providing the turbulence with free energy. On the other hand, $f_d = 0$ means that there is no parallel equilibration whatsoever, and only local gradients matter.

Fixed background gradient scenarios can also be easily run in this model. One just needs to solve Eq. 3.1 with $dP/dt = 0$, set $f_d = 1$, impose $g\left(L^{-1}_{\langle P\rangle_y,x}\right) = 1.0$ and, finally, prescribe a fixed value for the background gradient, $L^{-1}_{\langle P\rangle_y,x} = \partial_x \langle P\rangle_y / P_0$. With these choices, the nonlinear function reduces to $R_{nl}(n,\phi,P) = L^{-1}_{\langle P\rangle_y,x}\partial_y\phi$ such that $C_s\rho_s R_{nl}(n,\phi,P) = V_D\partial_y\phi$ where $V_D = C_s\rho_s/L_{\langle P\rangle_y,x} = (k_B T_e/eB)\, L^{-1}_{\langle P\rangle_y,x}$, a common form for the diamagnetic drift. In this case, assuming a constant external flow $\boldsymbol{u}_0 = U_0\hat{\boldsymbol{x}}$ yields a linear dispersion for perturbations of the form $\propto \exp\left[i\left(k_x x + k_y y\right) - i\omega t\right]$ given by:

$$0 = \left(\omega'\right)^2 - \omega'\left\{\left[1 - \sqrt{\epsilon}\,\xi\right]\omega_* - i\nu_{eff}\zeta\right\} - i\nu_{eff}\omega_* \tag{3.5}$$

where $k^2 = k_x^2 + k_y^2$, the frequency shift $\omega' = \omega - U_0 k_x$, the electron diamagnetic drift frequency $\omega_* = k_y V_D / \left(1 - \sqrt{\epsilon} + \rho_s^2 k^2\right)$, and the ϵ dependent contribution of the resistive coupling $\zeta = \left(1 + \rho_s^2 k^2\right) / \left(1 - \sqrt{\epsilon} + \rho_s^2 k^2\right)$. This linear dispersion relation, except for the U_0-shift, is identical to that of the standard DTEM model[16,17], as it shoud be.

We conclude this section by providing some details about the numerical scheme used to solve Eq. 3.1. The spatial domain considered is a doubly-periodic grid of 256×256 nodes in the Fourier space spanned by k_x and k_y. The scheme used is a standard spectral one, properly modified to avoid any aliasing problems, that uses the pseudo-spectral method to deal with nonlinearities. The temporal integration is done implicitly, using a scaled preconditioned Generalized Minimal Residual (GMRES) solver that combines well-established integration schemes[20]. Parallelization is achieved by using MPI and by taking advantage of parallel Fast Fourier Transform (FFT) routines, as well as other parallel numerical integration routines. All simulations have been initialized with random phases for all Fourier harmonics, and they have been advanced in time until a suitable quasi-steady state, with approximate balance between drive and losses, is established.

3.4 Transport characterization

There are many ways to define the characterize the nature of transport in a system[21,22]. Traditionally, transport of any conserved quantity P is termed diffusive if it can be described by an equation of the type,

$$\frac{\partial P}{\partial t} = \chi \frac{\partial^2 P}{\partial x^2}, \tag{3.6}$$

where χ is a transport coefficient. This equation implies that the local flux of the transported quantity is $\Gamma_P = -\chi \partial_x P$, thus pointing down the gradient, what is known as Fick's law. By extension, some authors define nondiffusive transport as any situation in which the evolution of P follows instead a transport equation of the form:

$$\frac{\partial^\beta P}{\partial t^\beta} = \chi_{\alpha,\beta} \frac{\partial^\alpha P}{\partial |x|^\alpha}. \tag{3.7}$$

for $x \in \mathbb{R}$ and $t \in \mathbb{R}^+$ where $\chi_{\alpha,\beta}$ is a scaling constant. The exponent ranges are $\alpha \in (0, 2)$ and $\beta \in (0, 1)$. This equation is a generalization of the more usual classical diffusive equation, where $\beta = 1$ and $\alpha = 2$, based on fractional derivatives. These fractional operators provide a smooth interpolation in between integer derivatives[23]. In contrast to the integer derivatives, that are local operators, fractional derivatives are integro-differential operators that are non-local in their variable of definition (either space or time). Thus, the type of transport that can be captured by Eq. 3.7 may be non-local (if $0 < \alpha < 2$) and non-Markovian (if $0 < \beta < 1$). The exponent of interest to us, however, is $H := \beta/\alpha$. Transport is called superdiffusive if $H > 1/2$, diffusive if $H = 1/2$ and subdiffusive if $H < 1/2$. The reason for this name is that any population of particles, whose transport is governed by Eq. 3.7 and that are initially localized in x, will spread faster (if $H > 1/2$) or slower (if $H < 1/2$) than its diffusive counterpart.

The transport exponent H can be estimated in many ways. A very useful way is to take advantage of the fact that transport equations like Eq. 3.6 and 3.7 can be derived from "microscopic considerations". It is well known that the classical diffusion equation can be obtained as the long-term, long-distance limit of either a continuous time random walk (CTRW) in which particles are advanced with Gaussian-distributed step-sizes, separated by exponentially-distributed waiting times. Also, the diffusion equation can be obtained from the "microscopic" Langevin equation, that expresses the position of each particle being transported as:

$$x(t) = x_0 + \int_0^t \xi(t')dt'. \tag{3.8}$$

In the same long-term, long-distance limit, by assuming a random forcing ξ with Gaussian statistics and zero time correlation except at zero lag (i.e., lack of memory along Lagrangian trajectories), the classical diffusion equation is easily recovered. Similarly, the fractional

transport equation can be derived from CTRW[24] in which steps are distributed according to a symmetric α-Lévy distribution with tail index $\alpha \in (0,2)$ and waiting-times distributed according to an extremal β-Lévy distribution with tail index $\beta \in (0,1)$[21,22,25]. It can also be derived as the long-term, long-distance limit of the generalized Langevin equation[11,26]

$$x(t) = x_0 + \frac{1}{\Gamma(H - 1/\alpha + 1)} \int_0^t (t - t')^{H-1/\alpha} \xi_\alpha(t') dt', \tag{3.9}$$

that assumes a non-random forcing with symmetric α-Lévy statistics and a correlation in time characterized with a Hurst exponent $H \in (0,1)$[27]. H is also the self-similarity exponent of the trajectory, $x(t)$. In that case, the resulting temporal exponent in the transport equation Eq. 3.7 is given by $\beta = \alpha H$.

As advertized, the connections of Eq. 3.7 with these "microscopic formulations" can be exploited to come up with methods to determine the fractional exponents in practical situations, and thus to provide ways to characterize the nature of transport. Among the different methods available, in this paper we will focus on one that exploits the connection with Eq. 3.9 to determine H. It just requires following the trajectories of massless tracer particles as they are advected by the turbulence. That is, to integrate in time their velocity, that is given by,

$$\dot{\boldsymbol{R}}(t) = \boldsymbol{E} \times \boldsymbol{B}/B^2 = C_s \rho_s \hat{\boldsymbol{z}} \times \boldsymbol{\nabla}_\perp \phi, \quad \boldsymbol{R}(t_0) = \boldsymbol{r_0}, \tag{3.10}$$

since the advection in our model is done by the turbulent fluctuating $E \times B$ velocity.

Since H represents the self-similarity exponent of the trajectory described by Eq. 3.9, it must also happen that it is the correlation (or Hurst) exponent of its derivative, or time series of the increments of the process. Or, in discrete form, H also represents the velocity series along the Lagrangian trajectory. The method we have chosen to determine this correlation exponent is the well-known R/S technique, that has been reliably used for more than sixty years[27]. Given a velocity series of length N represented as $\{V_k : 1 \leq k \leq N\}$, one just needs to construct the so-called rescaled range:

$$(R/S)_n = \frac{\max(0, X_1, \ldots, X_n) - \min(0, X_1, \ldots, X_n)}{\sigma_n^{1/s}} \tag{3.11}$$

where $X_k = V_1 + \cdots + V_k - k\bar{V}_n$ for $k \leq n$. The mean is defined as $\bar{V}_n = \sum_{i=1}^n V_i/n$. The s-variance is defined as $\sigma_n = \sum_{i=1}^n \left(V_i - \bar{V}_n\right)^s / (n-1)$, with $s < \alpha$, being $\alpha < 2$ the tail-exponent characterizing the velocity statistics (or, if Gaussian-distributed, $\alpha = 2$). It then happens that, if the signal is correlated with Hurst exponent H (and therefore, its integrated path is self-similar with the same exponent), one finds that,

$$(R/S)_n \propto n^H, \tag{3.12}$$

from which the exponent is readily obtained. It is fair to say that the R/S method has been criticized in the literature because it tends to somewhat overestimate exponents (for instance, R/S tends to yield $H \sim 0.55$ for random signals instead of 0.5), but it is extremely resilient to both noise and periodic perturbations[28], which is why it is our method of choice. It is also worth to note that the statistics of the determination of H are greatly improved by averaging the rescaled range for time n over all non-overlapping segments of size n in which the full time series can be broken, procedure that we have extensively used in this work.

3.5 Transport characteristics of cases run with a fixed background profile in the presence of an externally-imposed sheared flow

In fluid turbulence, a hierarchy of eddies exist due to the nonlinear turbulent cascade. These eddies decay with a rate inversely proportional to the eddy turnover time τ_e[1]. Inherently to the fixed gradient case, nonlinearities distribute energies from one scale to another yielding a self-similar cascade[16]. A shear flow can then be viewed as a large eddy with an associated small wavenumber k plus a shear strain rate that has a characteristic time τ_s. This means that an externally-imposed sheared flow acts as a selective mechanism that filters eddies of specific sizes. Eddies with turnover times smaller than the shear strain rate τ_s^{-1} survive, while eddies with correlation times larger than the shearing rate are sheared apart[1]. The added decorrelation acts to inhibit the transport across the sheared region, while enhancing advection in the flow direction. This inhibited transport has been recently shown to exhibit subdiffusive features across the flow, and to behave superdiffusively along the flow in recent gyrokinetic simulations with fixed background gradients[4,5].

In order to better understand later the action of an external flow in situations in which profile turbulent modification and flow generation happen simultaneously, self-consistently and in near-marginal conditions, we have started our analysis by looking first at the simpler (and more traditional) case in which profile modification is disabled. To do that, we have run the DTEM model in a fixed-background-mode. That is, we set $dP/dt = 0$, $f_D = 1$, impose $g\left(L^{-1}_{\langle P\rangle_y,x}\right) = 1.0$ and choose a value $L^{-1}_{\langle P\rangle_y,x} = 0.5$, so that a constant, fixed gradient provides free energy for the turbulence. These choices also bring us close to the majority of previous work by many authors, which should allow for a more meaningful comparison when we allow profile modification to happen in the next section.

In drift-wave turbulence, however, one needs to be careful. An additional mechanism exists, independent of the presence of self-generated sheared flows, that can yield subdiffusive radial transport, and superdiffusive poloidal transport. It emerges after the nonlinearly saturated state has been achieved due to the linear (poloidal) diamagnetic drift[29–33]. Hence, in order to demonstrate any subdiffusive influence of an externally-imposed flow, the shear strain rate τ_s^{-1} defined through Φ_0 must overcome that from the diamagnetic wave term. That is, the shear strain rate imposed by the external flow must effectively decorrelate

the eddies faster than the effect from the diamagnetic drift. We have made sure that this is the case by modifying some of the parameters that define the DTEM model, while keeping $\Phi_0 = 0$, until the resulting transport has diffusive features in all directions, implying that the action of the diamagnetic wave is negligible. The two parameters that have been varied in this search are ν and ϵ, that respectively represent the electron collisionality and the trapped electron fraction.

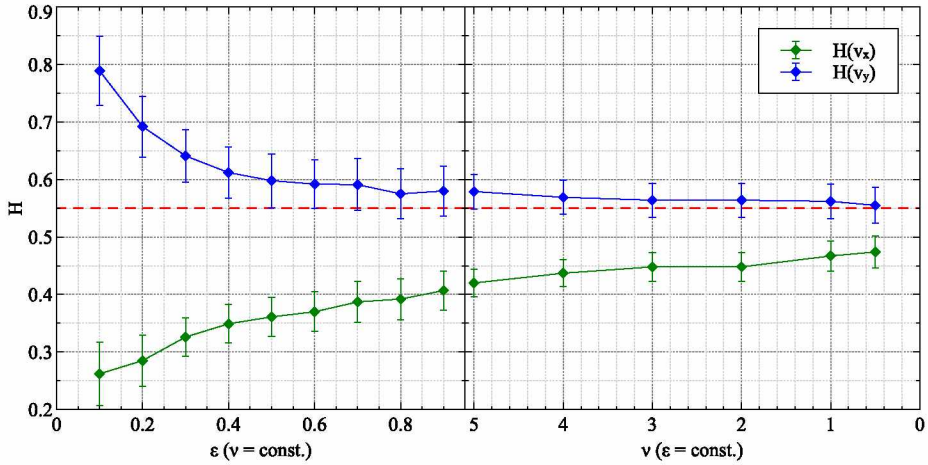

Figure 3.1: Transport exponent H showing the progression towards diffusion for two series of runs in which we fixed, respectively, the parameters $\nu = 5$ and $\epsilon = 0.9$. The transport exponent H for cases with varying ϵ (at $\nu = 5$) show a trend towards radial diffusion with increasing trapped electron fraction. On the other hand, cases with varying ν (at $\epsilon = 0.9$) move towards radial diffusion for decreasing collisionality. The red dashed line is the effective diffusive limit for the R/S analysis.

Fig. 3.1 shows, as a function of ν (for fixed $\epsilon = 0.9$) and ϵ (for fixed $\nu = 5$), the values of the transport exponent H, in the radial (x) and poloidal (y) direction, that result from the tracer analysis. It is apparent that, consistently with previous observations[29–33], radial subdiffusion (and superdiffusive poloidal motion) depends quite strongly on the value of ν. At the largest values of ν we have explored, the radial subdiffusive signature becomes quite strong with $H(v_x) < 0.3$ for $\epsilon < 0.2$ and $\nu = 5.0$. This subdiffusive signature, as previously said, comes primarily from the temporal decorrelation from the diamagnetic drift instead of from the action of any self-consistently generated sheared flow. At smaller values of ν, however, transport becomes more diffusive, as shown in the right frame of Fig. 3.1. From these results, we decided to move into a parameter regime in which the electron collisional relaxation becomes sufficiently small $\nu \to 0$ and the trapped electron fraction becomes large $\epsilon \to 1$ in order to isolate and make easier the analysis of the effect of external flows on transport in the model. Small ν means a reduced coupling between n and ϕ in Eq. 3.1 (i.e., the system moves away from electron adiabaticity), while a large ϵ increases the contribution of trapped particles to the evolution of the drift-wave, which places the model closer to the hydrodynamic limit of the Hasegawa-Wakatani model[34].

In this parameter regime, the ϕ equation becomes analogous to the 2D quasi-geostrophic equation while the n equation becomes a passive scalar. The disadvantage of this parameter regime, on the other hand, is that the linear growth rate becomes larger due to the quadratic nature of the eigen-frequencies from Eq. 3.5. This means that the turbulence becomes more susceptible to instabilities, particularly those of the Kelvin-Helmholtz type[35].

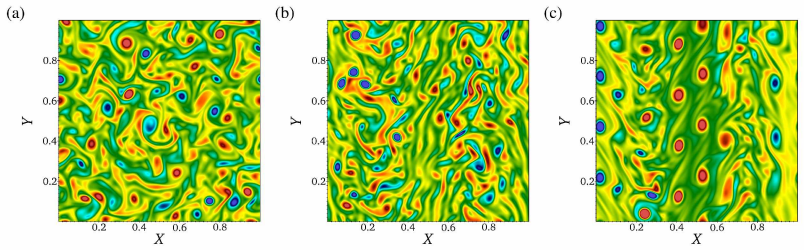

Figure 3.2: Vorticity field $\nabla^2\phi$ in real space for three values of Φ_0: (a) $\Phi_0 = 0.0$, (b) $\Phi_0 = 1.5$, and (c) $\Phi_0 = 3.0$ in the regime in which the linear wave contribution is weak. Transport is diffusive in the absence of external flow (a). Elongation in the poloidal direction becomes prominent with larger flow amplitude $\Phi_0 = 1.5$ (b). A Kelvin-Helmholtz instability occurs near the regions with largest shear at large enough external flow amplitude $\Phi_0 = 3.0$ (c).

Next, we proceeded to add external flows of varying amplitude Φ_0 to simulations run in the regime we just chose. The resulting vorticity fields, $\nabla^2_\perp\phi$ are shown in Fig 3.2 for some representative cases. It can be appreciated that the maximum value of Φ_0 that can be used is indeed limited by the onset of Kelvin-Helmholtz instabilities, as expected. As an illustration of the tracer analysis done, Fig. 3.3 shows a few rescaled ranges for the series of the x (or y) component of the tracer Lagrangian velocity. Two distinct regions are clearly visible. A first one, for timescales smaller than $\tau\Omega_i \sim 1.0$ corresponds to the self-correlation of turbulence, and are of no interest for the determination of the long-term properties of transport. The second region, for $\tau\Omega_i \gg 1.0$ is seen to scale as τ^H, thus defining the Hurst exponent. The transition timescale between these regions is seen to move to smaller values for larger Φ_0, though, which points to the reduction in the autocorrelation time of the turbulence as the shear strain time τ_s imposed by the external flow increases. At the larger timescales, it is clearly seen that radial subdiffusion is enhanced by the presence of the external flow. Radial transport becomes more subdiffusive, the stronger the shear is. In the poloidal direction, the reverse behavior is observed. The level of superdiffusion increases as the shear becomes stronger. In fact, the value of the Hurst exponent exceeds even the upper limit of 1, which we think is related to the presence of long-lived eddies that then allows the signal to be non-stationary.

We have collected the Hurst exponents obtained from all simulations in Fig. 3.4 as a function of the shear flow strength. As advertized, it is clear that radial transport can be forced to be more subdiffusive by means of externally applied flows with larger shear

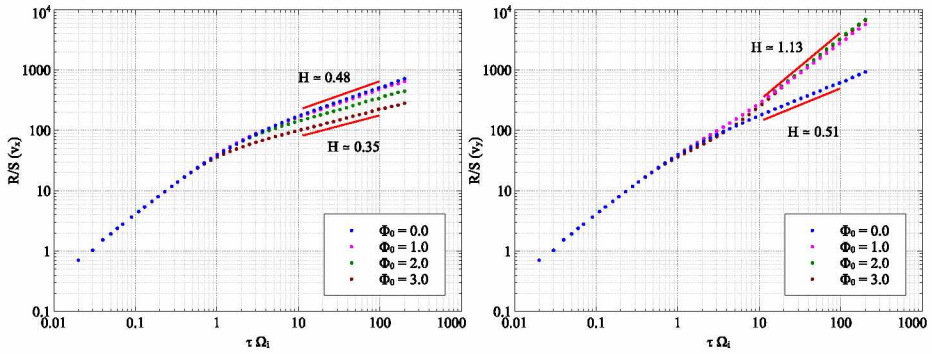

Figure 3.3: Transport exponents with varying external flow amplitude Φ_0 with a fixed gradient setup show subdiffusion in the cross-flow direction with increasing Φ_0 but superdiffusion in the poloidal direction.

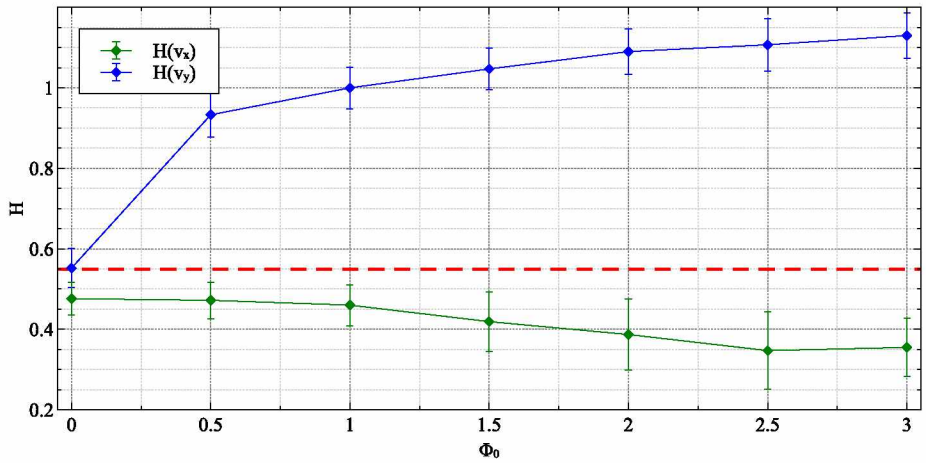

Figure 3.4: Hurst parameters with varying external flow amplitude on a fixed gradient show subdiffusion in the cross-flow direction but strongly superdiffusion in the poloidal direction. The radial subdiffusive transport signature saturates at $H \sim 0.35$ due to the onset of a shear-driven instability. Dashed red line denotes the diffusive limit for R/S analysis.

values; at the same time, poloidal transport becomes more superdiffusive. The possibility of controlling the dynamics ends, however, when the stability of the external flow is broken by the onset of Kelvin-Helmholtz instabilities at the positions of maximum flow shear. It is interesting to note that, in the case with fixed-gradients just examined, the value of H for radial transport (before any instability of the flow kicks in) saturates at around $H \sim 0.35$. This value is interestingly similar to the value obtained in pure Hasegawa-Wakatani models with self-consistent zonal flows[36]. This similarity points to the structure of the flow, and not the self-consistent interaction with the turbulence, as the more important factor in setting the value of the transport exponent H, at least in fixed-gradient simulations, as previously hinted at elsewhere[5].

3.6 Transport characteristics of cases run with profile evolution in the presence of an externally-imposed sheared flow

In this section, we proceed to explore the possibility of controlling the transport dynamics by means of externally-imposed sheared flows in the more realistic case in which a self-consistently evolving flux-driven profile replaces the fixed gradient used in the previous section. We have chosen as base case one with parameters $f_d = 0$ and $L_{c,P,x}^{-1} = 1$, so that a threshold local gradient exists in the radial direction. The source is chosen so that, in the case with no externally-imposed flows, radial transport is superdiffusive and poloidal transport subdiffusive.

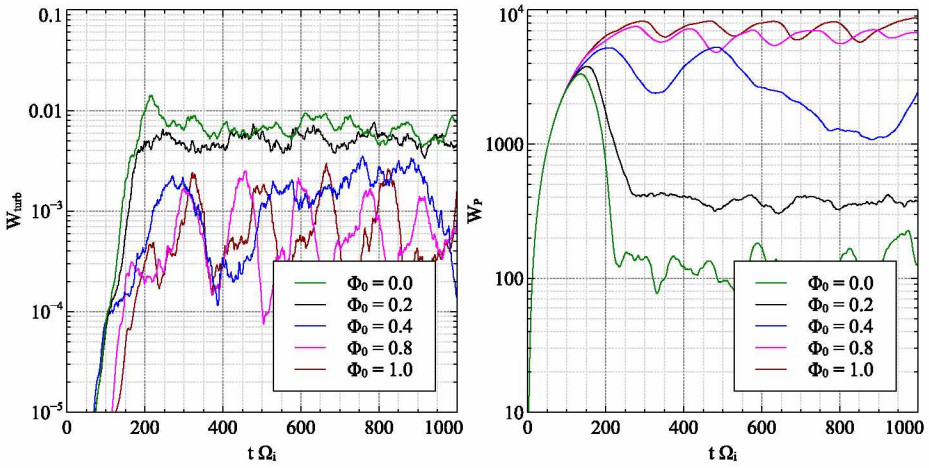

Figure 3.5: Proxies for total energy W_{turb} and W_P reach quasi steady-states when the local turbulence balances the sources. Radial relaxations are inhibited with increasing Φ_0, which is reflected by the increase in the time-averaged W_P ($\langle W_P \rangle_t$). However, the turbulence decreases with increasing Φ_0. For large enough flow amplitude, flow-driven instabilities induce relaxations in W_P, also reflected as oscillations in W_{turb}.

In order to better quantify what is going on, we will use several proxy functions. In particular, we monitor $W_P \propto \int_0^1 |P|^2 \, dxdy$ and $W_{\text{turb}} \propto \int_0^1 |n|^2 + |\phi|^2 \, dxdy$. The first one represents the energy stored in the background; the second, the energy in the turbulence. In addition, we use $\delta W_{\text{turb}} / \langle W_{\text{turb}} \rangle_t$ and $\delta W_P / \langle W_P \rangle_t$ where $(\delta W_{\text{turb}})^2 = \left\langle (W_{\text{turb}} - \langle W_{\text{turb}} \rangle_t)^2 \right\rangle_t$ and $(\delta W_P)^2 = \left\langle (W_P - \langle W_P \rangle_t)^2 \right\rangle_t$ to respectively measure the burstiness (or activity) of the turbulence and of the profile modification processes. Here, $\langle \cdot \rangle_s$ means average over s. Typically, an steady-state means that both $W_P \sim$ constant and $W_{\text{turb}} \sim$ constant. In fixed-gradient simulations, $\delta W_P / \langle W_P \rangle_t = 0$, whilst the value of $\delta W_{\text{turb}} / \langle W_{\text{turb}} \rangle_t$ increases with the importance of turbulence-induced transport. In simulations where profiles are evolved, $\delta W_P / \langle W_P \rangle_t > 0$, being small in cases in which there is scarce profile modification (for instance, in supramarginal cases where profile stay well above threshold everywhere), and large when profile modification is intense (as in near-marginal regimes).

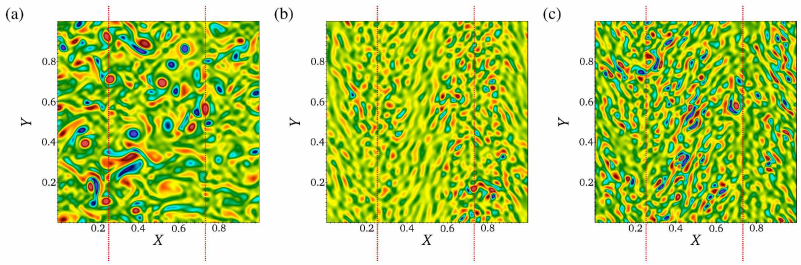

Figure 3.6: Vorticity $\nabla^2\phi$ for three values of Φ_0 are shown: (a) $\Phi_0 = 0.0$, (b) $\Phi_0 = 0.6$, and (c) $\Phi_0 = 1.0$. Radially elongated structures corresponding to radial relaxations are more prominent for $\Phi_0 = 0.0$ in (a) than when the external flow produces a shearing effect in (b) for $\Phi_0 = 0.6$. Turbulence suppression is also prominent in (b). At a larger $\Phi_0 = 1.0$, individual eddies return in (c). Dashed red lines denote the source at $x_{\text{source}} = 0.25$ and the sink at $x_{\text{sink}} = 0.75$.

Fig. 3.5 shows the time traces of some of these functions for several flux-driven simulations with externally-applied sheared flows of varying amplitude. As it is easily seen, the steady state is reached for times $t\Omega_i > 200 - 300$. Several other conclusions can be drawn from these traces. First, the saturated value of W_{turb} decreases with a non-zero Φ_0, which reflects the turbulence suppression carried out by the externally-driven flow (for instance, $W_{\text{turb}}(\Phi_0 = 0.4)/W_{\text{turb}}(\Phi_0 = 0.0) \simeq 0.3$, which corresponds to a reduction of turbulent energy by about 70%). This is also evident in Fig. 3.6, that shows the vorticity spatial field, $\nabla^2\phi$, for several of the simulations. Clearly, smaller vortical structures are present when comparing frames (a) ($\Phi_0 = 0.0$) and (b) ($\Phi_0 = 0.6$), as a result of the radial decorrelation felt by the turbulent eddies in the radial shear of the imposed flow. Corresponding to the decrease in W_{turb} for $\Phi_0 > 0.4$, transport becomes inhibited in the cross-flow direction, which steepens the local gradients (as revealed by the increasing ratios $W_P(\Phi_0 = 0.4)/W_P(\Phi_0 = 0.0) \simeq 8.8$, or $W_P(\Phi_0 = 1.0)/W_P(\Phi_0 = 0.0) \simeq 48$). There is also a significant oscillation observed in the time traces of energy for larger external amplitudes $\Phi_0 \geq 0.6$. The reason is that, as the cross-flow (i.e., radial) transport decreases for increasing Φ_0, the free energy in the gradients also increases, which in turn increases the turbulence until it can overcome the sheared flow. Also in response to the increase in the free energy, vortices start to become more prominent at larger flow amplitudes $\Phi_0 \geq 0.6$ (Fig. 3.6 (c)) since vortices can transport more material due to self-trapping[12,31]. The background energy W_P also reflects the bursts of fluctuation-induced transport corresponding to the oscillations in W_{turb}. These oscillations are reminiscent to the radial relaxation events induced by a fixed critical gradient ($\Phi_0 = 0.0$). With an externally driven sheared flow, the threshold is instead established by the balance between the sheared flow and the growth rates that are determined by the local gradients. When the local gradient is below this set threshold value, the sheared flow effectively reduces the turbulence. But, when the local gradient exceeds the threshold value, the turbulence relaxes the excess free energy. As a result, a similar turbulent relaxation is naturally established in a flux-driven system with

an external sheared flow.

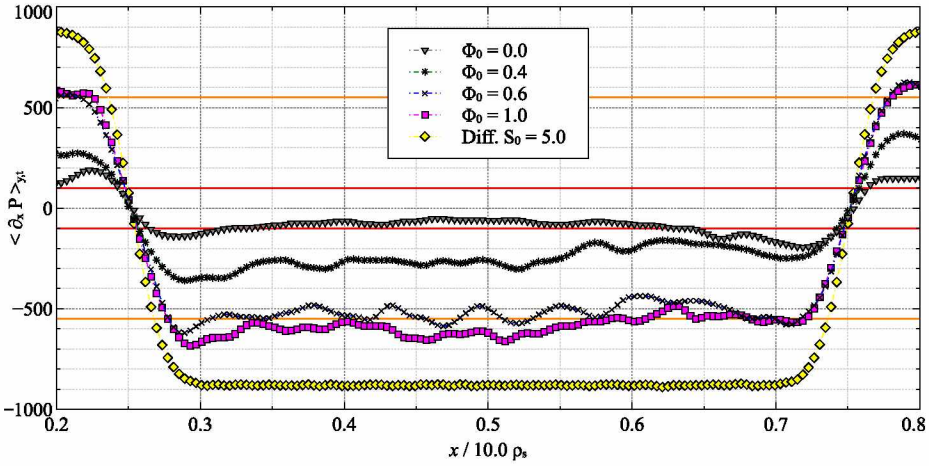

Figure 3.7: Time and poloidal averaged background gradient profiles for varying amplitudes of the externally-imposed radially-sheared poloidal flow. Red lines correspond to the critical gradient parameter used, $L_{c,P,x}^{-1} = 1$. Orange lines denote the approximate saturated gradient established at sufficiently large external flows ($\Phi_0 > 0.6$) around $L_{P,x}^{-1} = 5.5$. The source is located at $x_{\text{source}} = 0.25$, and the sink is at $x_{\text{sink}} = 0.75$

The impact of the externally-imposed radially-sheared poloidal flow on the background profile P is shown in Fig. 3.7, in which the time and poloidal averaged radial gradient of the background profile, $\langle \partial_x P \rangle_{y,t}$, can be seen. The diffusion dominated profile is obtained by solving Eq. 3.1 for P without the advection term $\boldsymbol{u} \cdot \boldsymbol{\nabla} P$ for a constant injection rate $S_0 = 5$. The resulting average profile has an almost constant slope between source and sink, determined by S_0. For the base case (i.e., the one with $\Phi_0 = 0.0$), the average gradient profile (shown with down triangles) sits near marginality as previously stated. The main consequence of the externally-imposed flow is, as seen clearly in Fig. 3.7, to increase the average slope which becomes, on average, supermarginal, although still less than the diffusive profile, implying that a significant amount of radial transport still goes through the turbulent channel. This is a result of the combination of the inhibition of cross-flow transport carried out by the external flow and the flow-driven instability that triggers the turbulence. The external sheared flow is another source of free energy that can induce turbulence. In consequence, the slope does not increase without bound. Instead, it saturates due to the external flow-induced instability at a new level (marked in orange in Fig. 3.7) that corresponds to approximately $L_{P,x}^{-1} \simeq 5.5$, that corresponds to the establishment of a new balance between the turbulence driven at that value of the gradient and the action of the externally-imposed sheared flow.

We have also probed the changes in the nature of transport caused by the externally-induced sheared flows by calculating the fractional exponent H, both in the radial and poloidal directions. The tracer rescaled range obtained for several of the simulations are shown in Fig. 3.8, both for the radial and poloidal directions. The obtained exponents are

shown, as a function of Φ_0, in Fig. 3.9. Similarly to the case with fixed-gradients, the region for timescales $\tau\Omega_i < 1$ represents the self-correlation of transport events, and is thus not interesting for long-term dynamics. For $\tau\Omega_i \gg 1$, one can see that the superdiffusive radial transport characteristic of the no-flow case ($\Phi_0 = 0.0$) transitions to subdiffusive at finite flow intensities. It is interesting to see that, for all intensities, the value of the exponent is very similar and around $H(v_x) \sim 0.4$. This suggests that the overall radial transport dynamics are relatively insensitive to the establishment of the limiting gradient imposed through the external sheared flow, as we discussed previously (Fig. 3.10). Similarly, the mildly subdiffusive poloidal transport of the no-flow case becomes strongly superdiffusive. Again, the over-estimation for $H > 1$ is due to the presence of long-lived eddies generated by the flow-driven instability. However, the deviation is less than the fixed-gradient set up since the instability can trigger relaxations in the profile, which, in turn, decreases the free energy in the gradient.

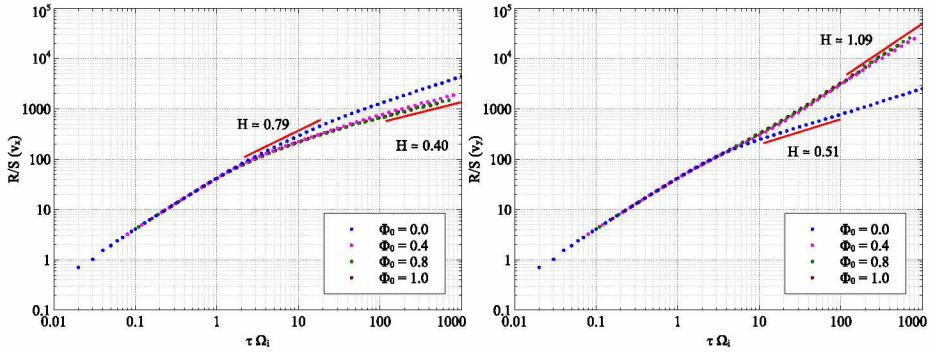

Figure 3.8: Transport exponents estimated from the R/S analysis with varying external flow amplitude Φ_0 with a flux-driven background profile also show subdiffusion in the cross-flow direction but superdiffusion in the poloidal direction.

We show a last glimpse into the change in the radial dynamics caused by the externally-imposed flow by looking at the evolution of the poloidal averaged radial flux $\langle\Gamma_{P,x}\rangle_y$, that can be calculated using $\Gamma_{P,x} = Pv_x = -P\partial_y\phi$ where $P > 0$ always (thus, the sign of the flux follows that of the flow.) Fig. 3.10 shows the temporal evolution of these fluxes for increasing external flow amplitudes, from $\Phi_0 = 0.0$ (frame (a)), to $\Phi_0 = 1.0$ (frame (d)). In the no-flow case, diagonal features are apparent that reflect the ongoing coherent transport events (i.e., avalanches) that propagate down (and sometimes up) the near-marginal gradient, reminiscent of what one observes in critical-threshold sandpile models[8]. When the externally-imposed flow is present, correlated transport events still event but are increasingly more scarce. Diagonal features in $\langle\Gamma_{P,x}\rangle_y$ are now interspersed without correlated events. This shows the impact of an external sheared flow on the cross-flow transport. Corresponding to the reduction in correlated flux events, the $\langle\partial_x P\rangle_{y,t}$ also becomes steeper on average as shown in Fig. 3.7. With a larger external flow amplitude of $\Phi_0 = 0.6$, $\langle\Gamma_{P,x}\rangle_y$ now shows regions of suppressed flux with down-gradient activity lasting

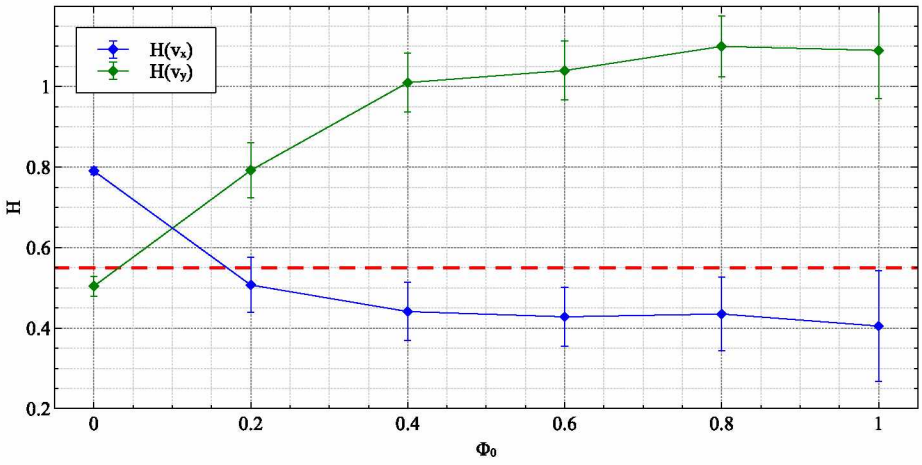

Figure 3.9: Transport exponents with varying external flow amplitude Φ_0 with a flux-driven background profile also show subdiffusion in the cross-flow direction but superdiffusion in the poloidal direction. Dashed red line denotes the diffusive limit for R/S analysis.

about $t\Omega_i \sim 100.0$ (Fig. 3.10 (c)). At $\Phi_0 = 1.0$ in Fig. 3.10 (d), the duration of flux events $\langle \Gamma_{P,x} \rangle_y$ becomes somewhat shorter than $\Phi_0 = 0.6$ to approximately $t\Omega_i \sim 50.0$. Down-gradient correlated flux events become relatively suppressed with larger enough external flow interspersed with bursts of correlated events. Bursts in the radial flux occur due to an additional critical gradient element naturally imposed by the external sheared flow. In this regime, the local non-zero critical gradient parameter $L_{c,P,x}^{-1} = 1$ is insufficient to decorrelate the external poloidal sheared flow. However, a new limiting gradient is stablished at about $L_{c,P,x}^{-1} \simeq 5.5$ that weakly induces down-gradient transport. Once $\partial_x P$ is large enough to trigger a radial transport event, correlated radial transport temporarily overcomes the imposed sheared external flow. Although the gradient steepens, the values for $\langle \Gamma_{P,x} \rangle_y$ stays about the same, which means that the total time integrated poloidal averaged flux becomes smaller. Smaller and lesser fluxes down-gradient reduces the transport from the sink to the source region with increasing Φ_0.

3.7 Conclusions

In this work, we have explored the possibility of using externally-induced radially-sheared poloidal flows to tune at will the dynamics of radial turbulent transport in realistic, flux-driven conditions. Several lessons have been learnt. First, that one can successfully use externally-imposed flows with sufficient amount of radial shear to decorrelate radial transport coherent events and make the nature of transport become diffusive or subdiffusive, even in cases of near-marginal turbulence that drive strong superdiffusive transport. The ability to use these flows, however, has been shown to be limited by the triggering of flow-driven instabilities, of the Kelvin-Helmholtz type, that are excited when the radial shear in the flow becomes too large. The appearance of these instabilities does not impede, however,

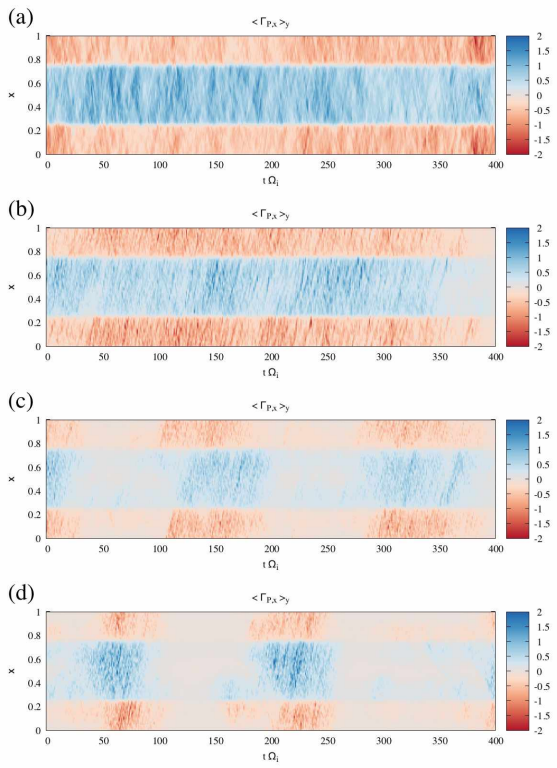

Figure 3.10: Poloidal averaged radial flux $\langle \Gamma_{P,x} \rangle_y$ with increasing values of the external flow amplitude Φ_0: (a) $\Phi_0 = 0.0$, (b) $\Phi_0 = 0.4$, (c) $\Phi_0 = 0.6$, and (d) $\Phi_0 = 1.0$. Increasing Φ_0 suppresses $\langle \Gamma_{P,x} \rangle_y$ for $\Phi_0 < 0.6$ and becomes less frequent.

the reaching of a steady-state in which radial transport retains its subdiffusive character.

In addition, the analysis presented here illustrates the fact, once more, that the proper study of turbulent transport in near-marginal conditions necessitates of a proper evolution of background profiles simultaneously with the turbulence, and of a wider framework to describe the overall transport dynamics that goes beyond the usual diffusive paradigm.

3.8 Acknowledgements

This work was supported in by US DOE contract number DE-FG02-04ER54741 with UAF and in part by a grant of HPC resources from the Arctic Region Supercomputing Center at the University of Alaska Fairbanks.

3.9 References

[1] P. W. Terry, Rev. Mod. Phys. **72**, 109 (2000).

[2] P. H. Diamond, S.-I. Itoh, K. Itoh, and T. S. Hahm, Plasma Phys. and Control. Fusion

47, R35 (2005).

[3] U. Stroth, P. Manz, and M. Ramisch, Plasma Phys. Control. Fusion **53**, 024006 (2011).

[4] R. Sánchez, D. E. Newman, J.-N. Leboeuf, V. K. Decyk, and B. A. Carreras, Phys. Rev. Lett. **101**, 205002 (2008).

[5] R. Sánchez, D. E. Newman, J.-N. Leboeuf, and V. K. Decyk, Plasma Phys. Control. Fusion **53**, 074018 (2011).

[6] P. Diamond and T. Hahm, Phys. Plasmas **2**, 3640 (1995).

[7] B. A. Carreras, D. Newman, V. E. Lynch, and P. H. Diamond, Phys. Plasmas **3**, 2903 (1996).

[8] D. E. Newman, B. A. Carreras, and P. H. Diamond, Phys. Lett. A **218**, 58 (1996).

[9] R. Sánchez and D. E. Newman, Plasma Phys. Control. Fusion **57**, 123002 (2015).

[10] D. Ogata, D. Newman, and R. Sánchez, Phys. Plasmas (submitted, 2016) .

[11] R. Sánchez, B. A. Carreras, D. E. Newman, V. E. Lynch, and B. P. van Milligen, Phys. Rev. E **74**, 016305 (2006).

[12] W. Horton, Rev. Mod. Phys. **71**, 735 (1999).

[13] D. E. Newman, P. W. Terry, P. H. Diamond, and Y. Liang, Phys. Fluids B **5**, 1140 (1993).

[14] W. Horton, Phys. Fluids **29**, 1491 (1986).

[15] Y. Liang, P. H. Diamond, X. Wang, D. E. Newman, and P. W. Terry, Phys. Fluids B **5**, 1128 (1993).

[16] D. E. Newman, P. W. Terry, P. H. Diamond, Y. Liang, G. G. Craddock, A. E. Koniges, and J. A. Crottinger, Phys. Plasmas **1**, 1592 (1994).

[17] R. Numata, R. Ball, and R. L. Dewar, Phys. Plasmas **14**, 102312 (2007), 10.1063/1.2796106.

[18] P. H. Diamond, Y.-M. Liang, B. A. Carreras, and P. W. Terry, Phys. Rev. Lett. **72**, 2565 (1994).

[19] V. Naulin, K. H. Spatschek, S. Musher, and L. I. Piterbarg, Phys. Plasmas **2**, 2640 (1995).

[20] A. C. Hindmarsh, P. N. Brown, K. E. Grant, S. L. Lee, R. Serban, D. E. Shumaker, and C. S. Woodward, ACM Trans. Math. Softw. **31**, 363 (2005).

[21] R. Metzler and J. Klafter, Phys. Reports **339**, 1 (2000).

[22] G. Zaslavsky, Phys. Rep. **371**, 461 (2002).

[23] I. Podlubny, *Fractional Differential Equations* (Academic Press, San Diego, CA, 1999).

[24] E. Montroll and H. Scher, J. Stat. Phys. **9**, 101 (1973).

[25] R. Sánchez, B. A. Carreras, and B. P. van Milligen, Phys. Rev. E **71**, 011111 (2005).

[26] I. Calvo, R. Sánchez, and B. A. Carreras, J. Phys. A: Math. Theor. **42**, 055003 (2009).

[27] H. E. Hurst, Trans. Amer. Soc. Civil Eng. **116**, 770 (1951).

[28] B. A. Carreras, B. P. van Milligen, M. A. Pedrosa, R. Balbín, C. Hidalgo, D. E. Newman, E. Sánchez, M. Frances, I. García-Cortés, J. Bleuel, M. Endler, C. Riccardi, S. Davies, G. F. Matthews, E. Martines, V. Antoni, A. Latten, and T. Klinger, Phys. Plasmas **5**, 3632 (1998).

[29] V. Naulin and K. H. Spatschek, Phys. Rev. E **55**, 5883 (1997).

[30] G. Manfredi and R. O. Dendy, Phys. Plasmas **4**, 628 (1997).

[31] V. Naulin, A. H. Nielsen, and J. J. Rasmussen, Physics of Plasmas **6**, 4575 (1999).

[32] S. V. Annibaldi, G. Manfredi, R. O. Dendy, and L. O. Drury, Plasma Phys. Control. Fusion **42**, L13 (2000).

[33] R. Basu, T. Jessen, V. Naulin, and J. J. Rasmussen, Phys. Plasmas **10**, 2696 (2003).

[34] A. Hasegawa and M. Wakatani, Phys. Rev. Lett. **50**, 682 (1983).

[35] S. Chandrasekhar, *Hydrodynamic and Hydromagnetic Stability* (Oxford University Press, 1961).

[36] J. M. Dewhurst, B. Hnat, and R. O. Dendy, Plasma Phys. Control. Fusion **52**, 025004 (2010).

Chapter 4 Using a passive scalar to characterize turbulent transport[1]

4.1 Abstract

From a theoretical and modelling point of view, following Lagrangian trajectories is the most straight forward way to characterize the transport dynamics. In real plasmas, following Lagrangian trajectories is difficult or impossible. Using a blob of passive scalar (a tracer blob) allows a quasi-Lagrangian view of the dynamics. Using a simple two-dimensional electrostatic plasma turbulence model, this work demonstrates that the evolution of the tracers and the passive scalar field is equivalent between these two fluid transport viewpoints. When both the tracers and the passive scalar evolve in tandem and closely resemble stable distributions, namely Gaussian distributions, the underlying turbulent transport character can be recovered from the temporal scaling of the second moments of both. This local transport approach corroborates the use of passive scalar as a turbulent transport measurement. The correspondence between the local transport character and the underlying transport is quantified for the different transport regimes ranging from subdiffusive to superdiffusive.

4.2 Introduction

Turbulence, and turbulent transport, has long been known to be an important process for efficient mixing. Under fully developed turbulence, different quantities can be transported much faster than molecular diffusion. This process has been an ongoing topic of interest particularly in context of fusion plasmas. Due to the conditions of fusion plasmas, diagnostics to measure plasma parameters are often challenging due in part to the necessary temperature and density requirements. By design, and unlike in neutral fluids, high density and temperature plasmas for nuclear fusion do not provide an ideal scenario for diagnostics. Hence, strategies and methodologies are developed in order to extract important plasma parameters. Diagnostic strategies can be segregated by their perturbative effects on the plasma, which can range from passive to predominantly invasive. This type of categorization is highly dependent on the plasma's operating regime. Most diagnostics are in an Eulerian (laboratory) frame though a few attempt a Lagrangian (plasma) frame. The Lagrangian and Eulerian frames have been fundamental viewpoints in understanding transport in turbulent medium. Transport diagnostics based on each viewpoint provide different but potentially equivalent insights into the turbulent transport process.

Transport diagnostics can be grouped into two main categories according to flow

[1]D. Ogata, D. E. Newman, and R. Sánchez. Using a passive scalar to characterize turbulent transport. Submitted to Physics of Plasmas (POP51266).

measurement strategies: Eulerian and Lagrangian[1]. The Eulerian measurement extracts velocities from a fixed frame (such as the laboratory frame), which is convenient for experimental measurements. For instance, a grid of temperature sensors is capable of monitoring temperatures at various fixed locations simultaneously. On the other hand, the Lagrangian measurement follows the flow, which gives a more intuitive sense of transport and is more appropriate in other circumstances such as the dispersion of localized sources. For example, injection of tracer particles or a colored dye in a transparent fluid or a smoke plume provides information on the Lagrangian flow trajectory. In general, analytical transport theory relies heavily on the Lagrangian viewpoint[2]. Although the full Eulerian and Lagrangian viewpoints are equivalent, analytically translation between them exist only in special circumstances[3].

In actual experiments, global transport measurements are often constrained both spatially and temporally, which restricts diagnostics being able to make local transport measurements more accurately than global measurements. There are often uncertainties as to whether the local transport measurements coincide with the underlying global transport measurements. This work aims to demonstrate additional requirements for local transport measurements to coincide with the underlying transport character by comparing and contrasting the measurements from both the Lagrangian and quasi-Lagrangian viewpoints. The quasi-Lagrangian frame is based on measurements done in the Eulerian frame, which is convenient in the laboratory frame. Simulations can provide an ideal testbed to explore the equivalence between the Lagrangian and quasi-Lagrangian frame in terms of relating the local and underlying transport measurement within different transport regimes. Only a single realization of the turbulent state with each transport regime is used to simulate the analysis process equivalent to a single experimental turbulent run. The results validate the notion that the transport characterization can be done through both the Lagrangian and quasi-Lagrangian viewpoints.

In this work, the measurement in the quasi-Lagrangian frame is represented by a passive scalar, which is a non-interacting field advected by the turbulent flow[4]. As the passive scalar spreads, it expands in size but the perturbation decreases in amplitude. The correlation between fluid elements becomes weaker as the cloud spreads. The fluctuations are transferred towards smaller scales with a constant flux down to the dissipative scale. At the dissipative scale, molecular diffusion absorbs the incoming flux and establishes the equilibrium between energy input and the dissipation. According to this picture, velocity correlations between fluid parcels determine the overall transport process.

The Lagrangian frame is represented by a tracer trajectory that tracks a trajectory of the flow with the benefit of a time history. A tracer is a massless marker of a fluid parcel that is advected by the turbulent flow. The advantage of using the Lagrangian frame in understanding the passive scalar mixing is that certain types of Lagrangian characteristics are conserved on average, which then determines S_n[5]. A note of caution, Lagrangian

tracers tend to cluster around boundaries, which can cause a false weighting of information about the flow[3].

The following sections are arranged as follows: Sec. 4.3 describes a numerical flux-driven setup of drift-wave turbulence model; the two methods of transport diagnostics used to characterize the nature of the turbulent transport in both the Lagrangian and quasi-Lagrangian frames will be explained in Sec. 4.4. In particular, the meaning of the transport exponents α, β, and H, will be explained. The results from the local transport analysis in terms of the transport exponents are divided into two sections in Sec. 4.5. First, in order to connect the results with previous work, Sec. 4.5.1 presents the characteristics of local transport in comparison with the underlying transport in cases where the turbulence is evolved with a fixed-profile. Secondly, in Sec. 4.5.2, similar cases are re-analyzed but using instead a flux-driven setup in which proper background evolution is enabled. Finally, Sec. 4.6 concludes the paper by summarizing the possible implications of using the quasi-Lagrangian frame to characterize turbulent transport.

4.3 Numerical model

The model that will be used in this paper is based on a collisional drift-wave model for plasma turbulence[6]. The model is formulated in a doubly-periodic slab geometry in a constant perpendicular magnetic field with $x \in [0,1]$ as the radial direction and $y \in [0,1]$ as the poloidal direction. The governing evolution equations for this electrostatic model are:

$$\begin{aligned} \frac{d}{dt}\left[\left(1-\sqrt{\epsilon}-\rho_s^2\nabla_\perp^2\right)\phi\right] &= -\left[1-\sqrt{\epsilon}\,\xi\right]C_s\rho_s R_{nl}\left(n,\phi,P\right)+\nu\sqrt{\epsilon}\left(n-\phi\right)-\mu\rho_s^2\nabla_\perp^4\phi \\ \frac{dn}{dt} &= \xi C_s\rho_s R_{nl}\left(n,\phi,P\right)+\nu_{eff}\left(\phi-n\right) \\ \frac{dP}{dt} &= S+D_P\nabla_\perp^2 P \end{aligned} \tag{4.1}$$

where n is the fluctuating density, ϕ is the fluctuating potential, and P is the background profile. The first two equations are similar to the standard DTEM model[6,7], except in that they include an additional dependence on the background profile P via the nonlinear function $R_{nl}\left(n,\phi,P\right)$, that will be discussed later. The third equation defines the evolution of the background profile P in the presence of an external drive S. The standard definitions of the coefficients appearing in the model are: $\rho_s = \left(k_B T_e/eB\right)/C_s$ is the ion gyroradius, $C_s = \sqrt{k_B T_e/m_i}$ is the ion sound speed, $\xi = \left(1+\alpha\eta_e\right)$ where $\eta_e = \partial\left(\ln T\right)/\partial\left(\ln n\right) = 2$ and $\alpha = 3/2$ for the instability criterion for destabilization of DTEM modes by electron collision[6], ϵ is the inverse aspect-ratio that gives the trapped electron fraction, μ is the viscosity coefficient, ν is the electron collisional relaxation due to trapping and detrapping, and $\nu_{eff} = \nu/\sqrt{\epsilon}$. The trapped electron fraction ϵ affects the instability of the drift-waves in relations to the regime of collisionality ν[6].

In the third equation in Eq. 4.1, the evolution of the background profile, P, is

determined by the source term S, a classical diffusion coefficient D_P, and the local flux $\mathbf{\Gamma}_P = \boldsymbol{u}P$, where $\boldsymbol{u} = C_s\rho_s\hat{\boldsymbol{z}} \times \boldsymbol{\nabla}\phi$. The inclusion of an evolution equation for P makes the simulation flux-driven, which means that $\mathbf{\Gamma}_P$ adapts itself to balance the incoming net drive. This drive is constructed as the sum of a Gaussian of a fixed-width, $G_w(x)$, and prescribed positive height, S_0, located at $x_{\text{source}} = 0.25$ and another Gaussian equal in magnitude but of reversed sign at $x_{\text{sink}} = 0.75$:

$$S(x) = S_0 \left[G_w(x - x_{\text{source}}) - G_w(x - x_{\text{sink}}) \right]. \tag{4.2}$$

$S_0[= 5]$ represents the injection rate for all flux-driven cases in this paper.

An incompressible externally-imposed flow has also been introduced in the model through the advective derivative operator, $d/dt = \partial_t + (\boldsymbol{u}_0 + \boldsymbol{u}) \cdot \boldsymbol{\nabla}$. The external flow is defined as $\boldsymbol{u}_0 = C_s\rho_s\hat{\boldsymbol{z}} \times \boldsymbol{\nabla}\phi_0$ where ϕ_0 is an externally defined electrostatic potential with a radial profile given by $\phi_0 = \Phi_0 \cos(2\pi x)$. In this way, the velocity profile is $\boldsymbol{u}_{\text{ext}} \sim \Phi_0 \sin(2\pi x)\,\hat{\boldsymbol{y}}$, reaching its maximum shear at $x = 0.5$.

Next, we discuss the nonlinear function $R_{nl}(n, \phi, P)$, that includes the threshold condition that introduces the possibility of profiles being near-marginal. The term is defined as:

$$\begin{aligned} R_{nl}(n, \phi, P) = {} & f_d \left[g\left(L^{-1}_{\langle P \rangle_y, x} \right) L^{-1}_{\langle P \rangle_y, x} \left(-\frac{\partial \phi}{\partial y} \right) \right] \\ & + (1 - f_d) \left[g\left(L^{-1}_{P,y} \right) L^{-1}_{P,y} \frac{\partial \phi}{\partial x} + g\left(L^{-1}_{P,x} \right) L^{-1}_{P,x} \frac{\partial \phi}{\partial y} \right] \end{aligned} \tag{4.3}$$

Its meaning is explained in depth in the companion paper[8], but we repeat the fundamentals here for clarity. The main ingredient is the function $g(L^{-1}_{s,z})$, defined as:

$$\begin{aligned} g(L^{-1}_{s,z}) = \frac{1}{2} \Big[& 2 + \tanh\left(\kappa \left(L^{-1}_{s,z} - L^{-1}_{c,s,z} \right) \right) - \\ & - \tanh\left(\kappa \left(L^{-1}_{s,z} + L^{-1}_{c,s,z} \right) \right) \Big] \end{aligned} \tag{4.4}$$

where $L^{-1}_{c,s,z}$ is a prescribed critical value for the gradient of field s in the z direction, $\kappa[= 20]$ prescribes the steepness of the hyperbolic tangent function, and $L^{-1}_{s,z} := \partial_z s / s_0$ is the local gradient (s_0 is an arbitrary normalization constant). The main point is that $g(L_{s,z})$ vanishes if $L^{-1}_{s,z} < L^{-1}_{c,s,z}$, and is equal to one if $L^{-1}_{s,z} > L^{-1}_{c,s,z}$, which introduces a threshold for the excitation of turbulence in the problem. When the proper conditions are met, the combination of the local critical gradient and the flux-driven setup permits the system to stay near-marginality. However, other thresholds are possible in Eq. 4.3 weighted by the $f_d \in (0, 1)$ factor. The first line introduces a threshold on the radial gradient of the poloidally averaged background profile. The second line presents two thresholds; one on the local radial gradient of the background profile, and another on the local poloidal gradient. This combination has been introduced to make possible the study of the importance of a partial parallel equilibration across magnetic surfaces[8], which might be an issue in tokamaks,

particularly closer to the edge where dynamics are more collisional, or in the neighbourhood of rational surfaces. If $f_d = 1$, it is assumed that any inhomogeneities along y are quickly equilibrated, and that only the poloidally-averaged background profile (denoted by $\langle\cdot\rangle_y$) matters in terms of providing the turbulence with free energy. On the other hand, $f_d = 0$ means that there is no parallel equilibration whatsoever, and only local gradients provide the turbulence with free energy. The value for f_d is set to $f_d = 0$ for all flux-driven cases in the paper.

Fixed background gradient cases are accessible by solving Eq. 4.1 with $dP/dt = 0$, set $f_d = 1$, impose $g\left(L^{-1}_{\langle P\rangle_y,x}\right) = 1$ and, finally, fix a value for the background gradient, $L^{-1}_{\langle P\rangle_y,x} = \partial_x \langle P\rangle_y / P_0$. With these choices, the nonlinear function immediately reduces to $R_{nl}(n,\phi,P) = L^{-1}_{\langle P\rangle_y,x}\partial_y\phi$ such that $C_s\rho_s R_{nl}(n,\phi,P) = V_D\partial_y\phi$ where $V_D = C_s\rho_s/L_{\langle P\rangle_y,x} = (k_B T_e/eB)\, L^{-1}_{\langle P\rangle_y,x}$. This is a common form for the diamagnetic drift.

The numerical scheme used to solve Eq. 4.1 is solved on a doubly-periodic grid of 256×256 nodes in the Fourier space spanned by k_x and k_y. A standard pseudo-spectral scheme, properly modified to avoid any aliasing problems, is used to deal with the nonlinearities. The temporal integration is done implicitly, using a scaled preconditioned Generalized Minimal Residual (GMRES) solver that combines well-established integration schemes[9]. Parallelization is achieved by using MPI and by taking advantage of parallel Fast Fourier Transform (FFT) routines, as well as other parallel numerical integration routines. All simulations have been initialized with random phases for all Fourier harmonics, and they have been advanced in time until a suitable quasi-steady state, with approximate balance between drive and losses, is established.

4.4 Local transport characterization

There are many ways to define the characterize the nature of transport in a system[10,11]. Traditionally, transport of any conserved quantity P is termed diffusive if it can be described by an equation of the type,

$$\frac{\partial P}{\partial t} = \chi \frac{\partial^2 P}{\partial x^2}, \tag{4.5}$$

where χ is a transport coefficient. This equation implies that the local flux of the transported quantity is $\Gamma_P = -\chi\partial_x P$, thus pointing down the gradient, what is known as Fick's law. By extension, some authors define nondiffusive transport as any situation in which the evolution of P follows instead a transport equation of the form:

$$\frac{\partial^\beta f}{\partial t^\beta} = \chi_{\alpha,\beta} \frac{\partial^\alpha f}{\partial |x|^\alpha}. \tag{4.6}$$

for $x \in \mathbb{R}$ and $t \in \mathbb{R}^+$ where $\chi_{\alpha,\beta}$ is a scaling constant. The exponent ranges are $\alpha \in (0,2)$ and $\beta \in (0,1)$. This equation is a generalization of the more usual classical diffusive equation, where $\beta = 1$ and $\alpha = 2$, based on fractional derivatives. These fractional operators provide a smooth interpolation in between integer derivatives[12]. In contrast to the integer derivatives, that are local operators, fractional derivatives are integro-differential operators that are non-local in their variable of definition (either space or time). Thus, the type of transport that can be captured by Eq. 4.6 may be non-local (if $0 < \alpha < 2$) and non-Markovian (if $0 < \beta < 1$). The exponent of interest to us, however, is $H := \beta/\alpha$. Transport is called superdiffusive if $H > 1/2$, diffusive if $H = 1/2$ and subdiffusive if $H < 1/2$. The reason for this name is that any population of particles, whose transport is governed by Eq. 4.6 and that are initially localized in x, will spread faster (if $H > 1/2$) or slower (if $H < 1/2$) than its diffusive counterpart.

The transport exponents α, β, and H can be estimated in many ways. A very useful way is to take advantage of the fact that transport equations like Eq. 4.5 and 4.6 can be derived from "microscopic considerations". It is well known that the classical diffusion equation can be obtained as the long-term, long-distance limit of either a continuous time random walk (CTRW) in which particles are advanced with Gaussian-distributed step-sizes, separated by exponentially-distributed waiting times. Also, the diffusion equation can be obtained from the "microscopic" Langevin equation, that expresses the position of each particle being transported as:

$$x(t) = x_0 + \int_0^t \xi(t')dt'. \tag{4.7}$$

In the same long-term, long-distance limit, by assuming a random forcing ξ with Gaussian statistics and zero time correlation except at zero lag (i.e., lack of memory along Lagrangian trajectories), the classical diffusion equation is easily recovered. Similarly, the fractional transport equation can be derived from a CTRW[13] in which steps are distributed according to a symmetric α-Lévy distribution with tail index $\alpha \in (0,2)$ and waiting-times distributed according to an extremal β-Lévy distribution with tail index $\beta \in (0,1)$[10,11,14]. It can also be derived as the long-term, long-distance limit of the generalized Langevin equation[15,16]

$$x(t) = x_0 + \frac{1}{\Gamma(H - 1/\alpha + 1)} \int_0^t (t - t')^{H-1/\alpha} \xi_\alpha(t')dt', \tag{4.8}$$

that assumes a non-random forcing with symmetric α-Lévy statistics and a correlation in time characterized with a Hurst exponent $H \in (0,1)$[17]. H is also the self-similarity exponent of the trajectory, $x(t)$. In this case, the resulting temporal exponent in the transport equation Eq. 4.6 is given by $\beta = \alpha H$.

The connections of Eq. 4.6 with these "microscopic formulations" can be exploited to come up with methods to determine the fractional exponents in practical situations, and

thus to provide ways to characterize the nature of transport. Among the different methods available, in this paper we will focus on two methods that exploits the connection with Eq. 4.8 to determine α and β. The first method exploits the connection between the solutions of Eq. 4.6 with the time scaling of distribution moments. The second method uses the propagator or the Green's function of Eq. 4.6 to determine the fractional exponents. The propagator is known in Laplace-Fourier space to be $P(k,s) = s^{\alpha H-1}/\left(\chi^{\alpha}_{\alpha,\beta}\,|k|^{\alpha} + s^{\alpha H}\right)$ where s is the Laplace transformed variable, and k is the transformed Fourier parameter. These two methods will be applied to both the Lagrangian viewpoint and the quasi-Lagrangian frame in connection with the Eulerian viewpoint, which will be discussed further.

The Lagrangian viewpoint requires following the trajectories of massless tracer particles as they are advected by the turbulence. That is, to integrate in time their velocity, that is given by,

$$\dot{\boldsymbol{R}}(t) = \boldsymbol{E} \times \boldsymbol{B}/B^2 = C_s \rho_s \hat{\boldsymbol{z}} \times \boldsymbol{\nabla}_{\perp}\phi, \quad \boldsymbol{R}(t_0) = \boldsymbol{r_0}, \tag{4.9}$$

since the advection in our model is done by the turbulent fluctuating $E \times B$ velocity.

On the other hand, the Eulerian viewpoint leading to the analysis in the quasi-Lagrangian frame follows the evolution of a passive scalar given by:

$$\frac{\partial \Theta}{\partial t} + \boldsymbol{u} \cdot \boldsymbol{\nabla}\Theta = \kappa \nabla^2 \Theta + f_{\Theta}(\boldsymbol{r}, t) \tag{4.10}$$

where κ is the scalar diffusivity and $f_{\Theta}(\boldsymbol{r}, t)$ is a source of scalar fluctuations. The passive scalar field can be thought of as an ensemble average over all Lagrangian trajectories. The behavior of the scalar field is governed by both the transport by the combined advection and diffusion, and the mixing or the irreversible decay of fluctuations[2,3,18,19]. A scalar blob is stretched and rolled by the flow. Due to the incompressibility criterion $\boldsymbol{\nabla} \cdot \boldsymbol{u} = 0$, tendril structures form on progressively smaller scales. At these scales, dissipation becomes more efficient and mixing occurs more rapidly leading to the smoothening of gradients. The quantity $|\nabla\Theta|^2$ is amplified by the action of the strain along the path. Analytically, the field at time t is related to an earlier time t' through the propagator

$$\Theta\left(\boldsymbol{r}, t\right) = \int dt' \int d\boldsymbol{r}'\, P_{\Theta}\left(\boldsymbol{r}, t | \boldsymbol{r}', t'\right) f_{\Theta}\left(\boldsymbol{r}', t\right) \tag{4.11}$$

where the Green's function $P_{\Theta}\left(\boldsymbol{r}, t | \boldsymbol{r}', t'\right)$ represent the probability of trajectories leaving from $\boldsymbol{r}'$ at time t' and arriving at $\boldsymbol{r}$ at time time t[18]. This formulation is identical to the Langevin formulation of the general transport equation (Eq. 4.8).

In order to elucidate further the inherent equivalence between the Lagrangian and Eulerian viewpoint in the context of transport measurements, we determine the local transport character from the two methods mentioned above using both the tracers and the passive scalar. The local transport results are then compared to the overall transport character

obtained in companion papers[8,20] from a different method using the well-known R/S analysis[17]. The R/S analysis provides H, which is the correlation (or Hurst) exponent of the velocity series along trajectory as described by Eq. 4.8. Although tracers provide Lagrangian information, the equivalence of the flow between the two frames $\boldsymbol{U}(t) = \boldsymbol{u}(\boldsymbol{R}(\boldsymbol{r},t),t)$ is a fundamental relationship that permits the natural translation of Lagrangian viewpoint into the Eulerian frame through tracers[2,21].

In order to eliminate mean flow effects, the local transport analysis for both the tracers and the passive scalar is done in a quasi-Lagrangian frame[2] such that $\tilde{\zeta}(\boldsymbol{r},t) = \zeta(\boldsymbol{r}+\boldsymbol{R}(t|\boldsymbol{r}_0,0),t)$ where ζ represents either the distribution of the tracer cloud or the passive scalar field, the tilde represents the shifted origin frame, and $\boldsymbol{R}(t|\boldsymbol{r}_0,0),t)$ is the Lagrangian trajectory of the origin passing through $\boldsymbol{r}_0$ at time zero. The quasi-Lagrangian frame for the passive scalar has been used in the Kolmogorov's original 1941 theory[2,3]. The inherent importance of the Lagrangian frame was then transferred to Kraichnan's reformulation of the direct interaction approximation (DIA). With this shift, the transport character is quantified in a frame that moves with the fluid. This quasi-Lagrangian formulation follows the same evolution as the Eulerian frame with an advective term replaced by $[\tilde{\boldsymbol{u}}(\boldsymbol{r},t) - \tilde{\boldsymbol{u}}(\boldsymbol{0},t)]\cdot\nabla$ where $\tilde{\boldsymbol{u}}(\boldsymbol{0},t)$ represents the velocity of the origin. The analysis in this paper is performed in this reference frame instead of strictly in a pure Eulerian frame.

In order to compare the local transport from both the tracers and the passive scalar, we initialize the tracers together with the passive scalar with an equivalent initial Gaussian distribution. The passive scalar evolves according to Eq. 4.10 with $f_\Theta(\boldsymbol{r},t) = \Psi(\boldsymbol{r}-\boldsymbol{r}_0)\delta(t)$ where $\Psi(\boldsymbol{r}-\boldsymbol{r}_0)$ is a Gaussian distribution centered at $\boldsymbol{r}_0 = (0.5, 0.5)$. The width of the Gaussian puff is limited by the numerical resolution and the periodic boundary conditions. The direction of interest is the down-gradient transport that corresponds to the radial or x-direction. Hence, all the results will be focused primarily on the radial transport direction, which is also referred to as the cross-drift in fixed-gradient scenarios or cross-flow direction when there is an externally imposed poloidal sheared flow.

Our first comparison between the local transport characteristics from the Lagrangian and the quasi-Lagrangian viewpoint is by quantifying the spread of both the tracers and the passive scalar through the second moments of the distribution. The size of the tracer cloud is defined through the variance or the mean-square displacement of all N tracers using the definition $\sigma_{tr}^2(t) = \left\langle [x(t) - \langle x(t)\rangle]^2 \right\rangle_N$ where $x(t)$ is the radial position of a tracer at time t, $\langle x(t)\rangle$ is the mean position of the tracer cloud, and the angular brackets $\langle \ldots \rangle_N$ denotes the averaged over N tracers. The size of the passive scalar field is also defined by the second moment of the field as $\sigma_{ps}^2 = \int\int [x - x_c(t)]^2 \Theta(\boldsymbol{r},t)dxdy/M$ where the total mass is $M = \int\int \Theta(\boldsymbol{r},t)dxdy$. The center of mass of the passive scalar is then defined by the first moment of the passive scalar field $x_c(t) = \int\int x\Theta(\boldsymbol{r},t)dxdy/M$. We use the center of mass to track the passive scalar, which then allows a translation from the Eulerian frame into the quasi-Lagrangian frame. According to the general transport equation, the scaled Gaussian

propagator $G(x-x',t-t') \propto \exp\left[-(x-x')^2/\chi(t-t')^\beta\right]$ where χ is the diffusivity and β is the temporal scaling for an initially peaked distribution $\psi(x,t) = \psi_0\delta(x)\delta(t)$ yields a second moment of $\langle x^2\rangle = \int x^2\,dx\left[\int\int G(x'-x,t'-t)\,\psi(x',t')\,dx'dt'\right] \propto \chi t^\beta$. This means that the power-law scaling of the second moment $\sigma_{tr}^2 \sim t^{\beta_{tr}}$ and $\sigma_{ps}^2 \sim t^{\beta_{ps}}$ provide the temporal scaling for the transport process under the assumption that the spatial distribution is a Gaussian distribution. The scaled Gaussian propagator is the solution to Eq. 4.6 when $\alpha = 2$, which describes fractional Brownian motion (fBm)[22].

Our second method of comparison between the tracers and the passive scalar exploits the propagators of Eq. 4.6. The propagator fitting method uses the fractional Lévy motion (fLm) propagator, which is the generalization of the Langevin formalism (Eq. 4.8). The propagators used for the fLm method is the symmetric α-Lévy distribution, which reduces to fBm when $\alpha = 2$. The distribution of the evolution of both the tracer cloud and the passive scalar is tracked in the quasi-Lagrangian frame, and the fLm propagators are then fitted in this frame. The advantage of using the full propagator instead of the moments is that both the temporal and spatial evolution are considered, which can be beneficial in circumstances where the lower order moments become unbounded. However, a turbulent field usually contains local features such as persistent eddies that can distort the fitting process. In order for the propagator fitting method to be viable, the distributions must follow the evolution of the family of α-stable Lévy distributions as defined by Eq. 4.6. As a consequence, the time evolution of the both the tracers and passive scalar need to be sufficiently converged or contain features close to the required stable distributions. Deviations from stable distributions can easily yield unclear propagator fits. This is often an issue in turbulence dominated conditions where non-universal features (flows, coherent structures, etc.) affect the probability distributions more readily, which, in turn, prohibits the convergence to stable distributions. Universality is more likely to occur for larger Re numbers[3]. Considering the Gaussian distribution, one of the well-known stable distributions and a subset of the α-stable Lévy distributions, higher moments of the distribution provide measures of deviation from a Gaussian distribution. Particularly, the excess kurtosis measures the deviation from a Gaussian distribution pertaining to its shape. It is calculated according to the common definition $K = \mu_4/\sigma^4 - 3$ where $K = 3$ is known to coincide with a Gaussian distribution. At each time, for a cloud of tracers, the fourth moment is then defined for a population of N tracers as $K = K_{tr}$ where $\mu_4 = \left\langle [x(t) - \langle x(t)\rangle]^4 \right\rangle_N$ and the second moment is $\sigma^2 = \sigma_{tr}^2$. The kurtosis of the passive scalar is defined in a similar manner as its second moment such that $K = K_{ps}$ where $\mu_4 = \int\int [x - x_c(t)]^4\,\Theta(\boldsymbol{r},t)dxdy/M$ and $\sigma^2 = \sigma_{ps}^2$. Deviations from other stable distributions such as the stable Lévy distributions become more involved due to the potential unboundedness of the lower order moments[12].

4.5 Local transport characteristics

The evolution of both the passive scalar and tracers evolve can be separated into different phases. Although analytically the Lagrangian frame represented by tracers corresponds exactly to the Eulerian frame represented by the passive scalar, there are some differences. In both the fixed-gradient and flux-driven cases during the initial phase for $t\Omega_i < 5$, both of the measures evolve quite similar to each other, which underscores the equivalence between the Lagrangian and Eulerian frames. Compared with the passive scalar, tracers do not have the added dissipation, which allow the flow statistics to be captured over a larger duration. This is the turbulent transport timescale. However, the limitation on the statistics can cause issues when attempting to resolve smaller probabilities in the tails of the distribution that is usually associated with nondiffusive signatures. The advantage of the passive scalar over the tracers is that it is not limited by the statistics or the limited number of tracers. But, the fluctuations decrease due to the diffusion coefficient κ, which sets a time limit of the field to gather meaningful information to about $t\Omega_i \sim 10$.

In connection with the turbulence statistics, a relevant consideration is the Schmidt number defined as the ratio of scalar diffusivity to kinematic viscosity $Sc = \nu/\kappa$, which is similar to the Prandtl number Pr for advected temperature field; $Pr = \nu/\alpha$ where α is the thermal diffusivity. For a given Re, the scalar mixing is different between the Kolmogorov-Obukhov-Corrsin (KOC) regime $Sc \leq 1$ and the Batchelor regime $Sc \gg 1$[3]. In the KOC regime, the scalar is advected by the turbulent inertial range; whereas, the mixing process occurs through smooth velocity structures in the Batchelor regime. According to the parameters for this work, the scalar mixing at large wave number k is in the KOC regime $Sc = \nu/\kappa \simeq 5.0 \times 10^{-5}/5.0 \times 10^{-3} = 10^{-2}$. The restriction on κ is the Gibb's artifact, which leads to a balance between the proper dynamics and numerical artifacts.

4.5.1 Local transport characteristics of cases run with a fixed background profile

In the fixed-gradient cases, the profile feedback term in Eq. 4.3 becomes $R_{nl}\left(n, \phi, P\right) = V_D \partial_y \phi$ such that Eq. 4.1 reduces to a conventional two-dimensional fluid drift-wave type model, and the turbulence is continuously driven by a fixed gradient source. The overall transport character differs in spatial direction depending primarily on the coupling ν between n and ϕ[23–26]. With large $\nu \to \infty$ corresponding to the adiabatic limit $n \sim \phi$ with a fixed phase, the cross-drift transport becomes subdiffusive while superdiffusive in the drift direction. In the regime where $\nu \to 0$, the transport becomes more diffusive. Hence, the transport character in the cross-drift direction can vary from diffusive to subdiffusive depending on the coupling between n and ϕ, which is then translated into the spread of the passive scalar and the dispersion of tracers shown in Fig. 4.1. With a large coupling $\nu = 5$, the linear wave term becomes dominant in the adiabatic regime, which then constrains the evolution for both σ_{tr}^2 and σ_{ps}^2 compared with the hydrodynamic regime $\nu = 0.5$. The

qualitative trend in this work corroborates previous passive scalar results in the context of the Hasegawa-Wakatani model[27]. It has been reported that the diffusion coefficients have been observed to have a similar qualitative trend to the tracers[26] in that the transport characteristic becomes more subdiffusive in the cross-drift direction with increasing coupling between n and ϕ.

A summary of the scaling $\sigma_{tr}^2 \sim t^{\beta_{tr}}$ and $\sigma_{ps}^2 \sim t^{\beta_{ps}}$ for the duration $1 < t\Omega_i < 10$ are shown in Tab. 4.1 in comparison with the overall radial transport character obtained from tracers over larger times through the velocity statistics using the R/S analysis. Both the power-law time scalings β_{tr} and β_{ps} are determined from the minimization of the least square within the duration $2 < t\Omega_i < 10$, and the errors in the estimates are determined from the fitting process. The values for the time scalings β_{tr} and β_{ps} also need to be considered in context of the deviation from stable distributions. The time trace for K_{tr} in Fig. 4.2 shows significant deviations from a Gaussian distribution during the timespan of interest, which are then reflected in the differences between the power-law scaling β_{tr}. Although the time evolution for K_{ps} in Fig. 4.2 does not show large deviations from a Gaussian distribution, the significant mismatch between K_{tr} and K_{ps} points to inherent differences in the measured dynamics. The difference is the reflected in the time evolution of the second moment σ_{ps}^2 and both the estimated power-law scalings β_{tr} and β_{ps} in contrast to the background turbulence represented by $H(v_x)$ from the R/S method. With $K_{tr} > 0$ for all cases during $t\Omega_i < 5$, the tracers exhibit heavier tails than a Gaussian distribution. On the other hand, $K_{ps} < 0$ for subdiffusive cases, which reflect the restriction on the passive scalar distributions compared to a Gaussian distribution. This is in direct relation to the limitations due to tracer statistics when compared to the passive scalar profile. With limited statistics, the tracers tend to show an increase in the tails of the distribution while the passive scalar already has adequate statistics to sample a larger spatial domain. The passive scalar is more sensitive to the spatial inhomogeneities but less sensitive to small scale local turbulent structures due to the diffusivity as compared to the tracers. On the contrary, tracers tend to be sensitive to local turbulent structures but less sensitive to spatial inhomogeneities. Significant deviations in the third moment of the distributions relating to the skewness were not observed since the distributions for both the tracers and the passive scalar remain somewhat symmetric. In Tab. 4.1, the only case where both the tracer and passive scalar distributions coincide most closely to Gaussian distributions (Fig. 4.4) is when an external poloidal sheared flow $\Phi_0 = 3$ is imposed on the background turbulence, which is when both the power-law scalings $\beta_{tr} \sim 0.65$ and $\beta_{ps} \sim 0.89$ are most similar to $\beta_{v_x} \sim 0.72$ from $H(v_x) \sim 0.36$ considering $\alpha \sim 2$ and using $\beta = 2H$.

In the parameter regime where the wave term becomes significant $\nu \to \infty$, there is a tendency of a subdiffusive signature in the radial direction due to the correlations induced by the linear wave term. By shifting into the hydrodynamic limit $\nu \to 0$ and $\epsilon \to 1$, the wave term becomes less dominant and the overall transport character tends

Table 4.1: Summary of scaling for $\sigma_{tr}^2 \sim t^{\beta_{tr}}$ and $\sigma_{ps}^2 \sim t^{\beta_{ps}}$ for the fixed-gradient cases over the initial duration $1 < t\Omega_i < 10$ when both the tracers and the passive scalar evolve relatively similar to each other show significantly different transport character from the overall radial transport character $H(v_x)$ from R/S analysis due to the deviations from stable distributions.

ν	ϵ	Φ_0	$H(v_x)$	β_{tr}	β_{ps}
5.0	0.3	0.0	0.26 ± 0.055	1.16 ± 0.011	1.06 ± 0.006
0.5	0.9	0.0	0.47 ± 0.028	1.50 ± 0.007	1.33 ± 0.003
0.5	0.9	3.0	0.36 ± 0.073	0.63 ± 0.006	0.89 ± 0.002

to $H(v_x) \sim 0.45$ in the cross-drift direction and $H(v_y) \sim 0.56$ in the drift direction. In this parameter regime, both σ_{tr}^2 and σ_{ps}^2 show a similar trend for $t\Omega_i < 10$ in Fig. 4.1. The diffusion term κ becomes dominant for $t\Omega_i > 10$ while the tracers continue to sample the turbulence. Although the transport characteristics are diffusive in both directions, the propagators from both the tracers and passive scalar still show strong dependence on the turbulence structures. The dependence on the individual turbulent state is shown in Fig. 4.3 by the distinct smaller peaks for $|dx| > 0.15$ surrounding the core $dx \sim 0$ in the distributions for both the tracers and passive scalar. These minor peaks are most notably seen at $t\Omega_i = 2.6$ in Fig. 4.3 with both the passive scalar and the tracers, which corresponds to trapping in turbulent structures. Non-universal features such as persistent eddies or trapping in eddies of different sizes affect the propagators more readily, which prohibits the convergence to stable distributions. In the timespan of interest, $t\Omega_i < 10$, the distributions for both the tracers and passive scalar deviate significantly from a Gaussian distribution as shown most notably through K_{tr} in Fig. 4.2, which confirms the significant difference in the temporal power-law scaling for both σ_{tr}^2 and σ_{ps}^2 shown in Tab. 4.1. In this type of cases, the propagators deviate from stable distributions, which distorts the extraction of the transport character of the underlying turbulence.

The local transport becomes slightly different when an external sheared poloidal flow with an amplitude of $\Phi_0 = 3$ is added to the fixed-gradient diffusive case. The transport characteristics for these parameters give a subdiffusive signature in the cross-flow direction $H(v_x) \sim 0.36$ and extremely correlated velocity statistics in the flow direction $H(v_y) \sim 1.13$ [20]. Contrasting to the diffusive case, the absolute spread of both σ_{tr}^2 and σ_{ps}^2 is smaller while the variance for the passive scalar spreads faster than the tracer dispersion as shown in Fig. 4.1. The relatively strong externally imposed sheared flow induces a flow-driven instability that generates persistent vortices near the maximum shear region $x \sim 0.5$. Due to the presence of these persistent turbulent structures near the injection location of the tracer cloud and the passive scalar distribution, most of the tracers are then trapped and advected with these structures. Although there are tracers located coincidentally on the periphery of the passive scalar, as the vortex becomes elongated with the shear, the limited number of tracers constrains the evolution of σ_{tr}^2. On the other hand, the passive scalar

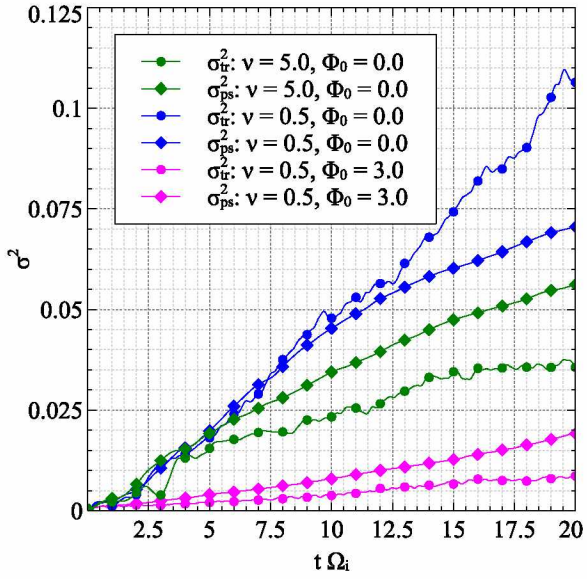

Figure 4.1: Time evolution of both σ_{tr}^2 (circle) and σ_{ps}^2 (diamond) show differences due to the overall transport regime. In the adiabatic limit ($\nu = 5$) without an external flow ($\Phi_0 = 0$), both σ_{tr}^2 spreads slower than σ_{ps}^2. In the hydrodynamic limit ($\nu = 0.5$) and no external flow ($\Phi_0 = 0.0$), the variance for both the passive scalar and the tracers evolves in a similar manner for $t\Omega_i < 10$ and diverges due to diffusion of the passive scalar. With an external flow $\Phi_0 = 3.0$, σ_{tr}^2 and σ_{ps}^2 evolve slower than the other cases.

is able to track the filaments, which is then reflected in the spread in σ_{ps}^2. The difference in σ_{tr}^2 and σ_{ps}^2 reflects an important aspect between the use of tracers and passive scalar. Both of the propagators in this case deviate slightly from stable Lévy distributions due to the vortex structure. The core of the distribution remains relatively Gaussian during the initial period as shown in Fig. 4.4. The vortex filaments are reflected in the passive scalar distributions as a superimposed asymmetric feature in the tails $|dx| > 0.2$. By fitting both the tracer and passive scalar distributions with a scaled Gaussian propagator $\alpha \sim 2$ in the time duration $1 < t\Omega_i < 10$, the fitted temporal exponents yield values of $\beta_{ps}^{prop} \sim 0.60$ and $\beta_{tr}^{prop} \sim 0.42$. Using the relation between the exponents $\alpha H = \beta$ and noting that $\alpha \sim 2$, the transport exponents are $H_{x,ps}^{prop} \sim 0.3$ and $H_{x,tr}^{prop} \sim 0.21$. The larger estimation for β_{ps}^{prop} compared with β_{tr}^{prop} comes from weighing the asymmetry in the tails of the passive scalar distributions. Although the exact values do not match the subdiffusive character obtained from the Lagrangian velocities at longer timespans $H(v_x) \sim 0.36$, both $H_{x,ps}^{prop}$ and $H_{x,tr}^{prop}$ reflects radial subdiffusion enabled by the poloidal decorrelation process imposed by the external poloidal flow. The relative proximity of the values between $H_{x,ps}^{prop}$ and $H_{x,tr}^{prop}$ from the propagator fitting method and $H(v_x)$ from the R/S of tracers at larger times suggest that the transport character is dominated by the trapping and detrapping in the flow-driven vortices.

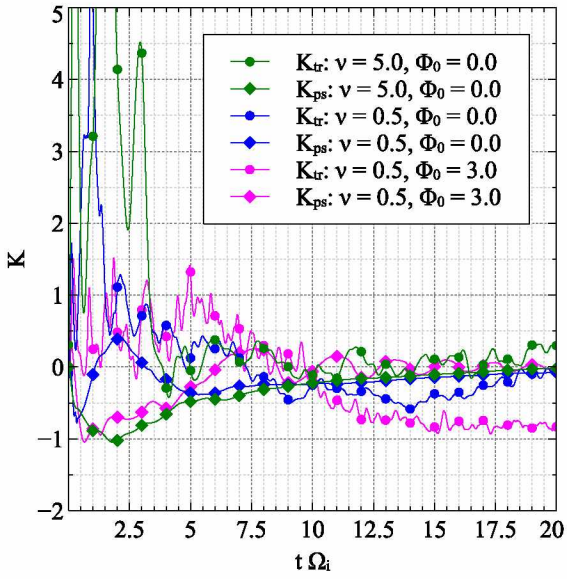

Figure 4.2: Time evolution of the excess kurtosis for both tracers K_{tr} (circle) and passive scalar K_{ps} (diamond) show deviations from a Gaussian distribution within the time duration of interest $t\Omega_i < 10$ for the fixed-gradient scenarios. Except for the hydrodynamic limit scenario $\nu = 0.5$ with an external flow $\Phi_0 = 3$, the large deviations in both scenarios without external flow prevents accurate measure of the underlying turbulent transport character.

4.5.2 Local transport characteristics of cases run with profile evolution

A flux-driven background profile provides the next additional complexity to the otherwise standard drift-wave model[8]. Two competing mechanisms arise due to the free energy in the background gradient: radial turbulent relaxations and self-generated poloidal flows. Radial turbulent relaxations occur primarily to decrease the gradient in the background field P in Eq. 4.1. On the other hand, the self-generated sheared flows can be generated predominantly near the source and the sink region due to the persistent inhomogeneous gradient in P that ultimately drives a sheared poloidal flow due to the asymmetry in the Reynolds stress term[28]. The two processes act in orthogonal directions to influence the radial transport character such that one process tends to dominate over another, which then dictates the dominant flow dynamics and the overall transport character. The radial transport signature when radial relaxation events dominate tends to be superdiffusive $H(v_x) > 0.5$ while the signature is subdiffusive $H(v_x) < 0.5$ when self-generated flows become prominent. Both of these processes have positive feedback in that they tend to maintain the dominant state. When the self-generated sheared poloidal flows become prominent, the cross-flow transport reduces, which further elevates the background gradient that can then drive stronger flows. As a result, stronger flows perpendicular to the gradient reduces the transport further. However, the positive feedback of the self-generated poloidal flow terminates when the gradient becomes large enough to initiate relaxations. In a similar manner, radial relaxations create pathways where the flow is predominantly

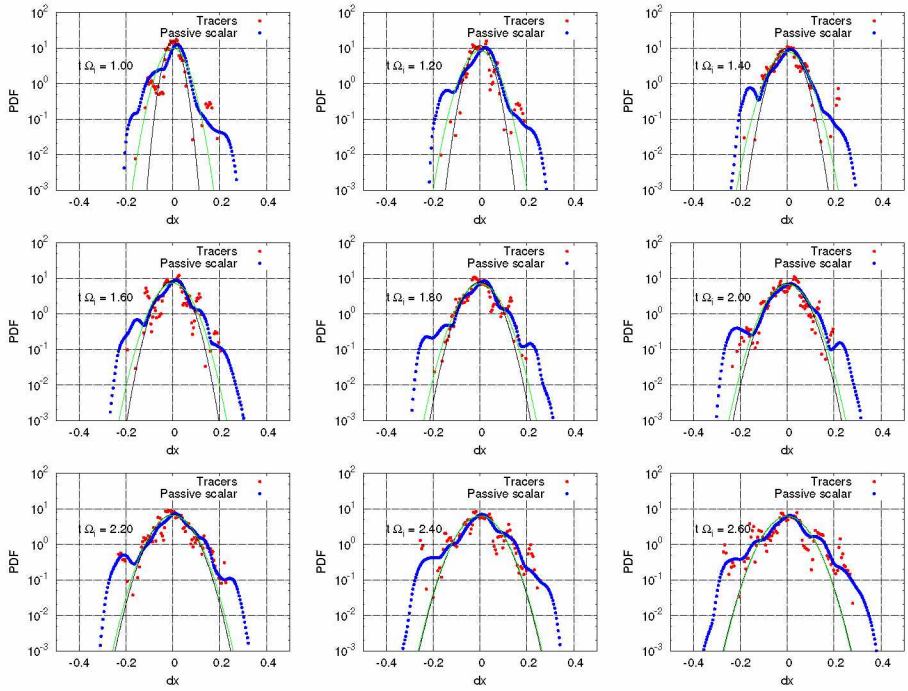

Figure 4.3: In the hydrodynamic limit $\nu = 0.5$, the propagators for both the passive scalar (blue dots) and the tracers (red dots) deviate from stable Lévy distributions. The black lines represent the diffusive process or Gaussian distribution propagators fit for the tracers' distribution, and the green lines denote the diffusive process fit for the passive scalar distribution.

down-gradient. These avalanche events prevent poloidal flows from developing, which allows for further down-gradient transfer. Relaxations terminate when the gradient becomes insufficient to drive the turbulence. The classical diffusive limit is achieved when the two competing processes are somewhat in balance. As a result of this competition and the inherent positive feedback property, the overall transport can be separated depending on the dominant process.

The evolution for both σ_{tr}^2 and σ_{ps}^2 depends on the dominant transport regime as shown in Fig. 4.6. In contrast to the fixed-gradient scenarios, the spatial inhomogeneity established by the source and sink becomes an important consideration when measuring σ_{tr}^2 and σ_{ps}^2. The source is located at $x = 0.25$, and the sink is at $x = 0.75$. When the center of the tracer cloud and the center of mass of the passive scalar field are relatively close to the center of the simulation box at $x \sim 0.5$, the maximum extent both the tracers and the passive scalar can achieve is about $dx \sim 0.25$. The center of the tracer cloud and the passive scalar drifts differently depending on the turbulence conditions as shown in Fig. 4.6. Hence, the tracers and the passive scalar can sample different regions of the turbulent flow. A typical time it takes for the spreading to occur is again on the order of $t\Omega_i < 10$. Within this initial timespan $1 < t\Omega_i < 10$, the scalings for both σ_{tr}^2 and σ_{ps}^2 are summarized in Tab. 4.2. The spatial distributions lack heavy-tails and are more similar to a Gaussian distribution than

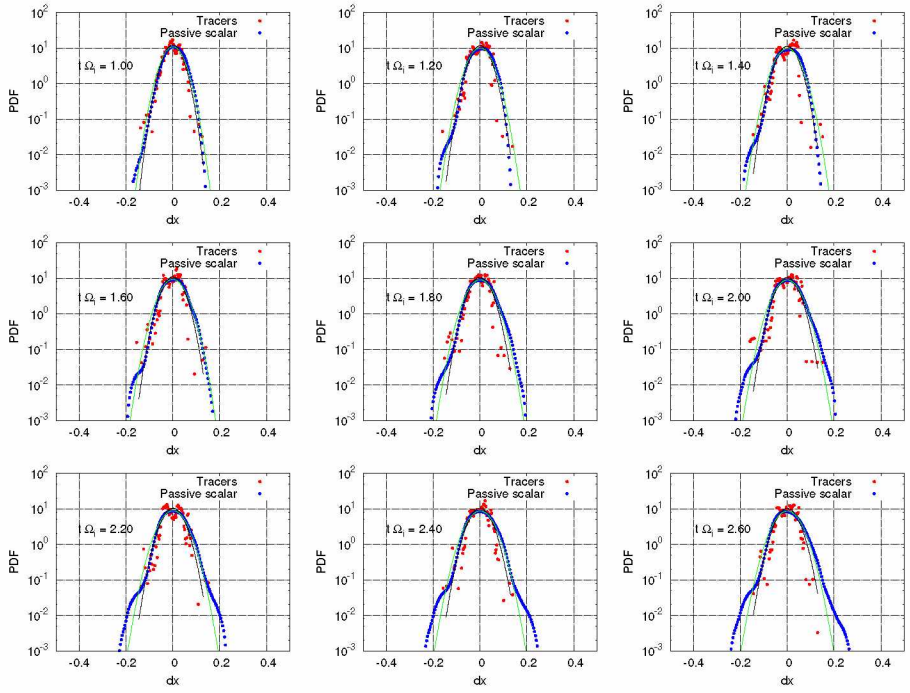

Figure 4.4: With an external sheared poloidal flow $\Phi_0 = 3$ imposed in the hydrodynamic parameter regime, propagators for both the passive scalar (blue dots) and tracers (red dots) are only coincident in the initial time $t\Omega_i < 2$. The black and green lines represent the Gaussian propagators fit for the tracers and the passive scalar respectively.

the fixed-gradient cases as shown through the time evolution of K_{tr} and K_{ps} in Fig. 4.7. The evolution for both K_{tr} and K_{ps} remained bounded in the range $-1 \leq K \leq 1$. Taking into account that the spatial distributions for both tracers and passive scalar are close to Gaussian distributions, the scalings β_{tr} and β_{ps} coincide closely to the background radial transport character represented by $H(v_x)$ obtained from R/S analysis of the tracer velocities at larger times. Using the connection between the propagators and the transport exponents, a scaled Gaussian propagator $G(x,t) \propto \exp\left(-x^2/\chi t^{\beta}\right)$ is then used to fit to passive scalar distributions over a time period $2 \leq t\Omega_i \leq 10$ to give the temporal exponent β_{ps}^{prop}. The significant errors in β_{ps}^{prop} are due to the fitting process that considers both the spatial and temporal feature of the distributions compared to the Gaussian propagator. Both σ_{tr}^2 and σ_{ps}^2 measure only the second moment without considering the errors from higher order moments of the distributions. The distortions in the passive scalar distributions arising from local turbulent features such as eddies translate into significant errors in β_{ps}^{prop}. Although the trend for β_{ps}^{prop} is qualitatively similar to both σ_{tr}^2 and σ_{ps}^2 as shown in Tab. 4.2, the exponent obtained from the propagator fitting scheme β_{ps}^{prop} tend to underestimate the time correlations due to both the boundary effects and the diffusion term, which permit significant deviations from Gaussian propagators. The similar trends in all the measures are not surprising considering the equivalence between the second moments and the Gaussian

propagators. The propagator fitting method was not applied to the tracer distributions due to the large scatter in the data, which tend to give poor fits.

Combined with the dissipation of the passive scalar, the boundary effects adds another constraint to both the dispersion of tracers and the spread of the passive scalar field. Without a critical gradient parameter $L_{c,P,x}^{-1} = 0$, both σ_{tr}^2 and σ_{ps}^2 evolve in a similar manner with $\sigma_{tr}^2 \sim \sigma_{ps}^2 \propto t\Omega_i$ for $2 < t\Omega_i < 10$ as shown in Fig. 4.6. Comparing to the case with $L_{c,P,x}^{-1} = 0$, both σ_{tr}^2 and σ_{ps}^2 spread faster due to radial relaxations enhanced by a non-zero critical radial gradient parameter $L_{c,P,x}^{-1} = 1$. Due to the classical diffusion term in the passive scalar, the tracers continue to follow the flow while the passive scalar spreads more slowly for $t\Omega_i > 7.5$. The reduction in the radial transport due to the imposed external flow $\Phi_0 = 0.2$ is reflected in the evolution of σ_{tr}^2 and σ_{ps}^2 being slower compared to the case without external flow.

Another distinguishing character between the tracers and the passive scalar pertains to the statistics of both quantities. Tracers have limited statistics, which then cause the tracer related quantities to be more sensitive to local turbulent structures. In contrast, the passive scalar evolves with a profile and a diffusion element, which then allows more sampling of the spatial domain than the tracers. The results of these differences can be seen in the almost opposite evolution for K_{tr} and K_{ps} during the very initial timespan $t\Omega_i < 2$ in Fig. 4.7. When $K_{ps} > 1$, K_{tr} tends have the opposite sign $K_{tr} < 0$. For instance in the case with $L_{c,P,x}^{-1} = 1$ corresponding to prominent radial relaxations, a $K_{ps} > 0$ during $t\Omega_i < 2$ indicates a heavier tail for the passive scalar due to the radial relaxation process. However, a $K_{tr} < 0$ indicates that the tracers have been slightly trapped in local turbulent structures, which then constrain the tails of the distribution to be less than a Gaussian distribution. This effect reinforces the observation that the passive scalar diagnostics is somewhat less sensitive to the local turbulent structures, which can provide a more accurate measure of the overall transport as compared with the tracers. The tracers, with their inherently limited statistics, are more sensitive to the local turbulent structures, which can be useful for detection of these structures, but less effective for characterizing the underlying transport in a short duration. Nonetheless, although both the tracers and the passive scalar can provide slightly different information on the turbulent dynamics, the coincidence between both the tracers and passive scalar measures defines the appropriate time range to identify the underlying transport character.

Without a critical gradient parameter $L_{c,P,x}^{-1} = 0$, the radial flow statistics are close to diffusive $H(v_x) \sim 0.49$ and slightly superdiffusive in the poloidal direction $H(v_y) \sim 0.60$[8]. The local self-generated poloidal flows inhibit strong radial relaxations, and transport remains close to diffusive between the source and the sink. The spread for both the tracers and the passive scalar remains fairly symmetric in both radial and poloidal directions as shown in Fig. 4.10 (a) that overlays selected tracers, the passive scalar, and the vorticity $\nabla^2\phi$ at time $t\Omega_i = 5$. The tracer dispersion and the spread of the passive scalar field coin-

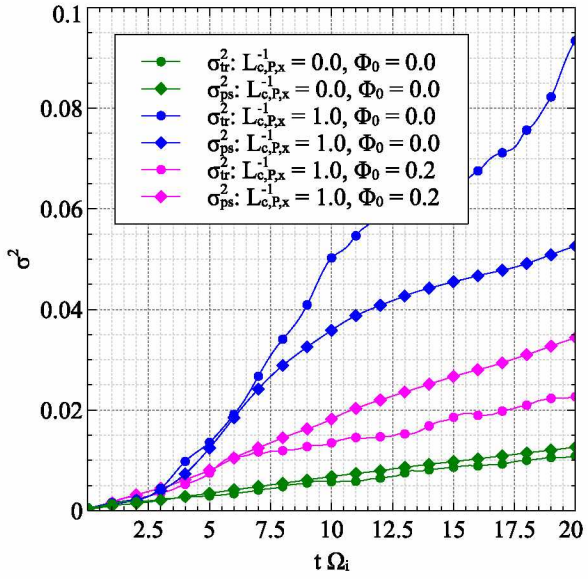

Figure 4.5: Time evolution of both σ_{tr}^2 (circle) and σ_{ps}^2 (diamond) show coincidence for $t\Omega_i < 7$. With radial relaxations ($L_{c,P,x}^{-1} = 1$) and without an external sheared flow ($\Phi_0 = 0$), both σ_{tr}^2 and σ_{ps}^2 evolve faster than the scenario without radial relations ($L_{c,P,x}^{-1} = 0$) and external flow ($\Phi_0 = 0.2$). With a sheared external flow ($\Phi_0 = 0.2$) added to the scenario with prominent relaxations, the radial decorrelation is reflected in the reduced evolution of both σ_{tr}^2 and σ_{ps}^2.

cide with each other for $t\Omega_i > 10$ as shown in Fig. 4.6. Over the duration $1 < t\Omega_i < 10$, the dispersion of the tracers scales as $\sigma_{tr}^2 \sim t^{0.87}$, and the passive scalar spreads as $\sigma_{ps}^2 \sim t^{0.95}$ (Tab. 4.2). An almost linear dependence in time suggests a classical diffusive character. The propagators for both the tracers and the passive scalar reveal the subtle restriction on the evolution of σ_{tr}^2 and σ_{ps}^2. While the spatial distributions are very close to Gaussian distributions ($\alpha \sim 2$) as shown in Fig. 4.8, the time evolution is slightly less than diffusive. By fitting the propagators with a time scaled Gaussian propagator $G(x,t) \propto \exp\left(-x^2/\chi t^\beta\right)$, the best fit occurs when $\beta \sim 0.7$ for the duration $2 < t\Omega_i < 10$ (Fig. 4.8). The slightly slower dispersion of the tracers compared to the passive scalar in Fig. 4.8 reflects the boundaries imposed by the self-generated poloidal flows at the source and sink. Correspondingly, this bounding effect by the flow also limits the drift of the centroid to be somewhat stationary at $x \sim 0.5$ for both the tracer could and the distribution of the passive scalar field as shown in Fig. 4.6 . The passive scalar distributions at later times $t\Omega_i = 8$ in Fig. 4.8 also develop additional distinct region for $|dx| > 0.2$ due to the constraint in radial advection imposed by the self-generated poloidal flow. However, as a consequence of the diffusion term in the passive scalar field, the passive scalar is able to spread into the self-generated flow region. Because of the diffusive element, the passive scalar becomes less sensitive to the turbulent flow structures compared with the tracers.

In the presence of radial relaxation events, both σ_{tr}^2 and σ_{ps}^2 reflect the superdiffusive

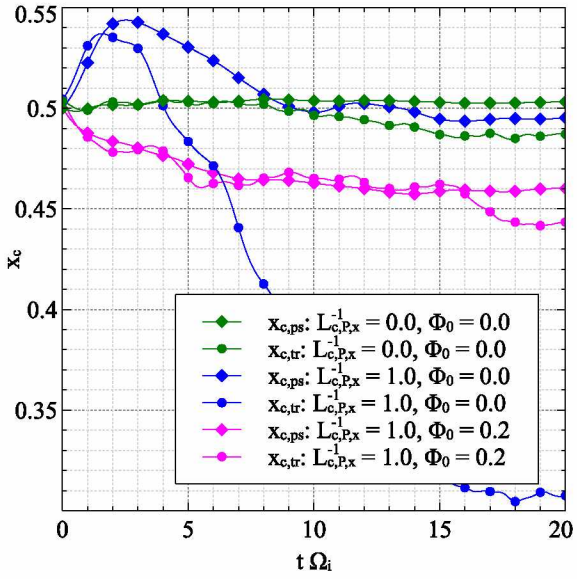

Figure 4.6: Time evolution curves for the centroid of the tracer cloud (circle) and the center of mass of the passive scalar (diamond) show strong divergence in the case with prominent radial relaxations ($L^{-1}_{c,P,x} = 1$). The centroids for both the tracers and the passive scalar drift towards the source in the case with an external flow ($\Phi_0 = 0.2$).

Table 4.2: Summary of scaling for $\sigma^2_{tr} \sim t^{\beta_{tr}}$ and $\sigma^2_{ps} \sim t^{\beta_{ps}}$ for flux-driven cases over the duration $1 < t\Omega_i < 10$ when both the tracers and the passive scalar evolve relatively similar to each other show qualitative similar trends to the overall radial transport character $H(v_x)$ from R/S analysis. The fitted exponent from the propagator fitting scheme β^{prop}_{ps} to the passive scalar field tend to underestimate the value.

$L^{-1}_{c,n,x}$	Φ_0	$H(v_x)$	β_{tr}	β_{ps}	β^{prop}_{ps}
0.0	0.0	0.49 ± 0.029	0.67 ± 0.006	0.91 ± 0.003	0.70 ± 0.099
1.0	0.0	0.79 ± 0.027	1.80 ± 0.009	1.76 ± 0.008	1.39 ± 0.189
1.0	0.2	0.51 ± 0.068	1.04 ± 0.007	1.09 ± 0.003	0.74 ± 0.151

process by evolving much faster than the case without prominent relaxations as shown in Fig. 4.6. With a nonzero $L^{-1}_{c,P,x} = 1$, radial relaxations dominate, and the radial transport becomes superdiffusive within the mesorange $H(v_x) \sim 0.79$ while the poloidal transport remains diffusive $H(v_y) \sim 0.51$[8]. During initial times $t\Omega_i < 4$, both the centroid of the tracer cloud and the passive scalar shows a slight drift towards the sink as shown in Fig. 4.6. Both the tracers and the passive scalar become elongated in the radial direction due to the relaxation process as shown in Fig. 4.10 (b), which compares selected tracers, passive scalar, and $\nabla^2\phi$ at time $t\Omega_i = 5$. For the time $t\Omega_i > 4$, the centroid of the tracers shows a drift towards the source (Fig. 4.6) while the passive scalar dissipates yielding an almost uniform distribution such that $x_{c,ps} \sim 0.5$. In the time range $t\Omega_i < 7$, both the tracers and the passive scalar spread at almost the same rate, but the tracers continue to disperse for $t\Omega_i > 10$ while the passive scalar spreads slower. At later times, the tracer

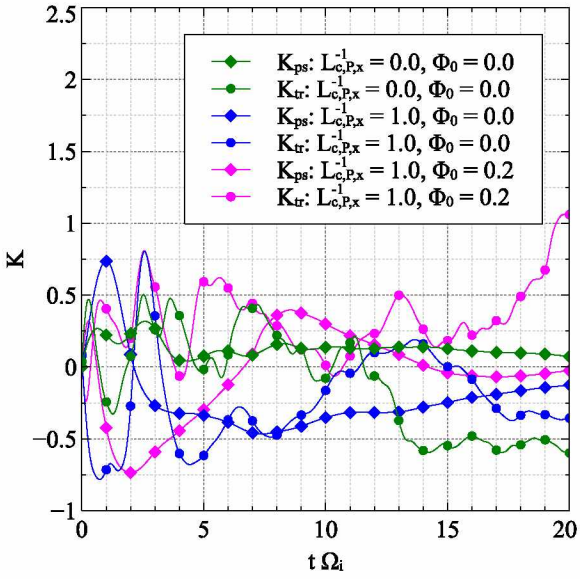

Figure 4.7: Time evolution of the excess kurtosis for both K_{tr} (circle) and K_{ps} (diamond) in the flux-driven gradient cases deviate from a Gaussian distribution within the time duration of interest $t\Omega_i < 10$.

cloud disperses and moves with a centroid into a somewhat different region of turbulence, which can once again give slightly different transport character. Also, the difference in the evolution between σ_{tr}^2 and σ_{ps}^2 can also be attributed to the diffusion term in the passive scalar field. As the scalar field extends into filaments due to advection (Fig. 4.10), gradients become steeper allowing diffusion to act more strongly. A faster than diffusive scaling for $3 < t\Omega_i < 7$ reflects the radial relaxation process that enhances the shearing effect on the passive scalar in the radial direction. This time duration also coincides with the drift of the center of mass of the passive scalar. Tracers at the periphery of the passive scalar are observed to follow the passive scalar up to $t\Omega_i \sim 7$ then the perturbation in the passive scalar becomes less distinguishable. During the initial phase $2 \leq t\Omega_i \leq 3.6$ shown in Fig. 4.9, there are two distinct regions that are accentuated by the spatial inhomogeneity. The core of the distributions $|dx| < 0.1$ for both tracers and passive scalar decreases faster than the sides $|dx| > 0.2$. The flattening in the core is due to the dominant radial transport process while the constrained sides is due to the boundary imposed by the sources. The self-generated poloidal flows in these regions are weaker than the radial relaxation events, which allows both the tracers and the passive scalar to evolve much more freely beyond $|dx| \sim 0.25$. Although there are characteristic differences between the evolution of the tracers and the passive scalar at later times $t\Omega_i > 10$, both quantities show that they remain similar in the initial time range, which inherently sets the timespan for which the Lagrangian and quasi-Lagrangian frame coincides. Consequently, this timespan sets the duration when local transport coincides with the underlying turbulent transport. The already intrinsic differences between both the Lagrangian and quasi-Lagrangian frames can complicate the

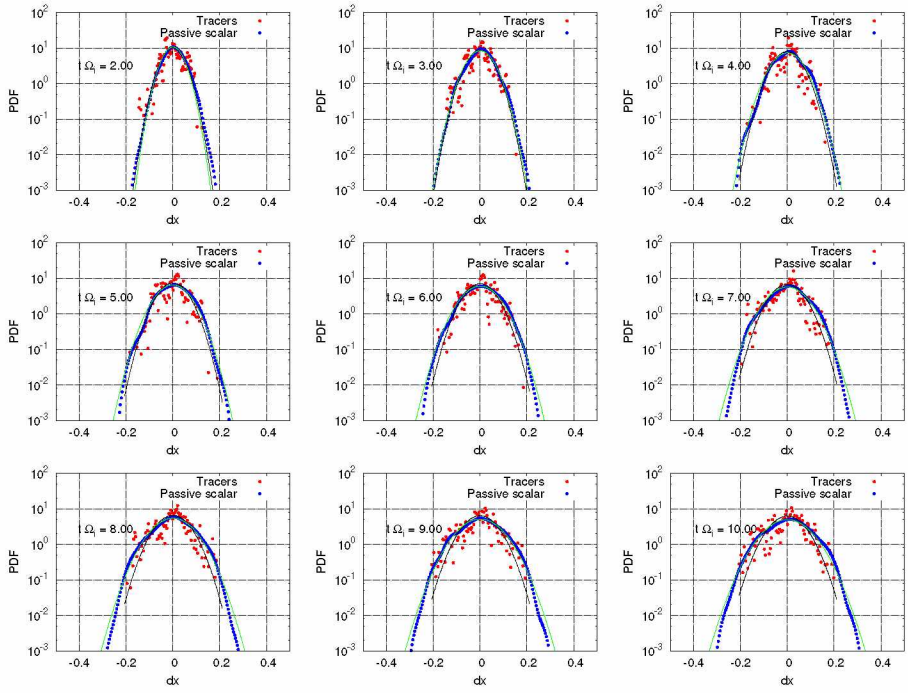

Figure 4.8: Propagators for the case without a critical radial gradient parameter $L_{c,P,x}^{-1} = 0$ during $2 \leq t\Omega_i \leq 10$ are close to Gaussians. Red dots represent the tracer distributions while the blue dots denote the passive scalar profile. The green and black lines denote the best propagators to the tracers and the passive scalar respectively.

process of drawing the equivalence between the two perspectives in the context of transport quantification at later times.

A non-zero externally imposed poloidal sheared flow $\Phi_0 = 0.2$ disrupts in the radial relaxation from the case with $L_{c,P,x}^{1} = 1$ to yield a diffusive signature in the cross-flow direction $H(v_x) \sim 0.51$ while the poloidal direction becomes superdiffusive $H(v_y) \sim 0.79$[20]. This case is selected instead of a larger external flow amplitude Φ_0 due to the flow-driven instability, which generates persistent vortices that can skew the local transport analysis. With the flow amplitude $\Phi_0 = 0.2$, the sheared flow is effective in reducing the radial relaxations but not strong enough to generate persistent vortices. Although $L_{c,P,x}^{-1} = 1$ still exists, the radial relaxations are insufficient to decorrelate the externally imposed poloidal flow, which ultimately provides an enhancement of the radial decorrelation mechanism. As shown in Fig. 4.6 for $t\Omega_i < 10$, both σ_{tr}^2 and σ_{ps}^2 evolve slower than the scenario with prominent relaxations but faster than the diffusive scenario. The difference in the evolution of the second moment measurements between different turbulence regimes reflect the underlying effect of competing mechanisms on the overall transport in the turbulent flow statistics. There is also a shift in the centroid of both the tracers and the passive scalar (Fig. 4.6), which coincides with the shearing induced by the external flow that separates a section of the tracer cloud and the passive scalar into two distinct components as shown in Fig. 4.10

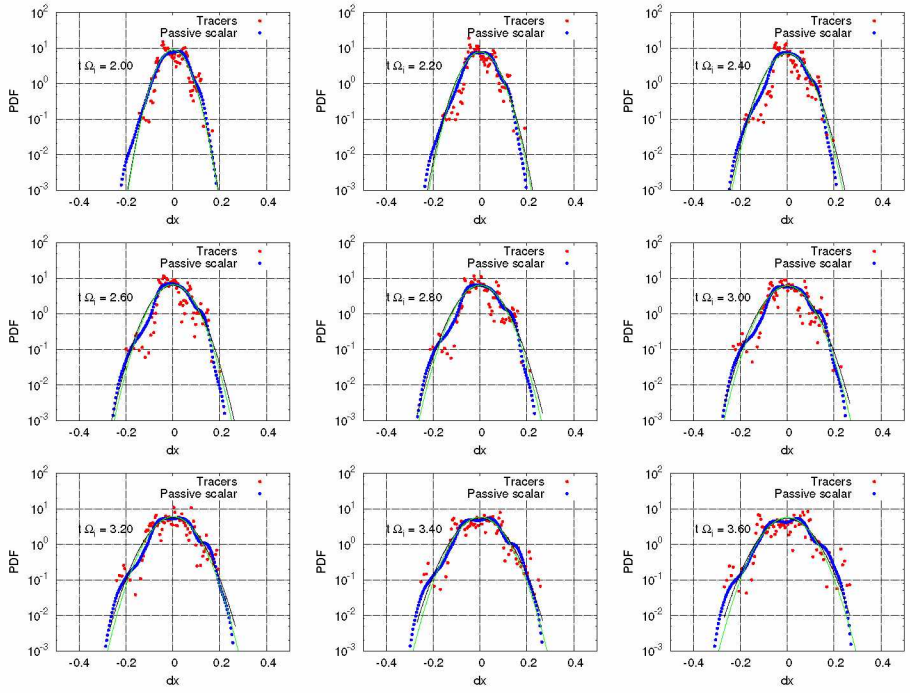

Figure 4.9: Propagators over the initial time span $2.0 \leq t\Omega_i \leq 3.6$ for the scenario with a critical radial gradient parameter $L_{c,P,x}^{-1} = 1.0$ show flattening in the core due to the radial relaxation process. The black lines represent the Gaussian propagators fit to the tracers' distributions while the green lines denote the fits to the passive scalar profiles.

(c) comparing selected tracers, passive scalar, and $\nabla^2\phi$. Contrasting with the case without an external flow but with a non-zero critical gradient, both the centroids of the tracers and the passive scalar evolves similarly for $t\Omega_i > 10$. During the initial time $t\Omega_i < 7$, $K_{ps} < 0$ (Fig. 4.7) also shows a similar trend to K_{ps} for the fixed-gradient case with $\Phi_0 = 3$ where the tails of the profile have been constrained by the sheared poloidal flow while $K_{tr} > 0$ reflect slightly heavier tails than a Gaussian distribution.

The underlying transport character can be recovered within a timespan when both the tracers and passive scalar evolve relatively similar to each other. This work has shown that fBm propagators can distinguish between different transport regimes to a certain extent. Although heavy tailed distribution are possible, local transport of this kind would likely more often produce data more similar to Gaussian distributions such as blobs from gas puff imaging (GPI) diagnostic [29]. This means that the transport dynamics is embedded in the temporal exponent β.

4.6 Conclusions

Due to the difficulty of experimentally tracking a fluid parcel, the passive scalar technique can be used to make measurements of turbulent transport. The equivalence between the passive scalar dynamics and Lagrangian tracers is used to connect the measurements

with analytical theory of turbulent transport. In this work, measurements of tracers enable the translation between the Lagrangian and the quasi-Lagrangian frame. While not considering additional complexity such as inertia effects, the diffusion in the passive scalar already provides an element that causes the two measures to diverge at larger times. Hence, this provides a consideration when employing a fluid measurement technique that acts as a passive scalar. The diffusion of a passive scalar is inherent to most physical systems, which can then give a slight misrepresentation of the transport character when considered outside of the range of its validity.

The equivalence between the tracers and passive scalar is expressed when both the evolution of the two measures coincide with each other. When both the evolution of the distribution of tracers and passive scalar are similar to stable distributions, the underlying transport character can be unsurprisingly recovered by fitting the propagators within this timespan. In the specific case when the propagators are similar to Gaussian distributions, the second moments of the tracers and the passive scalar become sufficient to quantify the transport character in different transport regimes. Different transport regimes have been identified from the local transport characterizations. Deviations from stable distributions present more difficulties in identifying the underlying transport such as when the local turbulent structures become dominant or the distribution of both the tracers and the passive scalar inadequately samples the flow statistics. This then provides a criterion for the puff width as compared to the typical compared local turbulent structures. These deviations from a Gaussian distribution can be detected with higher order moments for instance as shown in this work by inspecting the excess kurtosis. In cases when both the dispersion of the tracer cloud and the spreading of the passive scalar field coincide within initial times and follow qualitatively to the overall radial transport character, they tend to diverge from each other at longer times due to the diffusion in the passive scalar field. As a result, the diffusion inherently sets a temporal limitation on using passive scalar quantity as transport diagnostics for transport in a turbulent medium. Despite the known differences in passive scalar turbulence compared to the driving turbulent flows, the underlying transport character can still be recovered from a local measurement. Due to the inherent diffusion in the passive scalar evolution, it is less sensitive to local turbulent structures and able to sample a larger spatial domain compared to the tracers.

The second moments obtained from both the tracers and the passive scalar, the temporal exponent from the propagator fitting method have shown qualitative similarities to the overall transport characteristic. Within a time duration less than the effective diffusion time of the passive scalar, the local transport analysis can, to a certain extent, retrieve the underlying transport character. The transport character obtained within this relatively short timespan coincides with the overall transport due to the turbulence. Although this work has only extract the transport exponents from Gaussian distributions, the propagator fitting method can be a viable diagnostic when the distributions resem-

ble stable distributions, which supplements or circumvents the limitation of obtaining the transport character through the power-law scaling of the second moment. When the spatial distribution is close to Gaussian, the second moment measure provides sufficient transport characterization. However, in circumstances when the distribution becomes closer to stable Lévy distributions, the second moment becomes unbounded, and the power-law scaling of the second moment becomes insufficient in identifying the transport character. This work suggests that a technique based on a single realization of the local temporal evolution of a passive scalar field with limited diffusion can indeed represent the underlying transport, which supports its use as an experimental turbulent transport diagnostic.

4.7 Acknowledgements

This work was supported in by US DOE contract number DE-FG02-04ER54741 with UAF and in part by a grant of HPC resources from the Arctic Region Supercomputing Center at the University of Alaska Fairbanks.

4.8 References

[1] M. Lesieur, *Turbulence in Fluids*, 4th ed. (Springer, New York, 2008).

[2] G. Falkovich, K. Gawędzki, and M. Vergassola, Rev. Mod. Phys. **73**, 913 (2001).

[3] K. R. Sreenivasan and J. Schumacher, Phil. Trans. R. Soc. A **368**, 1561 (2010).

[4] A. S. Monin and A. M. Yaglom, *Statistical Fluid Mechanics* (MIT Press, Cambridge, Massachusetts, 1975).

[5] G. Falkovich and K. R. Sreenivasan, Physics Today **59**, 43 (2006).

[6] W. Horton, Rev. Mod. Phys. **71**, 735 (1999).

[7] D. E. Newman, P. W. Terry, P. H. Diamond, and Y. Liang, Phys. Fluids B **5**, 1140 (1993).

[8] D. Ogata, D. Newman, and R. Sánchez, Phys. Plasmas (submitted) (2016).

[9] A. C. Hindmarsh, P. N. Brown, K. E. Grant, S. L. Lee, R. Serban, D. E. Shumaker, and C. S. Woodward, ACM Trans. Math. Softw. **31**, 363 (2005).

[10] R. Metzler and J. Klafter, Phys. Reports **339**, 1 (2000).

[11] G. Zaslavsky, Phys. Rep. **371**, 461 (2002).

[12] I. Podlubny, *Fractional Differential Equations* (Academic Press, San Diego, CA, 1999).

[13] E. Montroll and H. Scher, J. Stat. Phys. **9**, 101 (1973).

[14] R. Sánchez, B. A. Carreras, and B. P. van Milligen, Phys. Rev. E **71**, 011111 (2005).

[15] R. Sánchez, B. A. Carreras, D. E. Newman, V. E. Lynch, and B. P. van Milligen, Phys. Rev. E **74**, 016305 (2006).

[16] I. Calvo, R. Sánchez, and B. A. Carreras, J. Phys. A: Math. Theor. **42**, 055003 (2009).

[17] H. E. Hurst, Trans. Amer. Soc. Civil Eng. **116**, 770 (1951).

[18] B. I. Shraiman and E. D. Siggia, Nature **405**, 639 (2000).

[19] Z. Warhaft, Annu. Rev. Fluid Mech. **32**, 203 (2000).

[20] D. Ogata, D. Newman, and R. Sánchez, Phys. Plasmas (submitted) (2017).

[21] P. K. Yeung, Annu. Rev. Fluid Mech. **34**, 115 (2002).

[22] R. Sánchez and D. E. Newman, Plasma Physics and Controlled Fusion **57**, 123002 (2015).

[23] G. Manfredi and R. O. Dendy, Phys. Plasmas **4**, 628 (1997).

[24] V. Naulin, A. H. Nielsen, and J. J. Rasmussen, Physics of Plasmas **6**, 4575 (1999).

[25] S. V. Annibaldi, G. Manfredi, R. O. Dendy, and L. O. Drury, Plasma Phys. Control. Fusion **42**, L13 (2000).

[26] R. Basu, T. Jessen, V. Naulin, and J. J. Rasmussen, Phys. Plasmas **10**, 2696 (2003).

[27] M. Priego, O. E. Garcia, V. Naulin, and J. J. Rasmussen, Phys. Plasmas **12**, 062312 (2005), 10.1063/1.1933779.

[28] P. W. Terry, Rev. Mod. Phys. **72**, 109 (2000).

[29] S. Zweben, W. Davis, S. Kaye, J. Myra, R. Bell, B. LeBlanc, R. Maqueda, T. Munsat, S. Sabbagh, Y. Sechrest, D. Stotler, and the NSTX Team, Nucl. Fusion **55**, 093035 (2015).

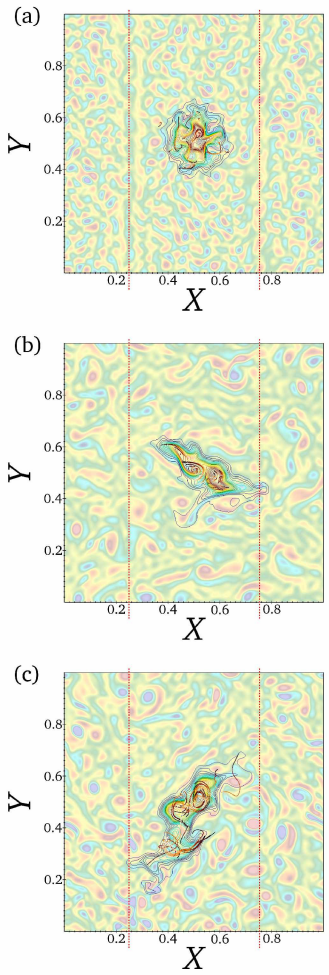

Figure 4.10: Selected tracers and passive scalar at time $t\Omega_i = 5$ overlaid on vorticity $\nabla^2\phi$ show similarities and differences depending on the turbulence regime. With $L_{c,P,x}^{-1} = 0$ (a), both the tracers and the passive scalar spread relatively equally in both directions reflecting the diffusive transport character. With $L_{c,P,x}^{-1} = 1$ (b), both the tracers and the passive scalar show elongation in the x-direction coinciding with the radial relaxations characteristic of this turbulence regime. With an external sheared poloidal flow $\Phi_0 = 0.2$, the tracers and the passive scalar are now elongated in the y-direction according to the imposed shear. Tracer trails are represented with dark colors being the most recent position and lighter colors for former positions. The passive scalar is shown with contour lines. Red dashed lines denote the location of the source at $x = 0.25$ and sink at $x = 0.75$.

Chapter 5 Conclusion

A scientific paradigm is defined in the 1960's according to Kuhn[1] as an incommensurable way of perceiving the world and practicing science in it. Although the notion of a paradigm can be generalized to social and cultural contexts, the focus here will only be in the context of scientific paradigms. A paradigm can include laws, theories, experimental measurements, and applications that are accepted examples of actual scientific practice. To be an accepted paradigm, a certain framework must seem better than competing frameworks, but it does not necessary need to explain all the facets of the natural phenomena. A paradigm becomes prominent when it is more successful than its contemporaries to understand the issue under interest. An example of this is the phenomenon of light where the wave and particle duality explains different facets more effectively than another. More importantly, each paradigm still possesses incomplete examples, which consequently motivates research in their respective paradigms. Each surpassed or supplemented paradigm is not necessarily a failure of the scientific method; for instance, Newtonian mechanics that has be superseded by General Relativity. More importantly, the paradigm sets up the framework at which the research is being directed in. However, research needs to be somewhat unattached from conceptual boxes, which retains a sense of arbitrariness to the endeavor. Science is usually motivated by certain assumptions of how the world operates, and its success derives, in part, from the community's ability to defend those assumptions, sometimes, at considerable cost. However, the commitment towards arbitrariness guarantees that novel ideas are not completely suppressed. When anomalies cannot be avoided and explained within existing framework, a new set of concepts must be developed leading to a new practice of science in order to accommodate the unanticipated observations. This transition can yield scientific revolutions.

Students starting in any scientific discipline will become familiar with the existing paradigms specific to that field, which is then one of the prerequisites for membership of that specific discipline. Standard reference texts are pedagogical means that perpetuate the current paradigms. As a result, fundamentals are often agreed upon and further research expands the current paradigms. The foundations are often agreed upon and taken for granted, which lessens the need to motivate from first principles and justify the use of each specific concept. Participants in the current paradigm, scientists and students alike, seemingly become part of a long-standing and static historical tradition unless they have been impacted by a paradigm shift. Scientific research under pre-existing paradigms constitutes concentrating on a small range of esoteric problems. This forces the investigation of a part of nature in detail, which is an essential part of the development of science. The success of scientific research is then a cumulative process that owes to its ability to solve problems to concepts and techniques close to those already in existence. Science cannot exist without a commitment to certain paradigms. Unanticipated novelty or a discovery

can emerge when techniques from the existing paradigm yield stubborn anomalous results that refuses to be assimilated into existing paradigms.

Several decades after its conception, sustainable nuclear fusion as an energy source still remains one of the outstanding engineering challenges of our time. Although the fundamental principles have been well known, the complex dynamics of this nonequilibrium system reveals our limited understanding of nature and, more specifically, turbulent transport. Confinement in tokamak plasmas for nuclear fusion has been an unsettled puzzle especially with the recognition of anomalous transport[2]. The persistent quandary of anomalous transport relating to unreconcilable differences between experimental measurements and theoretical predictions frames the issue in terms of a paradigm crisis. Hence, sustainable tokamak plasma operation requires a better understanding of the transport process in plasma turbulence. Despite the explosive improvements in computational capabilities, high fidelity whole device simulations of plasma turbulence remain computationally expensive and are intractable during actual device operation. Due to the nonlinear interplay between disparate scales, approaches to circumvent this obstacle such as reducing to low-dimensional transport models involve further understanding of the nature of plasma turbulent transport. Conventionally, transport models are based on the diffusive paradigm where effective transport coefficients are often derived from collisions and characteristic scales. However, the existing diffusive transport theory has been found to be inadequate to interpret the actual transport in fusion relevant plasmas.

In the language of paradigms, this thesis was realized at the juncture of two main paradigms: fluid turbulence[3] and SOC[4]. The SOC paradigm is being used heavily in this work to understand the phenomenon of transport in plasma turbulence. Although the impact of the SOC paradigm might not qualify as a scientific revolution associated with names such as Copernicus, Newton, Darwin, and Einstein, it certainly shifts the perspective in understanding plasma turbulence in the paradigm of magnetic plasma confinement for nuclear fusion in a tokamak device. With the increased awareness of anomalous transport supported by experimental evidence, a part of the tokamak fusion community recognizes that nature has somehow violated the conventional paradigm of diffusive transport. The paradigm of characteristic scales also permeates into the reasoning that shorter scale dynamics have negligible impact on larger scale dynamics, which is also the basis of modern numerical codes simulating tokamak plasmas. This view is quite different under the SOC paradigm. The failure or limitation of an existing framework is usually a precursor for the search for a new one, and it is often reflected by the proliferations of alternate theories within the same paradigm. For substantial change in interpretations, the existing paradigm cannot be rectified from within and would require a vital shift in the fundamental principles.

Like any shift in paradigm, the assimilation of the complementary paradigm from the convention is usually accompanied with resistance against a background of expectations. The advantage of the resistance ensures that the nascent paradigm must be rigorously vetted

in order to supplant the existing paradigm. The emergence of SOC in tokamak plasmas[5] is a response to a crisis in understanding anomalous transport that implicitly relates to plasma confinement time and, more importantly, the performance of tokamak devices. Although several relevant modifications have been proposed to mitigate the conflict posed by the evidence of anomalous transport with the diffusive paradigm, it is not until the adoption of the SOC paradigm that the conflict is easily resolved, namely that multiscale features are inherent to the nondiffusive framework. The use of SOC to further understanding plasma turbulence from different research groups also signifies some agreement in the direction of pursuit in understanding anomalous transport. However, the lack of dedicated experiments for SOC features in tokamak plasmas can be somewhat attributed to the lack of familiarity with it. Like most nascent candidate paradigms, the SOC paradigm has addressed only a handful of problems, and most of those solutions are still far from refined. As the experience with the SOC paradigm increases, experiments can then further pinpoint the features of SOC. At this stage, the SOC paradigm leading to the foundations of nondiffusive transport now offers a complementary approach towards understanding turbulent transport.

The transition to a new paradigm is often not a cumulative process. The new paradigm must be constructed from different fundamentals, and the assimilation process of a succeeding paradigm displaces the existing one. This is in process for the nondiffusive transport framework[6] where the fundamental propagators are stable Lévy distributions instead of a Gaussian distribution that remains the foundation of the diffusive transport framework. The stark difference from the nondiffusive transport framework is the use of fractional derivatives that express the correlations over space and time, which is quite different from the transport equation based solely on the diffusive paradigm where the lack of long range correlations reduce to characteristic scales. Although the nondiffusive transport can be seen as a competing paradigm for turbulent transport, it actually includes the existing paradigm of characteristic scales. Diffusive transport exists in regimes where SOC features are subdominant; diffusive transport is now a subset of nondiffusive transport. On the other hand, the features of the diffusive paradigm are inconsistent with the SOC paradigm, and practices or strategies based on characteristic scales must partially be reformulated.

Under the SOC paradigm for turbulent transport, the overall dynamics of a system becomes more complex than the sum of the dynamics from individual components. Common properties of SOC systems such as the profile resiliency and multiscale interactions are independent of the system. Elements for SOC-like models are: an evolving driving profile, an independent fueling process, the existence of critical gradients, and a process that relaxes the gradients. The turbulence relaxation paradigm coincides with the SOC paradigm quite closely, which appeals to study turbulence through a SOC perspective. The ubiquity of SOC features independent of the complexity of the model also strongly suggest some universal features of complex dynamics arising from the nonlinear interactions between individual parts. Since the SOC paradigm is still gathering support, the paradigm needs to

be motivated in the beginning as the foundation for this thesis. The somewhat extended motivation of this thesis allows the identification of the anomaly experienced regarding turbulent transport, which then leads to a need for a shift in perspective. Consistent with the practice in a paradigm, this work aims to expand on the fundamental paradigms and resists major substantiative claims. Hence, the overarching aim of this thesis is to add to the current scope where the candidate paradigm can be applied.

This work is distinguished from most other flux-driven work by making the connection between the sandpile model[7] and the standard drift-wave turbulence[8]. The model is based on both the paradigm involving characteristic scales and the multiscale paradigm. Rules for critical gradients were retained while the drift-wave turbulence sets up the instabilities and down-gradient transport. Characteristic scales were used to derive the base drift-wave turbulence model while the development of the flux-driven profile and the feedback to the turbulence are based on the SOC paradigm. The SOC elements were integrated into the pre-existing plasma fluid drift-wave turbulence paradigm by including a flux-driven profile and a critical gradient component. The results discussed in Chapter 2 and 3 identified the relative importance of each nondiffusive element, which expand and supplement the current understanding of the transport characteristics arising from a flux-driven profile. In addition to enabling enhanced down-gradient transport amplified through a critical gradient component, the simultaneous evolution of the profile also induces self-generated flows acting orthogonally to the gradient. Sheared flows then connect with another paradigm that addresses the impact of sheared flow on turbulent transport[9]. This dual reactions to the steepening of the local gradients are natural features of this model, which lead to nondiffusive signatures that reflect the dominant physical transport mechanism. The nonlinear interplay between the turbulence and the background profile allows a stiff profile within a range of fueling rates. A larger fueling rate can induce self-generated sheared flows perpendicular to the gradients through the asymmetry in the Reynolds stress term, which then naturally inhibits the down-gradient transport as discussed in Chapter 2. Due to a single critical gradient criterion in the model, the system becomes overdriven and SOC features such as extended avalanches diminish when the injection rate increases beyond a specific value. However, according to the paradigm of turbulence relaxation, the steepening of the gradients due to the reduced down-gradient transport tend to incite more instabilities such that the turbulence becomes the mechanism by which to transfer the accumulated energy. Coherent avalanche events then become more prominent as the profile sits closer to marginal. A steeper gradient would then be more susceptible to more vigorous relaxation events. Self-generated sheared flows and relaxation events occur simultaneously in response to the combination of a flux-driven profile and local critical gradients. The competition between profile relaxations and self-generated flows inevitably occurs when the turbulence and the profile are evolved simultaneously. This approach towards simultaneous evolution of both the fluctuations and the profile is a cornerstone of the SOC paradigm.

The transport effects due to the competing interactions between turbulence relaxations and sheared flows extend the applicability of the SOC paradigm on transport in fusion plasmas. With dominant sheared flows, the transport in the cross-flow direction can become suppressed, which is consistent with existing measurements and the paradigm on cross-flow transport. In systems with both a flux-driven background profile and sheared flows perpendicular to the gradient, the overall transport characteristics reflect the dominant mechanism. When sheared flows dominate, down-gradient transport becomes limited and the profile steepens, on average, to access larger growth rates that then drives turbulence. The dominant self-generated sheared flow occurring due to surface averaging the driving gradient presents a possible explanation for the turbulence mixing observed between the open-field region and the closed-field region in the tokamak's magnetic topology. However, subdiffusive transport is not reserved only for transport across sheared flows. Transport can be subdiffusive in regimes where trapping and detrapping process inhibits down-gradient transport as discussed in Chapter 3. Conversely, when turbulence relaxations dominate, the profile remain subcritical or near critical on average. Therefore, contrary to the normal diffusive paradigm, the standard diffusive regime occurs only as a special case when superdiffusive and subdiffusive transport mechanisms are somewhat balanced. Chapter 3 expands the dual reactions to include an external flow, which acts as an external forcing to the system. External sheared flows can limit the down-gradient transport; however, the extent to which external flows can reduce the cross-flow transport depends on the threshold for flow-driven instabilities. Flow-driven instabilities can drive the turbulence, which contradicts the intended purpose of driving the external sheared flows. Although the adverse effects flow-driven instabilities is undesirable in terms of confinement, the temporary turbulence mixing can provide a method to alleviate larger disruption events by controlling flow-driven instabilities.

The effects of the dual nature of flux-driven systems on turbulent transport demonstrate the complex dynamics exhibited by SOC-like systems that appeals to fusion plasmas. Although the results in Chapter 2 suggest that superdiffusive transport is inevitable when profiles sit near marginal, only a single background profile is evolved, which can be quite different in multispecies plasmas. With different channels of transport such as for ions and electrons, there can be scenarios where a marginal profile exists in one channel while another channel remains responsive to transfer energy and continuously alleviate large disruptions in a controlled manner. External sheared flows have been observed to reduce down-gradient transport and can be used to regulate plasma profiles possibly through external heating such as through radio-frequency waves[10]. Chapter 2 shows that the interplay between the flux-driven profile and external sheared flows also generate a dual effect on down-gradient transport. The external sheared flow reduces cross-flow transport and yield subdiffusive cross-flow transport. In conjunction, the external flow also inherently introduces another critical gradient condition as viewed through the SOC paradigm. Larger relaxations are then

observed when flow-driven instabilities are excited. Even though external sheared flows offer advantageous reduction in cross-flow transport, their applications must also take into account the development of flow-induced instabilities that can potentially excite effective mixing through turbulence.

The thesis ends in Chapter 4, which echoes the purpose of science in its pursuit to bring theory and measurements into closer agreement. The principal ideas in this chapter are the equivalent representation of turbulent flow information through the Lagrangian tracer particles and passive scalar[11] in the nondiffusive transport framework[6]. The results show the equivalence of the two ways of characterizing the dynamics of turbulent transport and extend the application of a passive scalar to quantify nondiffusive transport characteristics. The coincidence between tracers and the passive scalar in characterizing nondiffusive transport in specific regimes allow the application of more experimentally tractable methods for characterizing turbulent transport. The temporal scaling of the second moment and the propagator fitting method reveal the inherent differences between using tracers and a passive scalar to quantify transport characteristics. Given that measurements in laboratory frame is the preferred frame for experimental measurements, the results support the use of a passive scalar as a suitable measure for nondiffusive transport. The overall nondiffusive transport character when the distribution coincides with stable distributions and the width of the distribution spans more than a couple of turbulence structures. The results emphasize the limited applicability of quantifying transport using one realization of the turbulent state.

Returning to Kuhn's notion of a paradigm shift in the beginning of this section, the adoption of the SOC paradigm might not be immediately widespread but it is taking hold in the tokamak fusion community. The knowledge structure and relevant practices have been accumulated under this complimentary paradigm such as the identification of fundamental SOC ingredients as well as key features of SOC systems. The increasing acceptance of the nondiffusive transport framework also shows a transition from the diffusive paradigm that has ceased to function adequately under fusion relevant conditions. As an analog to political developments, a crisis is usually a prerequisite to revolution. However, science is not dependent on revolutions or paradigm shifts. The spirit of science depends on the discussion of competing theories, the willingness to investigate, the explicit discourse of discontent, and the return to fundamentals. The nondiffusive transport framework is a return to the fundamentals motivated by the crisis in the understanding of turbulent transport. This work spans the gap between an existing paradigm of characteristic scales and the contending paradigm based on SOC by incorporating elements from both paradigms. The nondiffusive transport framework is then used extensively to identify the transport characteristics, which then further extends the applicability of the new paradigm. As the SOC paradigm evolves to fruition in plasma turbulent transport, there will be more experimental measurements delineating SOC features. The continued and increased exploration basing on a different

paradigm, hopefully, lead to improvements in the predictions of turbulent transport, which will, ultimately, improve the confinement in fusion relevant conditions. Common to scientific paradigms, there will be other anomalies that will then ask for a different paradigm. Although science can be seemingly linear or cumulative, the history of science has evolved with punctuated instances of paradigm shifts. This is due to a somewhat fundamental truth that it is hard to make nature fit a set of paradigms.

[1] T. S. Kuhn, *The Structures of Scientific Revolutions*, 3rd ed. (The University of Chicago Press, Chicago, IL, 1996).

[2] B. A. Carreras, IEEE Trans. Plasma Sci. **25**, 1281 (1997).

[3] M. Lesieur, *Turbulence in Fluids*, 4th ed. (Springer, New York, NY, 2008).

[4] P. Bak, C. Tang, and K. Wiesenfeld, Phys. Rev. A **38**, 364 (1988).

[5] D. E. Newman, B. A. Carreras, and P. H. Diamond, Phys. Lett. A **218**, 58 (1996).

[6] R. Sánchez and D. E. Newman, Plasma Physics and Controlled Fusion **57**, 123002 (2015).

[7] T. Hwa and M. Kardar, Phys. Rev. A **45**, 7002 (1992).

[8] W. Horton, Rev. Mod. Phys. **71**, 735 (1999).

[9] P. W. Terry, Rev. Mod. Phys. **72**, 109 (2000).

[10] S. Panta and D. E. Newman, "Control of internal transport barriers in magnetically confined fusion plasmas," (2017), Nucl. Fusion (unpublished).

[11] G. Falkovich, K. Gawędzki, and M. Vergassola, Rev. Mod. Phys. **73**, 913 (2001).

Appendix A Sufficient sampling of R/S analysis for accurate identification of transport exponent in plasma turbulence[1]

A.1 Abstract

Insufficient sampling rate of a time series for R/S analysis can misrepresent the characteristics of a signal. This work shows that a diffusive transport character emerges from undersampling of subdiffusive Lagrangian velocity time series. The result reveals a caveat for using R/S analysis to characterize transport in turbulent medium. In a broader sense, a persistent or anti-persistent signal can be seemingly uncorrelated with undersampling.

A.2 Introduction

Rescaled range analysis (R/S) has been used extensively to quantify self-similarity in signals from the long time-lag scaling. The method has been proposed by Mandelbrot and Wallis[1] and based on hydrological data analysis by Hurst[2]. The exponent from the long-time scaling of R/S gives a measure of long-time dependencies in fluctuations. The estimation of the Hurst exponent is related to the fractional dimension of the time series[1]. For transport in turbulent fluids, the R/S of a Lagrangian velocity relates to the long-time evolution scaling of the second moment of Lagrangian trajectories; $\left\langle (\Delta r)^2 \right\rangle \sim t^{2H}$ where H is referred to as the transport, Hurst, or self-similarity exponent. In reference to measurements in fluids, a Lagrangian velocity refers to a velocity measured following the fluid motion, which is fundamental to measuring transport[3]. This contrasts with the Eulerian velocity where velocity is measured in a fixed reference frame with respects to the fluid motion. The scaling of the R/S estimates the transport exponent H, which identifies the transport regime within the general transport equation. According to the nondiffusive transport framework, the general transport equation is able to describe transport regimes that deviate from classical diffusion[4]. The general transport equation is defined by two parameters (α and β) relating to the family of distribution functions[5]. The exponent α reflects the spatial statistics, and β relates the temporal statistics. By comparing to a diffusive process, classical diffusion occurs when $H \sim 0.5$. Subdiffusion occurs when $H < 0.5$ (anti-correlated events or anti-persistent), and superdiffusion happens when $H > 0.5$ (correlated events or persistent). Depending on the sampling size in the time series, the R/S method usually overestimates Gaussian white noise to be $H > 0.5$[6]. In simulations for this work, a diffusive character is $H \sim 0.55$.

The measure of persistence in an arbitrary signal depends on the ordering of the

[1] D. Ogata, D. E. Newman, and R. Sánchez. Sufficient sampling of R/S analysis for accurate identification of transport exponent in plasma turbulence. Prepared for submission.

signal. It has been shown that known signals with $H \neq 0.5$ rearranged randomly will give a signature of $H \sim 0.5$ [7]. The reordering process introduces an artificial decorrelation mechanism that destroys correlations in the signal. In a similar manner, when identifying the transport characteristic in plasma turbulence, sufficiently small enough time lag resolution (dt) for the R/S analysis is an important criterion to accurately estimate the transport exponent. Due to the connection between transport character and the long-time scaling of the R/S analysis, this work has shown that a trace particle experiencing anti-correlated motion will exhibit a scaling with an exponent of $H \sim 0.5$ (diffusive) when the sampling rate for R/S ($f_s = dt_s^{-1}$) does not resolve the average Lagrangian velocity decorrelation time $\bar{\tau}_d$. Insufficient sampling rate f artificially introduces a decorrelation mechanism to the signal. As a result, the transport exponent is misinterpreted to be closer to diffusive rather than reflecting the signature of subdiffusive transport. The result from this work introduces an assumption in using R/S to identify transport signatures in turbulent fluids. In a broader sense not confined only to the R/S analysis, this result suggests a possible caveat towards characterization of persistence in an arbitrary signal. The dependence of R/S analysis on the chosen time lag has also been observed in gyrokinetics simulation of sprathermal ions in TORPEX [8]. The transport exponent can be misrepresented due to the modulations in the gyromotion of the ions.

A.3 Effect of sampling rate on transport exponents

In a simple slab geometry plasma fluid turbulence simulation with periodic boundary conditions, an external sheared flow in the poloidal direction with amplitude Φ_0 has been shown to inhibit transport across the shear region (radial direction) yielding subdiffusion with a transport exponent of $H \sim 0.3$ for a sufficiently large enough flow amplitude (Fig. A.1). The numerical model used has been documented elsewhere. One of the mechanisms to induce anti-correlated particle motion is through external shear velocity flow. Without a shear flow ($\Phi_0 = 0.0$), the transport is close to diffusive with $H \sim 0.55$ in both radial and poloidal directions. The Lagrangian velocity information is extracted by averaging over a population of 256 tracers. Tracers are particles following only the electrostatic $E \times B$ velocity. Tracers give the Lagrangian information about transport along the flow. The transport exponents have been decomposed in two orthogonal directions corresponding to the geometry of the simulation where the horizontal direction x corresponds to radial motion and the vertical direction y corresponds to the poloidal direction. With a sufficient sampling rate $f_s \sim f^*$ of the Lagrangian tracer's velocity for the R/S analysis, the subdiffusive character in the radial direction is recovered from the velocity data. With undersampling ($f_s < f^*$), the tracer's velocity is under-resolved. The undersampling results in a transport exponent that is closer to diffusive ($H(v_x) \sim 0.55$ for R/S).

Undersampling introduces an artificial decorrelation process responsible for the diffusive result. Although the tracers' positions trace the same paths (Fig. A.3), the R/S

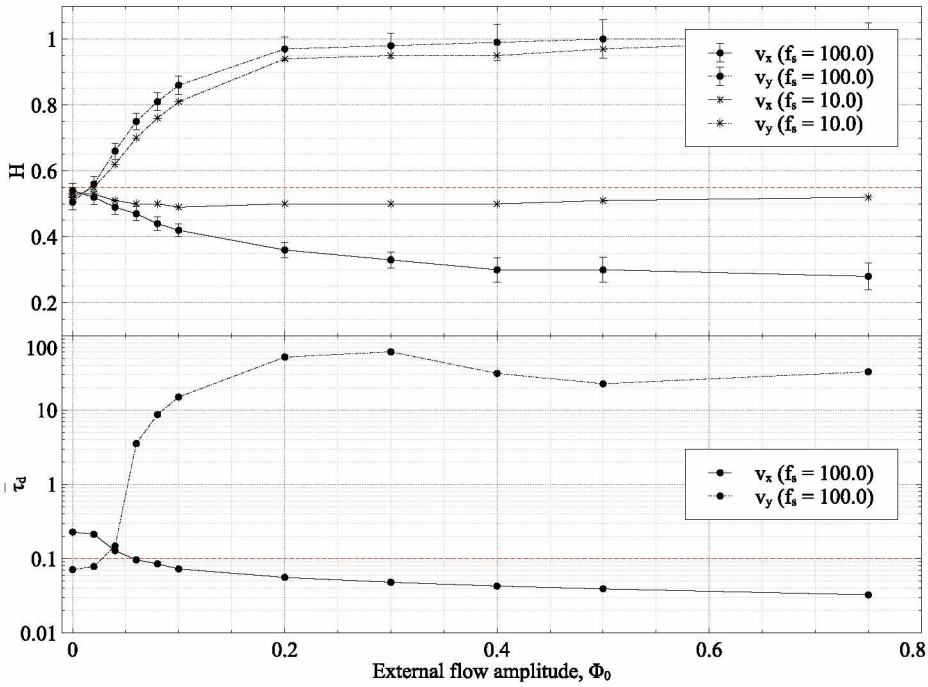

Figure A.1: Transport exponents H with varying external flow amplitude show subdiffusion in the cross-flow direction but superdiffusion in the flow direction. The dashed line in the average Lagrangian decorrelation time $\bar{\tau}_d$ represents the arbitrary sampling rate $f_s = 10.0$ for R/S that gives a diffusive character for $\Phi_0 > 0.1$ due to undersampling.

analysis uses the velocity data (Fig. A.2). In this sense, the decorrelation effect occurs in the velocity signal. Without the time resolved velocity data, the velocities appear to be uncorrelated between each time step, which yields a signature close to a classical diffusion. The misrepresentation of the transport exponent through the R/S analysis is related to the average Lagrangian decorrelation time of the velocity signal $\bar{\tau}_d$. As a demonstration in Fig. A.1, the sampling rate for R/S is set at an arbitrary rate ($f_s = 10.0$ or $dt_s = 0.1$) such that it is less than the decorrelation rate for $\Phi_0 > 0.1$. The frequency is normalized to the ion gyrofrequency $f \to f/\Omega_i$ and $t \to t\Omega_i$. The radial transport exponent becomes closer to diffusive $H(v_x) \sim 0.55$ when $\Phi_0 > 0.1$. This means that Φ_0 is large enough to produce a decorrelation rate faster than the specified sampling rate ($f_d = \tau_d^{-1} > f_s$). On the other hand, when the sampling rate is set to $f_s = 100.0$, the transport exponents reflect the subdiffusive character. The results do not change for larger sampling rates, $f_s > 100.0$.

An example of the undersampling impact on the radial transport exponent $H(v_x)$ is shown in Fig. A.2 with different sampling frequencies f_s. Identical velocity signal with a decorrelation time of $\tau \simeq 0.32$ is sampled at three frequencies. The sampling frequency $f_s = 100.0$ is already ten times greater than the simulation time step $f = dt^{-1} = 1000.0$. The velocity is well resolved up to $f_s = 10.0$, which is reflected in the identical subdiffusive or anti-persistent signature $H(v_x) = 0.32$. When $f_s = 1.0$, the insufficient time resolu-

tion introduces an artificial decorrelation element into the R/S analysis, which causes the signature to be diffusive or uncorrelated $H(v_x) \sim 0.55$.

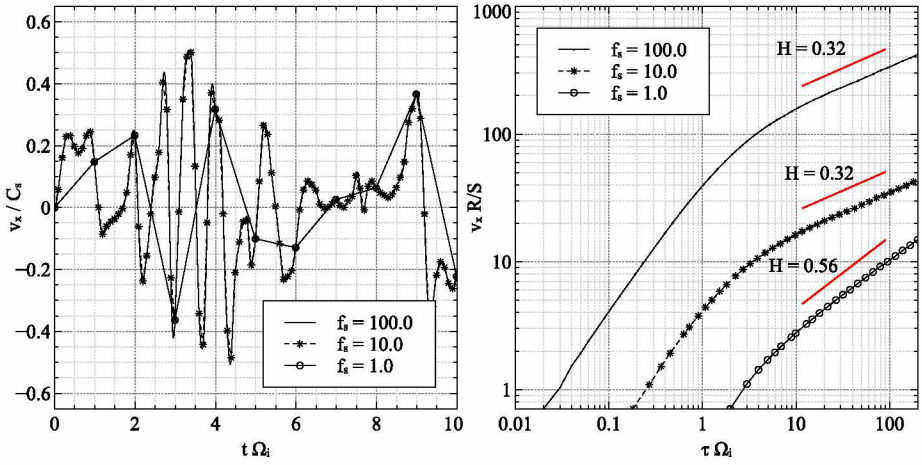

Figure A.2: The identical velocity signals at different sampling frequencies f_s (left) with corresponding H from R/S (right) show that the transport signature becomes diffusive $H(v_x) \sim 0.55$ when $f_s < f_*$.

An example of undersampled tracer trajectories shown in Fig. A.3 depict the misrepresentation of the transport exponent. Plotted here is the tracer's trajectory instead of the velocity time series used for the R/S. Although the tracer's trajectory is exactly the same in both cases, the transport exponent misrepresents the actual dynamics when the velocity is taken at a time step larger than the decorrelation time of the velocity signal. Although the scaling of $H \sim 0.5$ has been thought to be related to the convergence of the numerical integration algorithm, this effect is not due to the numerical integration scheme. The deviation in the transport exponent is due to the smallest dt chosen for the R/S analysis, which is an external contribution unrelated to the stability of the numerical integration scheme.

Up until this point, only anti-persistent signals have been discussed. Persistent signals can also be affected by the sampling rate. The extent of the deviation depends on the amount of persistency in the signal. For instance with the rainfall data yielding $H = 0.72$ [2], a reduction of f_s does not decrease the long-time scaling, which suggests persistency over large time scales. For signals that are not persistent on all time scales, such as the tracer motion in the poloidal direction, undersampling also introduces an artificial decorrelation mechanism and decreases the persistence of the signal. Compared to anti-persistent signals, a persistent signal on all time scales is less susceptible to dynamical misrepresentation due to undersampling. From these results, the decorrelation time $\bar{\tau}_d$ sets the minimum limit for data sampling in order to accurately produce the self-similar exponent. For R/S analysis, the difference between the actual exponent to $H \sim 0.55$ depends on the difference between f_d and f_s. For persistent and anti-persistent signals, the estimate is similar when $f_s \sim f_d$.

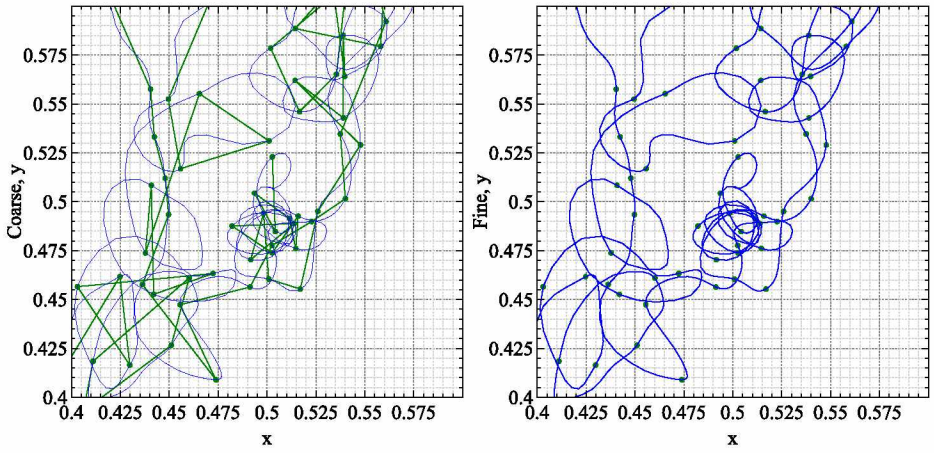

Figure A.3: Trajectories at different sampling rates $f_s = 10.0$ gives $H(v_x) = 0.49$ (left) while $f_s = 100.0$ gives $H(v_x) = 0.33$ (right) show approximately the same tendencies and does not reflect the flow dynamics used for R/S analysis.

However, the deviation becomes more noticeable when $f_d > f_s$ especially for anti-persistent signals.

Within the estimation of turbulent transport, undersampling leads to inaccurate interpretation of the transport process. A superdiffusive or subdiffusive process can be misrepresented as being close to diffusive due to an artificial decorrelation mechanism introduced from insufficient data sampling rate that does not properly resolve the degree of persistency in the velocity signal. As a result, when the data sampling rate f_s is physically set by data acquisition, transport in turbulence can have a diffusive signature due to undersampling ($f^* > f_s$). This also suggests that f_s needs to be increased when experimentally and technically possible in order to parse accurate character of the transport. Although this work suggests that $\bar{\tau}_d$ is a possible measure for an appropriate sampling rate ($f^* = f_d$), it is not possible to use this quantity as an indicator when $f_s < f_d$. The signature of an undersampled signal will be close to diffusive, which needs to be checked for convergence with a smaller sampling rate.

A.4 Conclusion

When using R/S for transport characterization, insufficient sampling rate can misrepresent subdiffusion to be be diffusive. This work also shows that insufficient sampling can affect the identification of superdiffusive transport exponents. The deviation from accurate estimation relates to the difference between the decorrelation time and the sampling time. A broader implication of this result relates to the characterization of persistence in an arbitrary time series. When referring to an arbitrary time series, the Hurst parameter reflects persistence. An undersampled time series can lead to a misrepresentation of the self-similarity characteristic of the data. This then leads to misrepresentation of the sig-

nal as lacking persistence instead of persistent or anti-persistent. Dynamics occurring at a shorter time scale can still be masked due to limitations in the acquisition of the signal itself. And, although this work is focused on the R/S analysis, the implication suggests a general limitation in characterizing time series due to sampling rate.

A.5 Acknowledgements

This work was supported in by US DOE contract number DE-FG02-04ER54741 with UAF and in part by a grant of HPC resources from the Arctic Region Supercomputing Center at the University of Alaska Fairbanks.

A.6 References

[1] B. B. Mandelbrot and J. R. Wallis, Water Resources Res. **4**, 909 (1968).

[2] H. E. Hurst, Trans. Amer. Soc. Civil Eng. **116**, 770 (1951).

[3] M. Lesieur, *Turbulence in Fluids*, 4th ed. (Springer, New York, 2008).

[4] G. Zaslavsky, Physics Reports **371**, 461 (2002).

[5] R. Sánchez, B. A. Carreras, D. E. Newman, V. E. Lynch, and B. P. van Milligen, Phys. Rev. E **74**, 016305 (2006).

[6] R. Weron, Physica A **312**, 285 (2002).

[7] B. A. Carreras, B. P. van Milligen, M. A. Pedrosa, R. Balbín, C. Hidalgo, D. E. Newman, E. Sánchez, M. Frances, I. García-Cortés, J. Bleuel, M. Endler, C. Riccardi, S. Davies, G. F. Matthews, E. Martines, V. Antoni, A. Latten, and T. Klinger, Phys. Plasmas **5**, 3632 (1998).

[8] A. Bovet, M. Gamarino, I. Furno, P. Ricci, A. Fasoli, K. Gustafson, D. Newman, and R. Sánchez, Nucl. Fusion **54**, 104009 (2014).

Appendix B Local blob spread analysis from GPI data on NSTX[1]

B.1 Abstract

Blob spreading has been quantified using the D_α signal from GPI diagnostic on NSTX. In the moving reference frame of a blob, and assuming a general non-diffusive formulation, blob spreading can be best fitted to the diffusive model. From this, the spreading of an individual blob can then be quantified in terms of a spreading coefficient, which is analogous to a diffusion coefficient. Blobs in H-mode and Ohmic plasmas in NSTX show distinguishing spreading coefficients. Spreading coefficients also depend on the proximity to the separatrix. This segregation can be used to characterize blobs in diffferent regimes. The spreading coefficient might be used as a quantitative measure of the local dynamics for blobs across machines and between experiments and simulations.

B.2 Background

Transport in the edge of tokamak devices has been an issue of strong interest for sustainable fusion plasmas. Plasma "blobs" are isolated structures in the plasma edge that moves generally into the scrape-off-layer (SOL)[1]. Hence, there is an interest in understanding the dynamics of blobs especially in the SOL region. Blob structure and motion can be quite complicated due to tokamak geometry, regime of collisionality, ion temperature effects, drift wave, parallel transport, and density gradients.

One of the principal blob investigations uses the gas-puff-imaging (GPI) diagnostic at National Spherical Torus Experiment (NSTX)[2]. It images the D_α line emission with a fast framing camera from injected neutral gas cloud at the edge of the device[1]. The view of the GPI diagnostic is aligned such that the horizontal direction (x) coincides with the radial direction across magnetic flux surfaces, and the vertical direction in the GPI view closely aligns with the poloidal direction (y). The same NSTX blob database as in Zweben *et al.*[3] is used in this analysis. There are two main plasma discharges in this database: Ohmic and H-mode. The criteria for shot selection are: constant plasma current, toroidal field, and applied heating power; lack of large MHD activity; lack of L-H or H-L transitions; aligned magnetic field to the GPI view; adequate GPI signal levels; and fairly fixed separatrix position.

The measured D_α light signal is due to the excitation of deuterium D_α line. The D_α signal is a function of primarily three factors: the local deuterium neutral density (n_0), the local electron density (n_e), and the local electron temperature (T_e); $S = n_0 f(n_e, T_e)$[4].

[1]D. Ogata, D. E. Newman, and S. J. Zweben. Local blob spread analysis from GPI data on NSTX. Prepared for submission to Physics of Plasmas.

The time-averaged light emission has been calculated using the 3D Monte Carlo simulation DEGAS2 and showed agreement in the 2D distribution and magnitude of the D_α signal with the time-averaged signal from quiescent H-mode discharges[5]. To date, direct interpretations of the GPI fluctuations in terms of physical quantities such as local electron density or temperature fluctuations require additional assumptions. In contrast, this work uses the processed D_α light to determine the spreading of a blob in a co-moving frame but does not interpret these results in terms of density nor temperature fluctuations.

This type of analysis has not been performed previously on experimental data or blob data. Due to the connection between transport and the evolution of particle distribution, the initial motivation stems from the interest in determining the turbulent transport characteristics in the plasma edge. The GPI diagnostic provides a suitable setup that allows the tracking of temporal and spatial dynamics in the plasma edge. This process has been used successfully quantify nondiffusive transport in plasma fluid simulations based on the drift-wave turbulence model[6].

This work is presented as follows: the proposed data analysis workflow from image treatment to the fitting process is outlined in Sec. B.3, the results from GPI data on NSTX are presented in Sec. B.4, known issues relating to the entire workflow are mentioned in Sec. B.5, and the conclusions and potential applications are in Sec. B.6.

B.3 Method

This work concentrated on plasma discharges with two plasma conditions: Ohmic and H-mode[3]. Tab. B.1 lists the main plasma parameters for the Ohmic and H-mode discharges used in this paper. The H-mode discharges had a slightly larger toroidal field and 4MW of neutral-beam-injection (NBI) power. The separatrix position $\rho = 0\,cm$ is determined by the EFIT separatrix position. The drift-wave gyroradius is calculated from $\rho_s = 100\,(M_i T_e)^{1/2}\,/Z_i B_t$[7] where $M_i = 2$, $Z_i = 1$, and B_t is the toroidal field at the GPI location. Blobs were identified and tracked from this shot database over a duration of $1\,ms$ (~ 400 frames) near the peak of the GPI signal.

There are three main steps in order to prepare GPI data for the propagator fitting: image treatment (Sec. B.3.1), blob identification and tracking (Sec. B.3.2), and blob extraction (Sec. B.3.3). After the preparation, the propagator fitting scheme is then applied to the processed data (Sec. B.3.4). The absolute D_α signal S from each GPI frame is submitted to the workflow, which is summarized in an expression for S'';

$$S'' = \frac{\left[\langle S'_{blob}\rangle_y\right]_{c,x} - \left\langle\left[\langle S'_{blob}\rangle_y\right]_{c,x}\right\rangle_{edge}}{\int \left[\langle S'_{blob}\rangle_y\right]_{c,x} - \left\langle\left[\langle S'_{blob}\rangle_y\right]_{c,x}\right\rangle_{edge} dx} \tag{B.1}$$

where S' is the subtracted D_α signal. The horizontal coordiante in a GPI frame is denoted

Table B.1: Plasma parameters for the discharges (adapted from Zweben *et al.*[3]).

	Ohmic	H-mode
Shot range	141 746-756	140 389-395
Time range (ms)	$213 - 214$	$535 - 550$
I_p (kA)	830	830
B_t (kG)	3.6	4.9
κ (elongation)	1.9	2.4
W_{MHD} (kJ)	32	220
$\bar{n}_e$ ($10^{13}\,cm^{-3}$)	1.6	5.2
P_{NBI} (MW)	0	4.0
$T_e(0)$ (eV)	530	920
$n_e(0)$ ($10^{13}\,cm^{-3}$)	2.3	5.6
$T_e(a)$ (eV)	13 ± 6	29 ± 17
$n_e(a)$ ($10^{13}\,cm^{-3}$)	0.37 ± 0.23	0.92 ± 0.54
$T_e(\rho = -2\,cm)$ (eV)	23 ± 4	134 ± 53
$n_e(\rho = -2\,cm)$ ($10^{13}\,cm^{-3}$)	0.47 ± 0.17	2.1 ± 0.47
$\rho_s(\rho = -2\,cm)$ (cm)	0.2	0.3
$\tau_{ei}(\rho = -2\,cm)$ (μs)	0.5	1.5
# blobs processed	41	53

with x and the veritcal is y. The *blob* subscript is a numerical process that isolates the blob within a specific region-of-interest (ROI). The ROI is selected from the largest extent of the blob over all frames that the blob exists. The poloidal averaging within the ROI is denoted by $\langle \ldots \rangle_y$. And, the centering of the horizontal slice is denoted by $[\ldots]_{c,x}$. The averaging process over the edge pixel values is denoted by $\langle \ldots \rangle_{edge}$.

B.3.1 Image treatment

The GPI data is treated before the propagator fitting method. GPI frames are extracted over a $1\,ms$ interval near the peak GPI light signal where each GPI frame is smoothed using a Gaussian filter that convolves over 3×3 neighboring pixels in 2D. Then, blobs are identified by applying the blob detection algorithm[8] to each subtracted D_α signal from each GPI frame. The subtracted D_α signal is defined as $S' = S - \langle S \rangle_t$. The time average $\langle \ldots \rangle_t$ is done over all frames within the $1\,ms$ time interval. Done this way, each GPI frame is subtracted by $\langle S \rangle_t$ in order to avoid the increase in D_α signal when a blob moves to the open-field region. This is a different approach to normalizing the D_α signal. Under the conditions that n_e and T_e fluctuations are highly correlated with each other, as predicted from edge turbulence theory[9,10], the local D_α fluctuations should have a direct relationship to the local electron density fluctuations.

The D_α light emission can be parametrized as $S = n_0 n_e^\gamma T_e^\eta$ where n_0 is the neutral deuterium density. For small fluctuations, $\delta S/S = \gamma\,(\delta n_e/n_e) + \eta\,(\delta T_e/T_e)$. Separate probe measurements of both δn_e and δT_e in the SOL have shown that $\delta n_e/n_e \gg \delta T_e/T_e$, which

suggests that $\delta S/S$ depends primarily on the electron density fluctuations. As a result, the relative D_α signal $\delta S/S$ relates to the fluctuations in the relative electron density, which then provides a direct correlation between S and n_e [1].

The normalized signal $\delta S/S$ gives a direct relation to electron density fluctuations, that is advantageous for relating the D_α light emission to the turbulence in the SOL. In a different viewpoint, the subtracted signal S' used in this work provides a more tractable quantity in terms of the presented workflow. The two approaches to treat the absolute D_α signal can be connected by considering $\delta S/S$ as the relative emission light intensity with respects to a time averaged light signal, which then gives $\delta S/S \rightarrow (S - \langle S \rangle_t) / \langle S \rangle_t = S' / \langle S \rangle_t$. Hence, the two approaches towards treating the light intensity is quite similar.

B.3.2 Blob identification and tracking

The blob detection algorithm [8] fits an ellipse to elevated D_α signal satisfying picked criteria where the defaults are used. Blobs are tracked by its centers of the ellipse with two criteria: lifetime and separation distance from centers. The lifetime of a blob is selected to be over 15 frames ($37.5\,\mu s$ for $dt = 2.5\,\mu s$ at $400,000\,\mathrm{Hz}$). The maximum separation between blobs in a subsequent frame is specified to be 10 pixels ($3.75\,cm$ for $dx = 0.375\,cm$/pixel at $24\,cm/64\,$pixel). Although a blob is tracked when both of the criteria are satisfied, there are still inaccuracies in tracking (i.e. blob "jumps"). An example of the blob tracking routine is visually shown by overlaid arrows in B.1 (#140389 at $532.72\,ms$ for 4MW NBI heated plasma). Concurrent with the tracked blob, a region-of-interest (ROI) is also identified by encasing the blob with a square region. The square is defined from adding 5 pixels ($1.875\,cm$) to the maximum of the major or minor radius. The selection of 5 pixels coincide with the maximum separation distance of 10 pixels of an identified blob between two successive frames. The maximum ROI for the lifetime of the tracked blob is then used to extract the data. After the ROI has been defined, this region is then centered in the middle of the GPI frame by shifting the center of the blob to $\sim 12\,cm$. Only the D_α signal in the ROI is considered for further processing. The entire process described in this section is denoted by the *blob* subscript in Eq. B.1.

B.3.3 Blob extraction

Next, the isolated blob is averaged in the vertical direction (y) just within the ROI. This gives a limited poloidal average sense, which is denoted by $\langle \ldots \rangle_y$. The averaging operation immediately collapses and mixes the data in the y-direction. Although there are significant structure in the poloidal direction, this operation focuses on the radial spreading in the blob's frame. A similar methodology can be done to investigate the poloidal spreading of the blob.

For quantification of evolution in the radial direction across the flux surfaces, a

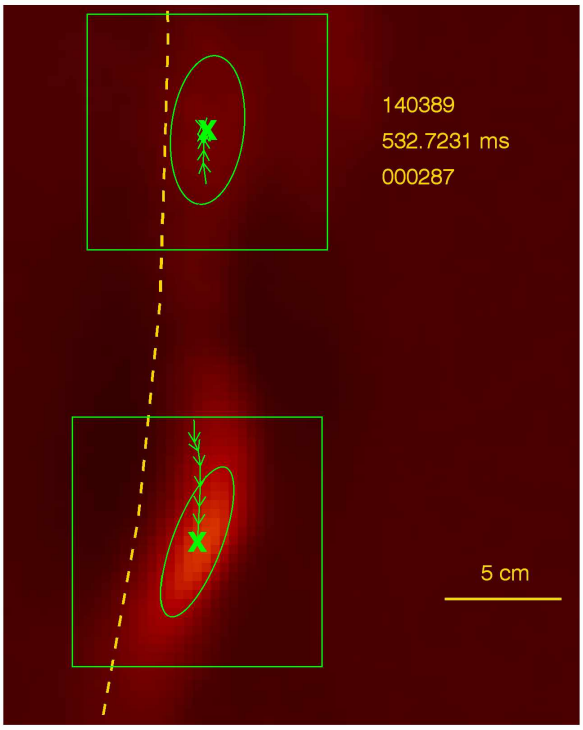

Figure B.1: Tracked blob in H-mode discharge (#140389) at $532.72\,ms$ demonstrates the blob tracking algorithm where the symbol "X" marks the estimated location of the maximum light signal, arrows denote previous positions, and a rectangular box denotes the ROI. The EFIT separatrix position is denoted by the dashed line.

horizontal slice is then taken through the blob's center in the y-direction. The horizontal data gives a somewhat relatively close measure to the radial transport of the blob. The slice is then centered on a coordinate $x \in [-12\,cm, 12\,cm]$ such that the blob's horizontal center is aligned with $x = 0.0\,cm$. This process involves shifting the data such that the blob center coincides with $x = 0.0\,cm$. In sum, the entire centering process selects only a slice of data at the y-center of the blob and shifts the x-center of the blob to $x = 0.0\,cm$. It is denoted by $[\ldots]_{c,x}$. Any data exceeding the limit is truncated.

Due to the outlined process of isolating the blob within a particular ROI, there exists region where the D_α signal is elevated. This is managed by taking the time average of the data at the edge (one pixel) of the extracted slice. The extracted data is then shifted depending on the average edge values. This entire process is denoted by $\langle\ldots\rangle_{edge}$

As the final step, the poloidal-averaged and recentered slice is then normalized by the horizontal total of this quantity, which is denoted by the integration,

$$\int \left[\langle S'_{blob}\rangle_y\right]_{c,x} - \left\langle \left[\langle S'_{blob}\rangle_y\right]_{c,x}\right\rangle_{edge} dx. \tag{B.2}$$

Fig. B.2 shows the time evolution of the extracted slices of a simulated diffusive data. Truncated data produces the sharp edges seen at larger times. The extracted data can then

be fed into a fitting routine where the solution of the general transport equation is fitted.

B.3.4 Propagator fitting

According to some authors[11,12], nondiffusive transport is defined as an extension of the traditional transport equation for an evolution of an arbitrary quantity $f(x,t)$ that follows the form:

$$\frac{\partial^\beta f}{\partial t^\beta} = \chi_{\alpha,\beta} \frac{\partial^\alpha f}{\partial |x|^\alpha}. \tag{B.3}$$

for $x \in \mathbf{R}$ and $t \in \mathbf{R}^+$ where $\beta \in (0,1]$ and $\alpha \in (0,2]$ are known as fractional transport exponents, and $\chi_{\alpha,\beta}$ is the fractional transport coefficient[13]. The operators in Eq. B.3 are integro-differential operators often referred to as fractional derivatives, which provide variable definitions between integer derivatives[14]. The non-local feature of these operators capture transport that deviates from classical diffusion. Eq. B.3 can be derived from the long-term, long-distance limit of a continuous time random walk (CTRW) process in which particle steps are distributed according to a symmetric α-Lévy distribution with a tail index $\alpha \in (0,2]$ and waiting-times distributed according to an extremal β-Lévy distribution with a tail index $\beta \in (0,1]$[11,12,15].

For a diffusive process, the spatial distribution converges to a Gaussian distribution where $\alpha \to 2$. Without memory, the process converges to a Markovian process where $\beta \to 1$. A diffusive process is then recovered with exponents $\alpha = 2$ and $\beta = 1$, which means that a diffusive process is now a subset of the possible solutions. Propagators are the Green's function to Eq. B.3. Hence, the connections of Eq. B.3 with the propagators can be exploited to provide methods to determine parameters α, β, and $\chi_{\alpha,\beta}$ that naturally leads to the characterization of transport. Among the several methods available, the fitting process for the propagators employs the nonlinear least-squares fitting (Levenberg-Marquardt) algorithm[16].

Although Eq. B.3 has been constructed primarily for turbulent transport processes, the propagators also provide a more general class of stable distributions for a fitting routine. The significance of these propagators is that the temporal and spatial dimensions are fitted simultaneously according to Eq. B.3 and the information of the dynamics are encoded into the fitted parameters; α, β, and $\chi_{\alpha,\beta}$.

B.4 Results

Best fits using Eq. B.3 are diffusive ($\alpha = 2$, $\beta = 1$, and $\chi_{2,1} = D$). Although analogous to a diffusion coefficient, the term spreading coefficient is used in describing D in order to distinguish from the transport of energy or particles. The temporal and spatial evolution of a generated diffusive process ($D_{in} = 10.0\, m^2/s$) passed through the image

processing workflow that gives S'' according to Eq. B.1 is shown in Fig. B.2. The result after the fitting process is shown in Fig. B.3 where α and β are fixed ($\alpha = 2$ and $\beta = 1$). The spreading coefficient is determined to be $D_{\text{fit}} = 7.8\,m^2/s$, which underestimates the input by a factor of ~ 0.22 due primarily to the clipping in the tails of the distribution (Fig. B.3) as required by the specification of the ROI (Sec. B.3). Using the same scheme as presented

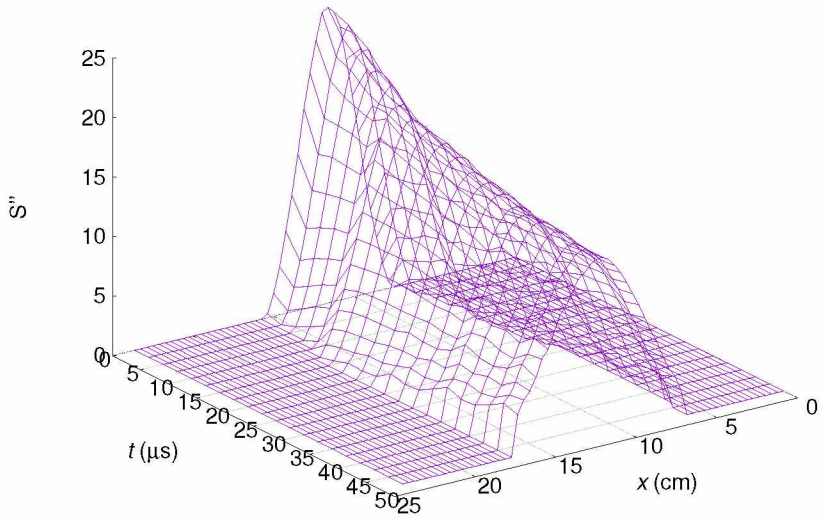

Figure B.2: Processed quantity S'' for generated 2D data for a diffusive process $\alpha = 2$, $\beta = 1$, and a diffusion coefficient of $D = 10.0\,m^2/s$ shows data clipping due to the ROI selection. The pixel dimension is equivalent to the GPI frame, and the the number of time frames correspond to a timespan of $\Delta t = 50\,\mu s$.

with the generated know data of a diffusive process, the workflow is applied to GPI data. As an example of the entire proposed workflow, an identified blob in a typical 4 MW of NBI (#140389) at about $532.72\,ms$ (bottom blob in Fig. B.1) are shown qualitatively in Fig. B.4 after the image processing and Fig. B.5. Although blobs often display peaked light distribution, there is no inherent constraint on the shape of the distribution. This is then reflected in the deviations from stable distributions at later times (Fig. B.4). For this blob, the fitting process is performed over nine frames starting at time $t \sim 532.72\,ms$ with a $dt = 2.5\,\mu s$. Hence, the spreading coefficient is determined over only a timespan of $\Delta t = 20.0\,\mu s$.

The entire process discussed in Sec. B.3 has been applied to about 90 qualified blobs from the NSTX database[3]. The results are summarized in Fig. B.6 according to the spreading coefficient D, the goodness-of-fit χ^2, and the blob regimes. Blobs considered near the EFIT separatrix position ($\rho = 0\,cm$) are within $\rho = +2\,cm$. Blobs in the SOL

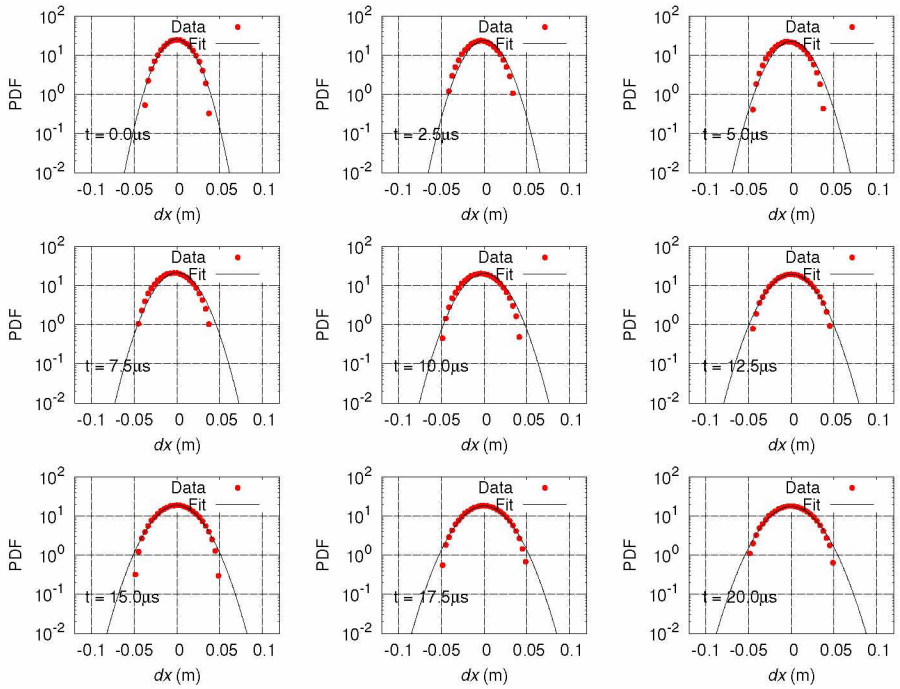

Figure B.3: Fitting for known generated data of $D_{in} = 10.0\,m^2/s$ at different times yield $D_{\text{fit}} = 7.8\,m^2/s$ with a goodness of fit $\chi^2 = 0.23$.

are $\rho > 2\,cm$ from the separatrix. Although there are still significant spread in D_{fit}, there is a clustering of average spreading coefficients for different blob regimes. For fits with $\chi^2 < 4$, there are distinctions between the plasma conditions and the location of the blobs. Blobs in H-mode plasmas in the SOL tend to have an average spreading rate of $\sim 1.54\,m^2/s$ (Fig. B.6). H-mode blobs near the separatrix show an average spreading rate of $\sim 0.64\,m^2/s$. Whereas, blobs in Ohmic plasmas near the separatrix tend to spread with a rate of $\sim 1.02\,m^2/s$. Although blobs in Ohmic plasmas and H-mode plasmas near the separatrix show relative coincidence with Gaussian distributions, there is a significant large variability in the values for H-mode blobs in the SOL. Blobs in Ohmic plasmas in the SOL and inside the separatrix ($\rho < -2\,cm$) for both plasma conditions tend not to follow Eq. B.3, which are poor candidates for the fitting process.

B.5 Discussions

The applicability of the this method depends on several factors. One of the notable issues pertaining to the method is that additional assumptions are required in order to interpret the spreading of the light signal to physical quantities such as electron density or temperature. Another factor that limits the tracking of the blob is that blobs can merge, split into smaller blobs, or simply dissociate. Particularly in H-mode plasmas, blobs can merge and tend to break in the SOL. Eq. B.3 is not suitable for blobs undergoing these type

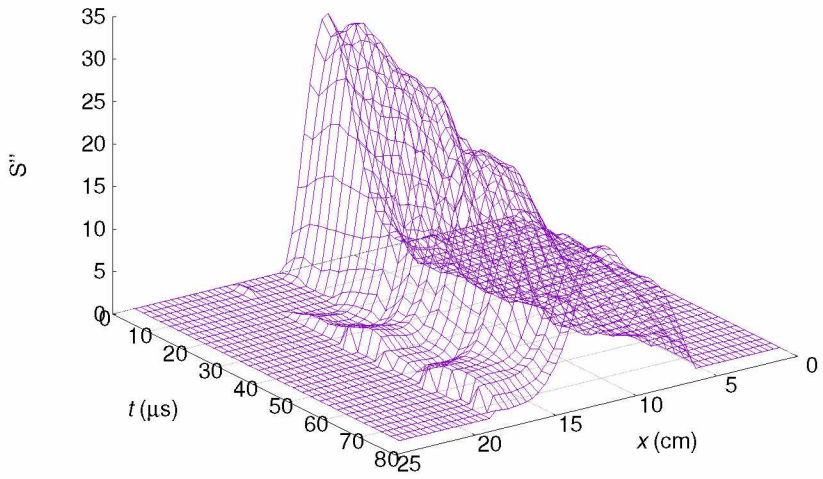

Figure B.4: Processed quantity S'' for a tracked blob in its reference frame that is detected at about $532.70\,ms$ in H-mode discharge (#140389) shows a decrease in D_α signal as it propagates over a timespan of $\Delta t = 75\,\mu s$. The number of pixels correspond to the width of the GPI frame of 64 pixels.

of processes. Pertaining to the image processing scheme outlined in Sec. B.3, the per-slice normalization adds additional weight on smaller and more confined signal, which then yields a smaller value for the spreading coefficient. Although the majority of the blobs tend to decrease in D_α signal[3] as they propagate into the SOL, the filtering process for candidate blobs inherently requires the light signal to decrease over time, which restricts the possible dynamics the blobs that can be fitted with Eq. B.3. As a result, the number of qualified blobs is about a third ($\sim$ 90) of the entire identified blob population ($\sim$ 300) using the prescribed workflow in Sec. B.3.

According to the theory of blob regimes, suitable blobs for this fitting scheme based on Eq. B.3 are primarily near the separatrix, which are categorized as being partially or fully resistively disconnected from the sheaths. This is attributed to the higher density and longer connection lengths[3]. As observed from this work, blobs experience a transition as it moves from the separatrix to into the SOL. This behavior might coincide with the regime change from inertial to sheath-connected regimes[3].

The large spread in D_{fit} for blobs in H-mode plasmas in the SOL suggests that the plasma conditions are more variable but not nondiffusive. The nonlinear processes (e.g. blobs splitting and merging) in the SOL of H-mode plasmas can lead to dynamics that cannot be simply described by Eq. B.3. In contrast, the blobs in H-mode plasmas near the

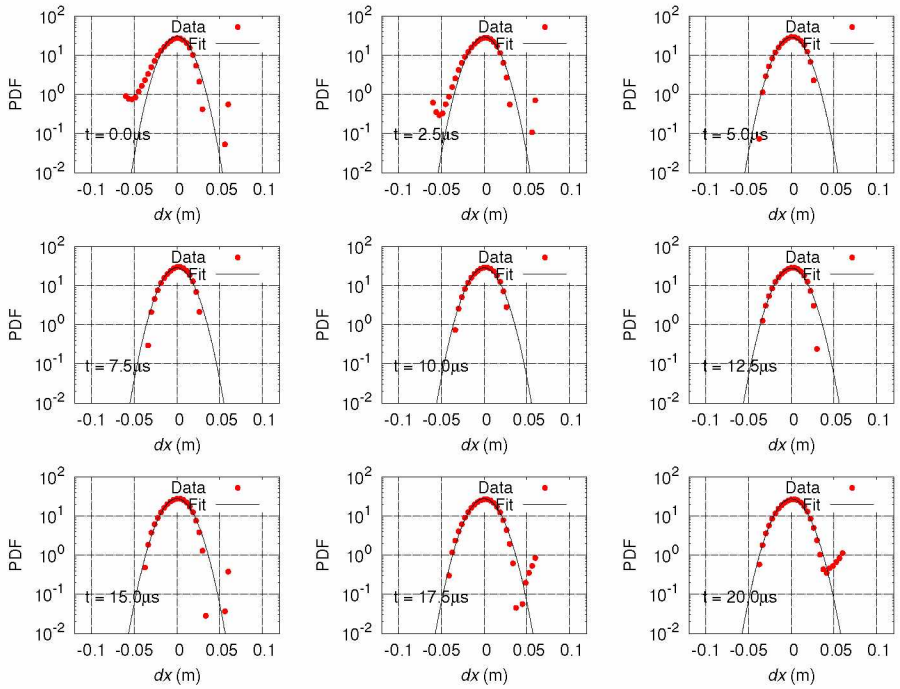

Figure B.5: Fitting process of a blob in its reference frame starting at about $532.70\,ms$ in H-mode discharge (#140389) yields $D_{\text{fit}} = 1.31\,m^2/s$ with a goodness of fit $\chi^2 = 0.81$. Each panel (left to right and top to bottom) denotes a time slice separation of one GPI frame ($dt = 2.5\,\mu s$).

separatrix have well-defined characteristics suitable for this analysis, which further suggests that the dynamics near the separatrix can be close to classical diffusion.

In H-mode discharges, blobs outside of the separatrix spread at rate that is more than twice faster than the blobs near the separatrix. This can be related to the previous analysis of $\delta S/S$ where the fluctuation increases, on average, outside of the separatrix ($\rho > +2\,cm$)[1]. The difference in the spreading rate is also consistent with the trend in $\delta S/S$ for blobs near the separatrix in Ohmic and H-mode discharges (i.e. Fig. 3(a) in Zweben *et al.*[1]). The relative light intensity $\delta S/S$ in Ohmic discharges is greater, on average, than the H-mode discharges, which can correspond to a larger spreading rate for blobs in Ohmic discharges.

For candidate blobs, the advantage of using the propagator fitting method developed from the nondiffusive framework defines a quantity that encodes the blob spreading dynamics independent of the physical plasma parameters. The change in the spread of a blob can reflect different plasma conditions. In addition, given that the GPI diagnostics measures the dynamics of quantities in an Eulerian frame, the correspondence between the transport measures in both the Lagrangian and Eulerian frame allows a possible measure of the underlying transport[17]. Hence, the fitted spreading coefficients used in conjunction with the GPI might relate to the underlying turbulent transport despite being performed

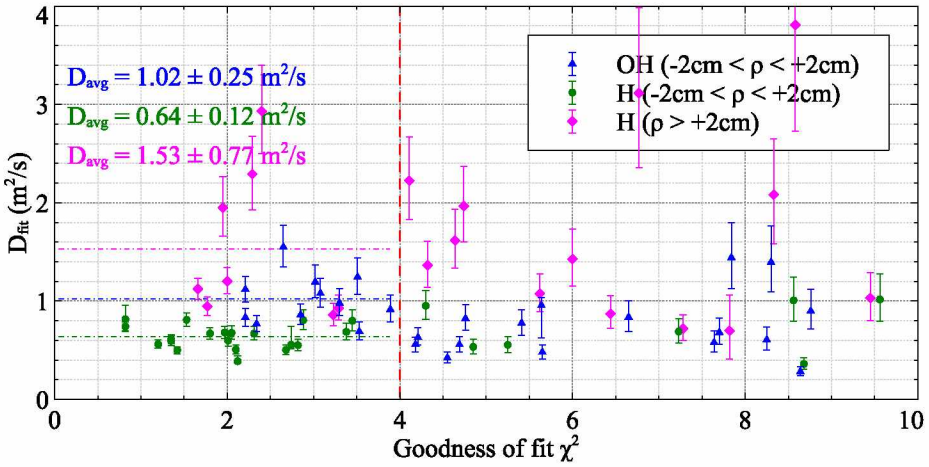

Figure B.6: Fitted diffusion coefficient for selected blobs from the NSTX database[3] can distinguish between plasma conditions. Blobs near the separatrix are quantified predominantly within $+2\,cm$ from the separatrix, and outside the separatrix corresponds to $> 2\,cm$. Blobs in H-mode near the separatrix show an average spreading coefficient that is almost half of the blobs near the separatrix in the Ohmic plasmas.

on only a short timespan of $\Delta t = 20.0\,\mu s$.

B.6 Conclusions

This work demonstrates the application of the propagator fitting approach towards quantifying the spreading of blobs in the SOL of NSTX. A fitting scheme is arranged by using the general transport equation as a fitting function to the D_α signal of a blob in its moving frame, which allows data to be fitted both temporally and spatially. Although best fits tend to be diffusive, the general transport equation admits a wider range of solutions.

The fitted spreading coefficients were segregated according the the spatial locations of the blobs in reference to the separatrix, which can distinguish between the behaviors in the closed-field region and the open-field region. Due to the significant spread in the data, the implications are not direct and warrant further investigations. The fitted coefficients give a measure of the local radial spreading of D_α emission intensity within the constrained time window. Blobs in H-mode plasmas in the SOL spread, on average, approximately three times faster than the blobs near the separatrix. For blobs near the separatrix, the spreading rate for blobs in Ohmic plasmas, on average, is approximately twice as fast as the blobs in H-mode plasmas.

Although the results cannot be directly relate to the transport properties in this plasma region nor to the transport of local physical quantities such as density or temperature, the spreading coefficient provides a dynamical measure of the data and can be used as a quantity for comparison between different experiments and simulations. Previous comparisons between experimental measurements and simulations rely heavily on local fluctuations

and the time averaged D_α signal. This approach can add to existing measures by providing a local dynamical quantity that depends only on the evolution of the envelope of D_α signal.

B.7 Acknowledgements

The authors would like to thank J. Myra, D. Stotler, T. Stoltzfus-Dueck, and R. Sánchez for helpful discussions.

This material is based upon work supported by the U.S. Department of Energy, Office of Science, Office of Workforce Development for Teachers and Scientists, Office of Science Graduate Student Research (SCGSR) program. The SCGSR program is administered by the Oak Ridge Institute for Science and Education (ORISE) for the DOE. ORISE is managed by ORAU under contract number DE-AC05-06OR23100.

B.8 References

[1] S. Zweben, W. Davis, S. Kaye, J. Myra, R. Bell, B. LeBlanc, R. Maqueda, T. Munsat, S. Sabbagh, Y. Sechrest, D. Stotler, and the NSTX Team, Nucl. Fusion **55**, 093035 (2015).

[2] S. Zweben, R. Maqueda, D. Stotler, A. Keesee, J. Boedo, C. Bush, S. Kaye, B. LeBlanc, J. Lowrance, V. Mastrocola, R. Maingi, N. Nishino, G. Renda, D. Swain, J. Wilgen, and the NSTX Team, Nucl. Fusion **44**, 134 (2004).

[3] S. J. Zweben, J. R. Myra, W. M. Davis, D. A. D'Ippolito, T. K. Gray, S. M. Kaye, B. P. LeBlanc, R. J. Maqueda, D. A. Russell, D. P. Stotler, and the NSTX-U Team, Plasma Phys. Control. Fusion **58**, 044007 (2016).

[4] D. P. Stotler, D. A. D'Ippolito, B. LeBlanc, R. J. Maqueda, J. R. Myra, S. A. Sabbagh, and S. J. Zweben, Contrib. Plasma Phys. **44**, 294 (2004).

[5] B. Cao, D. Stotler, S. Zweben, M. Bell, A. Diallo, and B. Leblanc, Fusion Sci. Tech. **64**, 29 (2013).

[6] J. A. Mier, R. Sánchez, L. García, B. A. Carreras, and D. E. Newman, Phys. Rev. Lett. **101**, 165001 (2008).

[7] D. A. Russell, D. A. D'Ippolito, J. R. Myra, J. M. Canik, T. K. Gray, and S. J. Zweben, Phys. Plasmas **22**, 092311 (2015).

[8] W. Davis, M. Ko, R. Maqueda, A. Roquemore, F. Scotti, and S. Zweben, Fusion Eng. Des. **89**, 717 (2014), proceedings of the 9th IAEA Technical Meeting on Control, Data Acquisition, and Remote Participation for Fusion Research.

[9] J. Myra, W. Davis, D. D'Ippolito, B. LaBombard, D. Russell, J. Terry, and S. Zweben, Nucl. Fusion **53**, 073013 (2013).

[10] S. J. Zweben, B. D. Scott, J. L. Terry, B. LaBombard, J. W. Hughes, and D. P. Stotler, Phys. Plasmas **16**, 082505 (2009).

[11] R. Metzler and J. Klafter, Phys. Reports **339**, 1 (2000).

[12] G. Zaslavsky, Physics Reports **371**, 461 (2002).

[13] F. Mainardi, Y. Luchko, and G. Pagnini, Frac. Calc. App. Anal. **4**, 153 (2007).

[14] I. Podlubny, *Fractional Differential Equations* (Academic Press, San Diego, California, 1999).

[15] R. Sánchez, B. A. Carreras, and B. P. van Milligen, Phys. Rev. E **71**, 011111 (2005).

[16] W. H. Press, S. A. Teukolsky, W. T. Vetterling, and B. P. Flannery, *Numerical Recipes in FORTRAN; The Art of Scientific Computing*, 2nd ed. (Cambridge University Press, New York, NY, USA, 1993).

[17] D. Ogata, D. Newman, and R. Sánchez, Phys. Plasmas (submitted) (2017).